Accounting for concrete plastic-damage and steel bars ductile-damage when modeling reinforced concrete columns in finite element applications

by

Nader Zad

B.S., Azad University, 2004
M.S., Kansas State University, 2018

AN ABSTRACT OF A DISSERTATION

submitted in partial fulfillment of the requirements for the degree

DOCTOR OF PHILOSOPHY

Department of Civil Engineering
Carl R. Ice College of Engineering

KANSAS STATE UNIVERSITY
Manhattan, Kansas

2023

Abstract

Testing full-scale structures in the laboratory is neither always doable nor financially feasible, especially for large structures. Therefore, these structures are often modeled with Finite Element Analysis (FEA) software and packages, such as Abaqus, to understand their actual behaviors under special simulated loading and material-behavioral considerations. The work in this dissertation addresses two main issues: The first is the accurate modeling of the material to account for plastic damage of the concrete, and the other is the modeling of the steel used in the reinforcement including the ductile damage of the metal.

The study of the concrete material is aimed at developing a material model that simulates load-induced cracking in reinforced concrete (RC) elements in the FEA structures. The simulation of complete stress-strain concrete behavior under tension and compression (including damage characteristics) requires the application of numerical material models, potentially producing the stress-strain curves. These models include strain-softening regimes that presuppose the use of ultimate compressive concrete strength and that can be practically implemented for existing or future RC structures. The method presented in this study is valuable because it assesses existing RC structures when detailed test results are not available. However, the implemented numerical models were slightly altered in order to compare them with the damage plasticity models available in the research literature. These mainly are the smeared crack concrete model, the brittle crack concrete model, and the concrete damage plasticity model, which are all typically suitable for RC elements. The methodologies proposed here provide accurate and realistic modeling of the plastic damage of reinforced concrete members. Although numerically extensive and very time-consuming, it is demonstrated that the material and damage modeling presented in this research study can be used to accurately represent the behavior of actual structural members tested in research laboratories. This suggests that it is applicable to structures for which experimental tests or monitoring data are not available.

With regards to the steel reinforcement, the structural steel modeling for cyclic response is essential for the functioning appraisal and design of steel structures. Though various mathematical models have been suggested and developed to simulate metal plasticity, only a few of them have been implemented in finite element method-based software such as Abaqus, which uses incremental plasticity procedures. This part of the dissertation research introduces and briefly describes a built-in "Isotropic, Kinematic, Johnson-Cook, User and Combined" hardening to model metal plasticity under cyclic loading. The plastic deformation is load path-dependent and irreversible. Implementation of this model is fundamentally significant for Abaqus users to increase understanding of the behavior and plasticity of steel and reinforced (concrete) structures.

Accounting for concrete plastic-damage and steel bars ductile-damage when modeling reinforced concrete columns in finite element applications

by

Nader Zad

B.S., Azad University, 2004
M.S., Kansas State University, 2018

A DISSERTATION

submitted in partial fulfillment of the requirements for the degree

DOCTOR OF PHILOSOPHY

Department of Civil Engineering
Carl R. Ice College of Engineering

KANSAS STATE UNIVERSITY
Manhattan, Kansas

2023

Approved by:

Major Professor
Hani G. Melhem

Copyright

Abstract

Testing full-scale structures in the laboratory is neither always doable nor financially feasible, especially for large structures. Therefore, these structures are often modeled with Finite Element Analysis (FEA) software and packages, such as Abaqus, to understand their actual behaviors under special simulated loading and material-behavioral considerations. The work in this dissertation addresses two main issues: The first is the accurate modeling of the material to account for plastic damage of the concrete, and the other is the modeling of the steel used in the reinforcement including the ductile damage of the metal.

The study of the concrete material is aimed at developing a material model that simulates load-induced cracking in reinforced concrete (RC) elements in the FEA structures. The simulation of complete stress-strain concrete behavior under tension and compression (including damage characteristics) requires the application of numerical material models, potentially producing the stress-strain curves. These models include strain-softening regimes that presuppose the use of ultimate compressive concrete strength and that can be practically implemented for existing or future RC structures. The method presented in this study is valuable because it assesses existing RC structures when detailed test results are not available. However, the implemented numerical models were slightly altered in order to compare them with the damage plasticity models available in the research literature. These mainly are the smeared crack concrete model, the brittle crack concrete model, and the concrete damage plasticity model, which are all typically suitable for RC elements. The methodologies proposed here provide accurate and realistic modeling of the plastic damage of reinforced concrete members. Although numerically extensive and very time-consuming, it is demonstrated that the material and damage modeling presented in this research study can be used to accurately represent the behavior of actual structural members tested in research laboratories. This suggests that it is applicable to structures for which experimental tests or monitoring data are not available.

With regards to the steel reinforcement, the structural steel modeling for cyclic response is essential for the functioning appraisal and design of steel structures. Though various mathematical models have been suggested and developed to simulate metal plasticity, only a few of them have been implemented in finite element method-based software such as Abaqus, which uses incremental plasticity procedures. This part of the dissertation research introduces and briefly describes a built-in “Isotropic, Kinematic, Johnson-Cook, User and Combined” hardening to model metal plasticity under cyclic loading. The plastic deformation is load path-dependent and irreversible. Implementation of this model is fundamentally significant for Abaqus users to increase understanding of the behavior and plasticity of steel and reinforced (concrete) structures.

Table of Contents

List of Figures x
List of Tables xiv
Acknowledgments........ xvii
Dedication xviii
Chapter 1 : Introduction 1
1.1 Goals and objectives 1
1.2 Organization of this dissertation 2
Chapter 2 : Modeling Plastic-Damage of Reinforced Concrete in Finite Element Applications ... 4
2.1 Introduction 4
2.2 Principle of Concrete Cracking 5
2.3 Dilation Angle at High Confining Pressure (ψ) 7
2.4 Eccentricity of the Potential Plastic Surface (e) 8
2.5 (γ) Parameter 8
2.6 Viscosity Parameter (μ) 8
2.7 Concrete Behavior 9
2.7.1 Concrete Compressive Behavior 9
2.7.2 Concrete Tensile Behavior 12
2.8 Fracture Energy 14
2.9 Developing the Material Model 14
2.9.1 Tension Stiffening Relationship 16
2.9.1.1 Interaction Between Concrete and Steel 18
2.9.2 Compressive Stress-Strain Relationship 18
2.10 Implementation of the Damage Model 21
2.11 Finite Element Modeling of the RC Column 25
2.12 Conclusion 34
2.13 Application to Future Research 34
3.14 Data Availability Statement 35
2.15 Acknowledgments 35
2.16 Notation List 35

Chapter 3 : Modeling Ductile-Damage of Steel of Reinforced Concrete Columns by Finite Element Method 40
3.1 Introduction 40
3.2 Historical Remarks 41
3.2.1 Pioneering Work 41
3.2.2. Classical Theory 42
3.3 One-Dimensional Stress-Strain Analysis 44
3.4 Plastic Behavior in Simple Tension and Compression 44
3.4.1. Monotonic Loading 44
3.4.2. Unloading and Reloading 45
3.4.3. Reversed Loading 47
3.5 Modeling of Uniaxial Behavior in Plasticity 48
3.5.1. Simplified Uniaxial Tensile Stress-Strain Curves 48
3.5.1.1. Elastic-Perfectly Plastic Model 48
3.5.1.2. Elastic-Linear Work-Hardening Model (Figure 3.6) 48
3.5.1.3. Elastic-Exponential Hardening Model 49
3.6 Tangent Modulus E_t and Plastic Modulus E_p 49
3.7 Hardening Rules 51
3.8 Hardening Plastic Stress Analysis 53
3.9 Bounding Surface Theory 54
3.10 Hardening in Abaqus 55
3.10.1. Isotropic Hardening 55
3.10.2. Kinematic Hardening 58
3.10.3. Johnson-Cook Hardening 61
3.10.4. User Hardening 61
3.10.5. Combined Isotropic Kinematic Hardening 61
3.10.6 von Mises stress 64
3.11 Parameters of Steel Stress-Strain Relationship (Mander Model) 65
3.12 Ramberg-Osgood Model 73
3.12.1 Equation Version 1 74
3.12.2 Equation Version 2 74

3.12.3 Equation Version 3 83
3.13 Linear Hardening 86
3.13.1 Linear kinematic hardening model 87
3.14 Prager's Hardening Rule 87
3.15 Abdel-Karim and Ohno Plasticity Model 89
3.16 Chaboche kinematic hardening rule 93
3.17 Ohno-Wang model I (OWI) 97
3.18 Chaboche model and Ohno-Wang model I (OWI) comparison 99
3.19 von Mises stress 101
3.20 Mander and Ramberg-Osgood Model Comparison 105
3.21 Finite Element Modeling of a Reinforced Concrete (RC) Column 107
3.22 Conclusion 110
3.23 Acknowledgments 111
Chapter 4 : Considering both Plastic-Damage of Concrete and Ductile-Damage of Reinforcing Steel in Finite Element Applications; Verification Problem #2 115
4.1 Introduction 115
4.2 Specimen Description 116
4.3 Concrete Behavior 117
4.3.1 Concrete Compressive Behavior 117
4.3.2 Concrete Tensile Behavior 119
4.4 Tension Stiffening Relationship 120
4.5 Compressive Stress-Strain Relationship 121
4.6 Implementation of the Damage Model 122
4.7 Steel Behavior 126
4.7.1 Parameters of Steel Stress-Strain Relationship (Mander Model) 126
4.7.1.1 Longitudinal Steel Bars 126
4.7.1.2 Transverse Steel bars 129
4.8 Ramberg-Osgood Model 132
4.8.1 Longitudinal Steel Bars 132
4.8.2 Transverse Steel Bars 135
4.9 Linear Hardening 139

4.9.1 Linear kinematic hardening model ... 139
4.10 Prager’s Hardening Rule ... 140
4.11 Abdel-Karim and Ohno Plasticity Model ... 140
4.12 Chaboche kinematic hardening rule ... 143
4.13 Ohno-Wang model I (OWI) ... 147
4.14 Chaboche model and Ohno-Wang model I (OWI) comparison ... 149
4.15 von Mises stress ... 151
4.16 Material Properties ... 154
4.17 Control Specimens ... 155
4.18 Test Procedure ... 155
4.19 Finite Element Modeling of the RC Column ... 155
4.20 Results ... 156
4.21 Conclusions ... 160
Chapter 5 : Summary, Conclusion and Recommendations ... 162
5.1 Summary ... 162
5.2 Conclusions ... 162
5.3 Recommendations for future work ... 163

List of Figures

Figure 2.1. Drucker-Prager failure surface [7] 6
Figure 2.2. Concrete triaxial failure space [8] 7
Figure 2.3. Idealized stress-strain curve for concrete in uniaxial compression 9
Figure 2.4. Modified Hognestad stress-strain curve for concrete in uniaxial compression 11
Figure 2.5. Tensile stress–strain curve of concrete 13
Figure 2.6. Sample tensile stress–strain curve of concrete 14
Figure 2.7. Stress-strain plots for damage plasticity 15
Figure 2.8. Terms for tension stiffening model 16
Figure 2.9. Terms for compressive stress-strain relationship 21
Figure 2.10. Tension Damage Model for 3,160 psi Concrete 23
Figure 2.11. Compression Damage Model for 3,160 psi Concrete 25
Figure 2.12. Specimen elevation 27
Figure 2.13. Column cross-section details 27
Figure 2.14. Top beam cross-section details 28
Figure 2.15. Isometric 3-D view 29
Figure 2.16. Applied displacement history per Sezen's research 30
Figure 2.17. Applied displacement history based on the experimental results for U1, Top (top lateral displacement) 30
Figure 2.18. Applied displacement history: calculated results 31
Figure 2.19. Relationship between lateral load and lateral displacement for experimental and numerical (Abaqus) test 32
Figure 2.20. Relationship between lateral displacement and vertical displacement for experimental and numerical (Abaqus) test 33
Figure 2.21. Relationship between lateral load and vertical displacement for experimental and numerical (Abaqus) test 33
Figure 3.1. Stress-strain diagram for mild steel 44
Figure 3.2. Stress-strain diagram for some other metals 45
Figure 3.3. Loading, unloading, and reloading paths 46
Figure 3.4. Bauschinger effect 47

Figure 3.5. Idealized stress-strain curve for elastic-perfectly plastic model 48
Figure 3.6. Idealized stress-strain curve for elastic-linear work-hardening model 48
Figure 3.7. Idealized stress-strain curve for elastic-exponential hardening model 49
Figure 3.8. Tangent modulus E_t 50
Figure 3.9. Plastic modulus E_p 50
Figure 3.10. Isotropic hardening 51
Figure 3.11. Kinematic hardening 52
Figure 3.12. Independent hardening 53
Figure 3.13. Unloading and reloading from a plastic state-hysteretic loop in a cycle of loading 54
Figure 3.14. Unloading and reloading from a plastic state-idealized stress-strain curve 55
Figure 3.15. Isotropic hardening 56
Figure 3.16. Isotropic hardening (with expanding yield surface due to plastic deformation) and the corresponding uniaxial stress-strain curve [10] 57
Figure 3.17. Reversed loading accompanied with isotropic hardening (a) yield surface; (b) which results in stress-strain curve [10] 58
Figure 3.18. Kinematic hardening 59
Figure 3.19. Kinematic hardening (a) translation $|x|$ of the yield surface with plastic strain; (b) The resultant strain-stress curve with shifted yield stress in compression (Bauschinger effect) [10] 60
Figure 3.20. Non-linear kinematic hardening and the resulting non-linear hardening stress-strain curve (saturates at stress $\boldsymbol{\sigma y + c\gamma}$) [10] 61
Figure 3.21. Combined kinematic and isotropic hardening [10] 62
Figure 3.22. Isotropic strain hardening model for steel [12] 63
Figure 3.23. Kinematic strain hardening model for steel [12] 63
Figure 3.24. Combined strain hardening model for steel [12] 63
Figure 3.25. Yield surface of von Mises for plane stress and correspondent in the stress-strain curve for two-dimensional uniaxial straining [10] 64
Figure 3.26. (a) the von Mises yield surface in plane stress for viscoplasticity with linear isotropic hardening, with viscous (overstress) stress σ_v, and (b) the associated stress-strain curve [10] 65
Figure 3.27. Parameters of stress-strain curve for reinforcing steel [13] 66

Figure 3.28. Mander stress-strain curve for longitudinal steel in tension ... 71
Figure 3.29. Mander stress-strain curve of transverse steel in tension ... 73
Figure 3.30. Idealized stress-strain curve for Ramberg-Osgood model ... 74
Figure 3.31. Engineering and true stress-strain curves for Ramberg-Osgood model (longitudinal) ... 78
Figure 3.32. Ramberg-Osgood true stress-true strain curve of the longitudinal steel in tension. 79
Figure 3.33. Engineering and true stress-strain curves of Ramberg-Osgood model for transverse steel ... 82
Figure 3.34. Ramberg-Osgood stress-strain curve of transverse steel in tension ... 83
Figure 3.35. Results of interpolation and approximation approaches considering the interval from 0.2% to $\boldsymbol{\varepsilon us}$: a) Grade 20, b) SS304, c) SS316L SLM XY [16], d) AlSi10Mg SLM Z [17] (RO: Ramberg-Osgood) ... 85
Figure 3.36. Results of interpolation and approximation approaches considering the interval from 0.5% to $\boldsymbol{\varepsilon us}$: a) Grade 20, b) SS304, c) SS316L SLM XY [16], d) AlSi10Mg SLM Z [17] ... 86
Figure 3.37. Chaboche model of longitudinal steel ... 96
Figure 3.38. Chaboche model of transverse steel ... 97
Figure 3.39. Ohno and Wang I (OWI) model of longitudinal steel ... 98
Figure 3.40. Ohno and Wang I (OWI) Model of transverse steel ... 99
Figure 3.41. Chaboche and Ohno-Wang model I (OWI) of the longitudinal steel comparison 100
Figure 3.42. Chaboche and Ohno-Wang model I (OWI) of the transverse steel comparison ... 101
Figure 3.43. Mander & Ramberg-Osgood model curves comparison for longitudinal steel ... 106
Figure 3.44. Mander & Ramberg-Osgood model curves comparison for transverse steel ... 107
Figure 3.52. Relationship between lateral load and lateral displacement for experimental and numerical (Abaqus) test ... 108
Figure 3.53. Relationship between lateral displacement and vertical displacement for experimental and numerical (Abaqus) test ... 109
Figure 3.54. Relationship between lateral load and vertical displacement for experimental and numerical (Abaqus) test ... 109
Figure 4.1. Specimen elevation ... 117
Figure 4.2. Column cross-section details ... 117

Figure 4.3. Modified Hognestad stress-strain curve for concrete in uniaxial compression....... 119
Figure 4.4. Sample tensile stress–strain curve of concrete 120
Figure 4.5. Tension damage model for 3,080 psi concrete 124
Figure 4.6. Compression damage model for 3,080 psi concrete.. 125
Figure 4.7. Mander stress-strain curve for longitudinal steel in tension.................................. 129
Figure 4.8. Mander stress-strain curve of transverse steel in tension 131
Figure 4.9. Engineering and true stress-strain curves for Ramberg-Osgood model (longitudinal) 134
Figure 4.10. Ramberg-Osgood stress-strain curve of the longitudinal steel in tension 135
Figure 4.11. Engineering and true stress-strain curves for Ramberg-Osgood model (transverse) 138
Figure 4.12. Ramberg-Osgood stress-strain curve of the longitudinal steel in tension 139
Figure 4.13. Chaboche model for the longitudinal steel 146
Figure 4.14. Chaboche model for the transverse steel 147
Figure 4.15. Ohno and Wang I (OWI) model for the longitudinal steel.................................. 148
Figure 4.16. Ohno and Wang I (OWI) Model for the transverse steel 149
Figure 4.17. Chaboche and Ohno-Wang model I (OWI) of the longitudinal steel comparison 150
Figure 4.18. Chaboche and Ohno-Wang model I (OWI) of the transverse steel comparison 151
Figure 4.19. Isometric 3-D view 156
Figure 4.20. Generalized load vs. deformation in terms of overall average strain for experimental test 157
Figure 4.21. Generalized load vs. deformation in terms of overall average strain 158
Figure 4.22. Generalized load vs. deformation in terms of localized strain at mid-height, at the location of Gauge 2 159
Figure 4.23. Generalized load vs. deformation in terms of localized strain at mid-height, at the location of Gauge 3 159

List of Tables

Table 2.1. Compressive stress-strain values for 3,160 psi (21.78 MPa) concrete 10
Table 2.2. Tensile stress-strain values for 3,160 psi (21.78 MPa) concrete 17
Table 2.3. Compressive stress-strain values for 3,160 psi (21.78 MPa) concrete 19
Table 2.4. Tensile Damage Values for 3,160 psi Concrete 22
Table 2.5. Compressive Damage Values for 3,160 psi (21.78 MPa) Concrete 23
Table 2.6. Plastic Properties of the Concrete 26
Table 3.1. Tensile stress, strain, plastic strain values for longitudinal steel (Mander)................ 68
Table 3.2. Tensile true stress-true strain values for longitudinal steel (Mander) 69
Table 3.3. Tensile true stress-true plastic strain values for longitudinal steel (Mander)............. 70
Table 3.4. Tensile stress, strain, plastic strain values of transverse steel (Mander) 71
Table 3.5. Tensile true stress-true strain values of transverse steel (Mander)............................. 72
Table 3.6. Tensile true stress-true plastic strain values of transverse steel (Mander) 72
Table 3.7. Tensile stress, strain, plastic strain values for longitudinal steel (Ramberg-Osgood) 75
Table 3.8. Tensile true stress-true strain values for longitudinal steel (Ramberg-Osgood) 76
Table 3.9. Tensile true stress-true plastic strain values for longitudinal steel (Ramberg-Osgood) 77
Table 3.10. Tensile stress, strain, plastic strain values for transverse steel (Ramberg-Osgood). 79
Table 3.11. Tensile true stress-true strain values for transverse steel (Ramberg-Osgood).......... 80
Table 3.12. Tensile true stress-true plastic strain values for transverse steel (Ramberg-Osgood) 81
Table 3.13. Mechanical properties of metallic alloys considered in this study on Ramberg-Osgood parameters identification 84
Table 3.14. Results of proposed interpolation approach (i) in comparison with results of the least square method (a) – experimental data are used in the interval from 0.2% to $\boldsymbol{\varepsilon us}$.............. 85
Table 3.15. Results of proposed interpolation approach (i) in comparison with results of the least square method (a) – experimental data are used in the interval from 0.5% to $\boldsymbol{\varepsilon us}$.............. 85
Table 3.16. C_i values in psi unit for longitudinal steel based on the Ramberg-Osgood model after modification 91

Table 3.17. γ_i values for longitudinal steel based on the Ramberg-Osgood model after modification 91
Table 3.18. C_i values in psi unit for transverse steel based on the Ramberg-Osgood model after modification 92
Table 3.19. γ_i values for transverse steel based on the Ramberg-Osgood model after modification 93
Table 3.20. Chaboche α and σ values (longitudinal) 93
Table 3.21. Chaboche α and σ values (transverse) 94
Table 3.22. Chaboche true plastic strain and Chaboche true stress of longitudinal steel 94
Table 3.23. Chaboche true plastic strain and Chaboche true stress of transverse steel 95
Table 3.24. Chaboche true plastic strain and Chaboche analytical true stress in psi of longitudinal steel 95
Table 3.25. Chaboche true plastic strain and Chaboche analytical true stress in psi of transverse steel 96
Table 3.26. Parameters of longitudinal steel for Ramberg-Osgood’s model derived from the MATLAB code 104
Table 3.27. Parameters of transverse steel for Ramberg-Osgood’s model derived from the MATLAB code 105
Table 4.1. Compressive stress-strain values for 3,080 psi (21.23 MPa) concrete 118
Table 4.2. Tensile stress-strain values for 3,080 psi concrete 120
Table 4.3. Compressive stress-strain values for 3,080 psi (21.23 MPa) concrete 122
Table 4.4. Tensile damage values for 3,080 psi concrete 123
Table 4.5. Compressive damage values for 3,080 psi concrete 124
Table 4.6. Tensile stress, strain, plastic strain values for longitudinal steel (Mander) 126
Table 4.7. Tensile true Stress-true strain values for longitudinal steel (Mander) 127
Table 4.8. Tensile true stress-true plastic strain values for longitudinal steel (Mander) 128
Table 4.9. Tensile stress, strain, plastic strain values of transverse steel (Mander) 129
Table 4.10. Tensile true stress-true strain values of transverse steel (Mander) 130
Table 4.11. Tensile true stress-true plastic strain values of transverse steel (Mander) 130
Table 4.12. Tensile stress, strain, plastic strain values for longitudinal steel (Ramberg-Osgood) 132

Table 4.13. Tensile true stress-true strain values for longitudinal steel (Ramberg-Osgood) 132
Table 4.14. Tensile true stress-true plastic strain values for longitudinal steel (Ramberg-Osgood) 133
Table 4.15. Tensile stress, strain, plastic strain values for transverse steel (Ramberg-Osgood) 135
Table 4.16. Tensile true stress-true strain values for transverse steel (Ramberg-Osgood)........ 136
Table 4.17. Tensile true stress-true plastic strain values for transverse steel (Ramberg-Osgood) 137
Table 4.18. C_i values in psi unit for longitudinal steel based on the Ramberg-Osgood model after modification 141
Table 4.19. γ_i values for the longitudinal steel based on the Ramberg-Osgood model after modification 142
Table 4.20. C_i values in psi unit for transverse steel based on the Ramberg-Osgood model after modification 142
Table 4.21. γ_i values for transverse steel based on the Ramberg-Osgood model after modification 142
Table 4.22. Chaboche α and σ values 143
Table 4.23. Chaboche α and σ values 144
Table 4.24. Chaboche true plastic strain and Chaboche true stress of longitudinal steel 144
Table 4.25. Chaboche true plastic strain and Chaboche true stress of transverse steel 144
Table 4.26. Chaboche true plastic strain and Chaboche analytical true stress (in psi) for the longitudinal steel 145
Table 4.27. Chaboche true plastic strain and Chaboche analytical true stress (in psi) of the transverse steel 146
Table 4.28. Parameters of longitudinal steel for Ramberg-Osgood's model (evaluated via a MATLAB code) 152
Table 4.29. Parameters of transverse steel for Ramberg-Osgood's model (evaluated via a MATLAB code) 153
Table 4.30. Plastic properties of the concrete 154

Acknowledgments

I would like to express my great appreciation to my major advisor (Professor Hani Melhem) for his continuing support and guidance throughout this research. I always wanted to learn more from him. I was impressed with his knowledge and professionalism. I also would like to express my sincerest gratitude to all my committee members from inside and outside of the Civil Engineering Department, including Professor Dunja Perić and Professor Krishna Ghimire from the Civil Engineering Department, and Professor Mohaned Al-Hamdi from the Department of Economics.

Dedication

This work is dedicated to my mother, wife, father, and brother for their continuous support.

Chapter 1 : Introduction

1.1 Goals and objectives

The goals and objectives of this research study are to provide an advanced and comprehensive reference for professional users of the finite element method (FEM) to correctly analyze their structures and structural components with accurate numerical models through FEM packages such as Abaqus. Engineers usually improve their numerical models by using finer mesh sizes, increasing the number of iterations for non-linear analysis, and altering the type of elements used in the analysis. However, for reinforced concrete structural elements subjected to dynamic loads, and excessive overloads, such as in the case of earthquakes, adequate results cannot be obtained unless the material properties of the concrete and steel are modeled correctly.

For the concrete, material properties in compression and tension can significantly change the results of the analysis. Also, concrete compressive elastic behavior, as well as plastic concrete behavior in strain softening during compression, must be considered, and concrete properties in tensile hardening, tensile softening, and local continuity effect must be defined during tension.

For the steel reinforcement, ductile damage needs to be modelled for both the longitudinal and the transverse rebars. Strain hardening rules has to be considered including isotropic and kinematic hardening, and their combination to obtain correct results simulating actual behavior.

Various material concepts, models, and formulations introduced and used in this research study include Belarbi and Hsu (2001) for the behavior of the concrete in tension, as well as modified Hognestad (1951) in compression and Tao et al. model (2014) for concrete damage parameters. For steel, the Mander model, Ramberg-Osgood model, Prager's hardening rule, Abdel-Karim and Ohno plasticity model, Ohno-Wang models, Chaboche kinematic hardening rule, and their various modifications were all studied and considered for modeling.

In this research investigation, in addition to modelling RC structural components through FEM using different material modeling approaches, experimental data performed and published elsewhere in the scientific literature are used to compare the results of the FEM to those obtained from physical/mechanical tests. This is aimed at validating the material concepts and methodologies used in the numerical modeling of the structural elements being considered.

A confirmation of the validity of the proposed material approaches has the following advantages. It is obvious that testing full-scale structures in the laboratory is not always doable or financially feasible, especially for large structures. Therefore, these structures are often modeled with Finite Element Analysis (FEA) software and packages, such as Abaqus, to understand their actual behaviors under particular simulated loading and material-behavioral considerations. It is therefore beneficial to establish enough confidence in analyzing RC structures with FEA when accurate and realistic material models are being used.

1.2 Organization of this dissertation

This chapter (Chapter 1) is the general introduction to the dissertation. The rest of the work is presented to the reader as described below.

In Chapter 2, the author is numerically verifying results from an experimental test performed by Sezen and Moehle (2006) at the University of California-Berkeley using FEM while including the best complete concrete concepts, materials, models, and formulation which could be used in finite element methods. By adopting the proposed accurate methods to represent material properties, it was possible to match the fundamental tests results. This verification study elucidated a good agreement between experimental and numerical results obtained with the proposed approaches, and the remarkable ability of the proposed methodology to replicate the experimental results obtained from testing actual full-size structural components.

In the first part of Chapter 3, various material models used in the literature to describe the complete and accurate steel behavior are presented. The structural steel modeling for cyclic response is essential for the functioning appraisal and design of steel elements. Though various mathematical models have been improved to simulate metal plasticity, only a few have been implemented in finite element method-based software, such as Abaqus, which uses incremental plasticity procedures. This research study introduces and briefly describes a built-in "Isotropic, Kinematic, Johnson-Cook, User and Combined" hardening to model metal plasticity under cyclic loading. The plastic deformation is load path-dependent and irreversible. Implementation of this model is fundamentally significant for Abaqus users to accurately model the behavior and plasticity of steel structures as well as steel bars in reinforced concrete structures.

In the second part of Chapter 3, findings from an experimental test done by Sezen and Moehle at the University of California-Berkeley are used to compare with FEA results numerically obtained using the best complete steel concepts, material, models, and formulation. In particular, the steel plastic behavior is modeled to describe material behavior of the longitudinal and transverse steels. Here as well and once again, by adopting the proposed accurate methods to represent material properties, it was possible to match the fundamental tests results. The second verification study elucidated an excellent concordance between experimental and numerical results obtained with the proposed approaches.

In Chapter 4, another experimental test done by Roy and Sozen (1964) at the University of Illinois Urbana-Champaign is used to verify the results obtained from the FEA when utilizing different concepts, material models, and formulations presented in Chapters 2 and 3 for both concrete and steel. Here too, a good match was obtained between the experimental data and the numerical results. This confirms once more the remarkable ability of the proposed methodology to replicate the experimental results obtained from testing actual full-size structural components.

Chapter 5 wraps up the work performed in this dissertation. First, the main models that have been studied, developed and presented in this research are summarized together with the research validation that has been done to validate the proposed concepts and procedures. Then, the conclusions and findings of the entire research study are given. Finally, recommendations for future research and possible additional work are suggested.

In this research study, we have two verification problems between experimental and numerical results obtained with the proposed approaches. The first one will be covered in Chapters 2 and 3, and the second one in Chapter 4.

Chapter 2 : Modeling Plastic-Damage of Reinforced Concrete in Finite Element Applications

Abstract

Testing full-scale structures in laboratory is not always doable nor financially feasible, especially for large structures. Therefore, such large structures are often modeled with Finite Element Analysis (FEA) software and packages, such as Abaqus, to understand their actual behaviors under special simulated loading and material-behavioral considerations. The work in this dissertation addresses a main issue, which is the accurate modeling of the material to account for plastic damage of the concrete.

The study of concrete material is aimed at developing a material model that simulates load-induced cracking in reinforced concrete (RC) elements in the FEA of structures. The simulation of complete stress-strain concrete behavior under tension and compression (including damage characteristics) requires the application of numerical material models, potentially producing the stress-strain curves. These models include strain-softening regimes that presuppose the use of ultimate compressive concrete strength and that can be practically implemented for existing or future RC structures. The method presented in this study is valuable because it assesses existing RC structures when detailed test results are not available. However, the implemented numerical models were slightly altered in order to compare them with the damage plasticity models available in the research literature. These mainly are the smeared crack concrete model, the brittle crack concrete model, and the concrete damage plasticity model, which are all typically suitable for RC elements. The methodologies proposed here provide accurate and realistic modeling of the plastic damage of reinforced concrete members. Although numerically extensive and very time-consuming, it is demonstrated that the material and damage modeling presented in this research study can be used to accurately represent the behavior of actual structural members tested in research laboratories. This suggests that it is applicable to structures for which experimental tests or monitoring data are not available.

Key Words: Plastic-Damage (Damage plasticity), Concrete, Abaqus, Cracking, Behavior, Compression, Tension, Material Model, Stiffening

2.1 Introduction

This study investigates concrete behavior under axial load and modeling parameters. Accurate modeling of reinforced concrete (RC) is quite complex when using finite elements (FE) packages. This is because the identification of the right material properties and the application of the most efficient model are critical to obtaining accurate results. The properties of concrete material in compression and tension can significantly change the results and the final shape of the stress-strain curve. Concrete compressive elastic behavior, as well as plastic concrete behavior in strain softening during compression, must be considered, and concrete properties in tensile hardening, tensile softening, and local continuity effect must be defined during tension [1].

- In 2002, Jirásek and Bažant [2] proposed an equation that identifies the eccentricity of the potential plastic surface (e).
- For the concrete tensile behavior, previous research [3] has suggested a value of $4\sqrt{f_c'}$ psi ($0.33\sqrt{f_c}$ MPa), or approximately half the value specified in ACI 318 for diagonal tension to reduce effective rupture modulus [3].
- Modified Wang & Hsu [4] proposed analytical expressions for concrete in tension for defining the concrete tensile stress based on the concrete tensile strain.
- In 2021, Yafei et al. [5] proposed a model to calculate the concrete ultimate tensile strain.
- Tao et al. [6] proposed an equation to determine the concrete damage parameters to implement the damage model.

The methodologies implemented in this research study are as follows:

- Concrete compressive behavior was defined through the modified Hognestad model.
- Concrete tensile behavior was adopted from Belarbi and Hsu model.
- The damage model of Tao et al. was applied. The modeling and methodologies proposed in this research study are worth investigating because they provide means to numerically verify experimental test results such as those obtained by Sezen and Moehle through mechanical testing. The numerical analysis verification of Sezen and Moehle's experimental tests is here being done for the first time by the author through Finite Element Analysis software (namely, Abaqus).

In this research study, the state-of-the-art methods are discussed that can be used to describe and anticipate the actual behavior of the concrete in tension and compression, which was verified through critical experimental tests by Professor Sezen and Moehle from the University of California-Berkeley. For the behavior of the concrete in tension as well as compression, also concrete damage parameters in tension as well as compression, there are extensive models proposed by different scientists. However, in this research study, the most accurate models for the behavior of the concrete in tension (Belarbi and Hsu), in compression (modified Hognestad), and concrete damage parameters (Tao et al.) were considered. If the models are not strong and good enough, we cannot get acceptable results from the Finite Element Method analysis software.

2.2 Principle of Concrete Cracking

A multi-surface plasticity model applied to the experimental model calibration identifies plasticity behavior for compression and scalar damage for tension. Strain compression can be plastic or elastic; each plastic strain increment is equal to the sum of a plastic part, which remained unchanged during unloading, and an elastic part, which is recovered after unloading. Hooke's law governs elastic strain, and a known flow rule governs plastic strain. A flow rule represents the link between the stress-strain relationship and a loading function for a work-hardening material. Flow rule occurs when the plastic flow is associated with the surface of a current loading. However, for some geotechnical materials, concrete, and rocks, an associated flow rule overestimates plastic volume expansion [1]. Because the material in this study was cohesive-frictional, no association of the assumed flow rule was identified. Figure 2.1 depicts the Drucker-Prager failure surface [7], while Figure 2.2 depicts the concrete failure surface from Ottosen [8].

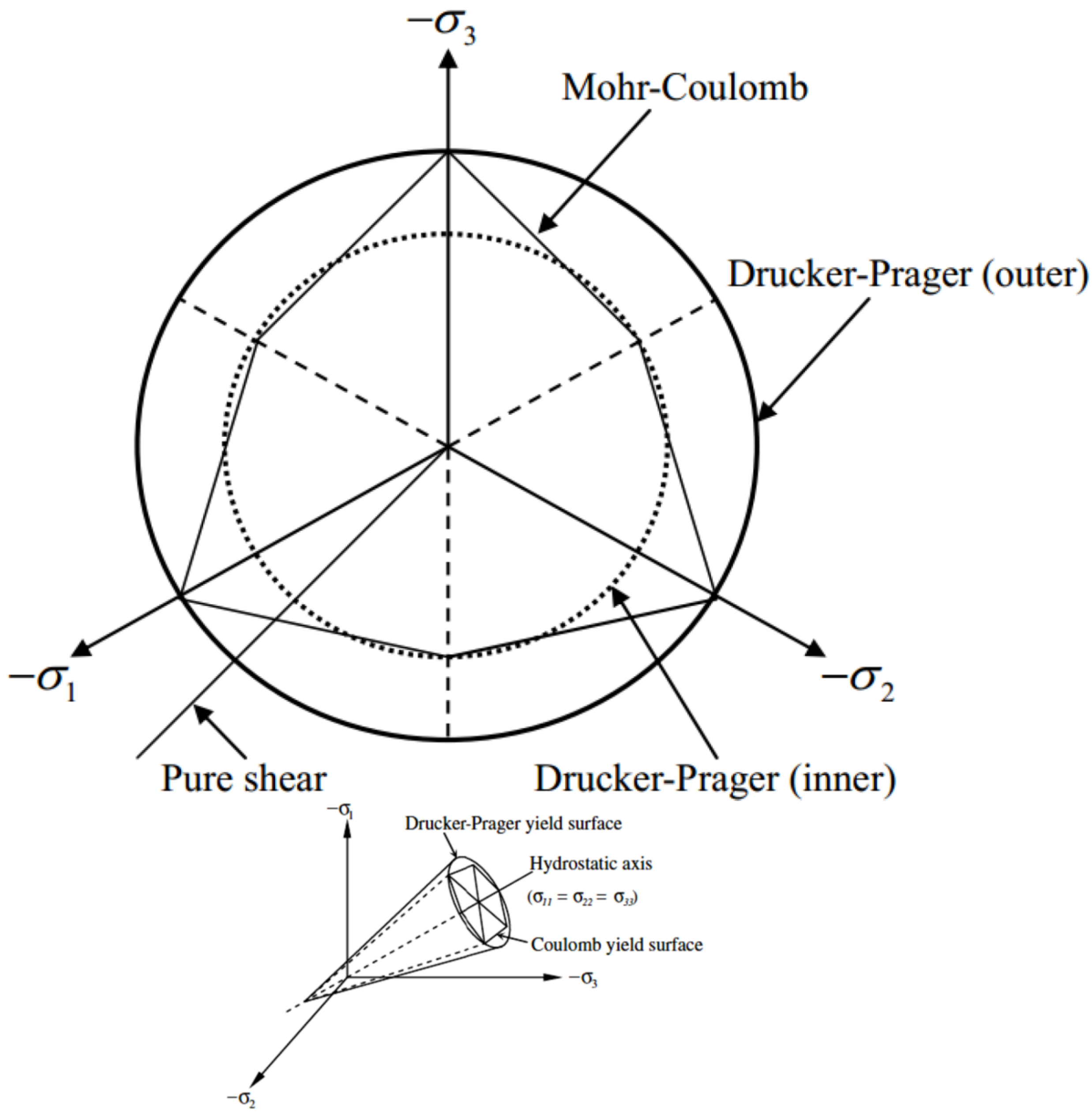

Figure 2.1. Drucker-Prager failure surface [7]

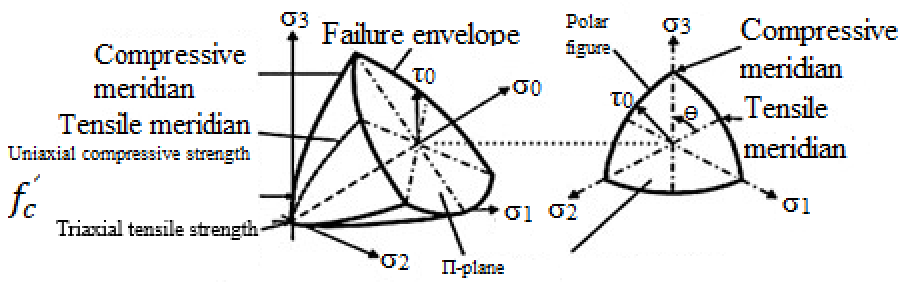

Figure 2.2. Concrete triaxial failure space [8]

The Finite Elements Analysis (FEA) software used in this study utilizes a modified material model proposed by Drucker-Prager for model calibration. This study also used failure criterion suggested by Lubliner and Oñate in 1989 [9] that was later modified by Lee and Fenves in 1998 [10], which presupposes the use of several characteristic parameters to enhance the complex simulation of concrete behavior (Equation 1) [9].

$$\boldsymbol{F\left(\bar{\sigma}, \tilde{\varepsilon}^{pl}\right) = \frac{1}{1-\alpha}\left(\bar{q} - 3\alpha\bar{p} + \beta\left(\tilde{\varepsilon}^{pl}\right)\langle\hat{\bar{\sigma}}_{max}\rangle - \gamma\langle-\hat{\bar{\sigma}}_{max}\rangle\right) - \bar{\sigma}_c\left(\tilde{\varepsilon}_c^{pl}\right) \leq 0} \tag{1}$$

α, γ: dimensionless material constant

$\bar{p}$: effective hydrostatic pressure

$\bar{q}$: Mises equivalent effective stress

$\bar{\sigma}$: effective stress tensor

$\hat{\bar{\sigma}}_{max}$: algebraically maximum eigenvalue of $\bar{\sigma}$ (maximum principal effective stress)

$\bar{\sigma}_c$: effective compression cohesion stress

2.3 Dilation Angle at High Confining Pressure (ψ)

$$\psi = \frac{-(\delta\varepsilon_v)}{(\delta\gamma)} \tag{2}$$

ε_v: volumetric strain

γ: shear strain

The dilation angle ψ stands for potential plastic plane at highly confining pressure. When the value of the parameter is small, the material develops a brittle behavior; high values indicate ductile behavior. Researchers have previously studied this parameter on a four-point loaded beam with the value of the dilation angle ranging between 20° and 40°. Other researchers have suggested a value range of 30° to 40°. A study conducted by Kupfer et al. in 1969 [11] indicated that for f_{cm} = 27.6 MPa (the cracking stress of concrete) and f_{ctm} = 3.5 MPa (the mean tensile strength of concrete), the 25° value represents the best behavior under biaxial compression. Another study found that the value of dilation angle was 38° for a normal-strength concrete with f_{cm} = 50 MPa, f_{ctm} = 2.8 MPa, and E_c = 19.7 GPa (concrete modulus of elasticity), meaning the dilation angle may range from 25° to 40° [1]. According to De Borst in 1986 [12], the dilation angles of pressure-dependent materials such as rocks, soils, and ordinary concrete are 20° higher than their internal friction angles.

2.4 Eccentricity of the Potential Plastic Surface (e)

The eccentricity of the potential plastic surface (e) controls the deviator plane envelope and defines the rate that indicates the function approach to the asymptote when the flow potential proceeds towards a straight line while the eccentricity approaches zero. This smooth and continuous flow potential ensures a unique definition of flow direction. In 2002, Jirásek and Bažant [2] proposed the following equation that identifies this parameter:

$$e = \frac{1+\epsilon}{2-\epsilon} \tag{3}$$

in which,

$$\epsilon = \frac{\bar{f}_t}{\bar{f}_b} \cdot \frac{\bar{f}_b^2 - \bar{f}_c^2}{\bar{f}_c^2 - \bar{f}_t^2} \tag{4}$$

$\bar{f}_c$: concrete uniaxial compressive strength

e: eccentricity parameter

$\bar{f}_t$: concrete uniaxial tensile strength

$\bar{f}_b$: concrete equibiaxial compressive strength

2.5 (γ) Parameter

Concrete behavior in compression strongly depends on the state of triaxial stress and the confinement pressure level. Parameter γ defines specimen behavior using the form of the deviator stress plane. The triangular shape of the deviator plane implies low confinement. In addition, a circular form similar to the Drucker-Prager model means that the concrete has experienced high confinement pressures. Hence, the accepted range of value for this parameter is $\frac{2}{3} < \gamma < 1$. Although extensive refinement has indicated a parameter value of $0.64 < \gamma < 0.8$, no difference in specimen behavior for higher values has been observed [1].

$$\gamma = \frac{3(1-\rho)}{2\rho-1} \tag{5}$$

$$\rho = \frac{(\sqrt{J_2})_{TM}}{(\sqrt{J_2})_{CM}} \tag{6}$$

J_2: second invariant of the stress deviator

TM: tensile meridian

CM: compressive meridian

2.6 Viscosity Parameter (μ)

Advanced material models that develop stiffness degradation and strain softening tend to result in convergence issues. The regulation of constitutive equations, one of the most common remediation approaches, makes the tangent material stiffness become positive for short-time increments, and software packages such as Abaqus apply a Duvaut/Lions regularization. High values for this parameter have resulted in compromising outcomes [1].

$\dot{\varepsilon}_{v}^{pl} = \frac{1}{\mu}\left(\varepsilon^{pl} - \varepsilon_{v}^{pl}\right)$ (7)

$\dot{d}_{v} = \frac{1}{\mu}(d - d_{v})$ (8)

$\sigma = (1 - d_{v})D_{0}^{el}: (\varepsilon - \varepsilon_{v}^{pl})$ (9)

$\dot{\varepsilon}_{v}^{pl}$: viscoplastic strain rate tensor

μ: viscosity parameter representing the relaxation time of the viscoplastic system

ε^{pl}: plastic strain evaluated in the inviscid backbone model

ε_{v}^{pl}: viscoplastic strain

$\dot{d}_{v}$: viscous stiffness degradation variable for the viscoplastic system

d: degradation variable evaluated in the inviscid backbone model

d_{v}: viscous stiffness degradation variable

D_{0}^{el}: initial (undamaged) elasticity matrix

2.7 Concrete Behavior

2.7.1 Concrete Compressive Behavior

The Hognestad stress-strain curve is commonly used to represent concretes with strengths up to about 6,000 psi (41.36 MPa) (Figure 2.3) (modified Hognestad) [13].

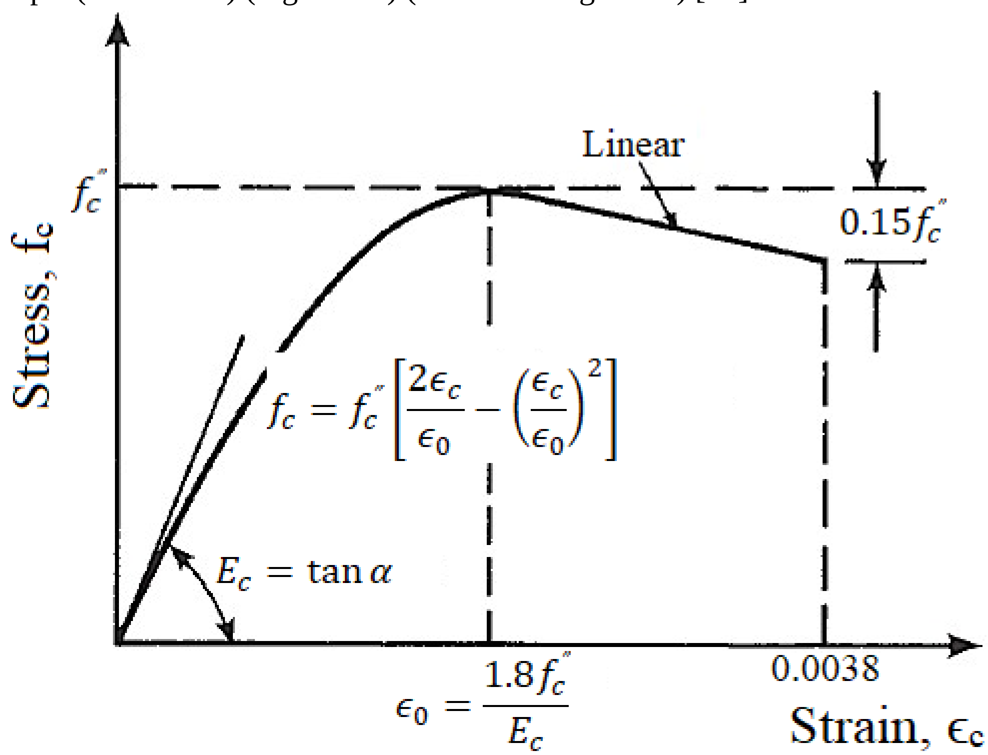

Figure 2.3. Idealized stress-strain curve for concrete in uniaxial compression

For $0 \leq \varepsilon_c \leq \varepsilon_0 \Longrightarrow f_c = f_c^{"}\left[2\frac{\varepsilon_c}{\varepsilon_0} - \left(\frac{\varepsilon_c}{\varepsilon_0}\right)^2\right]$ (10)

For $\varepsilon_0 \leq \varepsilon_c \leq \varepsilon_u \;\Longrightarrow\; f_c = f_c^{"}\left[1 - 0.15\left(\frac{\varepsilon_c - \varepsilon_0}{\varepsilon_u - \varepsilon_0}\right)\right]$ (11)

$$\varepsilon_c = \varepsilon_{total} \tag{12}$$

$$\varepsilon_{total} = \varepsilon_{elastic} + \varepsilon_{plastic} \Longrightarrow \varepsilon_{plastic} = \varepsilon_{total} - \varepsilon_{elastic} \tag{13}$$

$$\varepsilon_{elastic} = \frac{f_c}{E_c} \tag{14}$$

$$\varepsilon_{plastic} = \varepsilon_c - \frac{f_c}{E_c} \tag{15}$$

$$f_c^{"} = 0.9 f_c^{'} \tag{16}$$

$$E_c = 57{,}000\sqrt{f_c^{'}}\ (psi) \tag{17}$$

$$\varepsilon_0 = \frac{1.8 f_c^{"}}{E_c} \tag{18}$$

$$\varepsilon_u = 0.38\% = 0.0038 \tag{19}$$

In this research study, Specimen #4 from the experimental tests done by two well-established scientists in Structural and Earthquake Engineering (Professor Halil Sezen and Professor Jack P. Moehle) at the University of California, Berkley, was selected with average concrete compressive strength of 3,160 psi.

For the purpose of this study, a MATLAB code was written to describe the behavior of concrete with a compressive strength of $f_c^{'} = 3{,}160$ psi (21.78 MPa) in compression based on the modified Hognestad model. Table 2.1 shows the stress and strain values for concrete with a compressive strength of $f_c^{'} = 3{,}160$ psi (21.78 MPa).

Table 2.1. Compressive stress-strain values for 3,160 psi (21.78 MPa) concrete

Stress (psi)	Stress (N/m²)	Strain	Stress (psi)	Stress (N/m²)	Strain
0	0	0	2,766.5	19,074,400	0.002
344.87	2,377,86	0.0001	2,747.1	18,940,900	0.0021
667.47	4,602,070	0.0002	2,727.7	18,807,370	0.0022
967.78	6,672,650	0.0003	2,708.4	18,673,800	0.0023
1,245.8	8,589,580	0.0004	2,689.03	18,540,300	0.0024
1,501.5	10,352,700	0.0005	2,669.6	18,406,700	0.0025
1,735.01	11,962,500	0.0006	2,650.2	18,273,100	0.0026
1,946.1	13,418,500	0.0007	2,630.9	18,139,600	0.0027
2,135.08	14,720,900	0.0008	2,611.5	18,006,000	0.0028

2,301.6	15,869,600	0.0009	2,592.1	17,872,500	0.0029
2446.01	16,864,700	0.001	2,572.8	17,738,900	0.003
2,568.05	17,706,100	0.0011	2,553.4	17,605,390	0.0031
2,667.8	18,393,900	0.0012	2,534.07	17,471,800	0.0032
2,745.2	18,928,000	0.0013	2,514.7	17,338,300	0.0033
2,800.4	19,308,600	0.0014	2,495.3	17,204,700	0.0034
2,833.3	19,535,400	0.0015	2,475.9	17,071,200	0.0035
2,844	19,608,700	0.0016	2,456.5	16,937,700	0.0036
2,824.6	19,475,100	0.0017	2,437.2	16,804,000	0.0037
2,805.2	19,341,600	0.0018	2,417.8	16,670,500	0.0038
2,785.8	19,208,000	0.0019			

The corresponding stress-strain curve is illustrated in Figure 2.4.

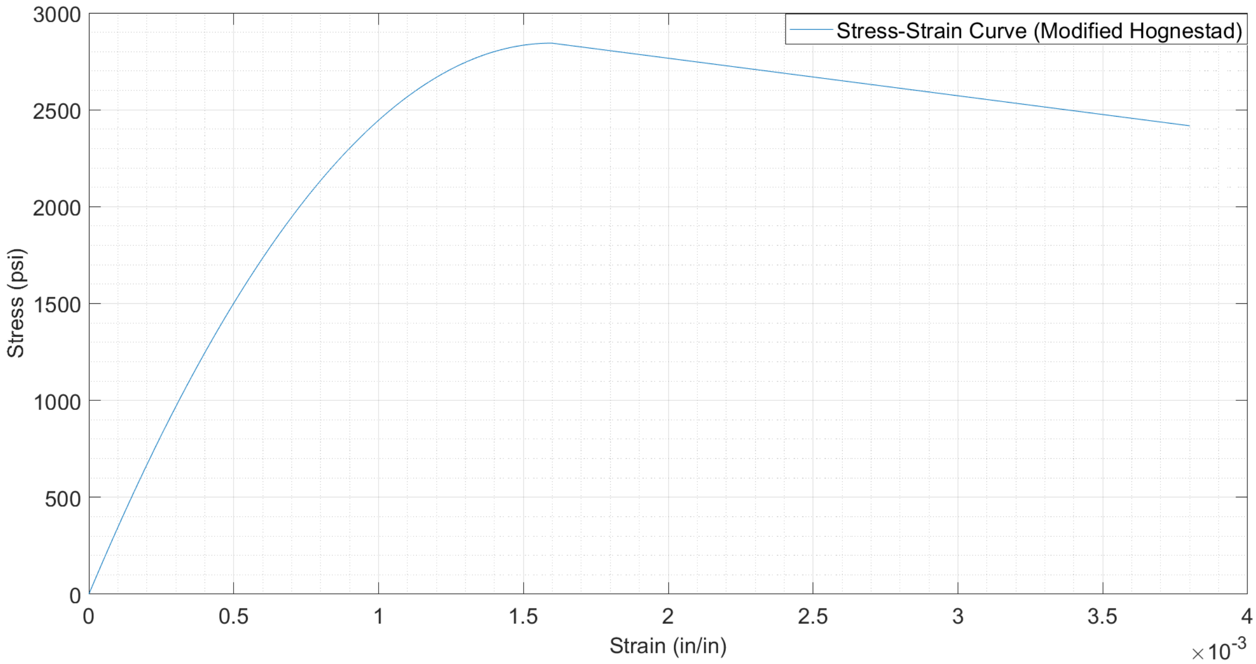

Figure 2.4. Modified Hognestad stress-strain curve for concrete in uniaxial compression

In Figure 2.4, the critical points are as follows:

(Strain, Stress (psi))
Start point: (0, 0)
(ε_0 = 0.0016 , $f_c^{''}$= 2,844)
Endpoint: (0.0038, 2,417.8)
For concrete damage plasticity, yield stress values for the concrete compressive stresses as in Equations 10 and 11, and the inelastic strain magnitudes for the concrete compressive plastic strain as in Equation 15 are used in this study to define the compressive behavior of concrete when using Abaqus.

2.7.2 Concrete Tensile Behavior

Section 9.5.2.3 of the ACI 318-08 Building Code defines the tensile flexural strength known as the modulus of rupture f_r to be used in deflection calculations as follows (Equation 20) [13].

$$f_r = 7.5\lambda\sqrt{f_c^{'}}\ (psi) \tag{20}$$

Because here λ is a modification factor, the value of λ should be based on the aggregate composition in the concrete mixture. Hence, λ = 1 for normal-weight concrete [14]. Previous research has suggested a value of $4\sqrt{f_c^{'}}$ psi ($0.33\sqrt{f_c}$ MPa), or approximately half the value specified in ACI 318 for diagonal tension to reduce effective rupture modulus [3].
Based on the tests of 35 full-size panels, Belarbi and Hsu in 1994 [15], Pang and Hsu in 1995 [16], Tamai et al. in 1987 [17], and Modified Wang & Hsu [4] proposed the following analytical expressions for concrete in tension:

$$\text{For } \varepsilon_t \leq \varepsilon_{cr} \rightarrow \sigma_t = E_c.\varepsilon_t \tag{21}$$

$$\text{For } \varepsilon_t > \varepsilon_{cr} \rightarrow \sigma_t = f_{cr}(\frac{\varepsilon_{cr}}{\varepsilon_t})^n = f_{cr}(\frac{\varepsilon_{cr}}{\varepsilon_t})^{0.4} \tag{22}$$

$$\varepsilon_{cr} = 0.00008\ mm/mm$$

$$E_c = 57{,}000\sqrt{f_c^{'}}\ (psi) \tag{23}$$

$$f_{cr} = \varepsilon_{cr} \cdot E_c = 0.00008 \times 57{,}000\sqrt{f_c^{'}} = 4.56\sqrt{f_c^{'}}\ (psi) \tag{24}$$

ε_t: total strain
ε_{cr}: cracking strain of concrete
σ_t: concrete stress for uniaxial tension
E_c: concrete modulus of elasticity
f_{cr}: cracking stress of concrete
n: rate of weakening
To calculate the concrete ultimate tensile strain, in 2021 Yafei et al. [5] proposed a model as follows:

$$\varepsilon_{tu} = \left(0.005f_c^{'} + 0.45\right)\varepsilon_0 \tag{25}$$

where $f_c^{'}$ unit is N/mm^2. For unit consistency, $f_c^{'}$ unit needs to be converted from *psi* to N/mm^2. ε_0

is the concrete compressive strain at the apex, which was proposed by Hognestad and covered in the previous section (Equation 18) as follows:

$$\varepsilon_0 = \frac{1.8 f_c^{''}}{E_c} \tag{18}$$

Figure 2.5 shows a typical tensile stress–strain curve for concrete.

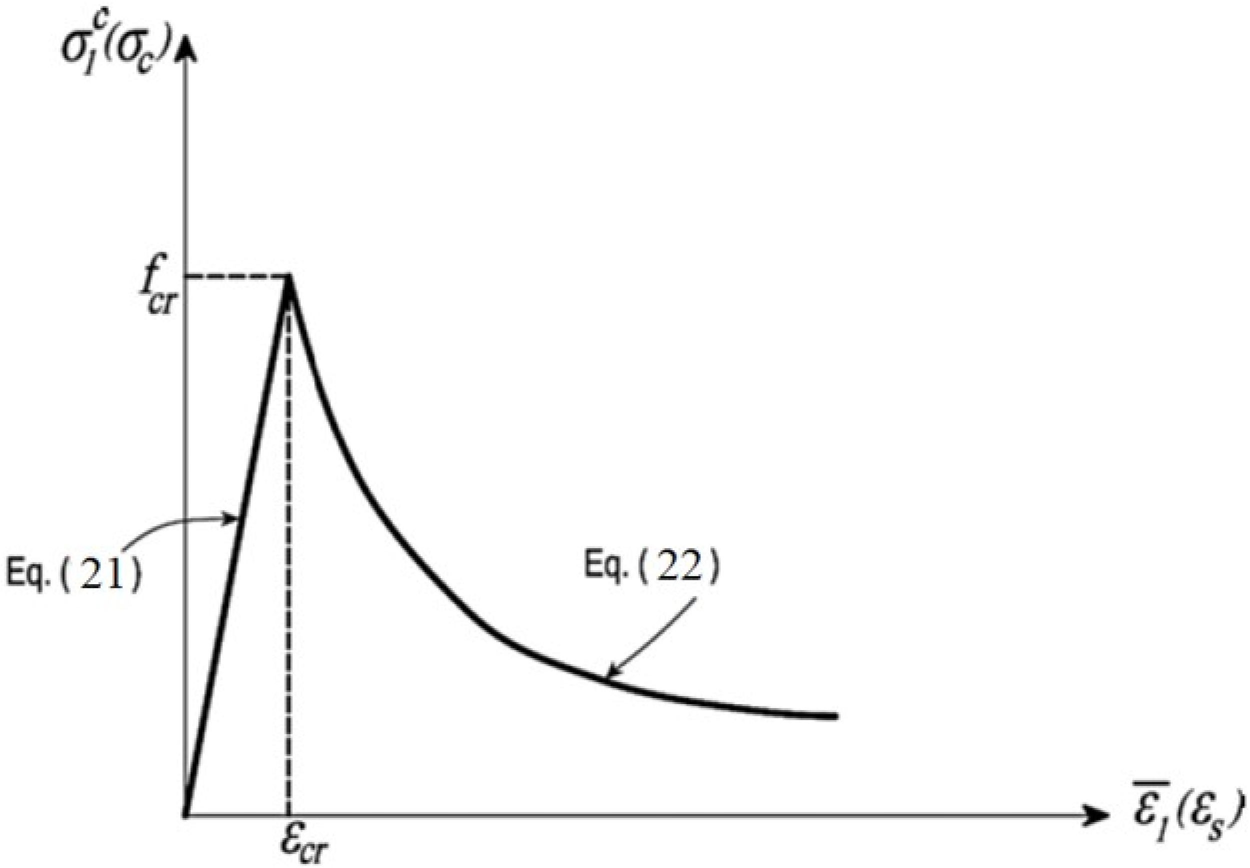

Figure 2.5. Tensile stress–strain curve of concrete

For this study, a MATLAB code was written to represent the behavior of concrete with a compressive strength of $f_c^{'} = 3{,}160$ psi (21.78 MPa) in tension based on the above models (Equations 21-25). The resulting stress-strain curve is illustrated in Figures 2.6.

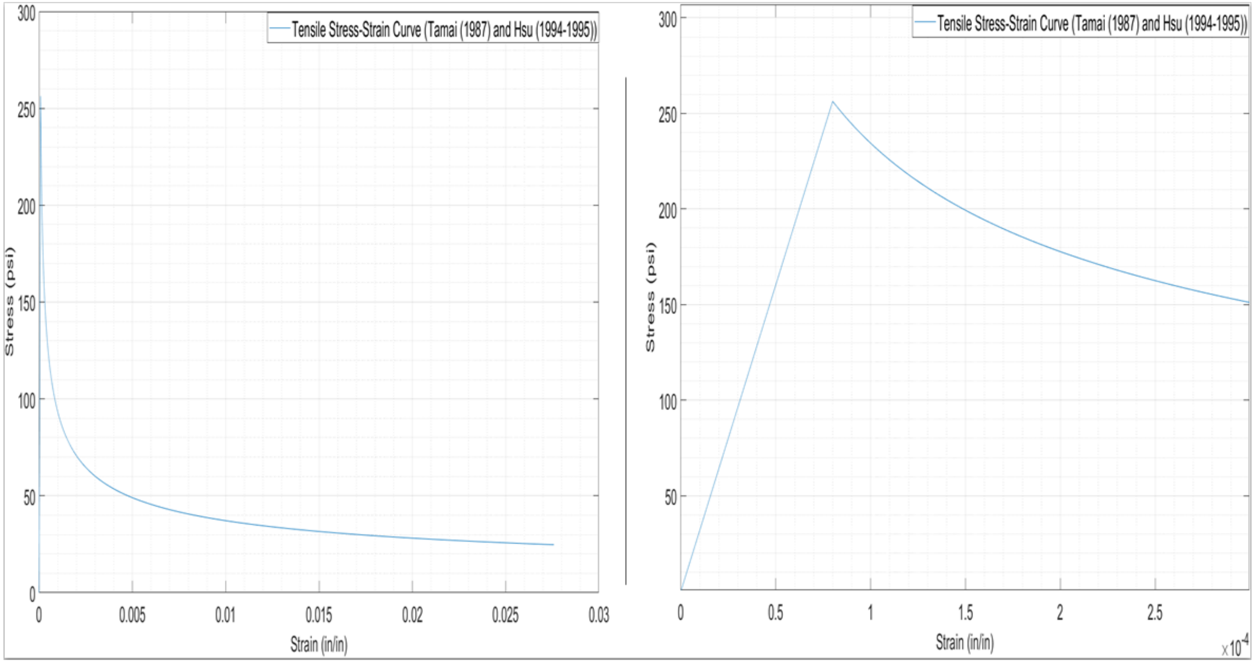

Figure 2.6. Sample tensile stress–strain curve of concrete

2.8 Fracture Energy

The fracture energy of concrete G_F is defined as the energy needed to propagate a tensile unit area crack. In the absence of experimental data, G_F may be estimated. This study used the CEB-FIP [18] model to estimate G_F (Equation 26):

$$G_F = (0.0469d_a^2 - 0.5d_a + 26)(\frac{f_c'}{10})^{0.7}(N/mm) \quad (26)$$

d_a: maximum aggregate size of the concrete

Results suggested that d_a is 20 mm when test data is not available.

There are two ways to define the concrete tensile behavior in Abaqus: The first way is to define the yield stress values, which are the tensile concrete stresses, in terms of the cracking strains, as will be described in Section 2.9.1. The second way is to define yield stress, which is the failure stress (cracking stress) of concrete along with the fracture energy. The first way was used in this study.

2.9 Developing the Material Model

Damage is implemented for simulating compression and tension behavior, as shown in Figure 2.7 [1]. The behavior is summarized below.

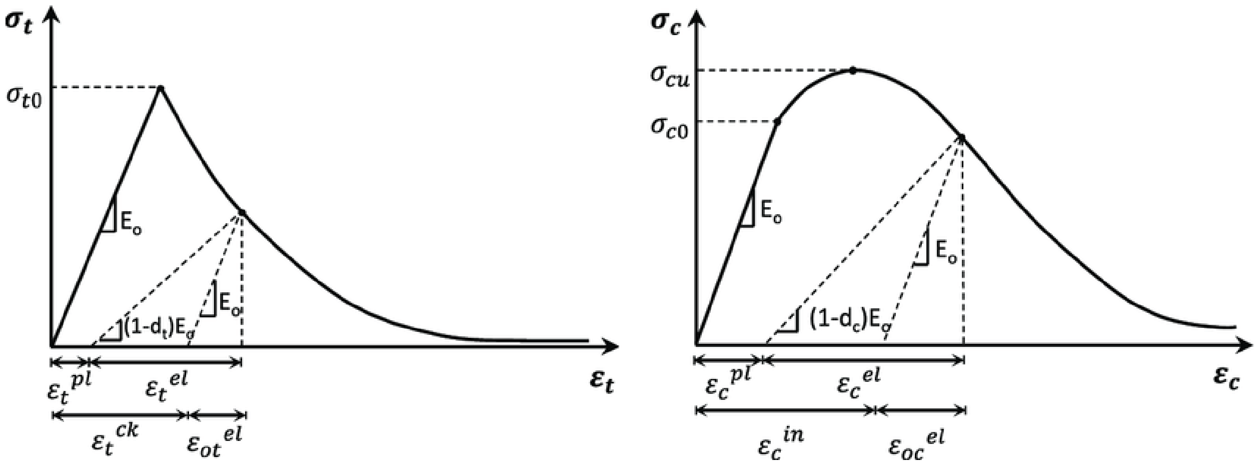

Figure 2.7. Stress-strain plots for damage plasticity

Figure 2.7 demonstrates the summary of damage implementation for simulating compression and tension behavior for the readers to initially become familiar with the concept.

The uniaxial compression response is linear until it reaches the initial crushing value of σ_{c0}. Typically, the behavior in the plastic regime is characterized by stress hardening followed by strain-softening above the ultimate stress, σ_{cu}. For uniaxial tension loads, the stress-strain curve adheres to a linear-elastic behavior until it reached σ_{t0}. The development of macro-cracks in the material volume leads to failures, and micro-crack propagation experiences tension softening or tension stiffening depending on the specimen type, leading to strain localization in the structure.

As shown in Figure 2.7, weakening of the unloading response can occur in any softening branch point when the element is unloaded, indicating damage to the elastic stiffness of the material. The d_t and d_c in the figures are variable scalar functions that are temperature-dependent and define the degradation of elastic stiffness of the material. The value of the parameters ranges from 0 to 1, with 0 indicating undamaged material, while 1 indicates failure.

$$\sigma_t = (1 - d_t)E_0\left(\varepsilon_t - \tilde{\varepsilon}_t^{pl}\right) \tag{27}$$

$$\sigma_c = (1 - d_c)E_0\left(\varepsilon_c - \tilde{\varepsilon}_c^{pl}\right) \tag{28}$$

σ_t: concrete tensile stress

d_t: concrete damage variable in tension

E_0: initial (undamaged) elastic stiffness of the material

ε_t: total tensile strain

$\tilde{\varepsilon}_t^{pl}$: equivalent plastic strain in tension

σ_c: magnitude of the uniaxial compression

d_c: concrete damage variable in compression

ε_c: total compression strain

$\tilde{\varepsilon}_c^{pl}$: equivalent plastic strain in compression

Damage simulation can be represented by a number of mathematical models. For instance, Abaqus software (SIMULIA) [19] simulates damage by applying crack models such as the smeared crack concrete model, the brittle crack concrete model, and the concrete damage plasticity model, which are suitable for RC elements. The current study uses the concrete damage plasticity model because it models complete inelastic concrete behavior in tension and compression, considering the characteristics of damage. Moreover, it is the only model that suits Abaqus/Standard and Abaqus/Explicit, making it possible to transfer the results between them. Consequently, a proper damage simulation model will be useful to implement the concrete damage plasticity model to analyze the RC structures under various combinations of loading (dynamic and static loadings). The concrete damage plasticity model assumes that the primary mechanisms of failure in concrete are compressive crushing and tensile cracking. Damage plasticity characterizes the uniaxial tensile and compressive behavior in this model [20]. Abaqus' damage plasticity model for concrete enables its user to control the effects of stiffness recovery throughout reversals of cyclic loading.

2.9.1 Tension Stiffening Relationship

To model the complete tensile behavior patterns of RC, this study used a post-failure stress-strain relationship for concrete exposed to tension (Figure 2.8) that accounts for strain-softening, tension stiffening, and reinforcement interaction with concrete [20].

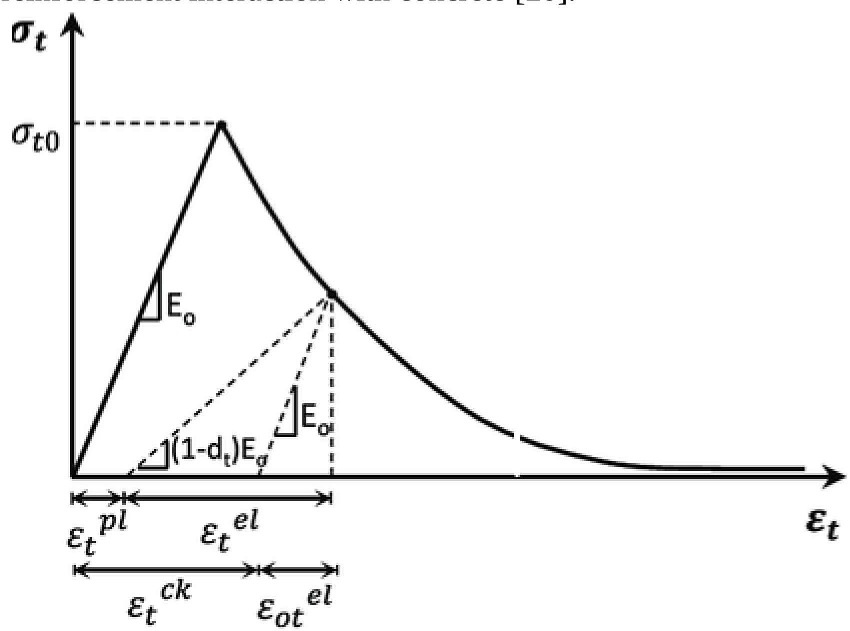

Figure 2.8. Terms for tension stiffening model

$$\tilde{\varepsilon}_t^{ck} = \varepsilon_t - \varepsilon_{0t}^{el} \tag{29}$$

$$\varepsilon_{0t}^{el} = \frac{\sigma_t}{E_0} \tag{30}$$

$\tilde{\varepsilon}_t^{ck}$: concrete cracking strain

ε_t: concrete total tensile strain

ε_{0t}^{el}: elastic strain corresponding to the undamaged material

σ_t: concrete tensile stress

E_0: concrete young's modulus

Table 2.2 shows tensile stress-strain values for concrete in tension with a compressive strength of $f_c^{'} = 3{,}160$ psi (21.78 MPa), including yield stresses and cracking strains. In Table 2.2, the first Yield Stress will be the concrete tensile stress corresponding to the tensile cracking stress of concrete (Equation 24) or concrete tensile failure stress.

Table 2.2. Tensile stress-strain values for 3,160 psi (21.78 MPa) concrete

Yield Stress(psi)	**Yield Stress(N/m²)**	**Cracking Strain**
256.33	1,767,370	0
175.31	1,208,730	0.0001
124.203	856,350	0.0002
97.2608	670,590	0.0003
80.456	554,730	0.0004
68.905	475,090	0.0005
60.444	416,750	0.0006
53.958	372,030	0.0007
48.818	336,590	0.00079
44.636	307,760	0.00089
41.163	283,810	0.00099
38.227	263,570	0.00109
35.714	246,240	0.00119
33.534	231,210	0.00129
31.624	218,040	0.00139
29.935	206,400	0.00149

28.431	196,030	0.00159
27.082	186,730	0.00169
25.867	178,350	0.00179
24.763	170,740	0.00189

The plastic strain values ($\tilde{\varepsilon}_t^{pl}$) defined earlier in Equation 27 were used to verify the damage curve accuracy, as presented in Equation 31 [20].

$$\tilde{\varepsilon}_t^{pl} = \tilde{\varepsilon}_t^{ck} - \frac{d_t}{(1-d_t)} \frac{\sigma_t}{E_0} \quad (31)$$

Negative and/or decreasing values of a tensile plastic strain imply incorrect damage curves, potentially resulting in an error message prior to the analysis [20].

2.9.1.1 Interaction Between Concrete and Steel

We must go to the Interaction module and Create Constraint to define the interaction between the concrete section and steel reinforcement.

Typically, in concrete structures analyzed with Abaqus, reinforcement is incorporated utilizing one-dimensional rods known as rebars can be defined individually or embedded in surfaces with a specific orientation. They are commonly utilized in conjunction with standard models of metal plasticity to depict the characteristics or properties exhibited by the rebar material and are placed on top of a mesh consisting of standard element types used for modeling concrete.

The method or technique used for modeling considers the behavior of concrete in which the rebar's impact is not considered. The repercussions linked to the boundary or point of contact between the rebar and the concrete, the behavior or characteristics of bond-slip, and the actions of dowels and their impact are simulated by introducing "tension stiffening" in the modeling of the concrete. This approximation emulates the load transfer through cracks via the rebar.

In intricate scenarios, describing the rebar accurately could be arduous; however, this must be utilized accurately during the process. This is crucial as it may lead to the analysis failing due to insufficient reinforcement in the critical areas within a model.

For this model, the author used the Embedded Region constraint. Then he selected embedded parts. Afterward, he selected all reinforcement, bars, and stirrups. For this embedded region's host, he selected the region and then selected the concrete section as a host for reinforcement.

2.9.2 Compressive Stress-Strain Relationship

Defining the stress-strain relationship of concrete requires that the concrete compressive stresses (σ_c) with concrete compressive inelastic strains ($\tilde{\varepsilon}_c^{in}$), as well as damage parameters (d_c) with inelastic strains ($\tilde{\varepsilon}_c^{in}$) be entered in a tabular format. Therefore, Equation 32 was used to convert the total strain values to the inelastic strains [20].

$$\tilde{\varepsilon}_c^{in} = \varepsilon_c - \varepsilon_{0c}^{el} \tag{32}$$

$$\varepsilon_{0c}^{el} = \frac{\sigma_c}{E_0} \tag{33}$$

$\tilde{\varepsilon}_c^{in}$: concrete compressive inelastic strains

ε_c: concrete total compressive strain

ε_{0c}^{el}: concrete elastic compressive strain corresponding to the undamaged material

σ_c: concrete compressive stresses

E_0: concrete young's modulus

Here again, a MATLAB code was written to represent the behavior of concrete with a compressive strength of $f_c^{'} = 3{,}160$ psi (21.78 MPa) in compression based on the modified Hognestad model. Table 2.3 shows the values of concrete in compression with a compressive strength of $f_c^{'} = 3{,}160$ psi (21.78 MPa), including yield stresses and inelastic strains. A MATLAB code was written to find a yield stress corresponding to an inelastic strain equals to zero.

Table 2.3. Compressive stress-strain values for 3,160 psi (21.78 MPa) concrete

Yield Stress(psi)	**Yield Stress(N/m²)**	**Inelastic Strain**
1,023.8	5,503,800	0
1,777.3	12,254,000	0.00033
2,480.06	17,099,400	0.00067
2,592.7	17,876,300	0.00268
2,311.5	15,937,900	0.00301
2,044.4	14,095,900	0.00335
1,803.01	12,431,300	0.00368
1,590.7	10,967,700	0.00402
1,406.7	9,699,030	0.00435
1,248.3	8,606,740	0.00469
1,112.1	7,668,210	0.00502
995.12	6,861,170	0.00536

894.23	6,165,510	0.00569
806.95	5,563,790	0.00603
731.17	5,041,250	0.00636
665.07	4,585,550	0.0067
607.18	4,186,400	0.00703
556.26	3,835,290	0.00737
511.27	3,525,130	0.0077
471.37	3,250,020	0.00804
435.84	3,005,050	0.00837

The concrete compressive plastic strain values ($\tilde{\varepsilon}_c^{pl}$) were calculated using Equation 34, but corrective measures had to be taken to ensure that the values were neither negative nor decreasing when they experienced increased stresses [20].

$$\tilde{\varepsilon}_c^{pl} = \tilde{\varepsilon}_c^{in} - \frac{d_c}{(1-d_c)}\frac{\sigma_c}{E_0} \tag{34}$$

$\tilde{\varepsilon}_c^{pl}$: concrete compressive plastic strain

Figure 2.9 presents a typical compressive stress-strain relationship with damage properties and terms [20].

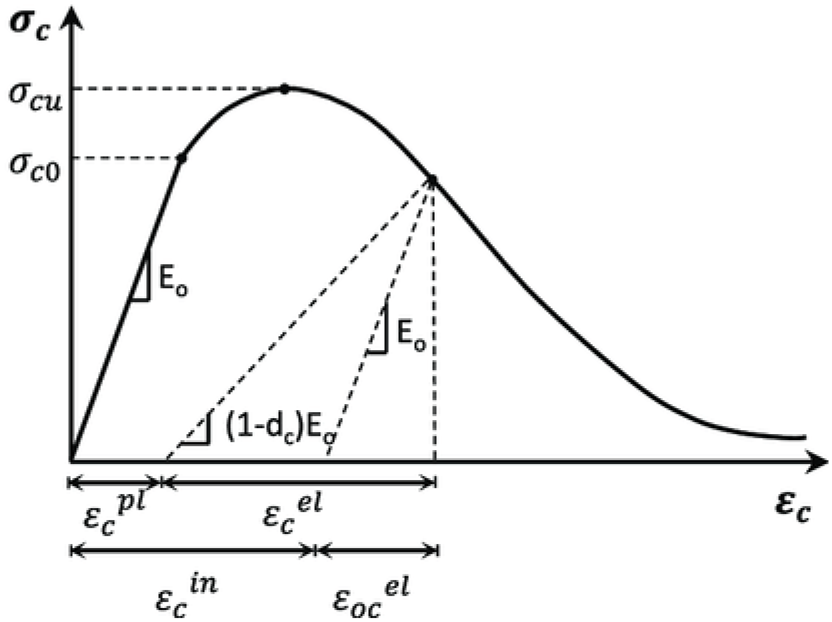

Figure 2.9. Terms for compressive stress-strain relationship

2.10 Implementation of the Damage Model

Tao et al. proposed the following equation to determine the concrete damage parameter [6]:

$$d = \begin{cases} \frac{(1-k)\varepsilon^p}{(1-k)\varepsilon^p + \frac{\sigma}{E_0}} & \text{if } \dot{\bar{\varepsilon}}^p \geq 0 \\ \frac{\varepsilon^p - (\varepsilon - \bar{\varepsilon}^e_{cr})}{\varepsilon^p - (\varepsilon - \bar{\varepsilon}^e_{cr}) + \frac{\sigma}{E_0}} & \text{if } \dot{\bar{\varepsilon}}^p < 0 \end{cases} \tag{35}$$

$$\dot{\bar{\varepsilon}}^p = \bar{\varepsilon}^p_i - \bar{\varepsilon}^p_{i-1} \tag{36}$$

$$\bar{\varepsilon}^p = \varepsilon - \frac{f}{E_0} \tag{37}$$

$$k = \frac{\sigma}{f} \tag{38}$$

$$k = \frac{\bar{\varepsilon}^p}{\varepsilon^p} \Longrightarrow \varepsilon^p = \frac{\bar{\varepsilon}^p}{k} = \frac{\bar{\varepsilon}^p}{\frac{\sigma}{f}} = \frac{\bar{\varepsilon}^p . f}{\sigma} \tag{39}$$

$$\bar{\varepsilon}^e_{cr} = \frac{\sigma}{E_0} \tag{40}$$

d: damage factor

$\dot{\bar{\varepsilon}}^p$: plastic strain rate with damage

$\bar{\varepsilon}^p$: plastic strain with stiffness degradation

f: either the tensile or compressive strength of concrete as appropriate

ε: total strain

E_0: elastic modulus of the concrete

σ: stress including compressive stress or tensile stress

ε^{p}: plastic strain without stiffness degradation

$\bar{\varepsilon}_{cr}^{e}$: elastic strain

Following the model described above (in this section of the research study), a MATLAB code was written to represent tensile damage of the concrete. Table 2.4 lists the tensile damage behavior of the concrete with a compressive strength of $f_c^{'} = 3{,}160$ psi (21.78 MPa), including damage parameter (d_t) and cracking strain $(\tilde{\varepsilon}_t^{ck})$.

Table 2.4. Tensile Damage Values for 3,160 psi Concrete

Cracking Strain	**Damage Parameter (*d_t*)**
0	0
0.0001	0.44522
0.0002	0.60695
0.0003	0.69221
0.0004	0.74539
0.0005	0.78194
0.0006	0.80872
0.0007	0.82924
0.00079	0.84551
0.00089	0.85875
0.00099	0.86974
0.00109	0.87902
0.00119	0.88698
0.00129	0.89388
0.00139	0.89993
0.00149	0.90527
0.00159	0.91003

0.00169	0.91429
0.00179	0.91814
0.00189	0.92163

Figure 2.10 depicts the tensile damage behavior of the concrete with a compressive strength of $f_c^{'} = 3{,}160$ psi, including damage parameter (d_t) and cracking strain ($\tilde{\varepsilon}_t^{ck}$).

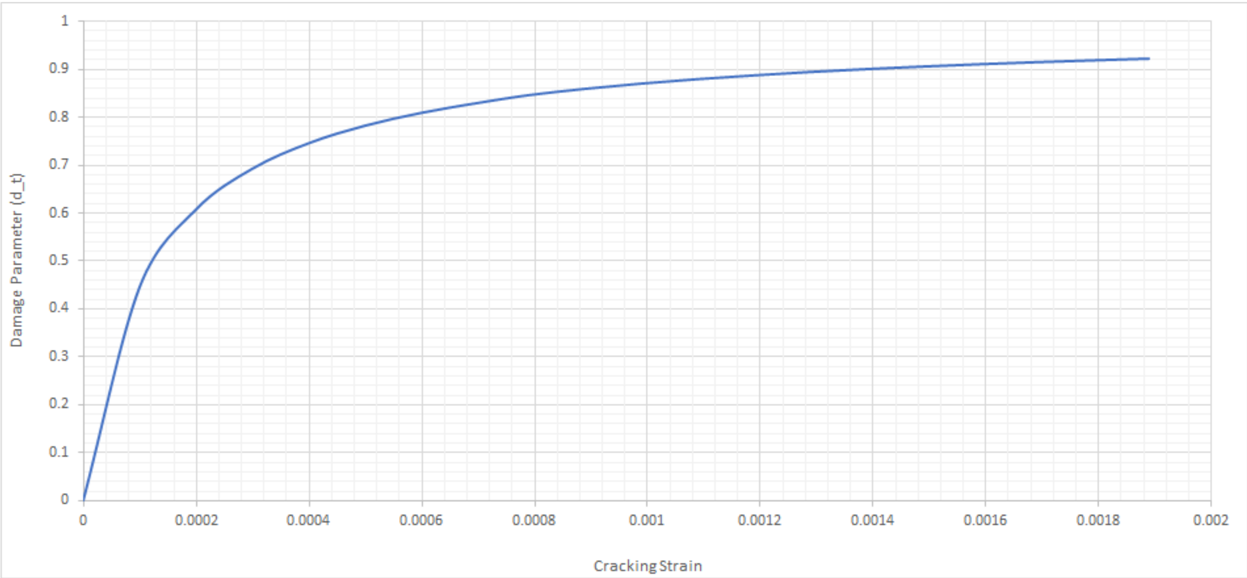

Figure 2.10. Tension Damage Model for 3,160 psi Concrete

In Figure 2.10, the critical points are as follows:

(Cracking strain, Tensile damage parameter)

Start point: (0, 0)
End of linearity: (0.0001, 0.44522)
Endpoint: (0.00189, 0.92163)
Similarly, following the model described above, another MATLAB code was written to represent the compressive damage of the concrete. Table 2.5 lists the compressive damage behavior of the concrete with a compressive strength of $f_c^{'} = 3{,}160$ psi (21.78 MPa), including damage parameter (d_c) and inelastic strain ($\tilde{\varepsilon}_c^{in}$).

Table 2.5. Compressive Damage Values for 3,160 psi (21.78 MPa) Concrete

Inelastic Strain	**Damage Parameter (d_c)**

0	0
0.00033	0
0.00067	0
0.00268	0.17951
0.00301	0.26848
0.00335	0.35303
0.00368	0.42943
0.00402	0.49661
0.00435	0.55483
0.00469	0.60497
0.00502	0.64804
0.00536	0.68509
0.00569	0.71702
0.00603	0.74463
0.00636	0.76862
0.0067	0.78953
0.00703	0.80785
0.00737	0.82397
0.0077	0.8382
0.00804	0.85083
0.00837	0.86207

Figure 2.11 shows the compressive damage behavior of the concrete with a compressive strength of $f_c^{'} = 3{,}160$ psi, including damage parameter (d_c) and inelastic strain ($\tilde{\varepsilon}_c^{in}$).

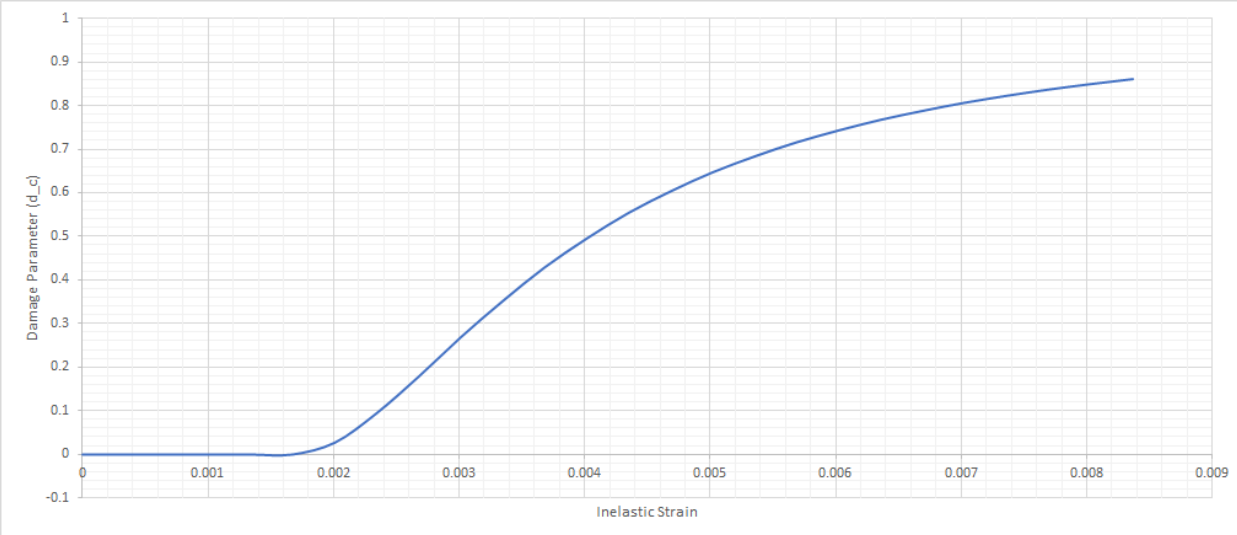

Figure 2.11. Compression Damage Model for 3,160 psi Concrete

In Figure 2.11, the critical points are as follows:
(Inelastic strain, Compressive damage parameter)
Start point: (0, 0)
End of linearity: (0.00067, 0)
Endpoint: (0.00837, 0.86207)

2.11 Finite Element Modeling of the RC Column

Columns with insufficient transverse reinforcement are subject to damage, including shear and axial load collapse, as demonstrated by actual earthquakes and simulated laboratory experience. The column in this investigation had modest transverse reinforcement, which is typical of non-seismic structures. Before the requirements for ductile detailing were widely recognized about 30 years ago, similar details were used in earthquake-resistant designs. Four full-scale columns with minimal transverse reinforcement subjected to quasistatic testing under unidirectional lateral load, with either constant or variable axial loads were tested previously by Sezen and Moehle to examine this behavior [21,22]. The column geometries, materials, and details were selected to represent a class of columns used in older existing buildings for which flexural yield would occur before shear failure. Here in this research, a specific specimen (Specimen #4) was selected over the other three columns from that experimental investigation for the following reasons:

- The axial load of 667 KN (150 kips) with standard load history until Δ_y (nominal yield displacement) followed by monotonic lateral displacement (as opposed to the other three specimens) to failure, more representative of response to a motion with a large pulse as may occur in forward directivity ground motions in the near field
- Low (light) axial load and cyclic lateral load
- The shear failure occurred after the flexural strength was reached

The experimental test results obtained by Sezen and Moehle were used here to verify the mathematical model and research methodologies introduced in this research study. In their experimental investigation, these researchers had not considered modeling their columns in Finite Element Analysis packages, such as Abaqus. It is worth emphasizing that the tested columns are examples of realistic columns that were implemented in vulnerable buildings 30 years ago.
This section investigates the behavior of a concrete column under axial and lateral load, and an analysis of a column under axial and lateral load is explained. As mentioned before, to verify model validity and accuracy, Specimen #4 from the experimental data of Sezen and Moehle [21, 22] was used to compare test results with those of the numerical modeling. Modeling parameters were discussed earlier in this research study, and some other values are given below in detail.
Material properties for steel and concrete included:

- **Steel**
  - *Density*

$$\rho_s = 0.282\ \frac{lb}{in^3}$$

$$g\frac{m}{s^2} = 386.08\frac{in}{s^2} \Longrightarrow Mass\ Density = \frac{0.282\frac{lb}{in^3}}{386.08\frac{in}{s^2}} = 0.0007304\frac{lbf.s^2}{in^4}$$

  - *Elastic*

$$E_s = 29 \times 10^6\ psi$$
$$\upsilon_s = 0.29$$

- **Concrete**
  - *Density*

$$\rho_c = 142.37\ \frac{lb}{ft^3} \Longrightarrow Mass\ Density = \frac{142.37\ \frac{lb}{ft^3}}{12^3 \times 386.08\frac{in}{s^2}} = 0.0002134\ \frac{lbf.s^2}{in^4}$$

  - *Elastic*

$$E_c = 57{,}000\sqrt{f_c^{'}} = 57{,}000\sqrt{3{,}160} = 3{,}204{,}190\ psi$$
$$\upsilon_c = 0.25$$

  - *Plasticity* is defined in Table 2.6.

Table 2.6. Plastic properties of the concrete

Dilation Angle (ψ)	Eccentricity (e)	f_{bo}/f_{co}	*K*	Viscosity Parameter (μ)
35°	0.1	1.16	0.667	0.0005

▪ Concrete Damage Plasticity

The Concrete Damage Plasticity models were previously defined in Tables 2.2 and 2.3. Figures 2.12, 2.13, and 2.14 show the specimen elevation, column, and top beam cross-section details.

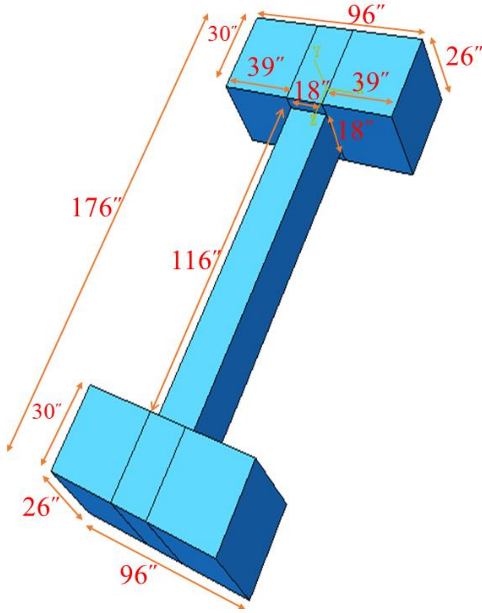

Figure 2.12. Specimen elevation

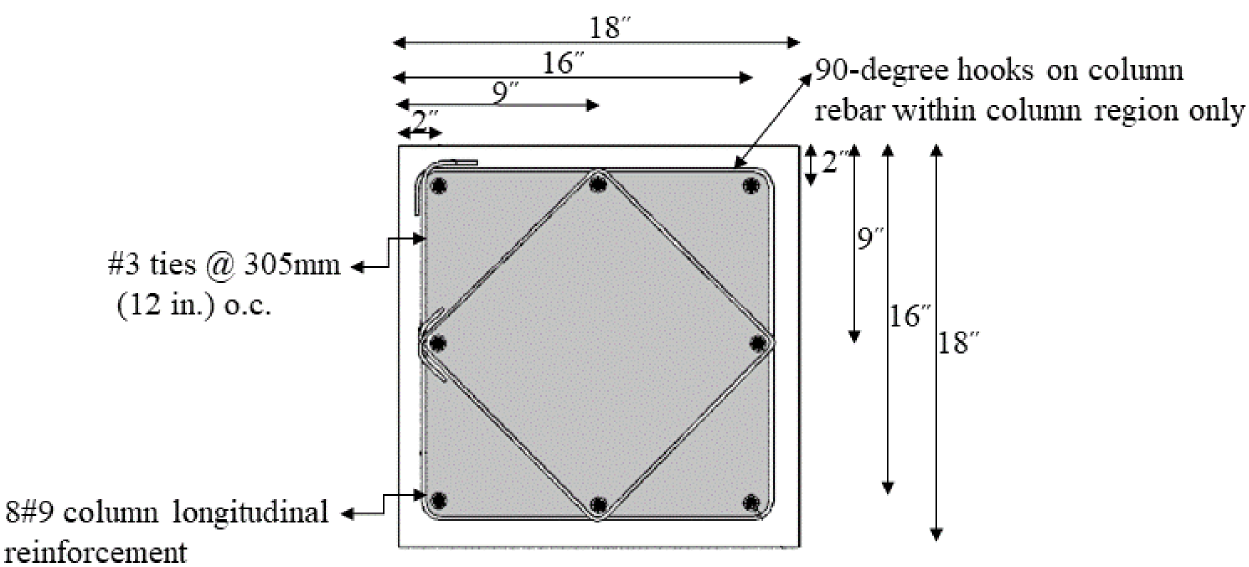

Figure 2.13. Column cross-section details

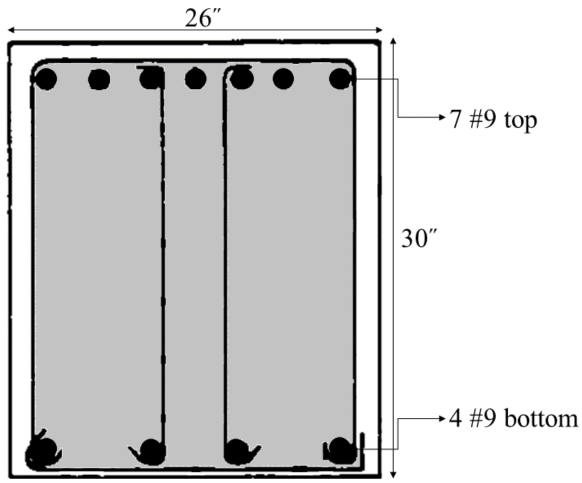

Figure 2.14. Top beam cross-section details

The general loading, support conditions, and reinforcement details of the RC numerical model are shown in Figures 2.15.

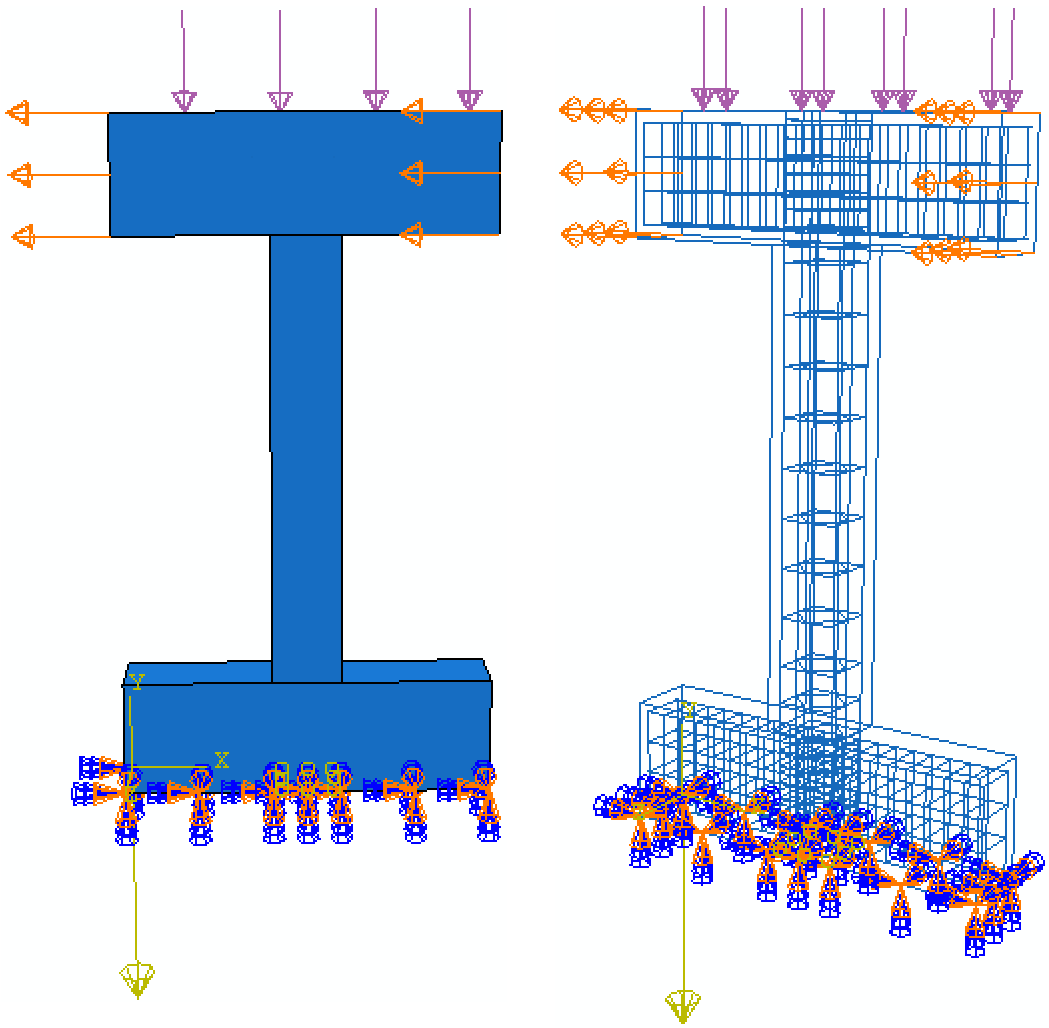

Figure 2.15. Isometric 3-D view

As shown in Figure 2.15, one end of the column was fixed, and the other end was free. Axial load was applied in the first step, and the lateral load was placed on the column in the second step. The column dimension was 18×18×116 in. (457.2 × 457.2 ×294,6.4 mm), and the dimensions of the top and bottom beams were 96×30×26 in. (2438.4×762×660.4 mm). Column clear height was 9 ft 8 in =116 in. (2946.4 mm), and the stirrup dimensions were 14×14 in. (355.6× 355.6 mm). The mean yield of the deformed longitudinal bars with diameters of 28.7 mm (No. 9) (0.99932 in^2) was 438 MPa (63 ksi), and the ultimate strength was 645 MPa (93.5 ksi). The mean yield of the deformed transverse bars with diameters of 9.5 mm (No. 3) (0.11044 in^2) was 476 MPa (69 ksi), and the ultimate strength was 724 MPa (105 ksi). The column had a constant compressive axial load equal to 667 KN (150 kips) (approximately $0.15f_c^{'}A_g$, where $f_c^{'}$ = measured concrete compressive strength and A_g = gross cross-sectional area) and standard lateral displacement history.

$0.15f_c^{'}A_g = 0.15 \times 3{,}160 \times 18 \times 18 = 153{,}576\ lbf$

The column was subjected to cyclic increments of lateral displacements, as described in Figures 2.16, 2.17, and 2.18 [22].

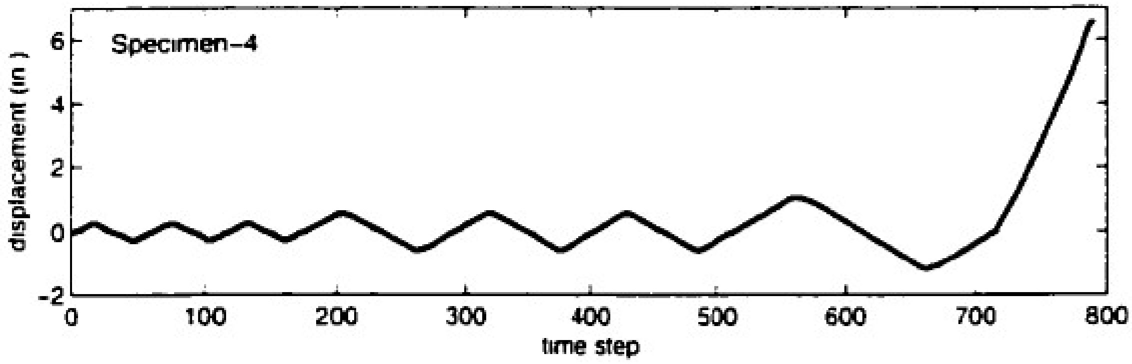

Figure 2.16. Applied displacement history per Sezen's research

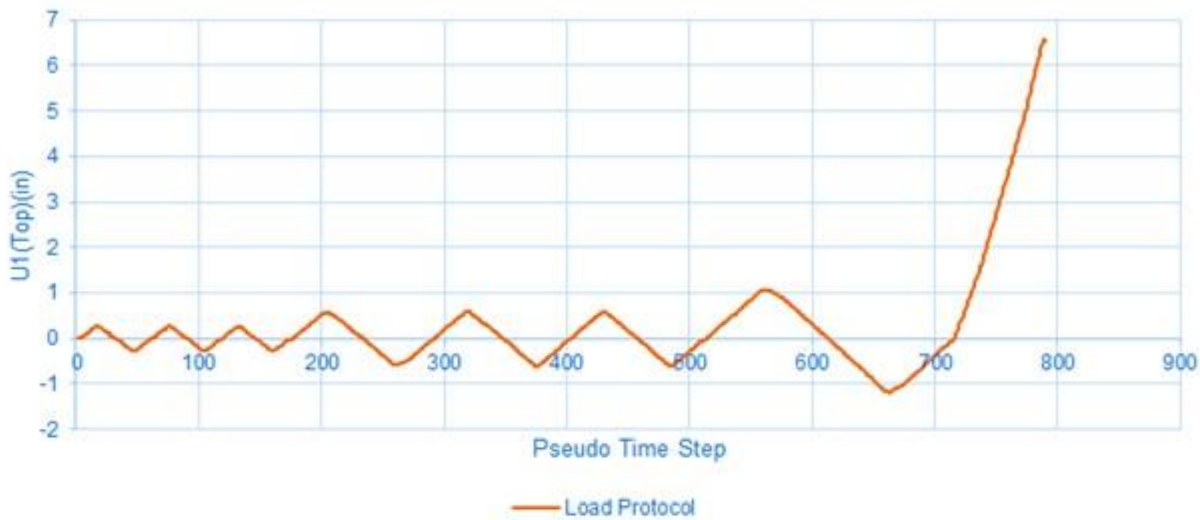

Figure 2.17. Applied displacement history based on the experimental results for U1, Top (top lateral displacement)

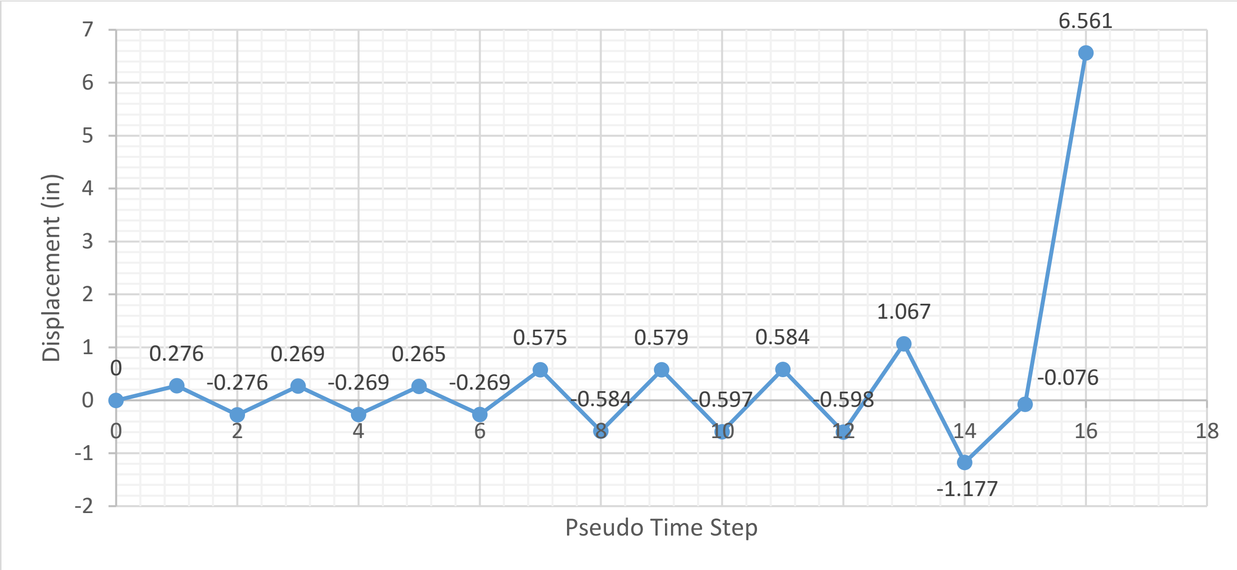

Figure 2.18. Applied displacement history: calculated results

Figure 2.16 shows the experimental test results. The author analyzed and calculated Figures 2.17 and 2.18; because the Figure 2.16 data was unavailable and was not provided by Professor Sezen. Figure 2.17 shows the experimental load protocol results for U1 at the top of the column in the inch versus pseudo time step. Figure 2.18 is the detailed results of the author's analysis of the peak points.

$$Axial\ pressure = \frac{150 \times 10^3}{96 \times 26} = 60.096\ psi$$

The effective monotonic loading resulted in the load-deformation response shown in Figures 2.19–2.21.

U1-Top: lateral displacement at the top of the column

RF1-Bottom: lateral load at the bottom of the column

U2-Top: vertical displacement at the top of the column

Direction 1 is X direction, direction 2 is Y direction, and direction 3 is Z direction.

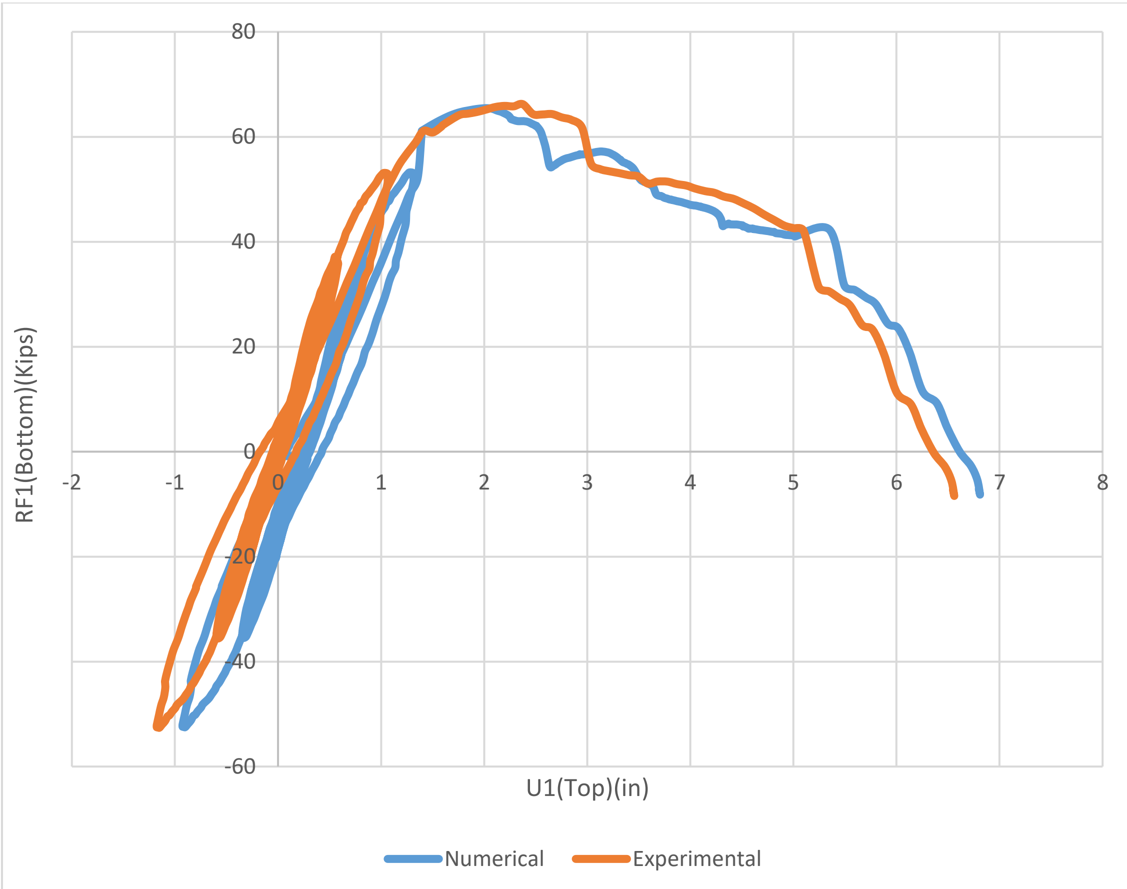

Figure 2.19. Relationship between lateral load and lateral displacement for experimental and numerical (Abaqus) test

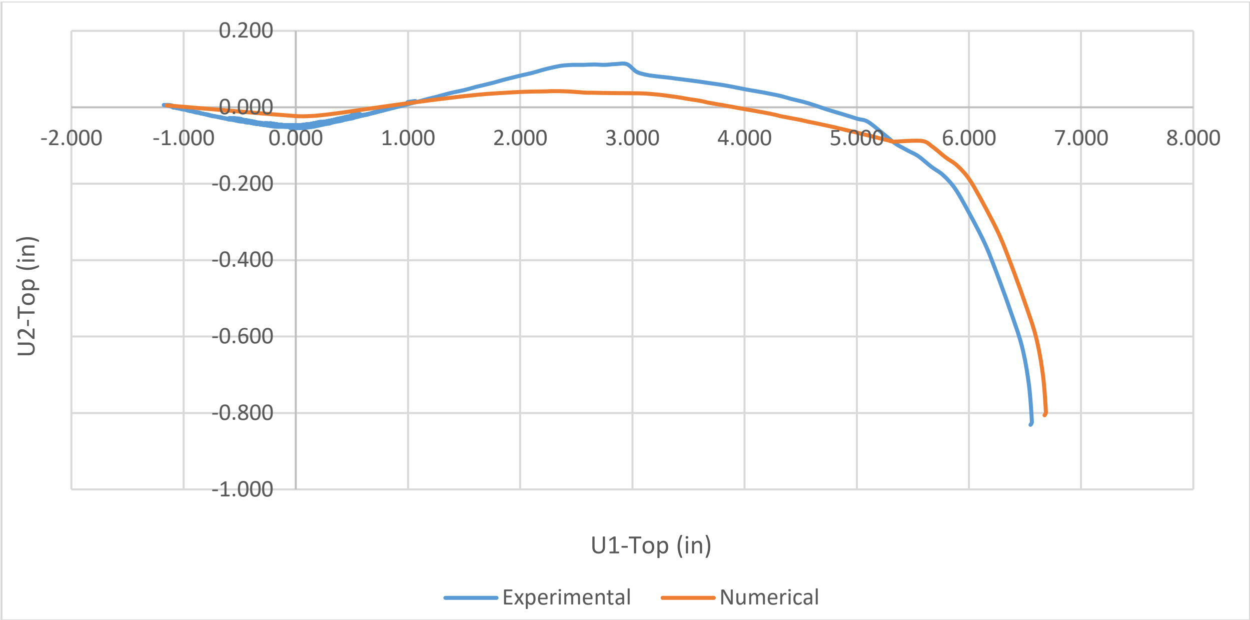

Figure 2.20. Relationship between lateral displacement and vertical displacement for experimental and numerical (Abaqus) test

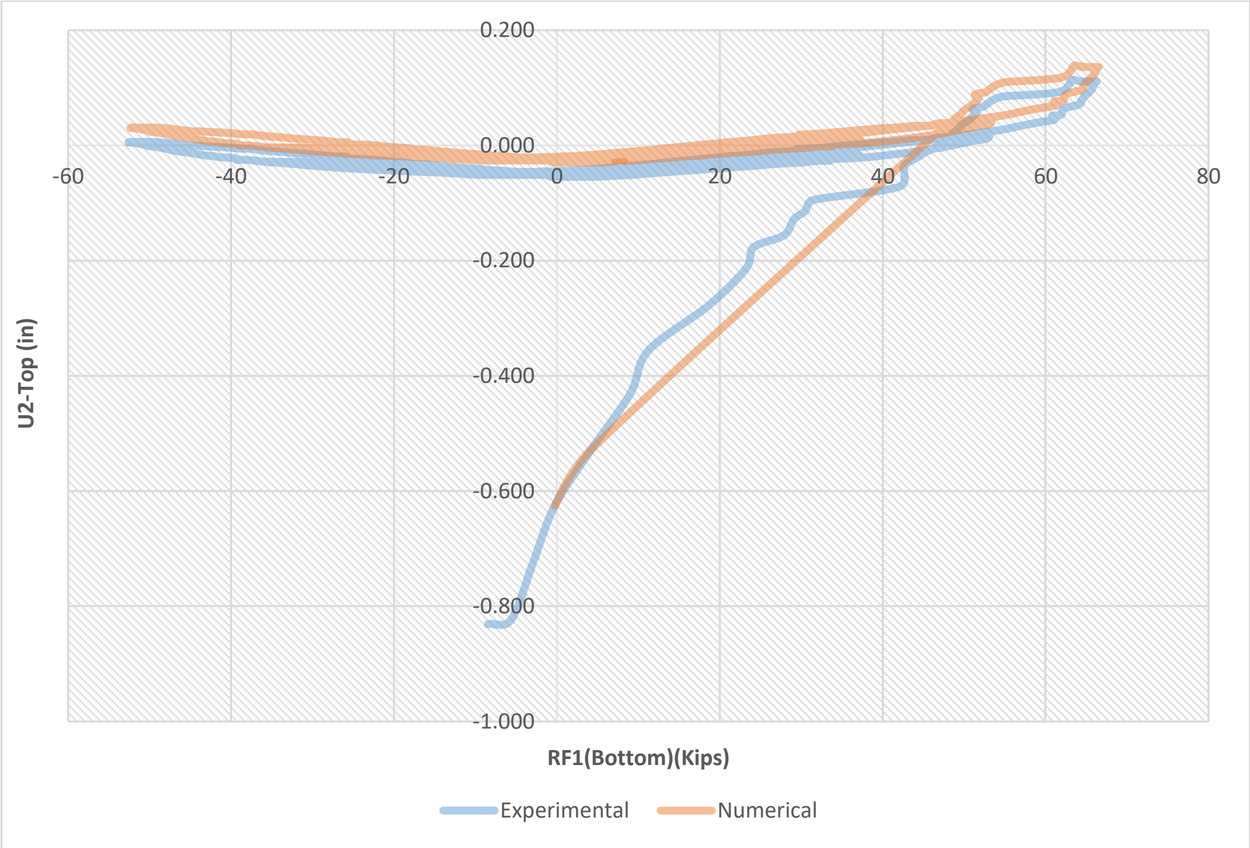

Figure 2.21. Relationship between lateral load and vertical displacement for experimental and numerical (Abaqus) test

Figures 2.19-2.21 elucidate a good concordance between experimental and numerical results calculated with the proposed approaches and the remarkable ability of the proposed methodologies to replicate the experimental results, specifically with respect to envelope curve; both models produce strikingly similar envelope results. The outcomes indicate that the Finite Element results using the above-proposed models are well-matched by experiment results.

As mentioned earlier (in Section 2.7.1 of this research study), the Hognestad concrete model is suitable for $f_c^{'}$ not greater than 6,000 psi. Consequently, the results will only be correct in such cases. For higher strength, whatever model is available and acceptable for concrete material modeling will need to be used accordingly.

2.12 Conclusion

The current study presents an effective implementation of a material model that simulates the nonlinear behavior of RC elements in finite elements applications. The material model requires the value of the maximum compressive concrete strength and uses two numerical techniques, for tension and compression, to describe the stress-strain curves.

The following are the conclusions and accomplishments of this research.

- The model used minimizes the number of tests required to develop an accurate material model when implementing a finite elements application.
- The modeling and methodologies proposed in this research study are valuable because they provide means to numerically verify experimental test results such as those obtained by Sezen and Moehle [22] through mechanical testing. The numerical analysis verification of Sezen and Moehle's experimental tests is here being done for the first time by the author through the means of Finite Element Analysis software (namely, Abaqus).
- The modeling and equations offer the ability to predict the behavior of the concrete and the steel. These were explicitly selected to match the physical characteristics of the structure in order to best represent and predict the experimental test specimens and results. The material models used and implemented here have been recently proposed and accepted in the current research literature.
- Although numerically extensive and very time-consuming, the material and damage modeling presented in this research study can be used to accurately represent the behavior of actual structural members for which experimental tests or monitoring data may not be available.

The procedure implemented here was applied to reinforced concrete only. For other construction materials such as steel or FRP, the appropriate material model will need to be incorporated into the FEM numerical solution. Future research is currently underway by the author.

2.13 Application to Future Research

This research may be extended to include other research areas. For instance, according to Nayal and Rasheed (2006), developing the stress-strain relationship for the tensile region requires implementing a numerical technique suitable for RC and fiber-reinforced concrete [23]. Although this current research emphasizes only RC elements, the similarity of the tension stiffening model in RC elements may allow the model to be adopted for fiber-reinforced concrete with minor parametric changes. Hsu and Hsu (1994) proved that the compressive stress-strain relationship could accurately represent the strain-softening regime and accurately simulate damage triggered by concrete crushing [24]. Thus, the presented material could be used for both RC and fiber-reinforced concrete elements to assess or simulate damage caused by concrete crushing and/or tensile cracking.

3.14 Data Availability Statement

All data and MATLAB codes that support the findings of this study are available from the author upon reasonable request.
A third party provided all data used during the study. Direct requests for these materials may be made to the provider as indicated in the Acknowledgements.
Professor Halil Sezen from Ohio State University provided all experimental data of Specimen #4 used in this research study, which also could be accessed through the following link:
https://datacenterhub.org/dataviewer/view/neesdatabases:db/aci_369_rectangular_column_database/
All the MATLAB codes are available upon reasonable request.

2.15 Acknowledgments

The author would like to express his great appreciation to Professor Halil Sezen from Ohio State University for providing experimental data of Specimen #4 and guidance in the concrete compressive behavior. The author also would like to thank Professor Y. Tao from the Xi'an University of Architecture and Technology and Professor Jian-Fei Chen from the Southern University of Science and Technology for guiding the definition of damage parameters. In addition, the author would like to express his sincerest gratitude to Professor James Wight from the University of Michigan-Ann Arbor for providing guidance in concrete compressive behavior.

2.16 Notation List

The following symbols are used in this chapter:

$\dot{d}_v$: viscous stiffness degradation variable for the viscoplastic system;

$\bar{f}_b$: concrete equibiaxial compressive strength;

$\bar{f}_c$: concrete uniaxial compressive strength;

$\bar{f}_t$: concrete uniaxial tensile strength;

D_0^{el}: initial (undamaged) elasticity matrix;

E_0: concrete young’s modulus;

E_0: elastic modulus of the concrete;

E_0: initial (undamaged) elastic stiffness of the material;

E_c: concrete modulus of elasticity;

d_c: concrete damage variable in compression;

d_t: concrete damage variable in tension;

d_v: viscous stiffness degradation variable;

f_{cr}: cracking stress of concrete;

$\bar{p}$: effective hydrostatic pressure;

$\bar{q}$: Mises equivalent effective stress;

CM: compressive meridian;

d: damage factor;

d: degradation variable evaluated in the inviscid backbone model;

d_a: maximum aggregate size of the concrete;

e: eccentricity parameter;

f: either the tensile or compressive strength of concrete as appropriate;

J_2: second invariant of the stress deviator;

n: rate of weakening;

TM: tensile meridian;

$\dot{\bar{\varepsilon}}^p$: plastic strain rate with damage;

$\hat{\bar{\bar{\sigma}}}_{max}$: algebraically maximum eigenvalue of $\bar{\sigma}$ (maximum principal effective stress);

$\tilde{\varepsilon}_c^{in}$: concrete compressive inelastic strains;

$\tilde{\varepsilon}_c^{pl}$: concrete compressive plastic strain;

$\tilde{\varepsilon}_c^{pl}$: equivalent plastic strain in compression;

$\bar{\varepsilon}_{cr}^e$: elastic strain;

$\bar{\varepsilon}^p$: plastic strain with stiffness degradation;

$\tilde{\varepsilon}_t^{ck}$: concrete cracking strain;

$\tilde{\varepsilon}_t^{pl}$: equivalent plastic strain in tension;

$\dot{\varepsilon}_v^{pl}$: viscoplastic strain rate tensor;

$\bar{\sigma}_c$: effective compression cohesion stress;

ε_{0c}^{el}: concrete elastic compressive strain corresponding to the undamaged material;

ε_{0t}^{el}: elastic strain corresponding to the undamaged material;

ε_c: concrete total compressive strain;

ε_c: total compression strain;

ε_{cr}: cracking strain of concrete;

ε^p: plastic strain without stiffness degradation;

ε^{pl}: plastic strain evaluated in the inviscid backbone model;

ε_t: concrete total tensile strain;

ε_t: total strain;

ε_t: total tensile strain;

ε_v: volumetric strain;

ε_v^{pl}: viscoplastic strain;

$\bar{\sigma}$: effective stress tensor;

σ_c: concrete compressive stresses;

σ_c: magnitude of the uniaxial compression;

σ_t: concrete stress for uniaxial tension;

σ_t: concrete tensile stress;

α, γ: dimensionless material constant;

γ: shear strain;

ε: total strain;

μ: viscosity parameter representing the relaxation time of the viscoplastic system;

σ: stress including compressive stress or tensile stress;

References

1. Ataei, Hossein, and Mohammadhossein Mamaghani. 2018. Finite Element Analysis: Applications and Solved Problems Using Abaqus®. United States.

2. Jirásek Milan, and Bažant Z. P. 2002. Inelastic Analysis of Structures. Chichester, West Sussex, England: Wiley.

3. Control of Deflection in Concrete Structures. 2003. Farmington Hills, MI: American Concrete Institute.

4. Wang, Taijun, and Thomas T.C Hsu. 2001. "Nonlinear Finite Element Analysis of Concrete Structures Using New Constitutive Models." Computers & Structures 79 (32): 2781–91. https://doi.org/10.1016/s0045-7949(01)00157-2.

5. Yafei, Lou, Zou Tao, Yang Jie, Jiang Tao, Zhang Qingfang, and Hong Hexuan. 2021. "A Simplified Uniaxial Stress-Strain Curve of Concrete and Its Application in Numerical Simulation." E3S Web of Conferences 283: 01045. https://doi.org/10.1051/e3sconf/202128301045.

6. Tao, Y., and J. F. Chen. 2014. "Concrete Damage Plasticity Model for Modeling FRP-to-Concrete Bond Behavior." Journal of Composites for Construction. American Society of Civil Engineers. April 21, 2014. https://ascelibrary.org/doi/10.1061/%28ASCE%29CC.1943-5614.0000482.

7. Prager, William. 1955. "The Theory of Plasticity: A Survey of Recent Achievements." Proceedings of the Institution of Mechanical Engineers 169 (1): 41–57. https://doi.org/10.1243/pime_proc_1955_169_015_02.

8. Ottosen, Niels Saabye. 1977. "A Failure Criterion for Concrete." Journal of Engineering Mechanics Division 103 (4): 527–35. https://www.researchgate.net/publication/248811634_A_Failure_Criterion_for_Concrete.

9. Lubliner, Jacob, and E Oñate. 1989. "A Plastic-Damage Model for Concrete." International Journal of Solids and Structures 25 (3): 299–326. https://doi.org/https://doi.org/10.1016/0020-7683(89)90050-4.

10. Lee, Jeeho, and Gregory L. Fenves. 1998. "Plastic-Damage Model for Cyclic Loading of Concrete Structures." Journal of Engineering Mechanics 124 (8): 892–900. https://doi.org/10.1061/(asce)0733-9399(1998)124:8(892).

11. Kupfer, Helmut, Hubert K. Hilsdorf, and Hubert Rusch. 1969. "Behavior of Concrete Under Biaxial Stresses." ACI Journal Proceedings 66 (8): 656–66. https://doi.org/10.14359/7388.

12. Borst, R. de. 1986. Non-Linear Analysis of Frictional Materials.

13. Building Code Requirements for Structural Concrete and Commentary (ACI 318-08): An ACI Standard. 2008. Detroit: American Concrete Institute.

14. Building Code Requirements for Structural Concrete (ACI 318-14): an ACI Standard and Commentary on Building Code Requirements for Structural Concrete (ACI 318R-14): an ACI Report. 2014. Farmington Hills, MI: American Concrete Institute, ACI.

15. Belarbi, Abdeldjelil, and Thomas T. C. Hsu. 1994. "Constitutive Laws of Concrete in Tension and Reinforcing Bars Stiffened by Concrete." Structural Journal. July 1, 1994. https://www.concrete.org/publications/internationalconcreteabstractsportal/m/details/id/4154.

16. Pang, Xiao-Bo David, and Thomas T. C. Hsu. 1995. "Behavior of Reinforced Concrete Membrane Elements in Shear." Structural Journal. November 1, 1995. https://www.concrete.org/publications/internationalconcreteabstractsportal/m/details/id/9661.

17. Tamai, Shinici, Hiroshi Shima, Junichi Izumo, and Hajime Okamura. 1987. “Average Stress–Strain Relationship in Post Yield Range of Steel Bar in Concrete.” Concrete Library of Japan Society of Civil Engineers (JSCE) 6: 117–29. http://www.infra.kochi-tech.ac.jp/shima/paper/1987/Average%20stress-strain%20in%20post%20yield%20range%20of%20steel%20bar%20(Tamai%2C%20CLI%201988).pdf.

18. “Ceb-Fip Model Code 1990.” 1993. https://doi.org/10.1680/ceb-fipmc1990.35430.

19. Getting Started with ABAQUS: Interactive Edition. 2008. Providence, RI: Dasssault Systèmes.

20. Wahalathantri, Buddhi, David Thambiratnam, Tommy Chan, and Sabrina Fawzia. 2011. “A MATERIAL MODEL FOR FLEXURAL CRACK SIMULATION IN REINFORCED CONCRETE ELEMENTS USING ABAQUS.” Proceedings of the First International Conference on Engineering, 260–64. https://eprints.qut.edu.au/41712/1/eddBE2011_260-264_Wahalathantri.pdf.

21. Sezen, Halil, and Jack P. Moehle. 2006. “Seismic Tests of Concrete Columns with Light Transverse Reinforcement.” ACI Structural Journal 103 (6): 842–49. https://doi.org/10.14359/18236.

22. Sezen, Halil. 2002. “Seismic Behavior and Modeling of Reinforced Concrete Building Columns.” Dissertation, ProQuest. Thesis (Ph. D in Engineering--Civil and Environmental Engineering)--University of California, Berkeley, Fall.

23. Nayal, Rim, and Hayder A. Rasheed. 2006. “Tension Stiffening Model for Concrete Beams Reinforced with Steel and FRP Bars.” Journal of Materials in Civil Engineering. American Society of Civil Engineers. December 1, 2006. https://ascelibrary.org/doi/abs/10.1061/%28ASCE%290899-1561%282006%2918%3A6%28831%29.

24. Hsu, L. S., and C.-T. T. Hsu. 1994. “Complete Stress — Strain Behaviour of High-Strength Concrete under Compression.” Magazine of Concrete Research 46 (169): 301–12. https://doi.org/10.1680/macr.1994.46.169.301.

Chapter 3 : Modeling Ductile-Damage of Steel of Reinforced Concrete Columns by Finite Element Method

Abstract

With regards to the steel reinforcement, the structural steel modeling for cyclic response is essential for the functioning appraisal and design of steel structures. Though various mathematical models have been suggested and developed to simulate metal plasticity, only a few of them have been implemented in finite element method-based software such as Abaqus, which uses incremental plasticity procedures. This part of the dissertation research introduces and briefly describes a built-in "Isotropic, Kinematic, Johnson-Cook, User and Combined" hardening to model metal plasticity under cyclic loading. The plastic deformation is load path-dependent and irreversible. Implementation of this model is fundamentally significant for Abaqus users to increase understanding of the behavior and plasticity of steel and reinforced (concrete) structures.

Key Words: Ductile-Damage; Steel; Abaqus; Cyclic; Plasticity; Finite Element Method (FEM); Isotropic; Kinematic; Combined hardening; Stress; Strain; Uniaxial; Elastic; Plastic; Yielding; Softening

3.1 Introduction

The plasticity theory contains the strains and stresses analysis in the plastic region of materials with ductile behavior, particularly metals. This research study introduces the fundamental concepts of plasticity theory by discussing the uniaxial stress-strain behavior of metals. Fundamental concepts such as elastic deformation, plastic deformation, yielding, plastic flow, hardening, softening, and the Bauschinger effect for reversed loading are also described. The most consequential characteristics of plastic deformation are its dependency on the load path and unchangeability. This research also utilizes a hardening parameter related to plastic work or plastic strain to investigate the history of loading and then relate the plastic modulus to this hardening parameter. The following research includes general techniques to extend stress-strain behavior in uniaxial conditions to three-dimensional situations [1].

The state of the art of steel behavior in reinforced concrete (RC) elements, including columns, was proposed by the Mander model applies to diverse steel kinds and grades, such as reinforcing steels with and without a specified yield plateau. This research study proposes various approaches to modeling the reinforcing steel bars (rebars) cyclic response when analyzing RC columns using the finite element method and using advanced built-in material models in Abaqus.

The novelty of this research study is that the author utilized the Ramberg-Osgood model with the most accurate of its parameters in the Finite Element Method. In addition, this research suggests significant and fundamental models and equations for evaluating the n and K (Ramberg-Osgood parameters) for the first time (Zad models and equations). These models and equations simplify the complicated methods of calculation of n and K and were verified by the fitting methodology.

In 1967, Ngo and Scordelis tried to use the finite-element approach to a reinforced concrete structure for the first time. Since then, the rapid development of the finite-element method to a reinforced concrete structure has revealed the incompleteness of material models for reinforced concrete, thereby limiting the future expansion of concrete structure analysis. Previous research efforts have focused on improving the mathematical description of the constitutive relationships of concrete materials and interaction modeling between reinforcement and concrete. Numerous modeling techniques have been presented up to now, including nonlinear elasticity, plasticity, endochronic theory, and damage theory [1]. According to the state-of-the-art research study entitled "Investigation of concrete material models for the analysis of seismic behavior of reinforced concrete under reversed cyclic load" done by Bohara et al. in 2019, they offered a novel approach in the reinforced concrete columns ductile-damage modeling by Finite Element Method, and an equation implemented to capture the softening during brittle and ductile damage with softening parameters [2].

3.2 Historical Remarks

3.2.1 Pioneering Work

The plasticity's origin as a limb of continua mechanics dates back to a series of papers on the extrusion of metals, written from 1864 to 1872, in which Tresca proposed the first yield condition, which states that a metal yields plastically when the maximum shear stress attains a critical value [3]. St. Venant actually formulated the theory in 1870 by introducing the basic constitutive relations for rigid, perfectly plastic materials in plane stress. This formulation's prominent characteristic is the proposal of a flow rule demonstrating that the strain rate or increment is compatible with the stress principal axes. Later in 1870, Levy obtained the general equations in three dimensions. Von Mises in 1913, in his influential paper, independently arrived at a similar generalization using his renowned, pressure-no sensitive yield criteria (octahedral shear stress yield condition, or J_2 theory) [1].

Prandtl lengthened the equations of the St. Venant-Levy-von Mises in 1924 for plane continuum problems to include the elastic component of strain, and Reuss later carried out their extension to three dimensions in 1930. In 1928, von Mises generalized his previous work for a rigid, perfectly plastic solid to include a general yield function and investigated the relationship between the direction of plastic strain rate and the regular or smooth yield surface, therefore, formally announcing the yield function use concept as a plastic potential in the increasingly stress-strain relationships of flow theory. The von Mises yield function is now regarded as a plastic potential for the St. Venant-Levy-von Mises-Prandt-Reuss stress-strain relations. In 1932 and 1933, Reuss studied the flow rule associated with the Tresca yield condition, that includes singular regime (discontinuities in derivatives with respect to stress or corner) [1].

Since problems involving flow or perfect plasticity were emphasized prior to 1940, the development of incremental constitutive relationships for hardening materials proceeded slowly. For example, in 1928, Prandtl attempted to formulate general relations for hardening behavior, and Melan, in 1938, generalized the concepts of perfect plasticity and discovered incremental relations for hardening solids with smooth (regular) yield surfaces. In 1938, Melan studied uniqueness theorems for elastic-plastic incremental problems for perfectly plastic and hardening materials based on limiting assumptions [1].

3.2.2. Classical Theory

The basic concepts and fundamental ingredients of the classical theory of metal plasticity were most intensely developed in the nearly twenty years after 1940. Independent of Melan's work in 1939, Prager used a significant paper published in 1949 to propose a general framework (similar to Melan's in 1938) for plastic constitutive relations for hardening materials with regular (smooth) yield surface. The yield (loading) function and the loading-unloading situations were accurately developed. The continuity condition, which is close to neutral loading, consistency condition which is used for plastic states' loading, uniqueness condition, and plastic deformation unchangeability condition, were developed and covered too. The connection between the convexness of the yield (smooth) surface, the normality to the yield surface and the singularity of the connected boundary-value problem was identified. In 1958, Prager extended this general framework to include thermal effects (non-isothermal plastic deformation) so that it allows the yield surface changing its form with temperature [1].

In 1951, when Drucker proposed and amplified the material stability postulate, a significant concept of work hardening was offered. In 1959, Drucker stretched his assumption to cover the phenomena of time-dependency like linear viscoelasticity and creep. Based on this postulate, the uniqueness of perfectly plastic and work-hardening solids has been proven [3] and various variational theorems have been formulated [1].

In 1948, Hill provided postulates that provide assumptions to help develop the framework of plasticity relations. Bishop and Hill extended the postulates in 1951 in their study of polycrystalline aggregates, and in 1961, Ilyushin considered nonnegative work in a cycle of straining (known as Ilyushin's postulate for material stability). However, the development approach for plasticity relations based entirely on Drucker's postulate is the most plausible [1].

In 1951–1952, Drucker, Greenberg, and Prager provided precise formulations of the two fundamental theorems of limit analysis (i.e., upper-bound and lower-bound theorems) for an elastic-perfectly (or ideally) plastic material, and Hill studied rigid-ideally plastic materials. However, Gvozdev likely is responsible for the previous theorems of limit analysis in 1936, with a translation of his paper from Russian by Haythornthwaite in 1960. The theorems are remarkably simple and intuitive. Since 1960, these theorems' application to the analysis of assorted problems' classes (e.g., metals forming processes, shells and plates, frames, and beams) has raised quickly for metallic structures and concrete and soil materials [1].

In 1953, Koiter further generalized plastic stress-strain relationship for a singular yield surface (i.e., corners or discontinuities in the direction of the normal vector to the yield surface) and the uniqueness and variational theorems for such cases. He was the first to use more than one yield, or loading function in the stress-strain relationship, with each active yield (loading) surface contributing to the plastic strain increment. Koiter showed that the slip theory of plasticity, originally introduced by Batdorf and Budiansky in 1949 and conceived as an alternative formulation to the classical flow theory, is a type of incremental (flow) theory with a singular yield condition composed of an infinite number of independent regular (smooth or continuously differentiable) plane yield functions. Sanders extended the concept in 1955 with a proposed mechanism to formulate subsequent yield surface [1].

Introduction of the “corner” concept by Borst (1982, 1984) ended a period of considerable controversy in which alternative frameworks for constitutive relations that admitted singular regimes in the yield surface were advanced. Further discussion on corner concept was included in the 1960 paper by Koiter and the 1953 paper by Prager, among many others [1].

3.3 One-Dimensional Stress-Strain Analysis

Complications from uniaxial stress typically occur for structures with only one non-zero principal stress component. This non-zero component can be either positive (uniaxial tension) or negative (uniaxial compression). One-dimensional problems are typically studied in structural plasticity to determine the elastic-plastic behavior of materials in structures under complex general stress conditions [4].

3.4 Plastic Behavior in Simple Tension and Compression

3.4.1. Monotonic Loading

Figure 3.1 shows the standard curve of mild steel for a simple tension sample [1].

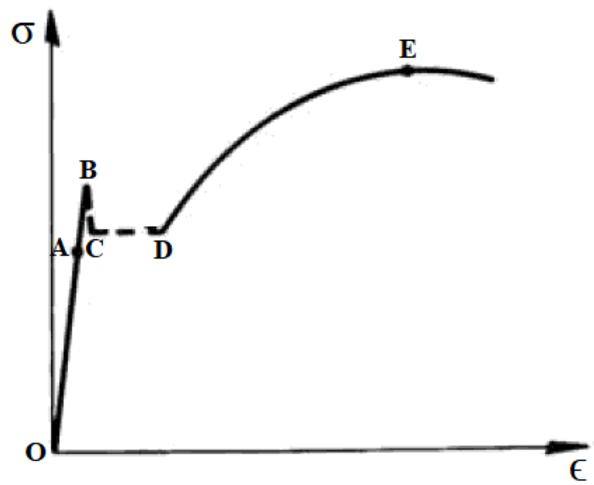

Figure 3.1. Stress-strain diagram for mild steel

The initial elastic region typically appears as straight-line OA, where A defines the limit of proportionality. With further straining the relationship between stress and strain is no longer linear, but the material is still elastic, and upon release of the load, the specimen reverts to its original length. The maximum stress point B at which the load can be applied without causing permeant deformation defines the elastic limit. Point B is titled the yield point too since it indicates the plastic or unchangeable deformation’s beginning. Minimal difference usually occurs between the proportional limit, A, and the elastic limit, B. Mild steel exhibits an upper yield point B and a lower yield point C. An extension at approximately constant load can be observed beyond point C. In general, the flat region CD's behavior is ascribed to as plastic flow. For most metals, however, neither a sharp yield point nor plastic flow is discernible, and a yield strength is generally defined by an offset yield stress, σ_{ys}, or initial yield stress, usually corresponding to 0.1% definition of strain, as shown in Figure 3.2 [1].

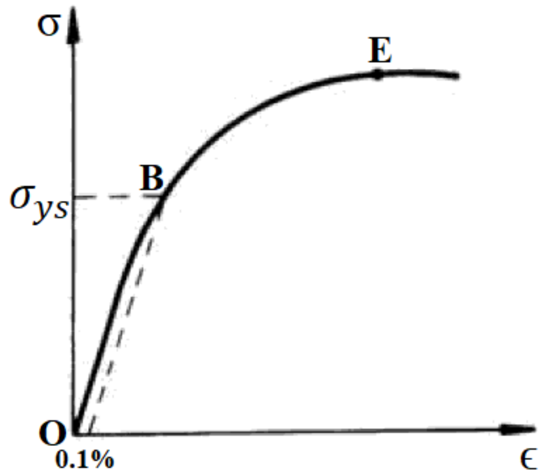

Figure 3.2. Stress-strain diagram for some other metals

Above the yield point, the response of the material is typically elastic and plastic, with the curve slope decreasing steadily and monotonically, resulting in eventual failure of the specimen at point E. A ductile material like mild steel incurs comparatively large strains without failure, but a brittle material such as cast iron fails after very little straining. The failures of metals are generally categorized as cleavage failure (e.g., cast iron) and shear failure (e.g., mild steel). Failure characteristics of geological materials, however, also depend on loading type. For example, concrete exhibits brittle behavior under tensile loading, but it may exhibit ductility before failure under compressive loading with confining pressure [1].

3.4.2. Unloading and Reloading

The behavior of a specimen initially loaded monotonically to a value beyond the initial yield point and then completely unloaded is shown in Figure 3.3 [1].

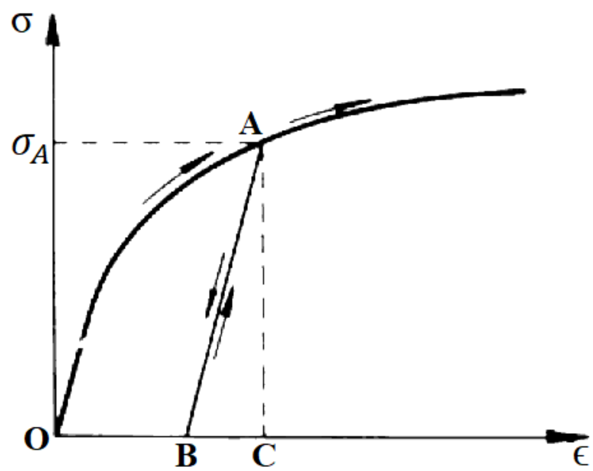

Figure 3.3. Loading, unloading, and reloading paths

As shown in Figure 3.3, the strain decreases along an almost elastic unloading line AB parallel to the initially linear region of the curve when the stress decreased. When the load is again zero at the end of unloading, the strain is not zero and a residual strain OB is present. The unrecoverable strain OB is a plastic strain, and the redeemable strain BC is the elastic strain. Once the specimen is reloaded, the stress-strain curve obeys the BA reloading path, equal to the AB unloading path. Hence, the material is considered elastic till the preceding maximum stress located at A is obtained once more. Stress σ_A is the subsequent yield stress, beyond which further plastic deformation is induced and the stress-strain curve follows the original curve for monotonic loading [1].

After the first yield point has been obtained for most of the materials, the stress-strain curve keeps rising, though the slope turns into successively less till the slope turns to zero as failure happens. Consequently, the subsequent yield stress increases with further straining. The effect of the material being able to withstand increased stress after plastic deformation is known as work or strain hardening since the material gets stronger the more it is strained or worked. A simple compression test of materials such as concrete or rock, however, reveals a region beyond the failure or peak point in which the slope of the curve is negative. Such behavior is called strain softening. This kind of materials weakens with successive straining beyond a specific limit or maximum stress [1].

3.4.3. Reversed Loading

Although a simple compression test on a metal revealed an almost identical stress-strain curve as a simple tension test, after plastic prestraining in tension of a specimen, the stress-strain of this specimen's curve in compression varied significantly from the curve which was achieved from reloading of this specimen in tension or non-disturbed specimen in compression. As shown in Figure 3.4, for the specimen with a preloading σ_y' in tension, its corresponding compressive yielding occurred at stress level σ_y'', which was less than the initial yield stress σ_y and much less than the subsequent yield point σ_y', a phenomenon known as the Bauschinger effect, which is usually present with stress reversal [1].

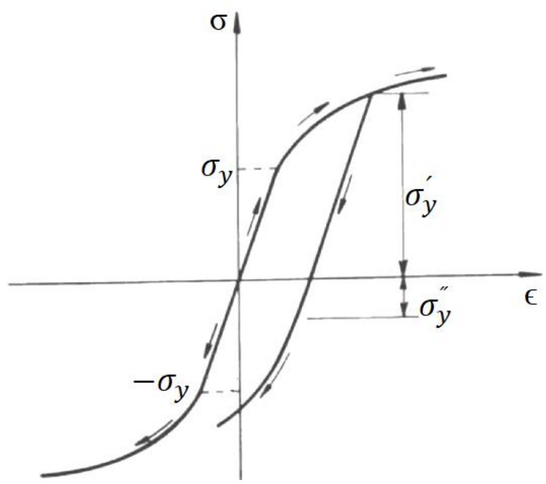

Figure 3.4. Bauschinger effect

Research results failed to demonstrate a one-to-one correspondence between stress and strain in a plastically deformed solid. In other words, the strain is not a function of stress alone; it depends on previous loading history, meaning the material is load-path dependent, as illustrated by the simple case of zero stress when residual strains of various magnitudes can be established by varying the loading history with the stress starting and finishing at zero [1].

The above discussion has supposed an individual stress-strain curve for compression or tension, without dependence on the straining rate. The current hypothesis is related to as time-independency and is credibly valid for structural metals under static load at room temperature. Rate effects are crucial for materials under dynamic loading conditions [1].

3.5 Modeling of Uniaxial Behavior in Plasticity

3.5.1. Simplified Uniaxial Tensile Stress-Strain Curves

The following models idealize the stress-strain behavior of the material to obtain a solution to a deformation problem [1].

3.5.1.1. Elastic-Perfectly Plastic Model

In this case, when yield takes place, the material will have a plastic deformation (Figure 3.5).

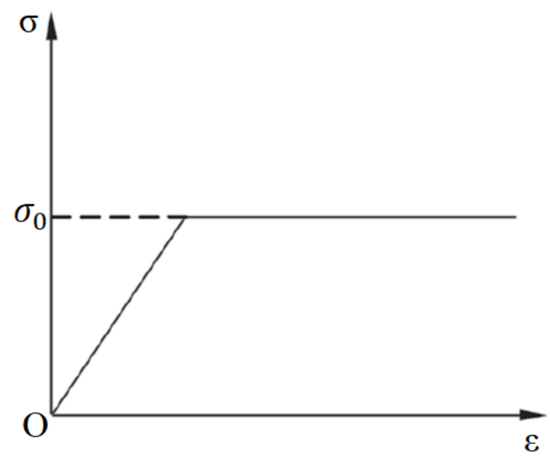

Figure 3.5. Idealized stress-strain curve for elastic-perfectly plastic model

In some instances, it is permissible and convenient to neglect the effect of work hardening, assuming that the plastic flow occurs as the stress has reached the yield stress σ_0 [1].

3.5.1.2. Elastic-Linear Work-Hardening Model (Figure 3.6)

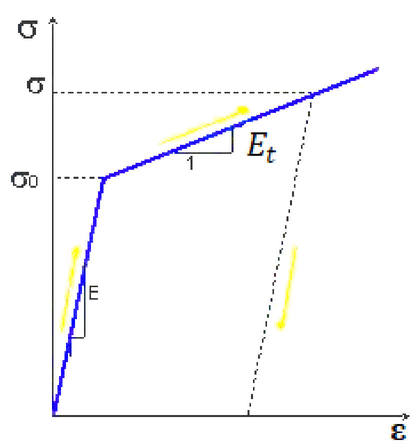

Figure 3.6. Idealized stress-strain curve for elastic-linear work-hardening model

The continuous curve of the elastic-linear work-hardening model is comprised of two straight lines, thereby replacing the smooth transition curve with a sharp breaking point, the ordinate of which is the elastic limit stress or yield strength σ_0. The first straight-line branch of Figure 3.6 has a slope of Young's modulus, E. The second straight-line branch, which idealizes the strain-hardening range, has a slope of $E_t < E$ [1].

E_t: tangent modulus

3.5.1.3. Elastic-Exponential Hardening Model

Figure 3.7 shows the elastic-exponential hardening model as defined with the Hooke's law (valid within the elastic region) and with the power expression (valid in the plastic region when $\sigma > \sigma_0$).

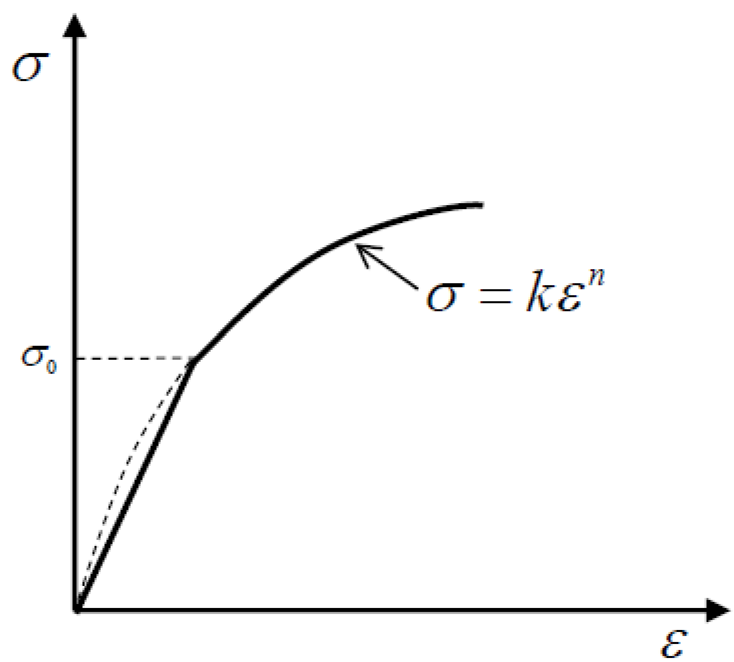

Figure 3.7. Idealized stress-strain curve for elastic-exponential hardening model

3.6 Tangent Modulus E_t and Plastic Modulus E_p

Because the elastic-plastic stress-strain response of a material is nonlinear, an incremental procedure is generally adopted to solve a deformation problem. Therefore, this research assumed that a strain increment, $d\epsilon$, consists of two parts: the elastic strain increment, $d\epsilon^e$, and the plastic strain increment, $d\epsilon^p$ (Figure 3.8) [1].

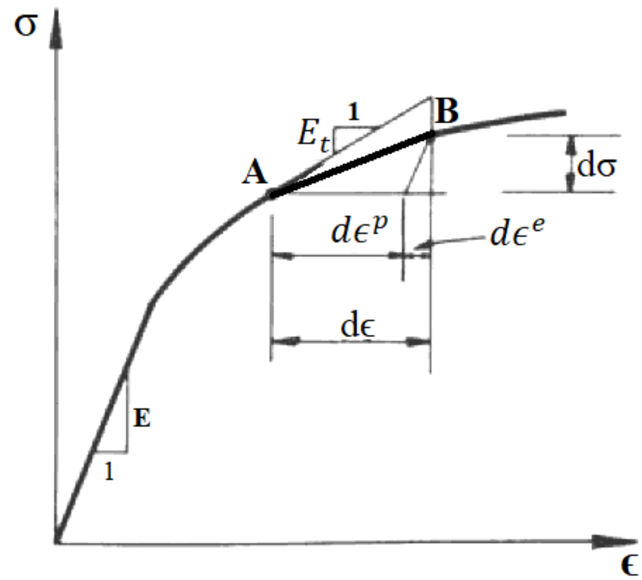

Figure 3.8. Tangent modulus E_t

The stress increment $d\sigma$ is related to the strain increment $d\epsilon$. For uniaxial loading, E_t is the current slope of the σ-ϵ curve (Figure 3.8). E_p is the plastic modulus, which, for uniaxial loading, is the slope of the σ-ϵ^p curve, as shown in Figure 3.9 [1].

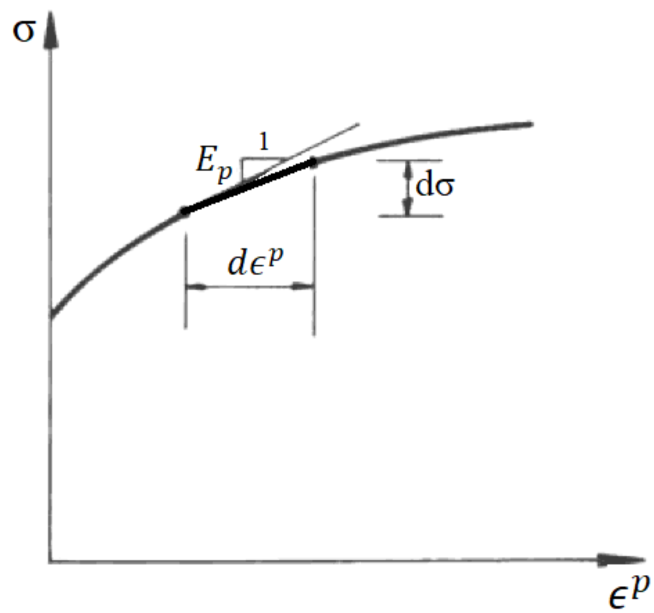

Figure 3.9. Plastic modulus E_p

Figures 3.8 and 3.9 show the relationship between the tangent modulus, Young modulus, and plastic modulus.

$$d\varepsilon = d\varepsilon_e + d\varepsilon_p \tag{1}$$

$$\frac{d\sigma}{E_t} = \frac{d\sigma}{E} + \frac{d\sigma}{E_p} \tag{2}$$

$$\frac{1}{E_t} = \frac{1}{E} + \frac{1}{E_p} \tag{3}$$

$$E_t = \frac{E \cdot E_p}{E + E_p} \tag{4}$$

3.7 Hardening Rules

As described, the phenomenon in which yield stress increases with plastic straining is known as work hardening, or strain hardening. For a material element under a reversed loading condition, the subsequent yield stress is usually determined by one of following three simple rules.

First, the *isotropic hardening* rule means the reversed compressive yield is assumed equal to the tensile yield stress, as shown in Figure 3.10, where $\left|\overline{B'C}\right| = |\overline{BC}|$, the reversed compressive yield stress $\sigma_{B'}$ is equal to the tensile yielding stress σ_B before load reversal [1]. This isotropic hardening rule completely neglects the Bauschinger effect because it assumes that a raised yield point in tension carries over equally in compression.

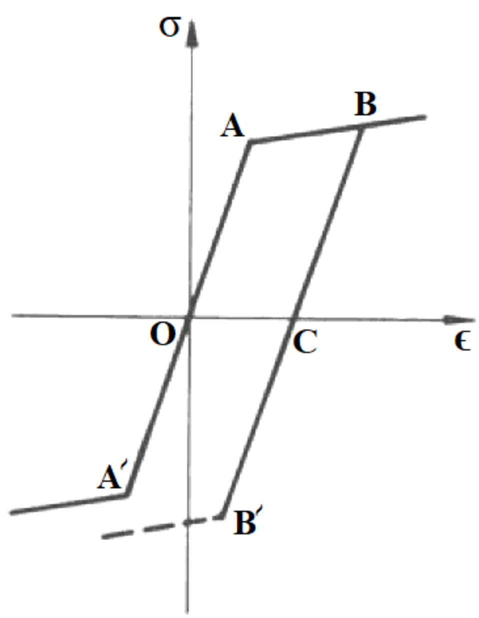

Figure 3.10. Isotropic hardening

Secondly, the *kinematic hardening* rule assumes that the elastic range is unchanged during hardening, meaning this rule fully considers the Bauschinger effect. Kinematic hardening for a linear hardening material is shown in Figure 3.11, where $\left|\overline{BB'}\right| = \left|\overline{AA'}\right|$, where the center of the elastic region moves along the straight line aa′ [1].

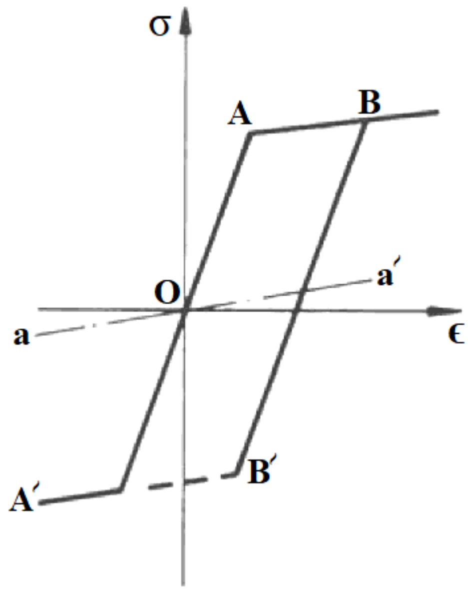

Figure 3.11. Kinematic hardening

In the third rule, the *independent hardening* rule, the material is assumed to be hardening independently in compression and tension, as illustrated in Figure 3.12, where $\overline{BC} > \overline{OA}$, but $\left|\overline{CB'}\right| = \left|\overline{OA'}\right|$; the material hardens only in tension, but it behaves like a virgin material under a reversed compressive loading condition [1].

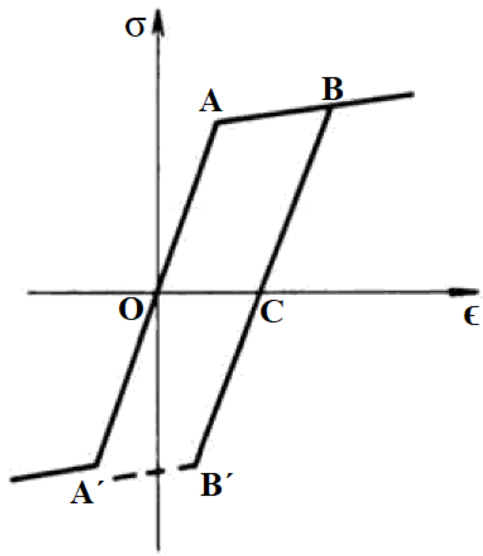

Figure 3.12. Independent hardening

3.8 Hardening Plastic Stress Analysis

Introduction

Most engineering materials exhibit work-hardening behavior. However, increasing a stress state beyond the initial yield surface and into the work-hardening range results in elastic and plastic deformations. When plastic deformation develops, a new yield surface, also called subsequent yield or loading surface, evolves. If the stress point moves inside the subsequent loading surface, the material behaves elastically and no plastic deformation occurs. Since loading surfaces change according to how the plastic deformation occurs, the stress-strain behavior of a work-hardening material is reliant on the loading route or loading history.

The *deformational theory* and the *incremental theory* pertain to work-hardening materials. The *deformational theory* neglects loading history dependency in stress-strain relationships by assuming that the stress state, σ_{ij}, determines the total strain and plastic strain state, ε_{ij} and ε_{ij}^{p}, respectively, if plastic deformation continues. Because of its relative simplicity, the deformational theory has been used extensively in engineering practice to solve elastic-plastic problems. The general validity of the theory is limited to the monotonically increasing loading in which the stress components increase nearly proportionally in a loading process (i.e., proportional loading) or no unloading occurs. In contrast, loading path dependency is assured in the *incremental theory*. In this theory, the plastic strain increment, $d\varepsilon_{ij}^{p}$, is related to the stress increment, $d\sigma_{ij}$, through the plastic deformation history, κ, and the current stress state, σ_{ij}.

The theory of perfect plasticity is the simplest type of incremental theory. Techniques such as flow rules used in perfect plasticity analysis can be extended to work-hardening analysis with minimal changes. The fundamental difference between perfect and hardening plasticity is that the yield surface is not fixed in the stress space for a hardening material. The rule governing the changes of subsequent yield surfaces is called the hardening rule. There are three basic elements in the development of work-hardening stress-strain relationships: loading criteria, flow rules, and hardening rules [4].

3.9 Bounding Surface Theory

The classical models of isotropic or kinematic hardening plasticity are simple and reasonably efficient for simple loading histories. However, for complex loading histories such as cyclic loading in the plastic range, these models are incapable of describing the observed hysteretic behavior shown in Figure 3.13 [1].

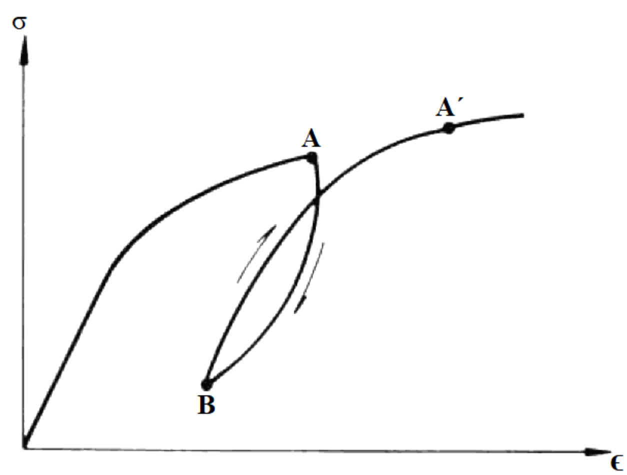

Figure 3.13. Unloading and reloading from a plastic state-hysteretic loop in a cycle of loading

One feature of cyclic behavior is the noncoincidence of the subsequent yield stress (***A***) and subsequent loading stress (***A´***). However, the idealized stress-strain curve of Figure 3.14 implies that the loading cycle is completely reversible, and no plastic deformation is recorded if no reversed yielding has occurred [1].

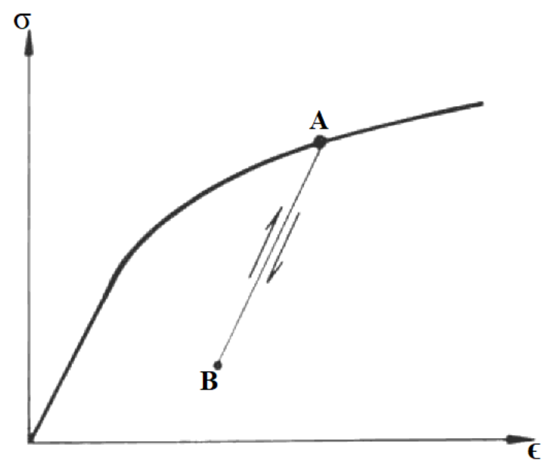

Figure 3.14. Unloading and reloading from a plastic state-idealized stress-strain curve

Additional plastic strains can occur only upon reloading to a stress state beyond point ***A***, and the subsequent behavior is identical to the obtained behavior if unloading had never occurred. Such inadequacy of the classical models has led to the development of alternative plasticity models. The bounding surface theory proposed by Dafalias and Popov in 1975 [5] and Krieg in 1975 [6] is an attempt to generalize the conventional flow theory to account for the cyclic behavior of materials [1].

3.10 Hardening in Abaqus

Hardening settings in Abaqus are Edit Material under Material Behavior. Abaqus software also contains more hardening rules for various materials in plastic modeling, such as cast iron plasticity, Drucker-Prager plasticity, Mohr-Coulomb plasticity, and clay plasticity. Therefore, a user can select any type of plasticity and corresponding hardening for a specific material. Abaqus software provides five options for steel: Isotropic, Kinematic, Johnson-Cook, User, and Combined [7].

3.10.1. Isotropic Hardening

For isotropic hardening, the yielding surface expands or contracts in all directions. By activating "Use strain-rate-dependent data," a user can define yielding stress for corresponding plastic strain; afterward, a new column is appended to the material input chart. Activation of the “Use temperature-dependent date” yields a new column for defining material properties in different temperatures. Each row of the table contains an assigned temperature and corresponding yield stress and plastic strain. Increasing the number of field variables allows a user to add any variable corresponding to yield stress and plastic strain. Sub-options such as Rate Dependent and Anneal Temperature define the stress and strain relationship of material when the strain rate is high and we have decreased hardening rate with changing temperature, respectively [7].

The size of the yielding surface R is influenced by isotropic hardening, which is proportional to the cumulative plastic strain $\hat{\varepsilon}_p$. The isotropic hardening's definition is as followings [8]:

$$R = R_0 + R_\infty\left(1 - e^{-b_{iso}.\hat{\varepsilon}_p}\right) \tag{5}$$

where $\hat{\varepsilon}_\mathrm{p}$ is the accumulated plastic strain; and material constants R_0, R_∞, and b_{iso} could be determined from experimental data by applying the curve fitting.

The hardening isotropic non-linear law is expressed as [9]:

$$\sigma_e = \sigma_0 + Q.\left[1 + exp\left(-b.\varepsilon_e^{pl}\right)\right] \tag{6}$$

σ_e: equivalent stress

σ_0: initial size of the yield surface

Q: maximum change in the size of the yield surface

b: rate at which the size of the yield surface changes as plastic straining progresses

ε_e^{pl}: equivalent plastic strain

Figures 3.15 illustrates the schematic isotropic hardening model.

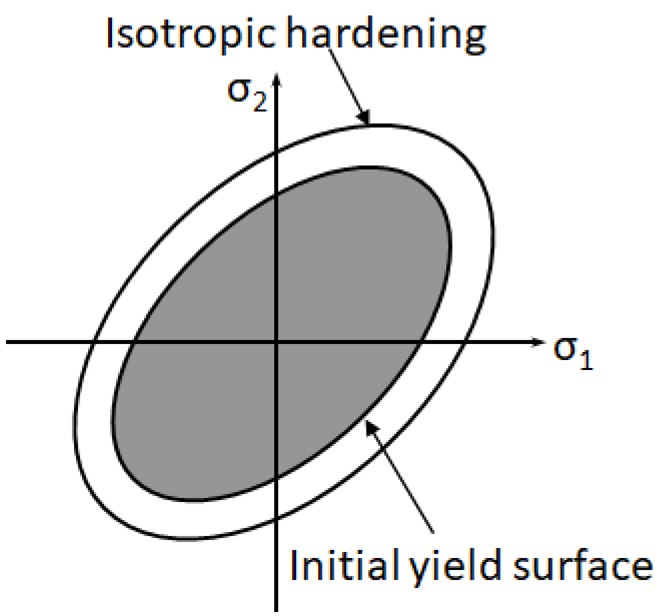

Figure 3.15. Isotropic hardening

Figure 3.16 shows a uniaxial stress-strain curve including nonlinear hardening and graphical depictions of the first and subsequent yield surfaces [10].

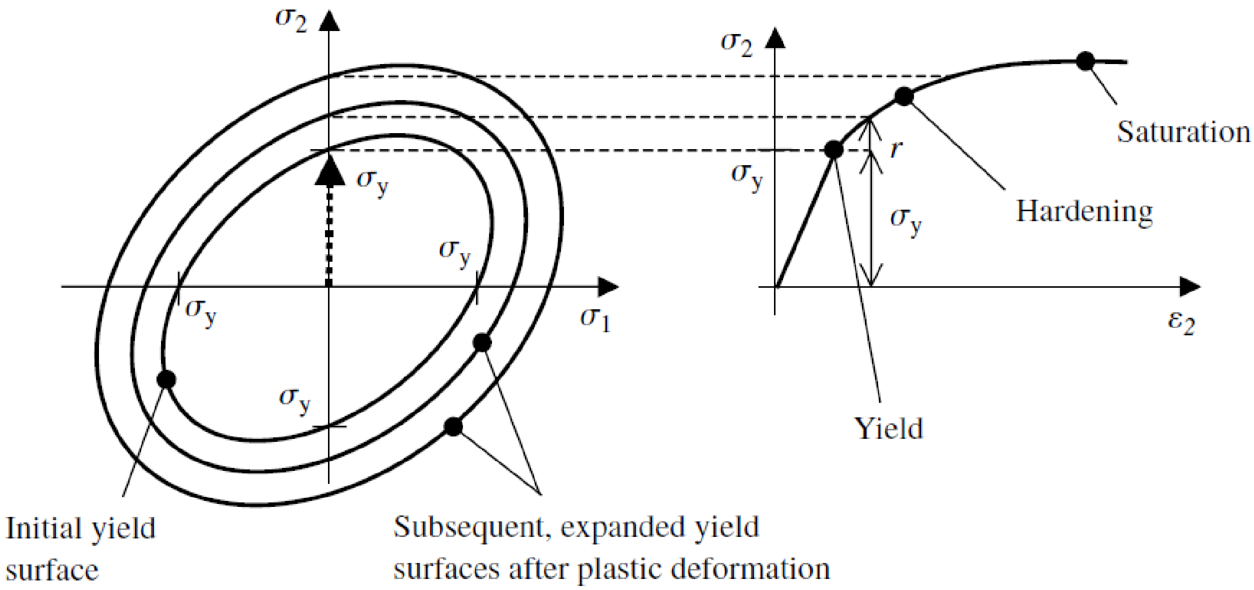

Figure 3.16. Isotropic hardening (with expanding yield surface due to plastic deformation) and the corresponding uniaxial stress-strain curve [10]

Figure 3.17 schematically presents a material that hardens isotropically. As shown, at load point (1), which corresponds to a strain ε_i, reversing the load causes the material to exhibit elastic behavior (i.e., below the yield stress) and linear stress-strain behavior continues until load point (2). At this point, the load point is once again located on the extended yield surface, and any plastic deformation arises from an increase in load. Figure 3.17 (b) demonstrates that isotropic hardening results in a vast elastic area during reversed loading, which is rarely observed in experimental studies [10].

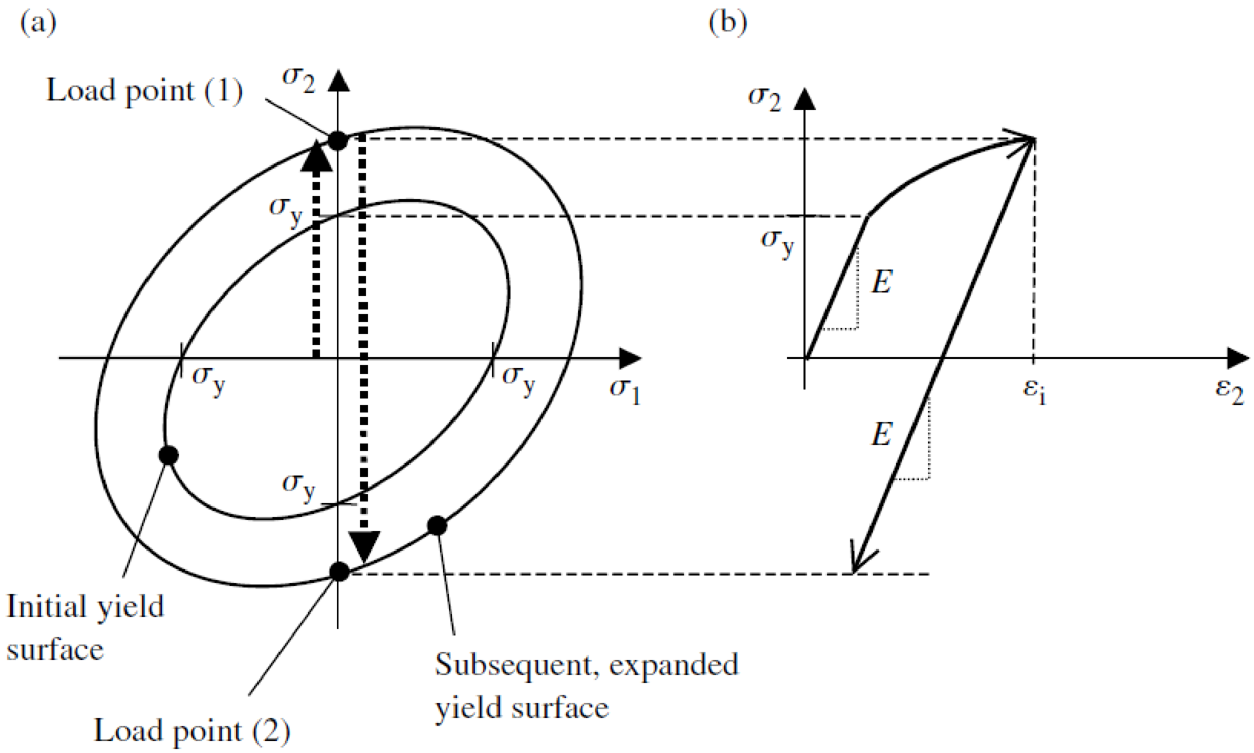

Figure 3.17. Reversed loading accompanied with isotropic hardening (a) yield surface; (b) which results in stress-strain curve [10]

3.10.2. Kinematic Hardening

Kinematic hardening simulates the inelastic behavior of materials that are subjected to cyclic loading, including a linear kinematic hardening model. To consider kinematic hardening for a material, a user must select the Kinematic option from the Hardening dropdown. As with isotropic hardening, toggling the "Use temperature-dependent date" option creates a new column for defining material properties in different temperatures. Each row of the table can contain a temperature and corresponding yield stress and plastic strain. Sub-options in kinematic hardening are *Oml* and *Anneal* Temperature. Selecting *Oml* (Oak Ridge National Laboratory) allows stainless steel 304 and 316 to be defined based on NE F9-5T (1981), including creep in these materials. *Anneal* Temperature is identical to on what mentioned for the isotropic hardening [7].

Kinematic hardening refers to the position of the yielding surface. The backstress α can be expressed based on Chaboche theory [23] as [8]:

$$\alpha = \alpha_1 + \alpha_2 + \alpha_3 = \frac{C_1}{\gamma_1}(1 - e^{-\gamma_1 . \varepsilon_p}) + \frac{C_2}{\gamma_2}(1 - e^{-\gamma_2 . \varepsilon_p}) + \frac{C_3}{\gamma_3}(1 - e^{-\gamma_3 . \varepsilon_p}) \quad (7)$$

where ε_p is the plastic strain, that could be computed as:

$$\varepsilon_{total} = \varepsilon_{elastic} + \varepsilon_{plastic} \Longrightarrow \varepsilon_{plastic} = \varepsilon_{total} - \varepsilon_{elastic} = \varepsilon - \frac{\sigma}{E_s} \tag{8}$$

C_1, γ_1, C_2, γ_2, C_3, γ_3 are parameters obtainable from experimental data with curve fitting [8] and E_s is steel Young modulus.

The non-linear kinematic hardening law is expressed as [9,11]:

$$\dot{\alpha} = \frac{C}{\sigma_e}(\sigma - \alpha)\dot{\varepsilon}^{pl} - \gamma.\alpha.\dot{\varepsilon}_e^{pl} \tag{9}$$

$\dot{\boldsymbol{\alpha}}$: backstress rate tensor

$\dot{\varepsilon}^{pl}$: plastic strain rate tensor

C: initial kinematic hardening modulus

σ_e: equivalent stress

σ: stress

α: backstress tensor

$\dot{\varepsilon}_e^{pl}$: equivalent plastic strain rate

γ: constant determining the rate at which the kinematic hardening modulus decreases with increasing plastic strains

The backstress tensor α indicates yield surface movement in a stress space, whereas σ_e denotes the size of the yield surface.

Figures 3.18 illustrates the schematic kinematic hardening model.

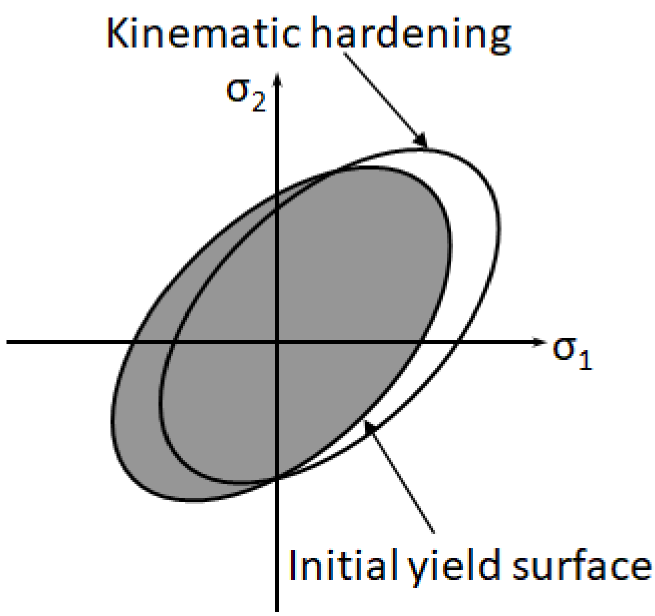

Figure 3.18. Kinematic hardening

In the case of kinematic hardening, the yield surface moves instead of stretching in stress space, as shown in Figure 3.19 [10].

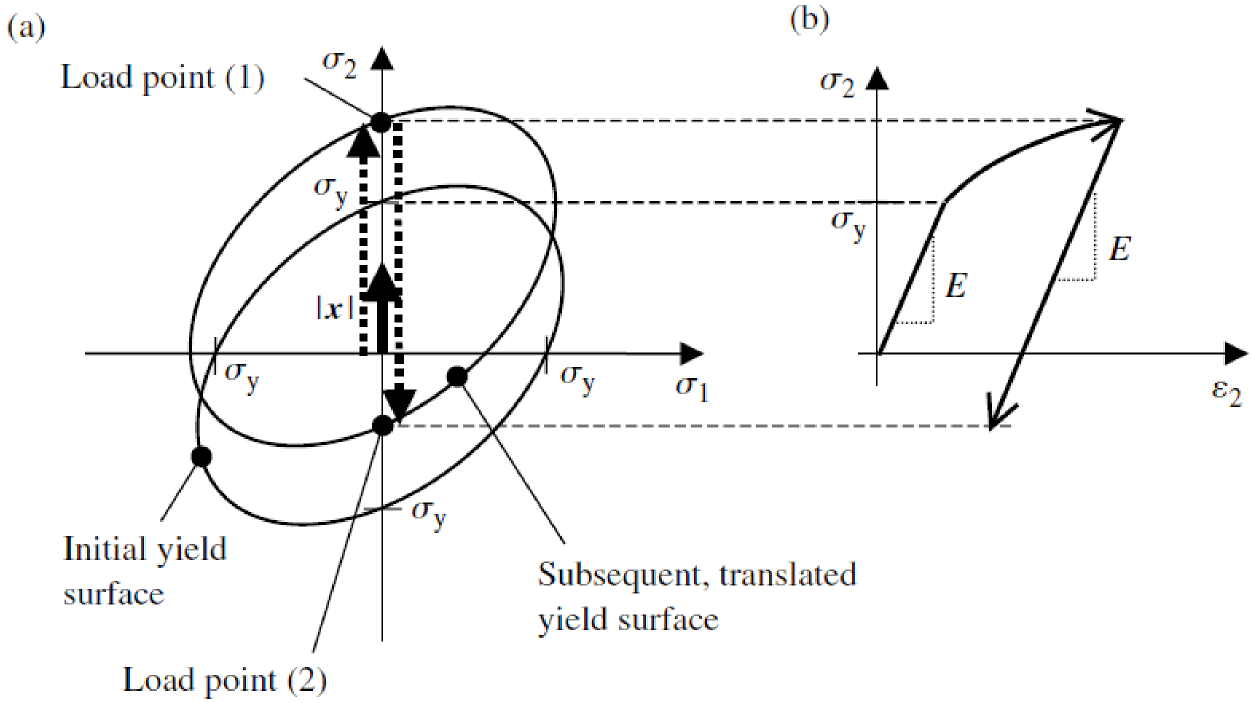

Figure 3.19. Kinematic hardening (a) translation |*x*| of the yield surface with plastic strain; (b) The resultant strain-stress curve with shifted yield stress in compression (Bauschinger effect) [10]

Figure 3.20 shows the resulting stress-strain curve for non-linear kinematic hardening with the translated yield surface [10].

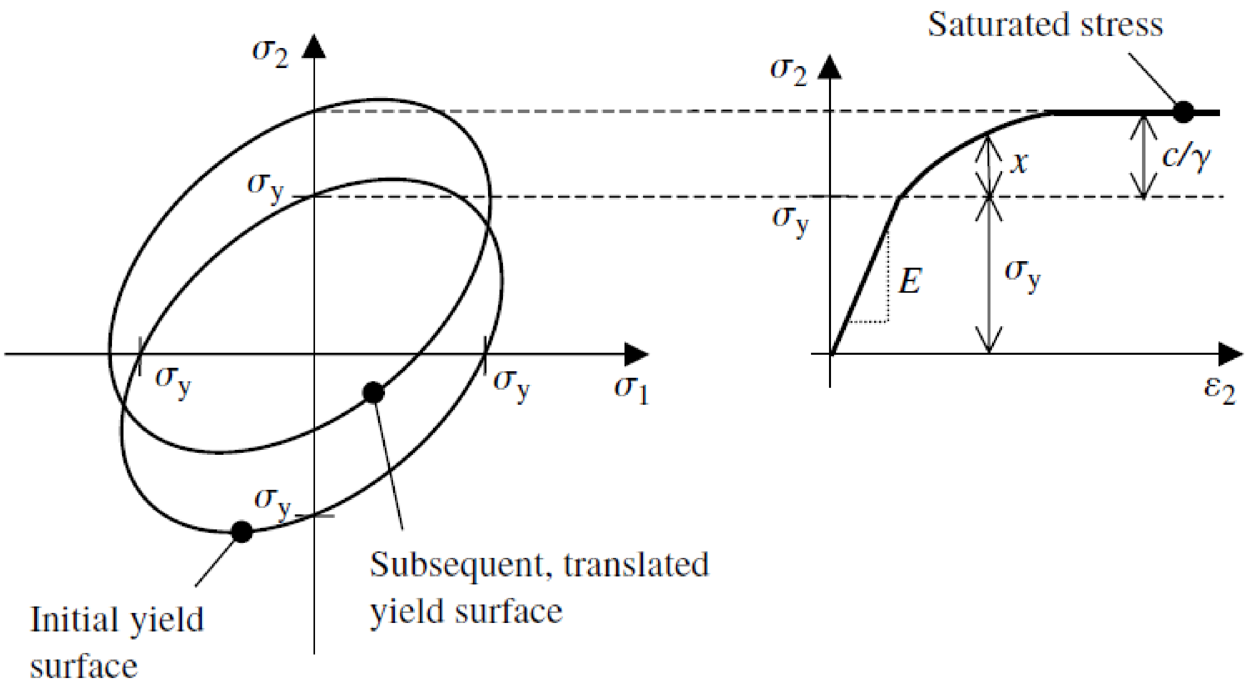

Figure 3.20. Non-linear kinematic hardening and the resulting non-linear hardening stress-strain curve (saturates at stress $\boldsymbol{\sigma_y} + \frac{c}{\gamma}$) [10]

3.10.3. Johnson-Cook Hardening

The Johnson-Cook plasticity model is a von Mises plasticity model with analytical forms of the hardening law and rate dependence. This model is suitable for high-strain-rate deformation of many materials, including most metals, and is typically used in adiabatic transient dynamic simulations [7].

3.10.4. User Hardening

User hardening allows a user to utilize the subroutine "UHARD" to define yield surfaces and isotropic and combined hardening models [7].

3.10.5. Combined Isotropic Kinematic Hardening

The equivalent stress' development explaining the yield surface's size as a function of the equivalent plastic strain additionally explains the model's isotropic hardening component. Selecting "Data type" on the dropdown menu allows access to data such as Half Cycle, Parameters, and Stabilized [7].

Materials that harden kinematically and isotropically are particularly appropriate for applications to cyclic plasticity in which, within an individual cycle, kinematic hardening is the dominant hardening process, resulting in the Bauschinger effect. However, the material also hardens isotropically over quite large numbers of cycles, such that the peak tension and compression stresses in a given cycle increase from one cycle to the next until saturation is achieved, as shown in Figure 3.21 [10].

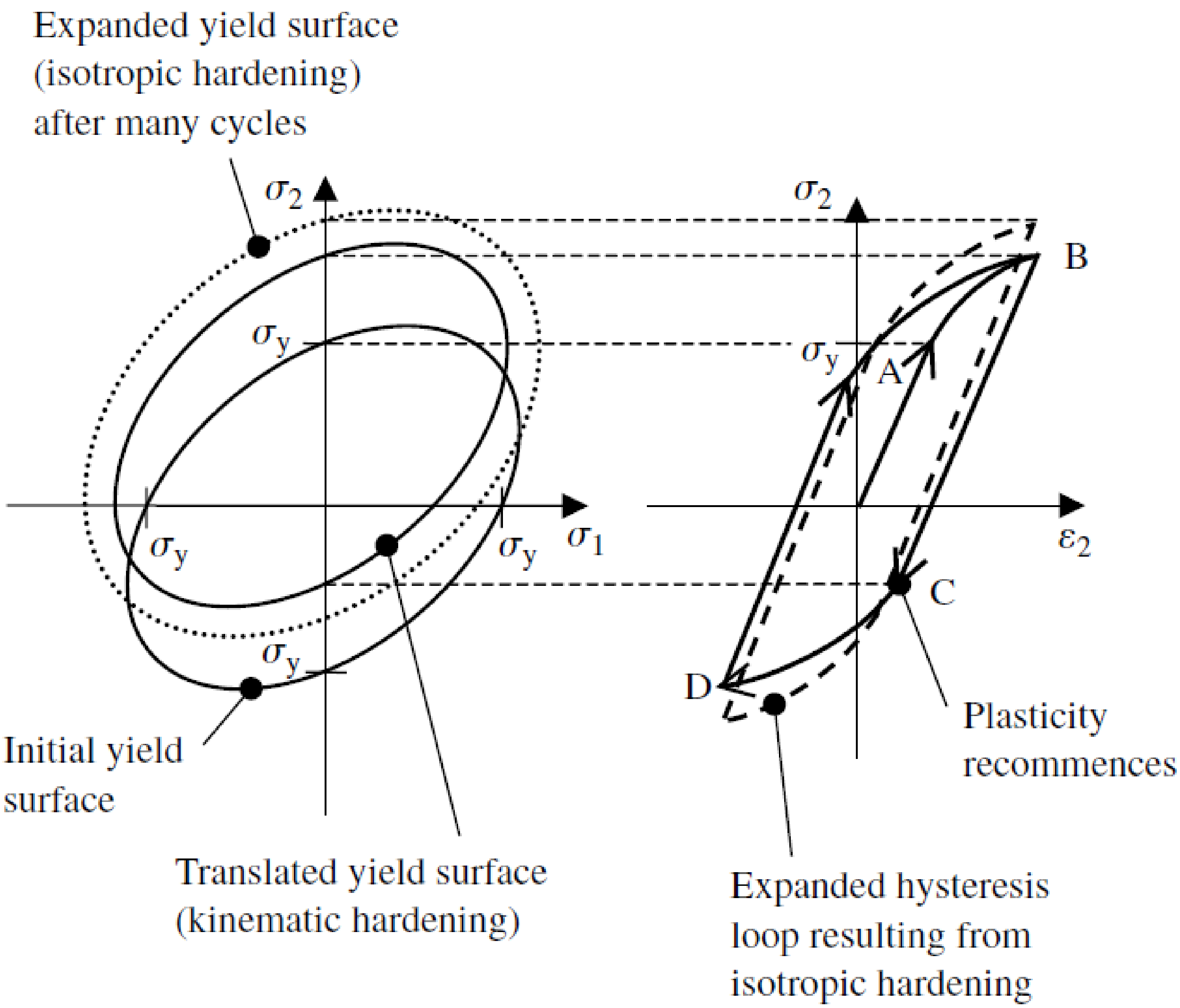

Figure 3.21. Combined kinematic and isotropic hardening [10]

Figures 3.22, 3.23, and 3.24 illustrate the strain hardening model for steel, including isotropic, kinematic, and combined hardening models.

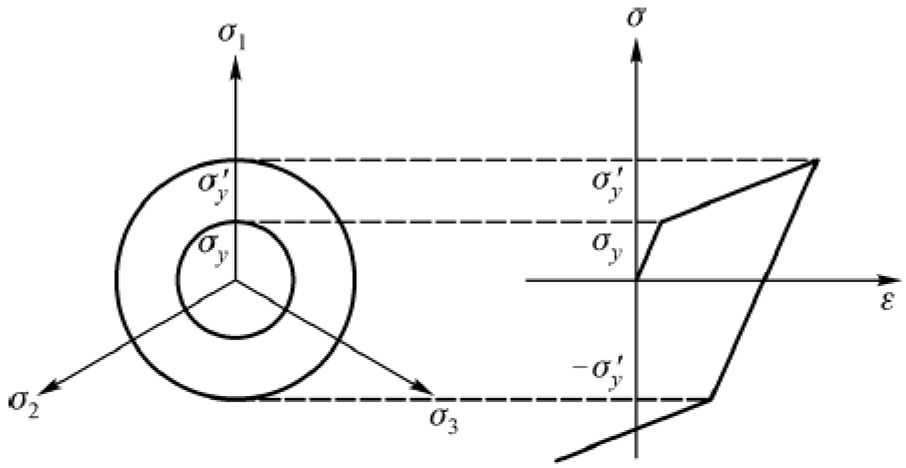

Figure 3.22. Isotropic strain hardening model for steel [12]

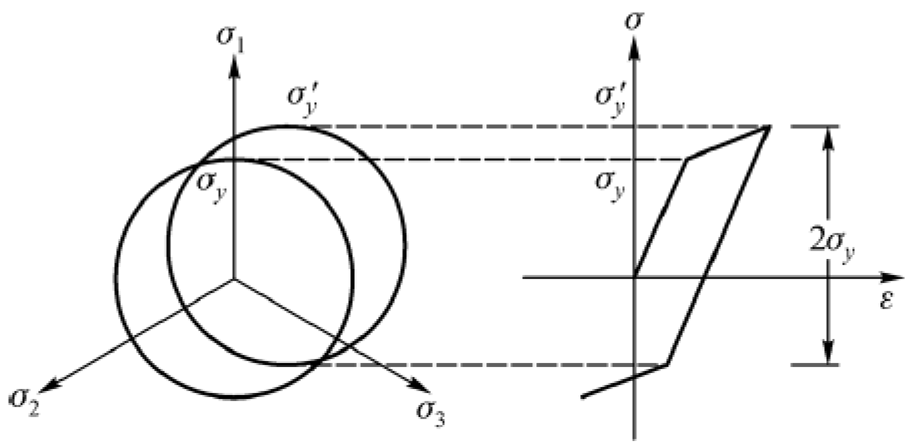

Figure 3.23. Kinematic strain hardening model for steel [12]

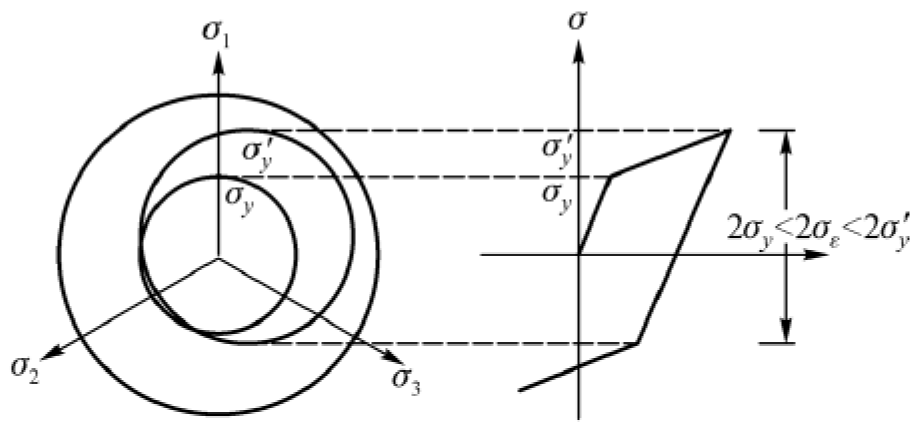

Figure 3.24. Combined strain hardening model for steel [12]

3.10.6 von Mises stress

Figure 3.25 shows the stress path taken relative to the yield surface for uniaxial, tensile loading [10].

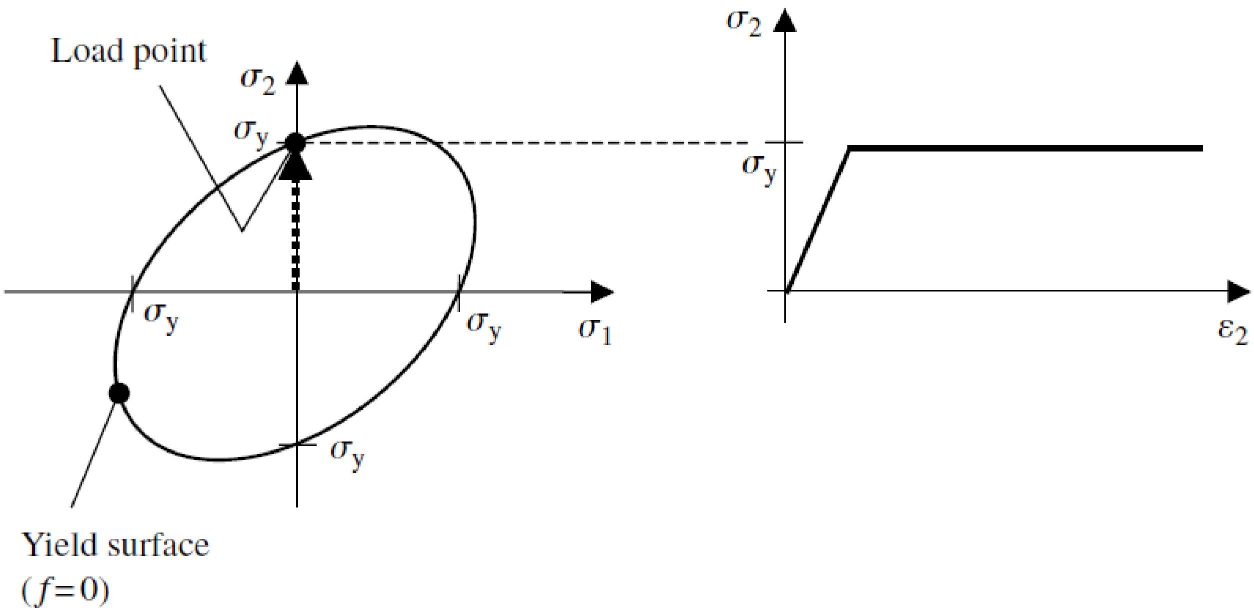

Figure 3.25. Yield surface of von Mises for plane stress and correspondent in the stress-strain curve for two-dimensional uniaxial straining [10]

Figure 3.26 shows the material's stress-strain response and the corresponding yield surface that was assumed to expand due to linear isotropic hardening [10].

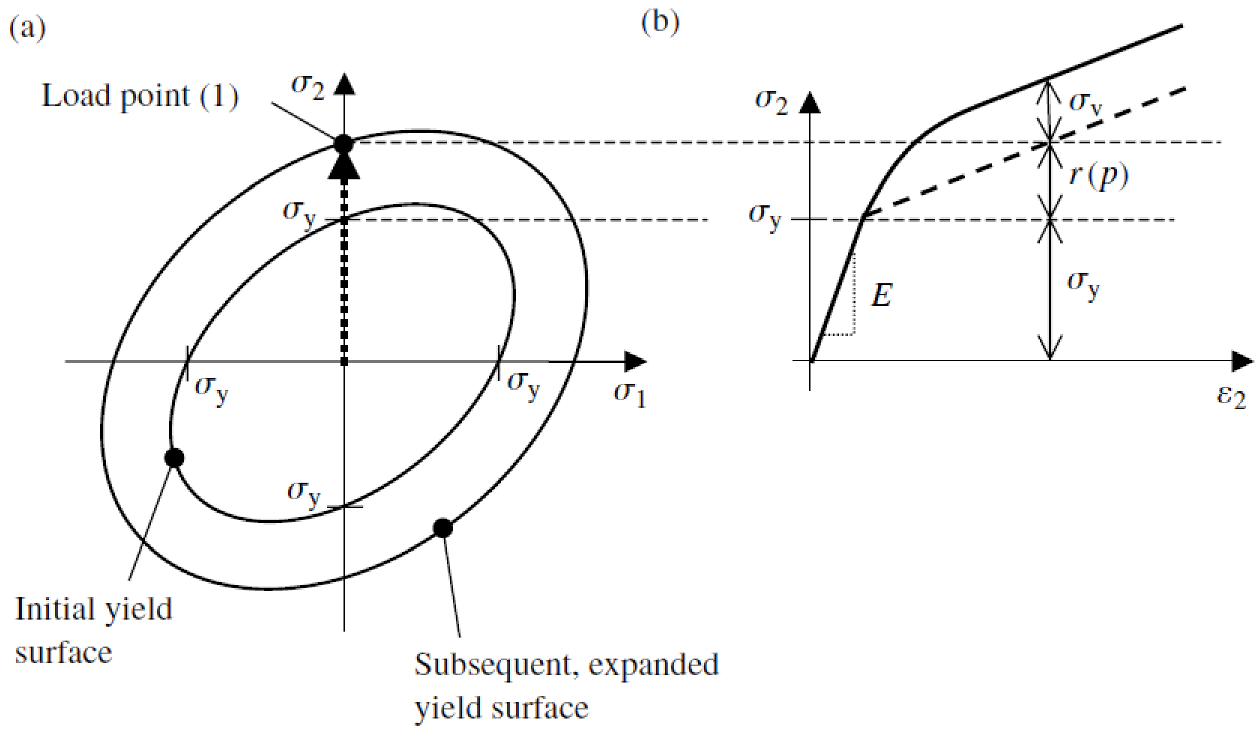

Figure 3.26. (a) the von Mises yield surface in plane stress for viscoplasticity with linear isotropic hardening, with viscous (overstress) stress σ_v, and (b) the associated stress-strain curve [10]

The most accurate and widely used models to show tensile steel behavior are the Ramberg-Osgood and Mander models.

3.11 Parameters of Steel Stress-Strain Relationship (Mander Model)

Mander et al. proposed a stress-strain relationship that accurately represents the strain-hardening range of steel bars (Figure 3.27, Equations 10 and 11) with seven material properties that define its shape: E_s, f_y, ε_{sh}, E_{sh}, f_u, ε_u, and ε_f [13]. The most significant advantage of this model is that it permits steel stress, f_s, to be calculated for any steel strain, ε_s, using a single statement for the whole response spectrum. Furthermore, the model applies to diverse steel kinds and grades, such as reinforcing steels with and without a specified yield plateau [13].

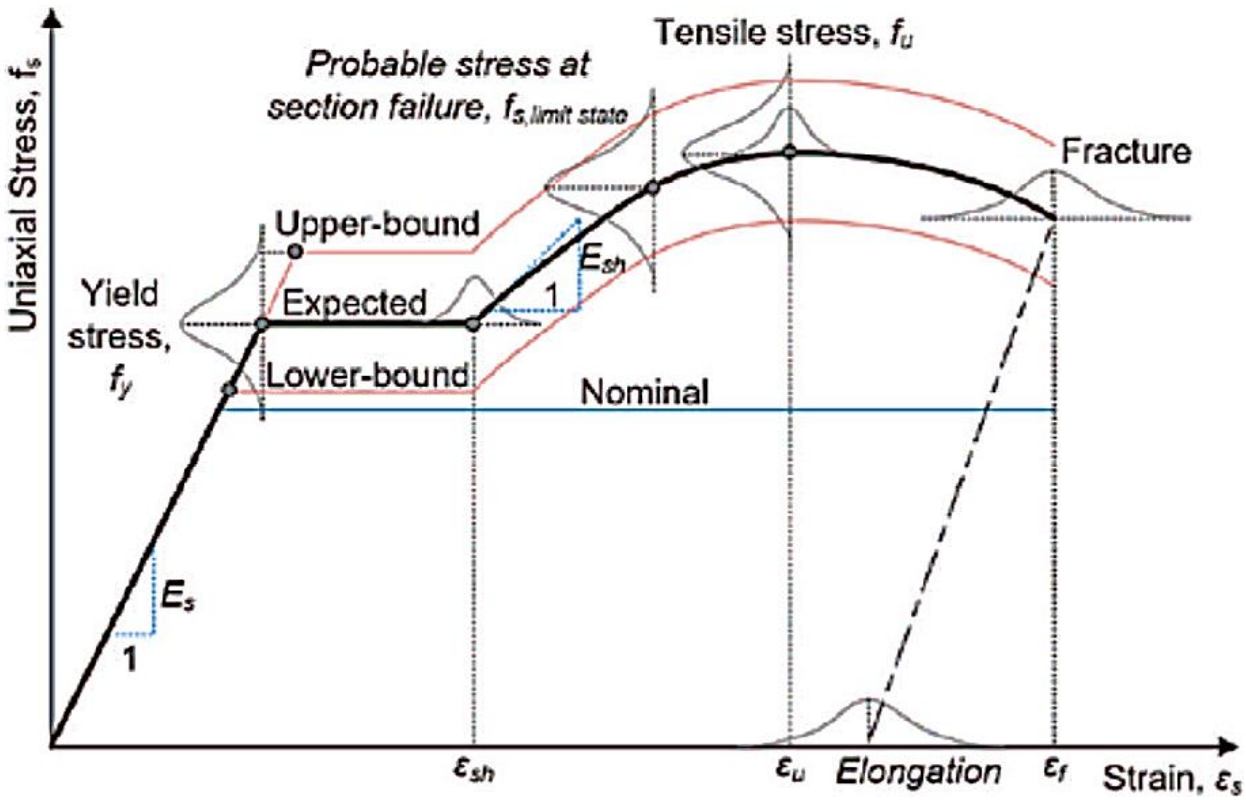

Figure 3.27. Parameters of stress-strain curve for reinforcing steel [13]

$$f_s = \frac{E_s \varepsilon_s}{\left\{1+\left|\frac{\varepsilon_s}{\varepsilon_y}\right|^{20}\right\}^{0.05} + \left|\frac{\varepsilon_s}{\varepsilon_f}\right|^{20}} + \frac{f_u - f_y}{1+\left|\frac{\varepsilon_s}{\varepsilon_f}\right|^{20}} \cdot \left|1 - \frac{|\varepsilon_u-\varepsilon_s|^p}{\{|\varepsilon_u-\varepsilon_{sh}|^{20p}+|\varepsilon_u-\varepsilon_s|^{20p}\}^{0.05}}\right| \tag{10}$$

$$p = \frac{E_{sh}(\varepsilon_u-\varepsilon_{sh})}{(f_u-f_y)} \leq 10 \tag{11}$$

f_s: reinforcing stress at strain ε_s

E_s: elastic modulus of reinforcement

ε_s: strain of interest

ε_y: yield strain

ε_f: fracture strain

f_u: ultimate tensile stress

f_y: yield stress

ε_u: strain at tensile strength

p: exponent to define strain hardening

ε_{sh}: strain at onset of strain hardening

E_{sh}: modulus at onset of strain hardening

Mean values of parameters in Equations 10 and 11 for the mill and laboratory datasets (ε_f, f_u, f_y, ε_u, ε_{sh}, E_{sh}) were provided in a table by Mander-Matamoros [13]. The extraction of ε_f, f_u, f_y, ε_u, ε_{sh}, and E_{sh} yields:

$$\sigma = E \cdot \varepsilon \Longrightarrow \varepsilon = \frac{\sigma}{E} \Longrightarrow \varepsilon_y = \frac{f_y}{E_s} \tag{12}$$

$$0 \leq \varepsilon_s \leq \varepsilon_f \Longrightarrow f_s = ? \tag{13}$$

The stresses and strains calculated in this research study are the nominal (engineering) stresses ($\sigma_0 = f_s$) and nominal (engineering) strains ($\varepsilon_0 = \varepsilon_s$). The Abaqus model for this research required true stress (σ_{true}) and true stain (ε_{true}), which can be calculated as:

$$\varepsilon_{s;true} = ln(1 + \varepsilon_0) = ln(1 + \varepsilon_s) \tag{14}$$

$$\sigma_{true} = \sigma_0(1 + \varepsilon_0) \Longrightarrow f_{s;true} = f_s(1 + \varepsilon_s) \tag{15}$$

$$\varepsilon_{total} = \varepsilon_{elastic} + \varepsilon_{plastic} \Longrightarrow \varepsilon_{plastic} = \varepsilon_{total} - \varepsilon_{elastic} \tag{16}$$

$$\varepsilon_{total} = \varepsilon_s \tag{17}$$

$$\varepsilon_{elastic} = \frac{f_s}{E_s} \tag{18}$$

$$\varepsilon_{plastic} = \varepsilon_s - \frac{f_s}{E_s} \tag{19}$$

$$\varepsilon_{plastic;true} = \ln\left(1 + \varepsilon_{plastic}\right) \tag{20}$$

In the Abaqus software, a user needs to select the following options for defining the intended characteristics of steel hardening:

Properties → Material Manager → Steel → Material Behaviors → Plastic → Hardening

Then the values for Yield Stress versus Plastic Strain should be inserted into the Abaqus model, as obtained from Equations 15 and 20, in a table format. One of these true plastic strain values is equal to zero, which requires the corresponding true stress for Abaqus to be the first point in the table.

This research utilized Specimen #4 from experimental tests conducted by prominent structural and earthquake engineering scientists, Professor Halil Sezen and Professor Jack P. Moehle, at the University of California, Berkley.

A MATLAB code was written to show the behavior of longitudinal steel in tension based on the Mander model, which shows the true stress corresponding to true plastic strain equals to zero. Table 3.1 lists the stress, strain, and plastic strain values of longitudinal steel with the following case study parameters, while Table 3.2 shows the true stress-true strain, and Table 3.3 depicts the true yield stresses and true plastic strains.

f_y = 63 ksi = 63×10^3 psi

f_u = 93.5 ksi = 93,500 psi

Parameters evaluation:

$$\begin{cases} f_u = 93.5 \text{ ksi} \Rightarrow \varepsilon_{sh} = ? \\ f_u = 78 \text{ ksi} \Rightarrow \varepsilon_{sh} = 0.014 \\ f_u = 95 \text{ ksi} \Rightarrow \varepsilon_{sh} = 0.013 \\ \varepsilon_{sh}(93.5) = 0.014 + (0.013 - 0.014) \cdot \dfrac{93.5 - 78}{95 - 78} = 0.013088 \end{cases}$$

$$\begin{cases} f_u = 93.5\ ksi \Rightarrow E_{sh} = ? \\ f_u = 78\ ksi \Longrightarrow E_{sh} = 1{,}200 \\ f_u = 95\ ksi \Longrightarrow E_{sh} = 1{,}000 \\ E_{sh}(93.5) = 12{,}00 + (1{,}000 - 1{,}200) \cdot \dfrac{93.5 - 78}{95 - 78} = 1{,}017.6\ ksi = \\ 1{,}017{,}647.05\ psi \end{cases}$$

$$\begin{cases} f_u = 93.5\ ksi \Longrightarrow \varepsilon_u = ? \\ f_u = 78\ ksi \Longrightarrow \varepsilon_u = 0.16 \\ f_u = 95\ ksi \Longrightarrow \varepsilon_u = 0.13 \\ \varepsilon_u(93.5) = 0.16 + (0.13 - 0.16) \cdot \dfrac{93.5 - 78}{95 - 78} = 0.13264 \end{cases}$$

$$\begin{cases} f_u = 93.5\ ksi \Longrightarrow \varepsilon_f = ? \\ f_u = 78\ ksi \Longrightarrow \varepsilon_f = 0.2 \\ f_u = 95\ ksi \Longrightarrow \varepsilon_f = 0.16 \\ \varepsilon_f(93.5) = 0.2 + (0.16 - 0.2) \cdot \dfrac{93.5 - 78}{95 - 78} = 0.16352 \end{cases}$$

$E_s = 29 \times 10^6\ psi$

Table 3.1. Tensile stress, strain, plastic strain values for longitudinal steel (Mander)

Stress (psi)	Strain	Plastic Strain
0.38347	0	-1.32E-8
63,186.7	0.01	0.0078211
69,459.3	0.02	0.017604
76,901.1	0.03	0.027348
82,471.8	0.04	0.037156

86,507.6	0.05	0.047016
89,319.8	0.06	0.05692
91,184.6	0.07	0.066855
92,342.9	0.08	0.076815
93,000.4	0.09	0.086793
93,326.3	0.1	0.096781
93,448.6	0.11	0.10677
93,431.3	0.12	0.11677
93,182.4	0.13	0.12678
92,149.8	0.14	0.13682
88,722.4	0.15	0.14694
80,925.9	0.16	0.15720

Table 3.2. Tensile true stress-true strain values for longitudinal steel (Mander)

True Stress (psi)	True Strain
0.38347	0
63,818.6	0.0099503
70,848.5	0.019802
79,208.1	0.029558
85,770.7	0.03922
90,833.004	0.04879
94,679.001	0.058268
97,567.5	0.067658
99,730.4	0.076961
101,370.5	0.086177
102,658.9	0.09531
103,727.9	0.10436
104,643.1	0.11332
105,296.2	0.12221
105,050.8	0.13102
102,030.7	0.13976
93,874.07	0.14842

Table 3.3. Tensile true stress-true plastic strain values for longitudinal steel (Mander)

True Yield Stress (psi)	True Plastic Strain
54,616.6	0
63,818.6	0.0077496
70,848.5	0.017359
79,208.1	0.026827
85,770.7	0.036263
90,833	0.045657
94,679	0.055004
97,567.5	0.064294
99,730.4	0.073522
101,370	0.082682
102,659	0.09177
103,728	0.10078
104,643	0.10972
105,296	0.11858
105,050	0.1274
102,030	0.13624
93,874.1	0.14518

The results showed the true plastic strain to be equal to zero at one point, requiring the true stress at this point to be the first point in the table for Abaqus. A MATLAB code was written to show the behavior of steel in tension based on the Mander model.

The stress-strain curve based on the Mander model of the longitudinal steel is shown in Figure 3.28.

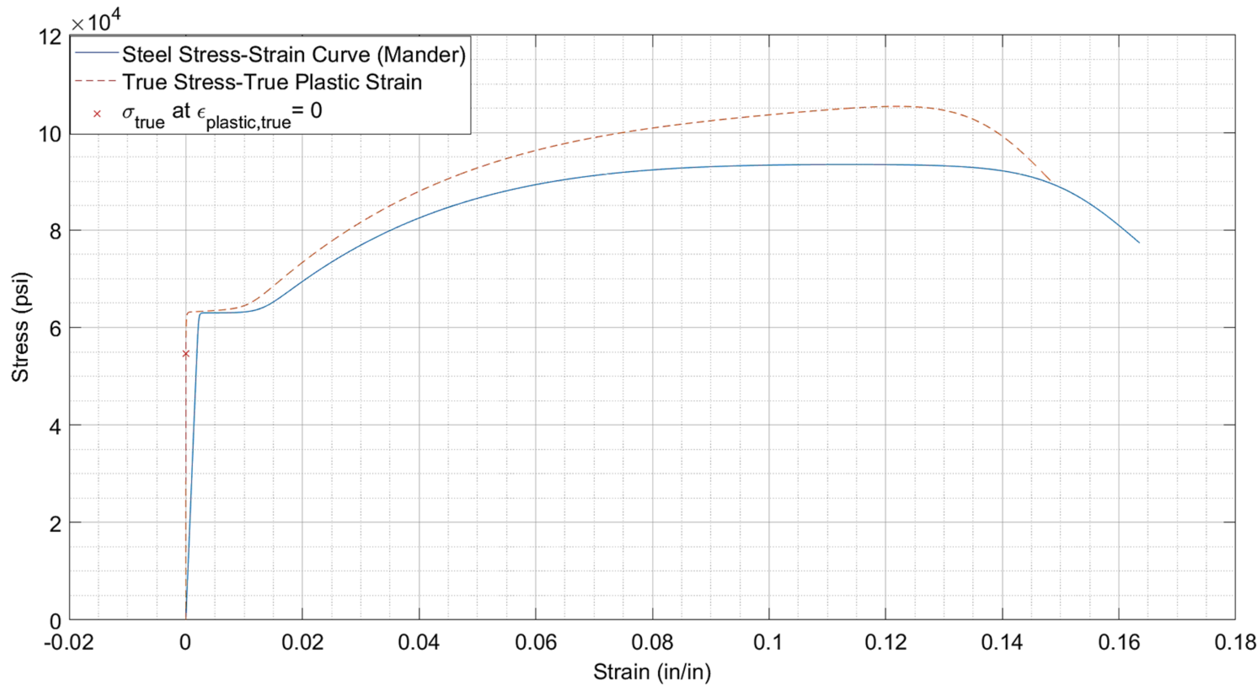

Figure 3.28. Mander stress-strain curve for longitudinal steel in tension

Another MATLAB code was written to show the behavior of transverse steel in tension based on the Mander model. Table 3.4 lists the stress, strain, and plastic strain values of transverse steel with the following case study parameters, Table 3.5 shows the true stress-true strain, and Table 3.6 depicts the true yield stresses and true plastic strains for transverse steel.

f_y = 69 ksi = 69×10^3 psi

f_u = 105 ksi = 105×10^3 psi

E_s = 29×10^6 psi

ε_{sh} = 0.009

E_{sh} = 1,200 ksi = 12×10^5 psi

ε_u = 0.1

ε_f = 0.13

Table 3.4. Tensile stress, strain, plastic strain values of transverse steel (Mander)

Stress (psi)	Strain	Plastic Strain
5.8844	0	-2.03E-07
70,898.3	0.01	0.0075552
80,645.7	0.02	0.017219
88,756.6	0.03	0.026939
94,823.4	0.04	0.03673

99,146.4	0.05	0.046581
102,025	0.06	0.056481
103,756	0.07	0.066422
104,634	0.08	0.076391
104,931	0.09	0.086381
104,803	0.1	0.096386
103,673	0.11	0.10642
98,379.7	0.12	0.1166
85,138.3	0.13	0.12706

Table 3.5. Tensile true stress-true strain values of transverse steel (Mander)

True Stress (psi)	True Strain
5.8844	0
71,607.3	0.0099503
82,258.6	0.019802
91,419.3	0.029558
98,616.3	0.03922
104,104	0.04879
108,147	0.058268
111,019	0.067658
11,3005	0.076961
114,375	0.086177
115,283	0.09531
115,077	0.10436
110,185	0.11332
96,206.3	0.12221

Table 3.6. Tensile true stress-true plastic strain values of transverse steel (Mander)

True Yield Stress (psi)	True Plastic Strain
60,430.2	0
71,607.3	0.0074811
82,258.6	0.016966
91,419.3	0.026406
98,616.3	0.03582
104,103	0.0452
108,146	0.054539
111,019	0.06383
113,005	0.073064

114,375	0.082233
115,283	0.091334
115,077	0.10039
110,185	0.10952
96,206.3	0.1189

The results showed the true plastic strain to be equal to zero at one point, requiring the true stress at this point to be the first point in the table for Abaqus. A MATLAB code was written to show the behavior of steel in tension based on the Mander model.

The stress-strain curve based on the Mander model of transverse steel is shown in Figure 3.29.

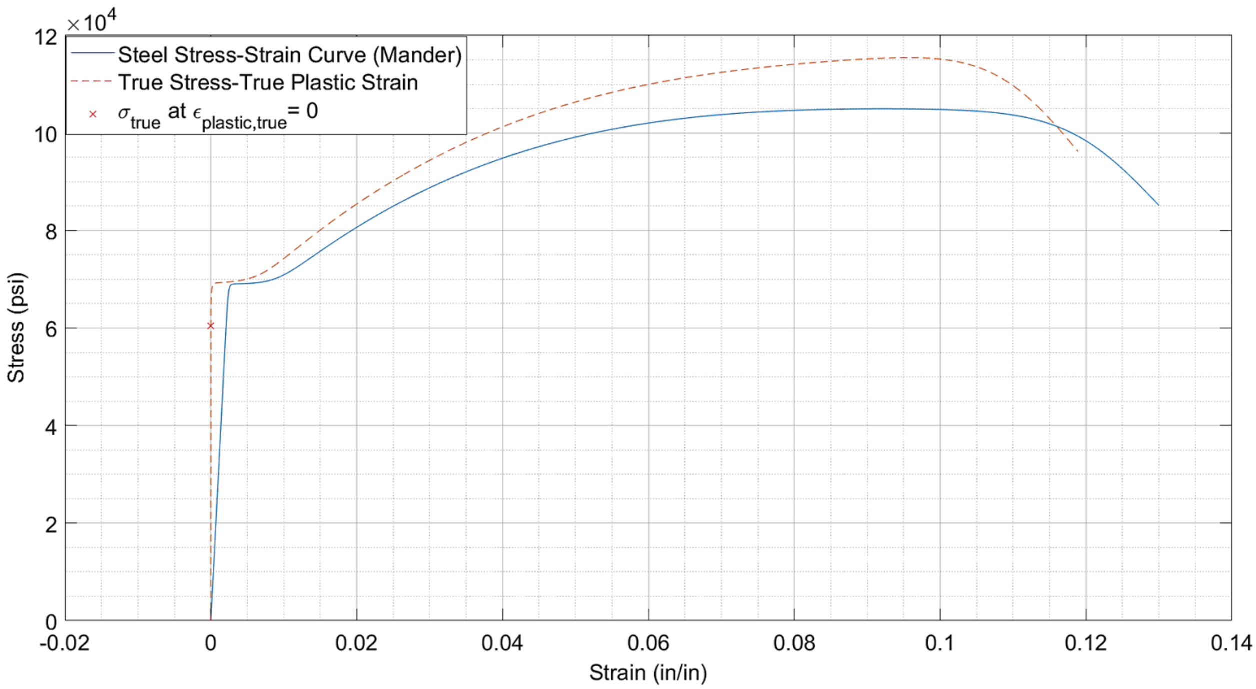

Figure 3.29. Mander stress-strain curve of transverse steel in tension

3.12 Ramberg-Osgood Model

Comparison to the tensile and compressive statistics for aluminum alloy, stainless steel, carbon steel, and carbon-steel sheets in Technical Note No. 840 from the National Advisory Committee for Aeronautics (NACA) says that the formula is sufficient for the majority of these materials [14].

3.12.1 Equation Version 1

Equation and model 21 was derived from the Ramberg-Osgood original model proposed by Chen and Han in 1987 [1]. The nonlinear stress-strain curve shown in Figure 3.30 has the following expression:

$$\epsilon = \frac{\sigma}{E} + a\left(\frac{\sigma}{b}\right)^n \tag{21}$$

a, b, n: material constants [1]

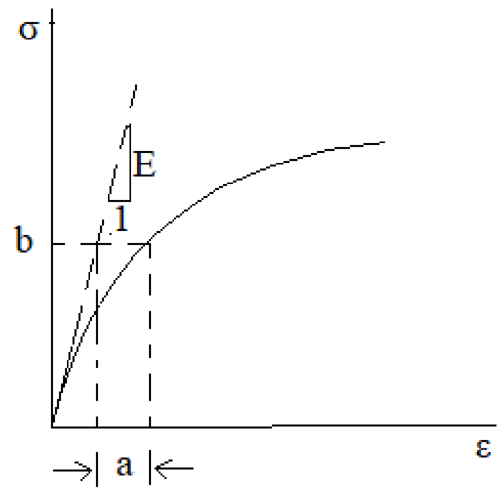

Figure 3.30. Idealized stress-strain curve for Ramberg-Osgood model

The initial slope of the curve in the figure takes the value of Young's modulus E at $\sigma = 0$ and decreases monotonically with increased loading. Because the model has three parameters, it allows a better fit of real stress-strain curves [1].

3.12.2 Equation Version 2

Equations and models 22-24 were proposed by the Metallic Materials Properties Development and Standardization (MMPDS) Handbook in 2002 [15].

$$\varepsilon = \frac{\sigma}{E} + 0.002\left(\frac{\sigma}{F_{ty}}\right)^n \tag{22}$$

$$n = \frac{\ln\left(\frac{\varepsilon_{us}}{0.2}\right)}{\ln\left(\frac{F_{tu}}{F_{ty}}\right)} \tag{23}$$

$$\varepsilon_{us} = 100\left(\varepsilon_r - \frac{F_{tu}}{E}\right) \tag{24}$$

$$0 \le \sigma \le F_{tu} \tag{25}$$

$$\varepsilon_{total} = \varepsilon_{elastic} + \varepsilon_{plastic} \Longrightarrow \varepsilon_{plastic} = \varepsilon_{total} - \varepsilon_{elastic} \qquad (26)$$

$$\varepsilon_{elastic} = \frac{\sigma}{E} \qquad (27)$$

$$\varepsilon_{plastic} = \varepsilon - \frac{\sigma}{E} \qquad (28)$$

$$\sigma_{true} = \sigma(1+\varepsilon) \qquad (29)$$

$$\varepsilon_{true} = \ln(1+\varepsilon) \qquad (30)$$

$$\varepsilon_{plastic;true} = \ln\left(1+\varepsilon_{plastic}\right) \qquad (31)$$

n: Ramberg-Osgood coefficient

E: Young modulus

F_{tu}: ultimate strength

F_{ty}: yield strength

ε_r: strain at rupture

σ: stress

ε_{us}: uniform strain = plastic strain at end of uniform elongation (at maximum tension load (F_{tu}))

ε: strain

MATLAB and Excel codes were written to describe the behavior of longitudinal steel in tension based on the Ramberg-Osgood model. Table 3.7 lists the stress, strain, plastic strain values of longitudinal steel based on this model, Table 3.8 shows the corresponding true stress-true strain values of longitudinal steel, and Table 3.9 depicts the true yield stresses and true plastic strains.

Table 3.7. Tensile stress, strain, plastic strain values for longitudinal steel (Ramberg-Osgood)

Stress (psi)	Strain	Plastic Strain
0	0	0
50,00	0.00017241	1.2109E-15
10,000	0.00034482	2.6644E-12
15,000	0.00051724	2.4033E-10
20,000	0.00068966	5.8623E-09
25,000	0.00086213	6.984E-08
30,000	0.001035	5.2879E-07
35,000	0.0012098	2.9283E-06
40,000	0.0013922	1.2898E-05
45,000	0.0015994	4.7698E-05
48,102.4	0.0017587	0.0001

50,000	0.0018778	0.00015366
55,000	0.0023393	0.00044276
60,000	0.0032324	0.0011634
63,000	0.0041724	0.002
65,000	0.005071	0.0028296
70,000	0.0088568	0.0064431
75,000	0.016447	0.01386
80,000	0.031138	0.028379
85,000	0.058565	0.055634
90,000	0.10805	0.10494
93,500	0.16352	0.1603

Table 3.8. Tensile true stress-true strain values for longitudinal steel (Ramberg-Osgood)

True Stress (psi)	True Strain
0	0
5,000.8	0.00017239
10,003.4	0.00034476
15,007.7	0.0005171
20,013.7	0.00068942
25,021.5	0.00086176
30,031	0.0010344
35,042.3	0.001209
40,055.6	0.0013912
45,071.9	0.0015981
48,187	0.0017571
50,093.8	0.001876
55,128.6	0.0023365
60,193.9	0.0032272
63,262.8	0.0041637
65,329.6	0.0050582
70,619.9	0.0088179
76,233.5	0.016313
82,491	0.030663
89,978	0.056915
99,724.6	0.1026
108,790	0.15145

Table 3.9. Tensile true stress-true plastic strain values for longitudinal steel (Ramberg-Osgood)

True Yield Stress (psi)	True Plastic Strain
48,187.01	0
50,093.8	0.00015365
55,128.6	0.00044266
60,193.9	0.0011627
63,262.8	0.001998
65,329.6	0.0028256
70,619.9	0.0064224
76,233.5	0.013765
82,491	0.027984
89,978	0.054142
99,724.6	0.099798
108790	0.14868

The results showed the true plastic strain to be equal to zero at one point, requiring the true stress at this point to be the first point in the table for Abaqus. The elastic limit is the stress corresponding to zero plastic strain. Nowadays, the tracking of yield surface is done experimentally with 100 με offset of plastic strain or less. Thus, the elastic limit can be chosen as the stress calculated by the Ramberg-Osgood equation for 0.0001 axial plastic strain. Therefore, we have:

$\varepsilon_{plastic} = 0.0001$

In the Ramberg-Osgood equation:

$$\varepsilon = \frac{\sigma}{E} + 0.002\left(\frac{\sigma}{F_{ty}}\right)^n$$

$$\varepsilon_{total} = \varepsilon_{elastic} + \varepsilon_{plastic} \Rightarrow \frac{\sigma}{E} + 0.0001 = \frac{\sigma}{E} + 0.002\left(\frac{\sigma}{F_{ty}}\right)^n \Rightarrow 0.002\left(\frac{\sigma}{F_{ty}}\right)^n = 0.0001$$

A MATLAB code was written to solve and evaluate the elastic limit stress.

Elastic limit stress = 48,102.4 psi → True stress = 48,187.01 psi

The engineering and true stress-strain curves of longitudinal steel are illustrated in Figure 3.31.

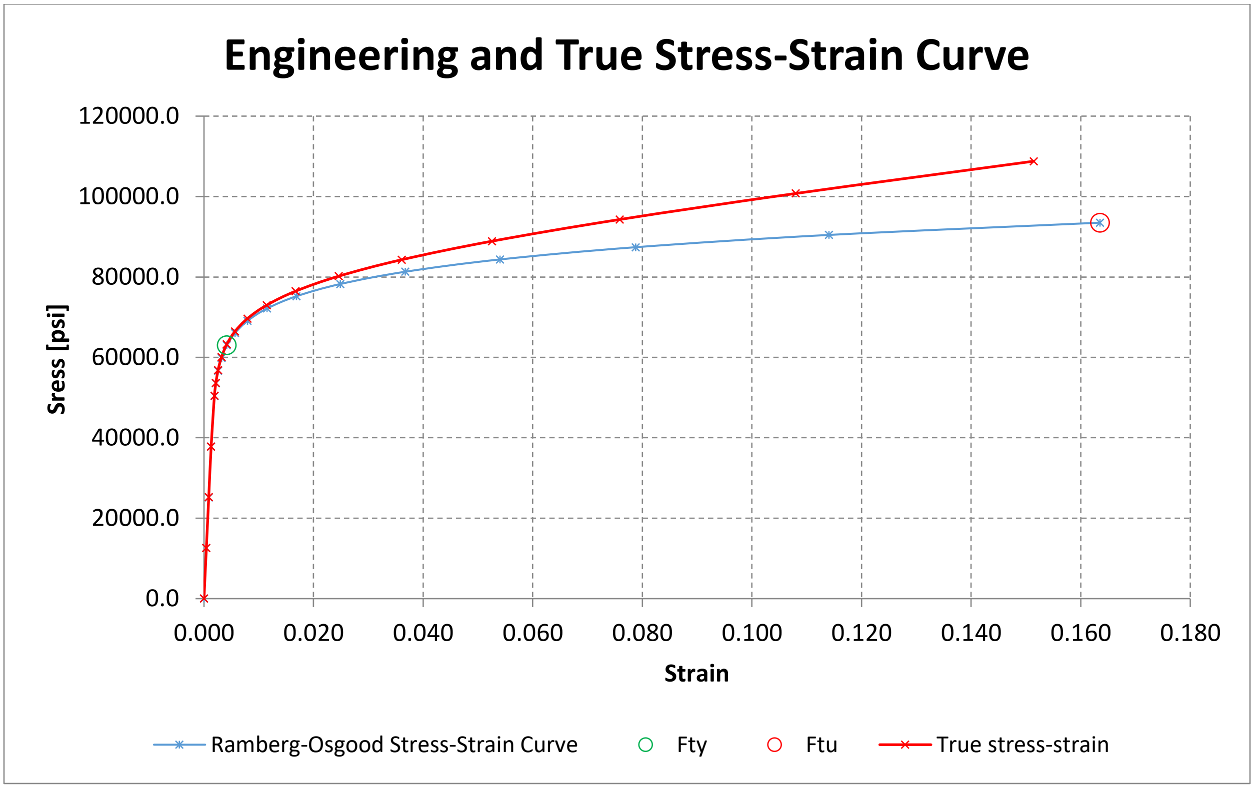

Figure 3.31. Engineering and true stress-strain curves for Ramberg-Osgood model (longitudinal)

The true stress-true strain curve based on the Ramberg-Osgood model for the longitudinal steel obtained from MATLAB is illustrated in Figure 3.32.

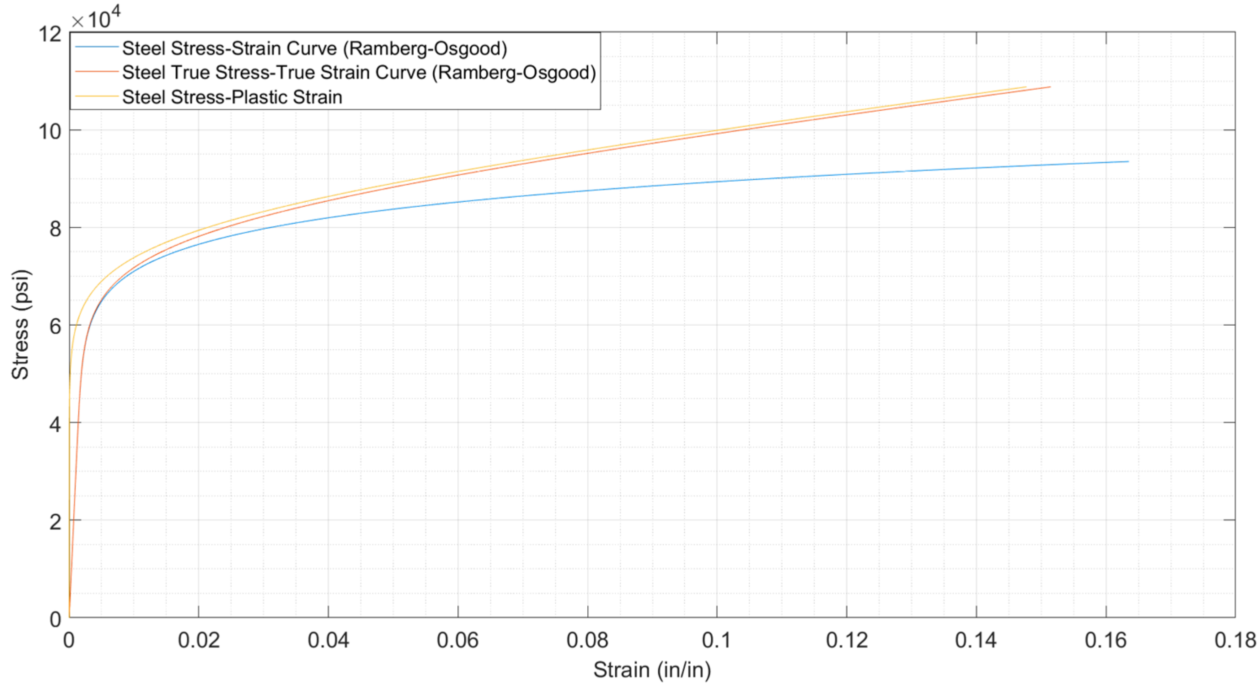

Figure 3.32. Ramberg-Osgood true stress-true strain curve of the longitudinal steel in tension

MATLAB and Excel codes were written to show the behavior of transverse steel in tension based on the Ramberg-Osgood model. Table 3.10 lists the stress, strain, and plastic strain values of transverse steel based on this model, Table 3.11 shows the corresponding true stress-true strain values of transverse steel, and Table 3.12 depicts the true yield stresses and true plastic strains.

Table 3.10. Tensile stress, strain, plastic strain values for transverse steel (Ramberg-Osgood)

Stress (psi)	Strain	Plastic Strain
0	0	0
5,000	0.00017241	1.1078E-14
10,000	0.00034482	1.0404E-11
15,000	0.00051724	5.7037E-10
20,000	0.00068966	9.7714E-09
25,000	0.00086215	8.8504E-08
30,000	0.001035	5.3566E-07
35,000	0.0012093	2.4547E-06
40,000	0.0013884	9.1767E-06
45,000	0.001581	2.9365E-05
50,000	0.0018072	0.000083118
50,945	0.0018567	0.0001
55,000	0.0021095	0.00021303

60,000	0.002572	0.00050306
65,000	0.0033503	0.0011089
69,000	0.0043793	0.002
70,000	0.0047191	0.0023053
75,000	0.0071427	0.0045565
80,000	0.011376	0.0086183
85,000	0.018613	0.015682
90,000	0.030681	0.027578
95,000	0.050313	0.047037
100,000	0.081508	0.078059
105,000	0.13	0.12637

Table 3.11. Tensile true stress-true strain values for transverse steel (Ramberg-Osgood)

True Stress (psi)	True Strain
0	0
5,000.8	0.00017239
10,003.4	0.00034476
15,007.7	0.0005171
20,013.7	0.00068942
25,021.5	0.00086178
30,031.05	0.0010344
35,042.3	0.0012086
40,055.5	0.0013875
45,071.1	0.0015798
50,090.3	0.0018056
51,039.6	0.001855
55,116.02	0.0021073
60,154.3	0.0025687
65,217.7	0.0033447
69,302.1	0.0043697
70,330.3	0.004708
75,535.7	0.0071173
80,910.1	0.011312
86,582.1	0.018442
92,761.3	0.03022
99,779.7	0.049088
108,150.8	0.078356
118,650	0.12221

Table 3.12. Tensile true stress-true plastic strain values for transverse steel (Ramberg-Osgood)

True Yield Stress (psi)	True Plastic Strain
51,039.6	0
55,116	0.00021301
60,154.3	0.00050294
65,217.7	0.0011083
69,302.1	0.001998
70,330.3	0.0023027
75,535.7	0.0045461
80,910.1	0.0085813
86,582.1	0.015561
92,761.3	0.027204
99,779.7	0.045964
108,150.8	0.075162
118,650	0.119

The results showed the true plastic strain to be equal to zero at one point, requiring the true stress at this point to be the first point in the table for Abaqus. The elastic limit is the stress corresponding to zero plastic strain. Nowadays, the tracking of yield surface is done experimentally with 100 με offset of plastic strain or less. Thus, the elastic limit can be chosen as the stress calculated by the Ramberg-Osgood equation for 0.0001 axial plastic strain. Therefore, we have:

$\varepsilon_{plastic} = 0.0001$

In the Ramberg-Osgood equation:

$$\varepsilon = \frac{\sigma}{E} + 0.002\left(\frac{\sigma}{F_{ty}}\right)^n$$

$$\varepsilon_{total} = \varepsilon_{elastic} + \varepsilon_{plastic} \Rightarrow \frac{\sigma}{E} + 0.0001 = \frac{\sigma}{E} + 0.002\left(\frac{\sigma}{F_{ty}}\right)^n \Rightarrow 0.002\left(\frac{\sigma}{F_{ty}}\right)^n = 0.0001$$

A MATLAB code was written to solve and evaluate the elastic limit stress.

Elastic limit stress = 50,945.03 psi → True stress = 51,039.6 psi

The engineering and true stress-strain curves of transverse steel are illustrated in Figure 3.33.

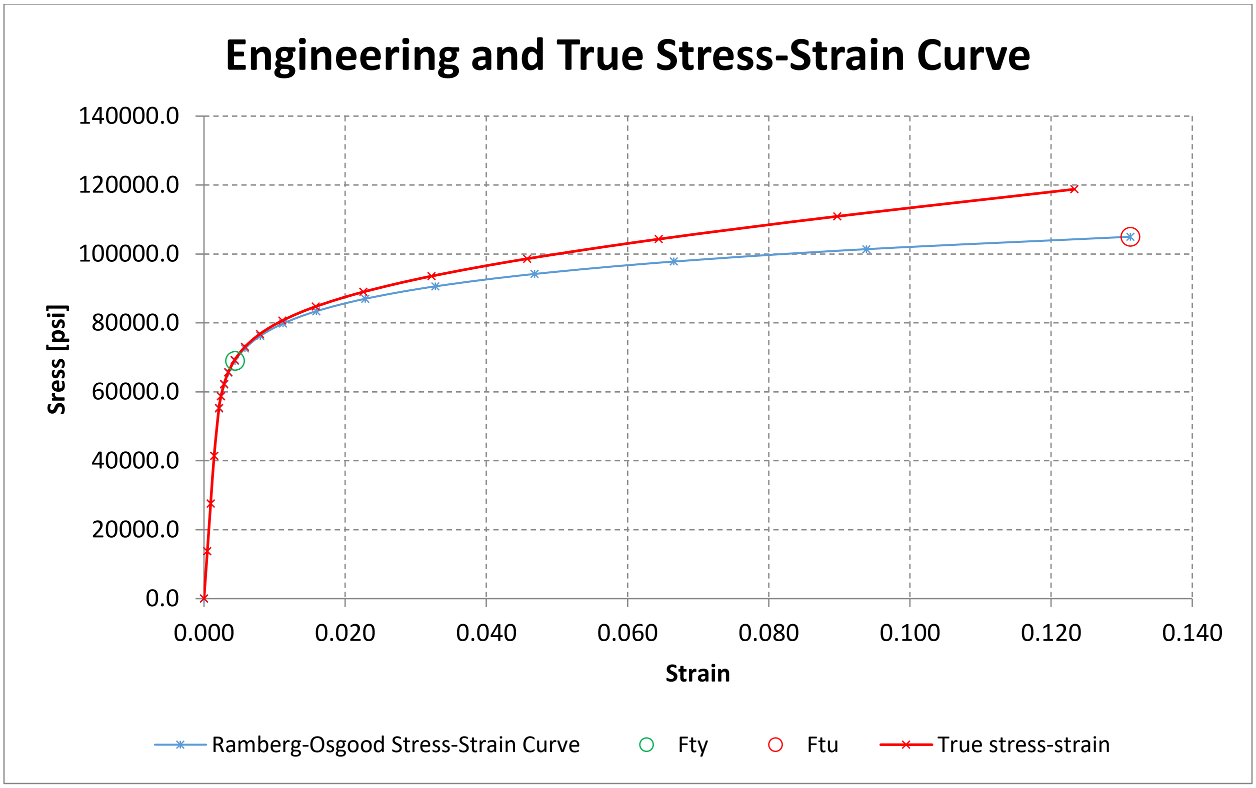

Figure 3.33. Engineering and true stress-strain curves of Ramberg-Osgood model for transverse steel

The true stress-true strain curve based on the Ramberg-Osgood model for the transverse steel by MATLAB is illustrated in Figure 3.34.

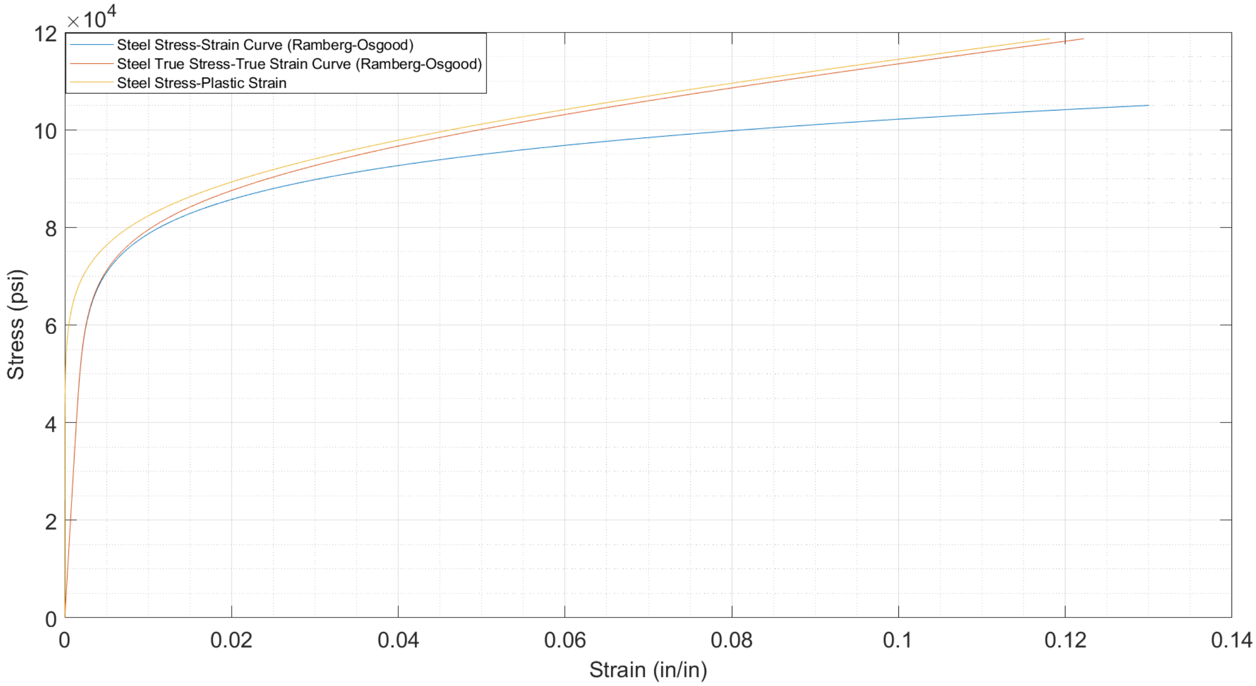

Figure 3.34. Ramberg-Osgood stress-strain curve of transverse steel in tension

3.12.3 Equation Version 3

Equation 32 is the original Ramberg-Osgood model and equation from 1943 [15].

$$\varepsilon = \frac{\sigma}{E} + \left(\frac{\sigma}{K}\right)^n \tag{32}$$

n, *K*: Ramberg-Osgood parameters

After extensive research and numerous investigations over the years, this research is suggesting significant and fundamental models and equations for evaluating the *n* and *K* (Ramberg-Osgood parameters) for the first time (Zad models and equations). These models and equations simplify the extremely complicated methods of calculation of *n* and *K* and was verified by the fitting methodology.

$$n = \frac{ln\left(\frac{\varepsilon_{us}}{0.5}\right)}{ln\left(\frac{F_{tu}}{F_{ty}}\right)} \tag{33}$$

$$\varepsilon_{us} = 100\left(\varepsilon_r - \frac{F_{tu}}{E}\right) \tag{34}$$

The author did not offer the ε_{us} equation.

$$K = \frac{F_{ty}}{\sqrt[n]{0.005}} \tag{35}$$

In order to show the applicability of the proposed approach, equations (32-35) were applied to tensile test data obtained from four steels, including Grade 20, SS304, SS316L SLM XY [16], and AlSi10Mg alloy provided by selective laser melting (SLM) technology (Z direction) (Z is the direction the load applies on the steel specimen surface) of 3D printing [17]. Basic mechanical properties necessary as input in this study are stated in Table 3.13.

Table 3.13. Mechanical properties of metallic alloys considered in this study on Ramberg-Osgood parameters identification

Material	$\boldsymbol{E}$ **(psi)**	$\boldsymbol{F_{ty}}$ **(psi)**	$\boldsymbol{F_{tu}}$ **(psi)**	$\boldsymbol{\varepsilon_{us}}$ **(in/in)**
Grade 20	2.976E+07	41,393.2	68,665.9	0.17155
SS304	2.682E+07	63,255.8	96,996.1	0.32322
SS316L SLM XY	2.652E+07	74,952.0	92,663.8	0.18410
AlSi10Mg SLM Z	1.029E+07	38,722.3	59,685.8	0.02922

The results of the interpolation approach based on equations (32-35) are directly compared with the approximation by the least square method in Figure 3.35.

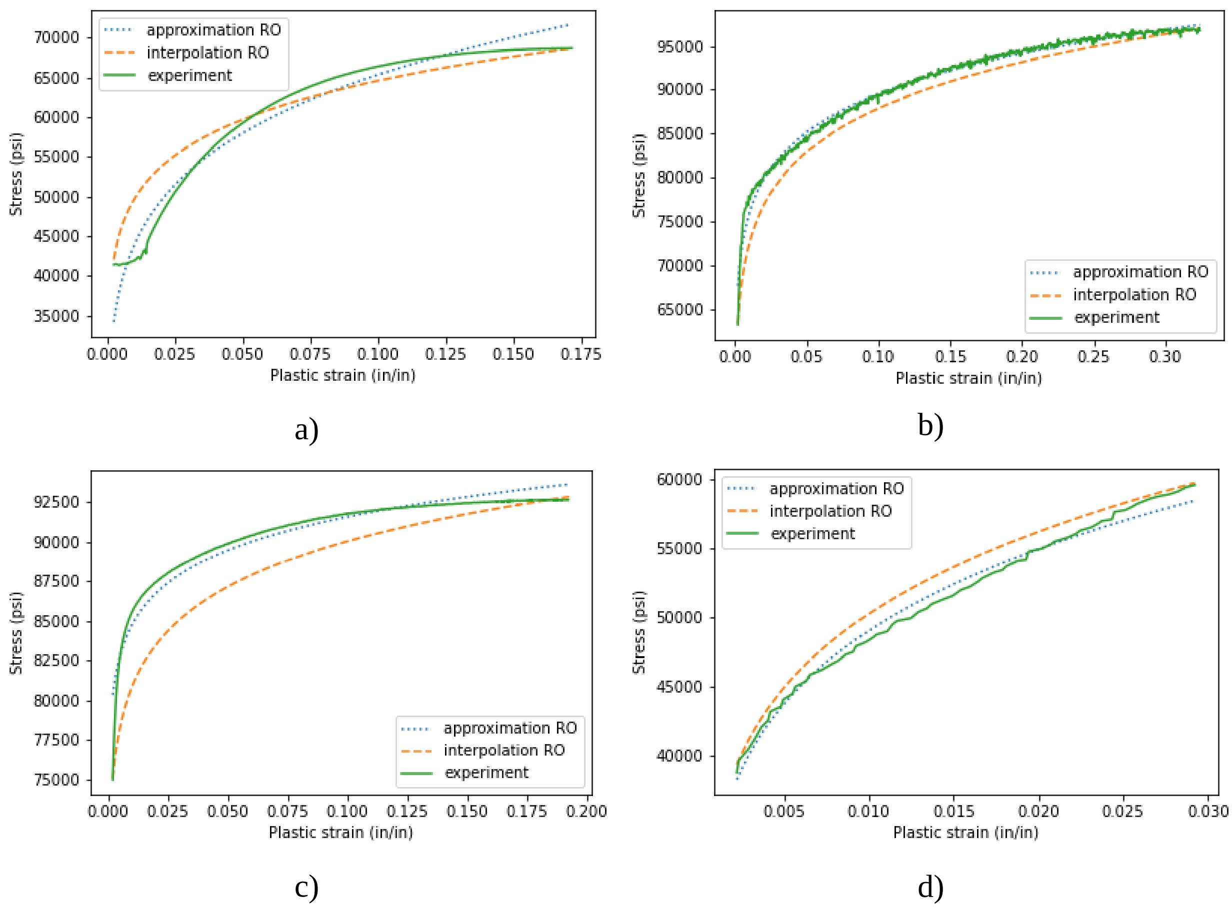

Figure 3.35. Results of interpolation and approximation approaches considering the interval from 0.2% to $\boldsymbol{\varepsilon_{us}}$: a) Grade 20, b) SS304, c) SS316L SLM XY [16], d) AlSi10Mg SLM Z [17] (RO: Ramberg-Osgood)

Pearson's correlation coefficient and standard deviation were calculated using least squares with index a and the interpolation approach with index i for the interpolation case. Both values are presented together with *K* and *n* in Table 3.14.

Table 3.14. Results of proposed interpolation approach (i) in comparison with results of the least square method (a) – experimental data are used in the interval from 0.2% to $\boldsymbol{\varepsilon_{us}}$

Material	K_a (psi)	n_a	R_a^2	Std_a (psi)	K_i (psi)	n_i	R_i^2	Std_i (psi)
Grade 20	97,100	5.810	0.9575	1,613.7	83,904	8.796	0.8325	2,985.7
SS304	105,683	13.89	0.9885	594.9	106,657	11.90	0.9054	1,028.4
SS316L SLM XY	98,999	29.62	0.9414	723.0	100,319	21.32	0.3867	1,342.6
AlSi10Mg SLM Z	104,245	6.097	0.9888	623.5	105,536	6.198	0.9445	623.1

It should be noted that Pearson's correlation coefficient is calculated in a log-log scale.

As it is clear from the graphs in Figure 3.35 a, b, c, and Table 3.14, it might be more accurate to use a higher value of strain than 0.2% of plastic strain for the definition of yield strength and as a lower bound of the experimental data range. The author prepared a Python code to verify this possibility considering the 0.5% of plastic strain option. The results are presented for all four materials in Figure 3.36 and Table 3.15.

Table 3.15. Results of proposed interpolation approach (i) in comparison with results of the least square method (a) – experimental data are used in the interval from 0.5% to $\boldsymbol{\varepsilon_{us}}$

Material	K_a (psi)	n_a	R_a^2	Std_a (psi)	K_i (psi)	n_i	R_i^2	Std_i (psi)
Grade 20	99,017	5.564	0.9676	1,537.4	88,394	6.980	0.9208	2,080.1
SS304	105,363	14.20	0.9898	524.3	104,408	15.34	0.9835	674.2
SS316L SLM XY	97,780	34.91	0.9855	267.6	97,780	31.49	0.8635	352.1
AlSi10Mg SLM Z	109,641	5.666	0.9872	505.5	109,746	5.800	0.9440	512.5

The yield strength F_{ty} is usually available with 0.2% offset of plastic strain for metallic alloys in literature, but it works well for materials without necking (compare Figure 3.35d and Figure 3.36d and the results in Tables 3.14 and 3.15 for AlSi10Mg). For ductile materials, the choice of 0.5% brings a more accurate characterization of stress-strain behavior as observed on four selected steels (compare the results in Tables 3.14 and 3.15 for steels). It should be mentioned that 0.5 was used instead of 0.2 in equation (33), and 0.005 was used instead of 0.002 in equation (35).

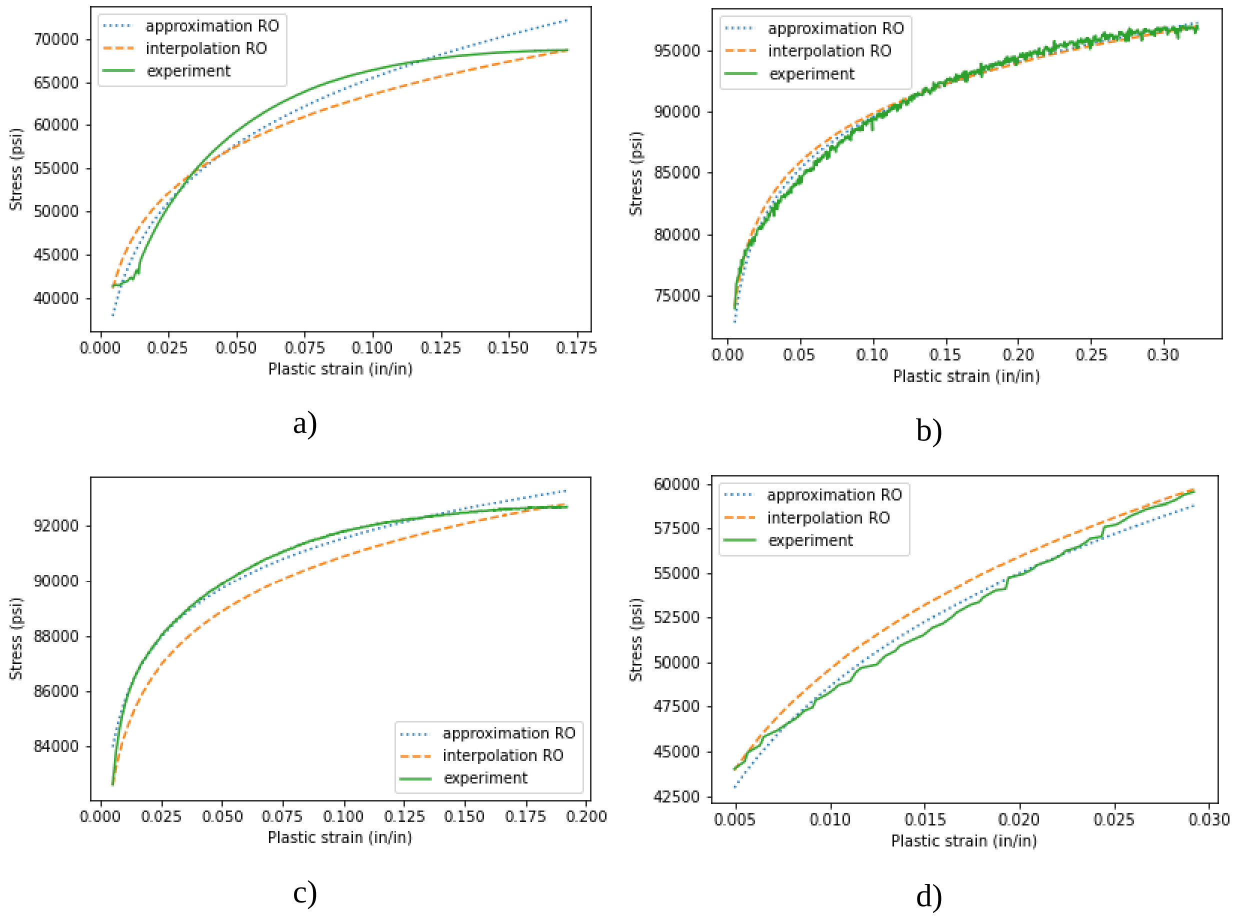

Figure 3.36. Results of interpolation and approximation approaches considering the interval from 0.5% to $\boldsymbol{\varepsilon_{us}}$: a) Grade 20, b) SS304, c) SS316L SLM XY [16], d) AlSi10Mg SLM Z [17]

For the longitudinal steel, the Ramberg-Osgood parameters are as follows:

n = 11.103

K = 110,259.4 psi

For the transverse steel, the Ramberg-Osgood parameters are as follows:

n = 9.8984

K = 129,274.8 psi

3.13 Linear Hardening

Prager's Hardening Rule and the Linear kinematic hardening model of the material are the same, as proposed by Prager, but the way of its material constant calibration is different (C or C_0).

3.13.1 Linear kinematic hardening model

Test data derived from a half-cycle of a unidirectional compression or tension experimental test should be linearized because this simplistic model just could only prophesy linear hardening. Typically, measurements of the stabilized behavior in strain cycles are used to generate data over a range of strain that corresponds to the anticipated range in the application. Abaqus requires just two data pairs to establish this linear behavior [18].

$$C = \frac{\sigma - \sigma|_0}{\varepsilon^{pl}} \quad (36)$$

$\sigma|_0$: yield stress at zero plastic strain

σ: yield stress

ε^{pl}: plastic strain at yield stress

C: linear kinematic hardening modulus

Longitudinal steel:

$\sigma = \sigma_y = 63{,}000\ psi$

Based on the Ramberg-Osgood model's MATLAB code:

$\sigma|_0 = 48{,}102.4\ psi$

$\varepsilon^{pl} = 0.002$

$$C = \frac{63{,}000 - 48{,}02{,}4}{0.002} = 7{,}448{,}790 \text{ psi}$$

Transverse steel:

$\sigma = \sigma_y = 69{,}000\ psi$

Based on the Ramberg-Osgood model's MATLAB code:

$\sigma|_0 = 50{,}945.03\ psi$

$\varepsilon^{pl} = 0.002$

$$C = \frac{69{,}000 - 50{,}945.03}{0.002} = 9{,}027{,}480\ psi$$

3.14 Prager's Hardening Rule

The material parameter of Prager's hardening rule should depend on the strain range based on the problem. For example, the Prager's Hardening Rule is often given as [19]:

$$C_0 = \frac{\sigma_u - \sigma_{y0}}{\varepsilon_{u,eq}} \quad (37)$$

C_0: material parameter of Prager's hardening rule

σ_u: true stress at the tensile strength

$\varepsilon_{u,eq}$: plastic strain at σ_u

σ_{y0}: initial yield stress

$$\sigma_{true} = \sigma(1+\varepsilon) \tag{38}$$

Longitudinal steel:

Ultimate stress = 93,500 psi

Based on the MATLAB code results:

Ultimate strain = 0.13264

$\sigma_u = 93{,}500(1+0.13264) = 105{,}901\ psi$

$\sigma_y = \sigma_{y0} = \sigma_0 = 63{,}000\ psi$

Based on the Ramberg-Osgood model's MATLAB code:

$\varepsilon_{u,eq} = 0.12942$

$$C_0 = \frac{105{,}901 - 63{,}000}{0.12942} = 331{,}485\ psi$$

Transverse steel:

$\sigma_y = \sigma_{y0} = \sigma_0 = 69{,}000\ psi$

Ultimate stress = 105,000 psi

Based on the MATLAB code results:

Ultimate strain = 0.1

$\sigma_u = 105{,}000(1+0.1) = 115{,}500\ psi$

$\varepsilon_{u,eq} = 0.096379$

$$C_0 = \frac{115{,}500 - 69{,}000}{0.096379} = 482{,}467\ psi$$

To define the plastic behavior of steel in Abaqus, the hardening behavior of steel first needs to be specified. The combination isotropic/kinematic hardening model expands upon the linear model [20], and the combined non-linear isotropic/non-linear kinematic hardening model is an extension of the non-linear model. This study combined the linear and non-linear models to model the cyclic loading of a material with nonlinear isotropic/kinematic hardening [21]. Three following options are derived from the resulting steel model:

- Half Cycle: for preparing the stress-strain data taken from the first half cycle of an experiment involving compression or tension in a single direction [21].
- Parameters: to specify the kinematic hardening parameters C_k and γ_k directly [21].
- Stabilized: to provide stress-strain data derived from the specimen's stabled cycle exposed to strain cycles with symmetry [21].

Regardless of which of the above three options is chosen, Abaqus requires the Yield stress and Plastic Strain or Yield Stress At Zero Plastic Strain, Kinematic Hardening Parameter C_i, and Gamma γ_i. The number of backstresses will define the value of i, meaning that we will have C_1, C_2, …, C_i and γ_1, γ_2,…, γ_i. Yield stress or steel stress is based on the steel model used for analysis, and extraction of plastic strains was performed from the MATLAB code results; while the Yield Stress At Zero Plastic Strain was calculated in advance, kinematic hardening parameters C_i and γ_i range will be computed in the following sections.

Abaqus then offers a Sub-options menu to enter additional data [21]. Cyclic hardening, which includes equivalent stress and equivalent plastic strain, were selected, and the data were extracted from the MATLAB code results (will be covered in Section 3.19, von Mises stress). Equivalent stress and equivalent plastic strain selections required a set of data to be defined for Abaqus at this stage.

3.15 Abdel-Karim and Ohno Plasticity Model

Unsymmetric stress cycles between specified limits will result in phenomena called progressing creep or ratchetting towards the mean stress [20]. The advantage of the Abdel-Karim and Ohno plasticity model is the possibility of calculating the steady ratcheting rate, which can be subsequently used to extrapolate the cycle-by-cycle accumulated quantity. In addition, the advantage of the Abdel-Karim and Ohno kinematic hardening rule is the stability of the plastic strain rate after the transient part fades [22].

The nonlinear kinematic hardening rule of Abdel-Karim and Ohno (AKO) is based on the linear superposition of backstress parts, according to Chaboche et al., 1979 [23]. The AKO model is unavailable in Abaqus and must be implemented by a suitable approach like a user subroutine and algorithm.

$$a = \sum_{i=1}^{M} a^{(i)} \tag{39}$$

whereas the evolution of the *i-th* backstress part is directed by:

$$da^{i} = \frac{2}{3} C_i d\varepsilon_p - \mu_i \gamma_i a^{(i)} dp - \gamma_i H(f_i) \langle d\lambda_i \rangle a^{(i)} \tag{40}$$

C_i, γ_i: parameters of plasticity model

dp: equivalent plastic strain increment

μ_i: ratcheting parameter

$H(f_i)$: Heaviside step function

Macaulay brackets: $\langle x \rangle = \frac{(x+|x|)}{2}$ (41)

$d\lambda$: plastic multiplier

a: deviatoric part of backstress

M: number of backstresses

The choice $\mu_i = 0$ obtains the multilinear model of Ohno and Wang for all i (model of type I according to Ohno and Wang, 1993 [24] will be marked as OWI).

This study offered the kinematic hardening rule in accordance with the Abdel-Karim and Ohno (AKO) cyclic plasticity model [25], resulting in a calibrated AKO model. The chosen points of the stress-strain curve specify the values of the fundamental material properties directly (C_i, γ_i) by the following relations [26]:

$$C_i = \frac{\sigma_{(i)} - \sigma_{(i-1)}}{\varepsilon_{p(i)} - \varepsilon_{p(i-1)}} - \frac{\sigma_{(i+1)} - \sigma_{(i)}}{\varepsilon_{p(i+1)} - \varepsilon_{p(i)}} \; for \; i \neq M \quad (42)$$

$$C_M = \frac{\sigma_{(M)} - \sigma_{(M-1)}}{\varepsilon_{p(M)} - \varepsilon_{p(M-1)}} \quad (43)$$

$$\gamma_i = \frac{1}{\varepsilon_{p(i)}} \; for \; all \; i \quad (44)$$

C_i, γ_i: parameters of plasticity model

$\sigma_{(i)}$: stress of the given ***i***-th point

$\varepsilon_{p(i)}$: plastic strain of the given ***i***-th point

The number of pairs of C_i and γ_i will provide the number of backstresses. The sum of C_i and γ_i parameters pairs will represent the backstresses number [26].

Longitudinal steel:

For calculating the C_i and γ_i values, the first point of consideration is the elastic limit, which is the stress corresponding to zero plastic strain. Nowadays, the tracking of yield surface is done experimentally with 100 με offset of plastic strain or less. Thus, the elastic limit can be chosen as the stress calculated by the Ramberg-Osgood equation for 0.0001 axial plastic strain. Therefore, we have:

$\varepsilon_{plastic} = 0.0001$

In the Ramberg-Osgood equation:

$$\varepsilon = \frac{\sigma}{E} + 0.002\left(\frac{\sigma}{F_{ty}}\right)^n$$

$$\varepsilon_{total} = \varepsilon_{elastic} + \varepsilon_{plastic} \Rightarrow \frac{\sigma}{E} + 0.0001 = \frac{\sigma}{E} + 0.002\left(\frac{\sigma}{F_{ty}}\right)^n \Rightarrow 0.002\left(\frac{\sigma}{F_{ty}}\right)^n = 0.0001$$

A MATLAB code was written to solve and evaluate the elastic limit stress.

Elastic limit stress = 48,102.4 psi

The second point should be the yielding point. Therefore, the C_i and γ_i values are illustrated in Tables 3.16 and 3.17.

Table 3.16. C_i values in psi unit for longitudinal steel based on the Ramberg-Osgood model after modification

C_1	24,025,900
C_2	1,177,350
C_3	1,026,230
C_4	706,413
C_5	324,358
C_6	153,870
C_7	72,745.6
C_8	28,034.7
$C_M = C_9$	185,443

Table 3.17. γ_i values for longitudinal steel based on the Ramberg-Osgood model after modification

γ_1	10,000
γ_2	500.49
γ_3	353.89
γ_4	155.7
γ_5	72.644
γ_6	35.734
γ_7	18.469

γ_8	10.02
γ_9	6.7257

The Plastic option and then the Hardening option were selected in Abaqus to define the plastic behavior of the steel. Combined (hardening) was then selected, followed by Parameters in the Datatype section, resulting in Yield Stress At Zero Plastic Strain, Kinematic Hardening Parameter "C_i, and Gamma γ_i". The C_i and Gamma γ_i in this stage were the C_i and γ_i, which were calculated based on the AKO plasticity model. The number of *i* depends on the number of discrete points in the model.

Transverse steel:

For calculating the C_i and γ_i values, the first point of consideration is the elastic limit, which is the stress corresponding to zero plastic strain. Nowadays, the tracking of yield surface is done experimentally with 100 με offset of plastic strain or less. Thus, the elastic limit can be chosen as the stress calculated by the Ramberg-Osgood equation for 0.0001 axial plastic strain. Therefore, we have:

$\varepsilon_{plastic} = 0.0001$

In the Ramberg-Osgood equation:

$$\varepsilon = \frac{\sigma}{E} + 0.002\left(\frac{\sigma}{F_{ty}}\right)^n$$

$$\varepsilon_{total} = \varepsilon_{elastic} + \varepsilon_{plastic} \Rightarrow \frac{\sigma}{E} + 0.0001 = \frac{\sigma}{E} + 0.002\left(\frac{\sigma}{F_{ty}}\right)^n \Rightarrow 0.002\left(\frac{\sigma}{F_{ty}}\right)^n = 0.0001$$

A MATLAB code was written to solve and evaluate the elastic limit stress.

Elastic limit stress = 50,945.03 psi

Therefore, the C_i and γ_i values are depicted in Tables 3.18 and 3.19.

Table 3.18. C_i values in psi unit for transverse steel based on the Ramberg-Osgood model after modification

C_1	20,167,400
C_2	1,216,630
C_3	1,054,020
C_4	988,361
C_5	519,250
C_6	281,939
C_7	156,583

C_8	87,418.4
C_9	47,237.2
$C_M = C_{10}$	239,460

Table 3.19. γ_i values for transverse steel based on the Ramberg-Osgood model after modification

γ_1	10,000.4
γ_2	500.49
γ_3	434.27
γ_4	219.96
γ_5	116.53
γ_6	64.262
γ_7	36.758
γ_8	21.755
γ_9	13.304
γ_{10}	8.4027

3.16 Chaboche kinematic hardening rule

For pure monotonic tension, we have [23]:

$$\sigma = \sigma_Y + \alpha = \sigma_Y + \sum_{i=1}^{M} \frac{C_i}{\gamma_i}(1 - e^{-\gamma_i \cdot \varepsilon_p}) \tag{45}$$

M: number of backstresses

α: backstress

ε_p: plastic strain

σ: Chaboche analytical stress

For the longitudinal steel based on the Ramberg-Osgood model and Chaboche kinematic hardening rule for pure monotonic tension, the values of α and σ were coded and calculated in MATLAB and is depicted in Table 3.20.

Table 3.20. Chaboche α and σ values (longitudinal)

Alpha Chaboche	Chaboche Analytical True Stress (psi)
0	48,182.2
10,525.05	58,707.2
13,121.9	61,304.1
19,478.6	67,660.8

25,137.1	73,319.3
31,071.3	79,253.6
37,660.3	85,842.5
44,733.5	92,915.7
49,554.9	97,737.1

For the transverse steel based on the Ramberg-Osgood model and Chaboche kinematic hardening rule for pure monotonic tension, the values of α and σ were coded and calculated in MATLAB and is illustrated in Table 3.21.

Table 3.21. Chaboche α and σ values (transverse)

Alpha Chaboche	Chaboche Analytical True Stress (psi)
0	51,034.5
12,782.6	63,817.2
14,049.3	65,083.8
20,521.6	71,556.1
26,423.8	77,458.4
31,955.8	82,990.3
37,711.3	88,745.8
43,802.2	94,836.8
50,062.7	10,1097
56,040.3	107,075

For the longitudinal steel, the Chaboche true plastic strain, as well as the Chaboche true stress values, were coded in MATLAB and calculated as illustrated in Table 3.22.

Table 3.22. Chaboche true plastic strain and Chaboche true stress of longitudinal steel

Chaboche True Plastic Strain	Chaboche True Stress (psi)
0	48,187
0.001998	63,262.8
0.0028256	65,329.6
0.0064224	70,619.9
0.013765	76,233.5

0.027984	82,491
0.054142	89,978
0.099798	99,724.6
0.14868	108,790

For the transverse steel, the Chaboche true plastic strain, as well as the Chaboche true stress values, were coded in MATLAB and calculated as depicted in Table 3.23.

Table 3.23. Chaboche true plastic strain and Chaboche true stress of transverse steel

Chaboche True Plastic Strain	Chaboche True Stress (psi)
0	51,039.6
0.001998	69,302.1
0.0023027	70,330.3
0.0045461	75,535.7
0.0085813	80,910.1
0.015561	86,582.1
0.027204	92,761.3
0.045964	99,779.7
0.075162	108,150.8
0.119	118,650

Table 3.24 illustrates the Chaboche analytical true stress in psi and Chaboche true plastic strain, and Figure 3.37 depicts the Chaboche model for longitudinal steel.

Table 3.24. Chaboche true plastic strain and Chaboche analytical true stress in psi of longitudinal steel

Chaboche True Plastic Strain	Chaboche Analytical True Stress (psi)
0	48,182.2
0.001998	58,707.2
0.0028256	61,304.1
0.0064224	67,660.8
0.013765	73,319.3
0.027984	79,253.6

0.054142	85,842.5
0.099798	92,915.7
0.14868	97,737.1

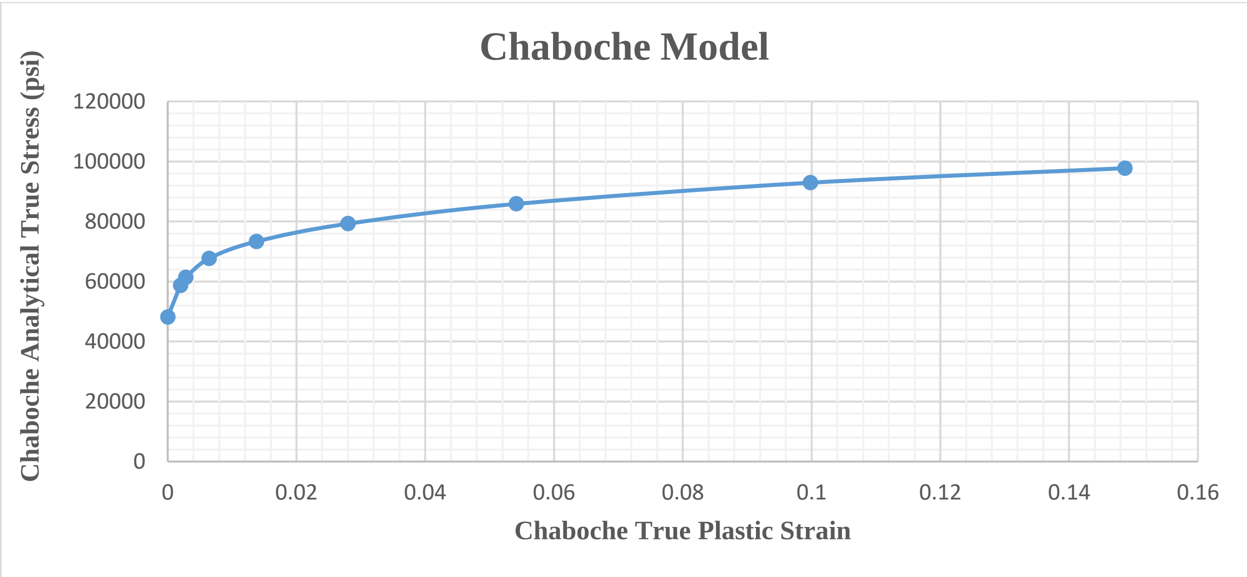

Figure 3.37. Chaboche model of longitudinal steel

Table 3.25 illustrates the Chaboche analytical true stress in psi and Chaboche true plastic strain, and Figure 3.38 depicts the Chaboche model for transverse steel.

Table 3.25. Chaboche true plastic strain and Chaboche analytical true stress in psi of transverse steel

Chaboche True Plastic Strain	Chaboche Analytical True Stress (psi)
0	51,034.5
0.001998	63,817.2
0.0023027	65,083.8
0.0045461	71,556.1
0.0085813	77,500
0.015561	82,990.3
0.027204	88,745.8
0.045964	94,836.8
0.075162	101,097

0.119	107,075

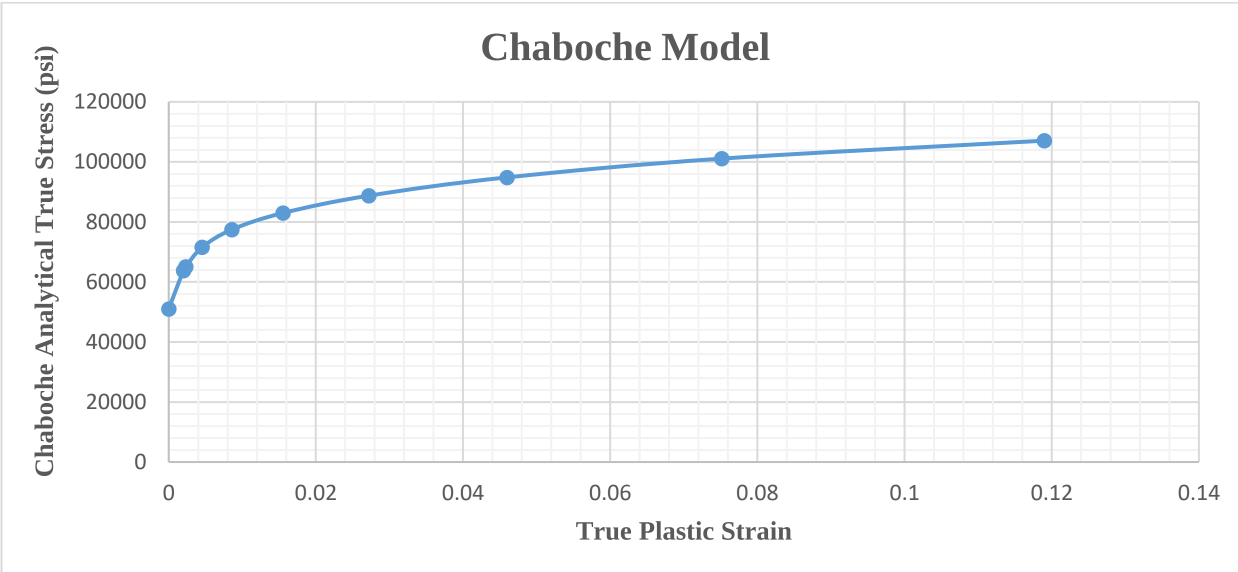

Figure 3.38. Chaboche model of transverse steel

3.17 Ohno-Wang model I (OWI)

Now, for the OWI diagram, we need the true stress versus true plastic strain calculated in the previous sections. Figure 3.39 illustrates the Ohno and Wang I (OWI) model for the longitudinal steel.

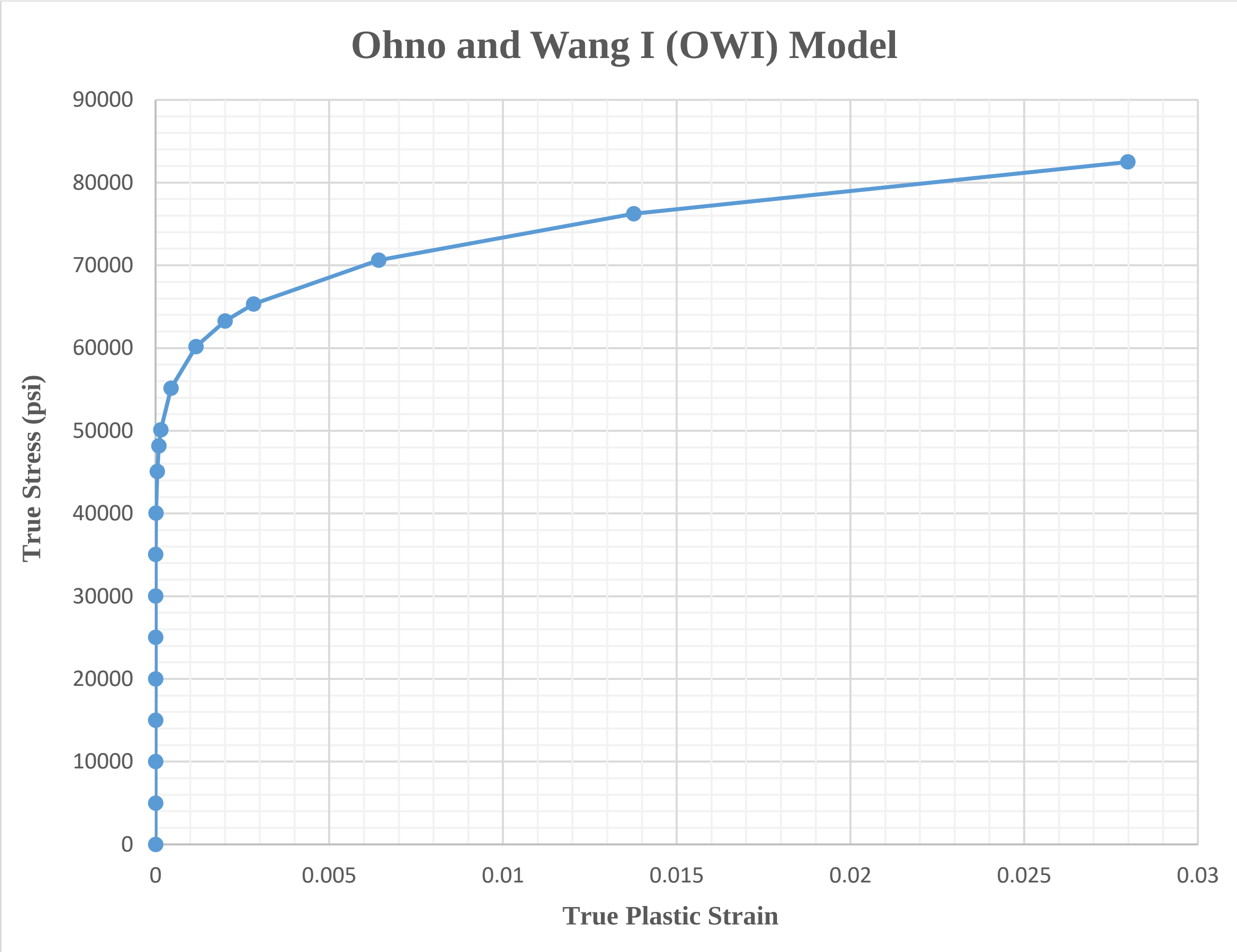

Figure 3.39. Ohno and Wang I (OWI) model of longitudinal steel

Figure 3.40 depicts the Ohno and Wang I (OWI) model for the transverse steel.

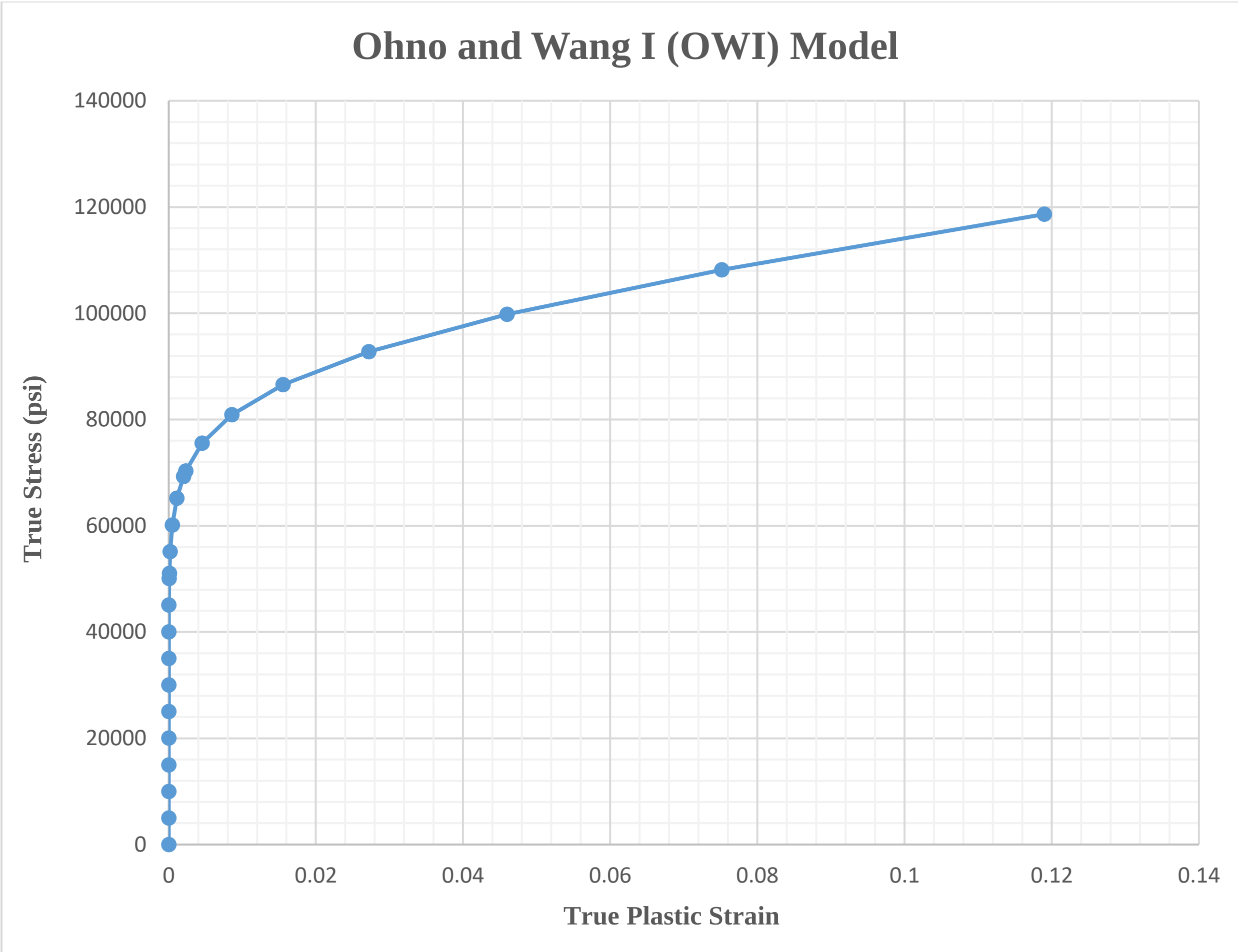

Figure 3.40. Ohno and Wang I (OWI) Model of transverse steel

3.18 Chaboche model and Ohno-Wang model I (OWI) comparison

Figure 3.41 compares the Chaboche and Ohno-Wang model I (OWI) for the longitudinal steel.

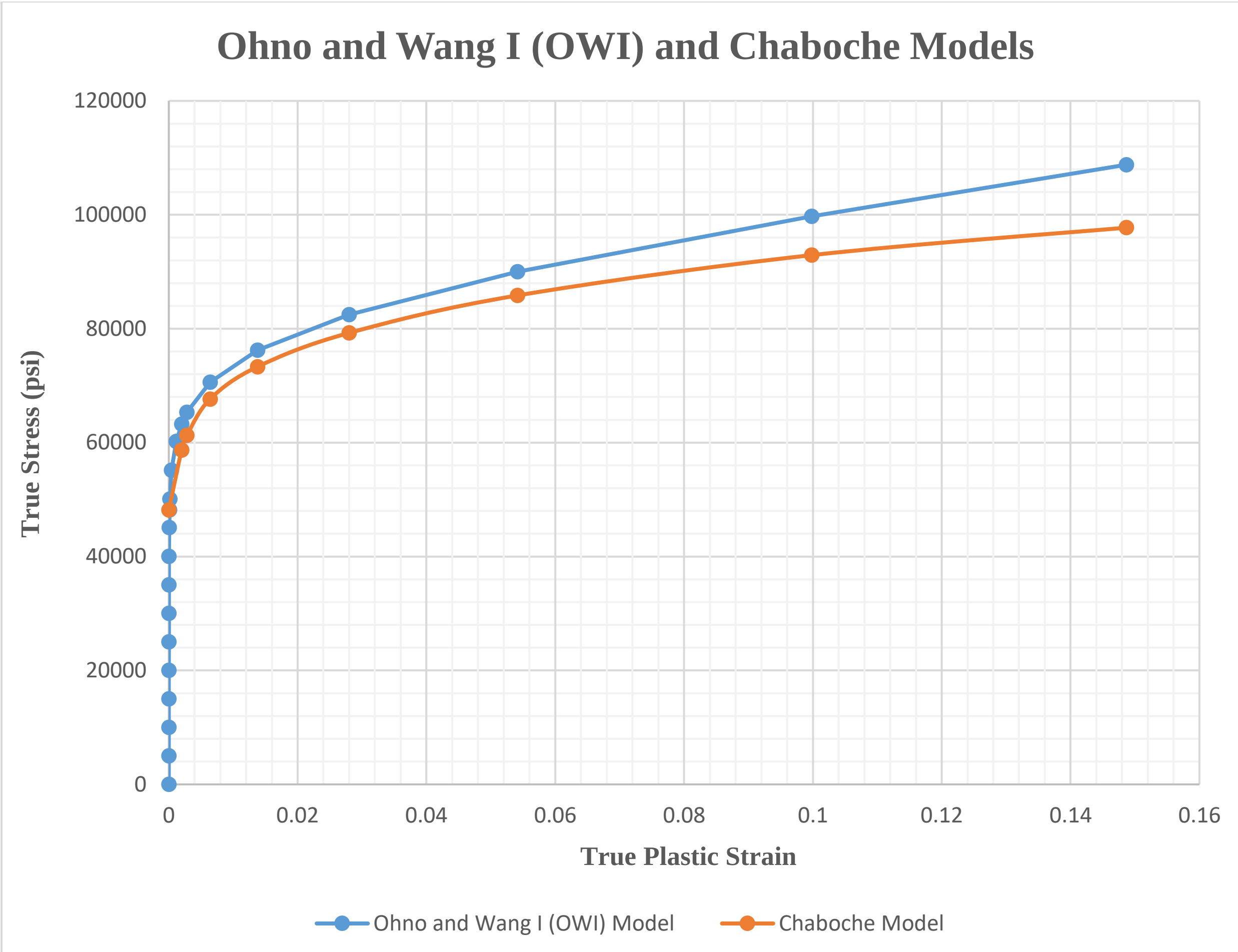

Figure 3.41. Chaboche and Ohno-Wang model I (OWI) of the longitudinal steel comparison

Figure 3.42 compares the Chaboche and Ohno-Wang model I (OWI) for the transverse steel.

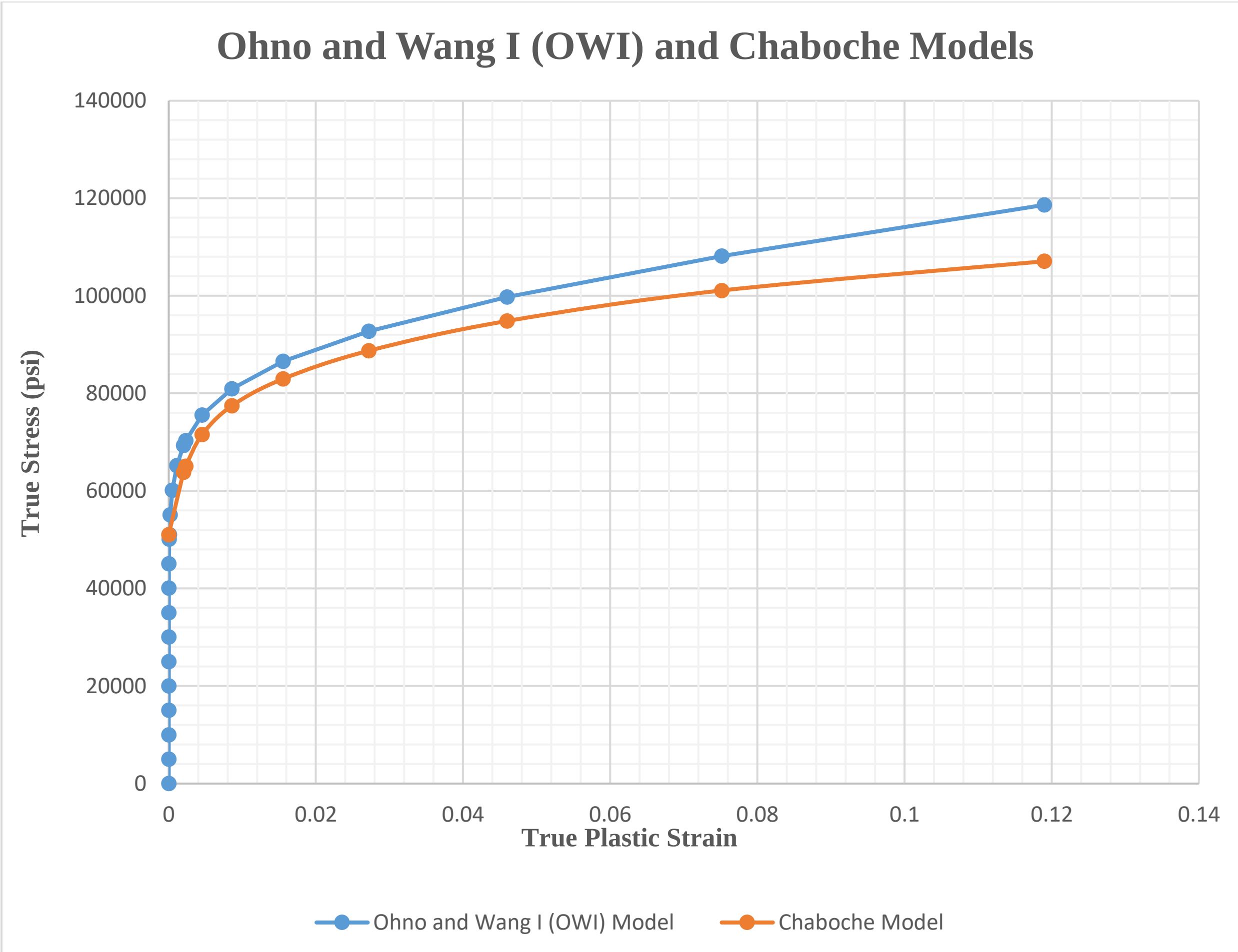

Figure 3.42. Chaboche and Ohno-Wang model I (OWI) of the transverse steel comparison

Figures 3.41 and 3.42 elucidate an excellent concordance between Chaboche and Ohno-Wang model I (OWI) results. The models produce strikingly similar results.

3.19 von Mises stress

The second invariant of the deviatoric stress tensor (Pa^2), $J_{2'}$, is defined as [27]:

$$J_{2'} = -\frac{1}{6}[(\sigma_1 - \sigma_2)^2 + (\sigma_2 - \sigma_3)^2 + (\sigma_3 - \sigma_1)^2] \qquad (46)$$

σ_1, σ_2, σ_3: principal stress (Pa)

In the case of simple tension, yielding (σ_Y as yield strength) occur when

$\sigma_1 = \sigma_Y$

σ_Y: yield stress (Pa)

$\sigma_2 = \sigma_3 = 0$

$J_{2'} = -\frac{1}{6}[\sigma_1{}^2 + \sigma_1{}^2] = -\frac{1}{6}[2\sigma_1{}^2] = -\frac{2}{6}[\sigma_1{}^2] = -\frac{1}{3}[\sigma_1{}^2]$ (47)

Yield criterion of the von Mises stress indicates that yielding will take place when the deviatoric stress tensor's second invariant ($J_{2'}$) approaches a critical value, or:

$p(-J_{2'}) = 1$ (48)

$$p = \frac{3}{\sigma_Y{}^2} \Rightarrow \sigma_Y{}^2 = \frac{3}{p}$$

$$p(-J_{2'}) = 1 \Longrightarrow p = \frac{1}{-j_{2'}} = -\frac{1}{j_{2'}}$$

$\sigma_Y{}^2 = \frac{3}{p} = \frac{3}{-\frac{1}{j_{2'}}} = -3J_{2'} \Rightarrow \sigma_Y = \sqrt{(-3J_{2'})}$ (49)

p: parameter in stress criterion (Pa^{-2})

By defining an equivalent stress (σ_{eq1}) as

$\sigma_{eq1} = (-3J_{2'})^{\frac{1}{2}} = \sqrt{(-3J_{2'})}$ (50)

σ_{eq1}: equivalent stress criterion #1 (Von Mises) (Pa)

von Mises criterion also indicates that yielding will take place once the equivalent stress approaches a critical point value ($\sigma_{eq1c} = \sigma_Y$).

σ_{eq1c}: critical value of σ_{eq1} (Pa)

$$\sigma_{eq1} = \sigma_Y$$

Longitudinal steel:

$\sigma_y = \sigma_Y = \sigma_1 = 63{,}000$ psi

$\sigma_2 = \sigma_3 = 0$

$$J_{2'} = -\frac{1}{3}[\sigma_1{}^2] = -\frac{1}{3}(63{,}000^2) = -1{,}323 \times 10^6\ psi^2$$

$$\text{p} = \frac{3}{\sigma_Y{}^2} = \frac{3}{63{,}000^2} = 7.5585 \times 10^{-10}$$

$$\sigma_{eq1} = \sigma_Y = 63{,}000\ psi$$

Transverse steel:

$\sigma_y = \sigma_Y = \sigma_1 = 69{,}000$ psi

$\sigma_2 = \sigma_3 = 0$

$$J_{2'} = -\frac{1}{3}[{\sigma_1}^2] = -\frac{1}{3}(69{,}000^2) = -1{,}587 \times 10^6\ psi^2$$

$$\mathrm{p} = \frac{3}{{\sigma_Y}^2} = \frac{3}{69{,}000^2} = 6.3011 \times 10^{-10}$$

$$\sigma_{eq1} = \sigma_Y = 69{,}000\ psi$$

Evaluation of equivalent plastic strain and von Mises equivalent stress is as follows:

$$\sigma_{eq} = \sqrt{\tfrac{3}{2}\boldsymbol{s}:\boldsymbol{s}}\ [28] \tag{51}$$

σ_{eq}: Von Mises Equivalent Stress

$\boldsymbol{s}$: deviatoric part of the stress tensor

Symbol (:) means the contraction. The contraction is defined using Einstein's summing rule as $a_{ij} = \boldsymbol{b}:\boldsymbol{c} = b_{ij}C_{ij}$.

$$\vec{\sigma} = \begin{bmatrix} \sigma_{11} & \sigma_{12} & \sigma_{13} \\ \sigma_{21} & \sigma_{22} & \sigma_{23} \\ \sigma_{31} & \sigma_{32} & \sigma_{33} \end{bmatrix} \tag{52}$$

At yield under a uniaxial stress state:

$\sigma_{11} = \sigma$

$\sigma_{22} = \sigma_{33} = 0$

$$\sigma_{eq} = |\sigma| \tag{53}$$

The equivalent plastic strain is defined as

$$\varepsilon_{eq} = \sqrt{\tfrac{2}{3}\overrightarrow{\boldsymbol{\varepsilon_p}}:\overrightarrow{\boldsymbol{\varepsilon_p}}} \tag{54}$$

ε_{eq}: equivalent plastic strain

$\overrightarrow{\boldsymbol{\varepsilon_p}}$: plastic strain tensor

Uniaxial strain is a kind of loading when ε_{11} is non-zero, although all other strain components are zero [29].

Uniaxial strain $\Rightarrow \varepsilon\varepsilon = \vec{\varepsilon} = \varepsilon_{11}$

$$\varepsilon\varepsilon = \vec{\varepsilon} = \begin{bmatrix} \varepsilon_{11} & \varepsilon_{12} & \varepsilon_{13} \\ \varepsilon_{21} & \varepsilon_{22} & \varepsilon_{23} \\ \varepsilon_{31} & \varepsilon_{32} & \varepsilon_{33} \end{bmatrix} \tag{55}$$

$$\varepsilon_{eq} = \left|\varepsilon_{11}^{p}\right| \tag{56}$$

$$\phi = \frac{3}{2} \cdot \frac{\varepsilon_{eq}}{\sigma_{eq}} \tag{57}$$

ϕ: variable factor of proportionality

Table 3.26 demonstrates the parameter values based on results of the Ramberg-Osgood model's MATLAB code written for longitudinal steel.

Table 3.26. Parameters of longitudinal steel for Ramberg-Osgood's model derived from the MATLAB code

σ_{eq} (psi)	**ε_{eq}**	**ϕ**
0	0	
5,000	1.2109E-15	3.6329E-19
10,000	2.6644E-12	3.9966E-16
15,000	2.4033E-10	2.4033E-14
20,000	5.8623E-09	4.3967E-13
25,000	6.984E-08	4.1904E-12
30,000	5.2879E-07	2.6439E-11
35,000	2.9283E-06	1.255E-10
40,000	1.2898E-05	4.8369E-10
45,000	4.7698E-05	1.5899E-09
48,102.4	0.0001	3.1183E-09
50,000	0.00015366	4.6099E-09
55,000	0.00044276	1.2075E-08
60,000	0.0011634	2.9086E-08
63,000	0.002	4.7619E-08
65,000	0.0028296	6.5299E-08
70,000	0.0064431	1.3806E-07
75,000	0.01386	2.7721E-07
80,000	0.028379	5.3211E-07
85,000	0.055634	9.8179E-07
90,000	0.10494	1.7491E-06
93,500	0.1603	0.0000025717

Table 3.27 illustrates the parameter values based on the Ramberg-Osgood model's MATLAB code for transverse steel.

Table 3.27. Parameters of transverse steel for Ramberg-Osgood's model derived from the MATLAB code

σ_{eq} (psi)	ε_{eq}	ϕ
0	0	
5,000	1.1078E-14	3.3236E-18
10,000	1.0404E-11	1.5606E-15
15,000	5.7037E-10	5.7037E-14
20,000	9.7714E-09	7.3285E-13
25,000	8.8504E-08	5.3102E-12
30,000	5.3566E-07	2.6783E-11
35,000	2.4547E-06	1.052E-10
40,000	9.1767E-06	3.4412E-10
45,000	2.9365E-05	9.7883E-10
50,000	0.000083118	2.4935E-09
50,945.03	0.0001	2.9443E-09
55,000	0.00021303	5.8101E-09
60,000	0.00050306	1.2576E-08
65,000	0.0011089	2.5591E-08
69,000	0.002	4.3478E-08
70,000	0.0023053	4.94E-08
75,000	0.0045565	9.113E-08
80,000	0.0086183	1.6159E-07
85,000	0.015682	2.7675E-07
90,000	0.027578	4.5963E-07
95,000	0.047037	7.4269E-07

3.20 Mander and Ramberg-Osgood Models Comparison

A MATLAB code was written to show the behavior of longitudinal steel in tension based on the Mander as well as Ramberg-Osgood models for engineering (nominal) and true stress-strain curves as shown in the comparison illustrated in Figure 3.43.

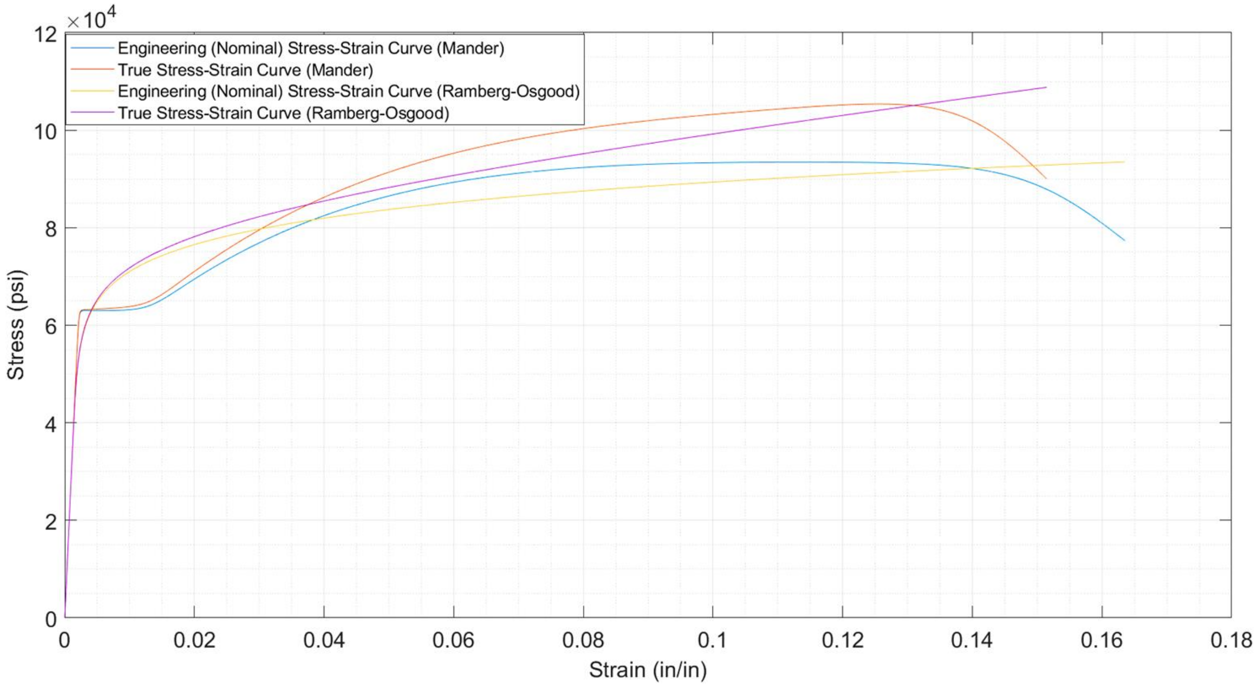

Figure 3.43. Mander & Ramberg-Osgood model curves comparison for longitudinal steel

The behaviors of the four plots in Figure 3.43 are identical up to approximately 50,000 psi, which is less than the yielding point of 63,000 psi.

Another MATLAB code was written to show the behavior of transverse steel in tension based on the Mander and the Ramberg-Osgood models for engineering (nominal) and true stress-strain curves. Figure 3.44 compares these models for transverse steel.

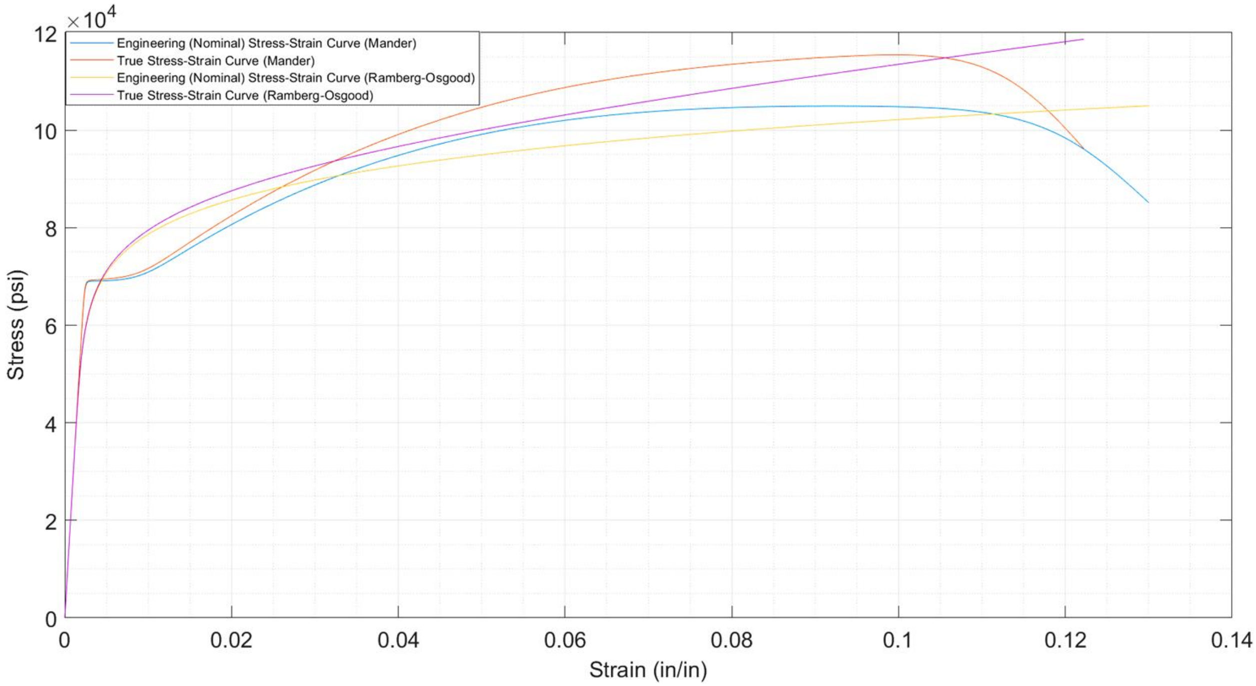

Figure 3.44. Mander & Ramberg-Osgood model curves comparison for transverse steel

The behaviors of the four plots in Figure 3.44 are identical up to approximately 55,000 psi, which is less than the yielding point of 69,000 psi.

3.21 Finite Element Modeling of a Reinforced Concrete (RC) Column

The experimental verification of the steel modeling approaches discussed in this Chapter (Chapter 3) is the same one presented in Chapter 2. (The experiment described in Chapter 2 uses the steel plasticity modeling presented in this Chapter). For details about the mechanical testing and the numerical model, the reader here is referred to Section 2.11 of Chapter 2 for the description of the experiment and the verification of the results. Additional information about the FEM modeling is given in the following paragraphs.

The boundary conditions of the numerical model are such that the bottom of the prism is fixed in all three translational degrees of freedom, and the top of the prism is free.

Steel specifications in Abaqus:

- 3D
- Deformable
- Wire
- Type: Planar
- Beam
- Truss

Mesh:

- Approximate element size: 40
- Instant Type: Dependent (mesh on part)

Element Type:

- Element Type: Family is Truss, which changed the reinforcement element type to T3D2 (a 2-nodes linear 3-D truss)

Analysis Step:

- Static, General
- Nlgeom for performing nonlinear analysis
- Automatic Incrementation

The effective monotonic loading resulted in the load-deformation response shown in Figures 3.52–3.54 (repeated here from Chapter 2 primarily for the reader's convenience).

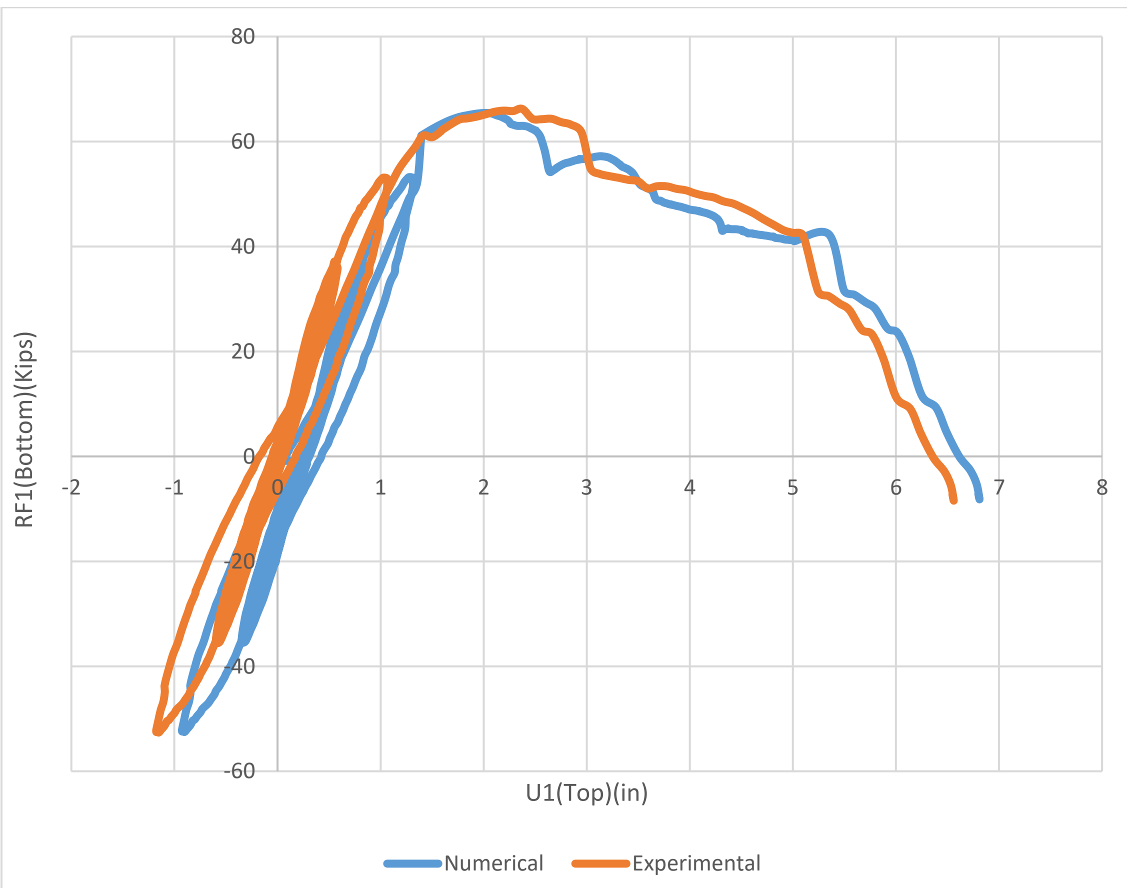

Figure 3.45. Relationship between lateral load and lateral displacement for experimental and numerical (Abaqus) test

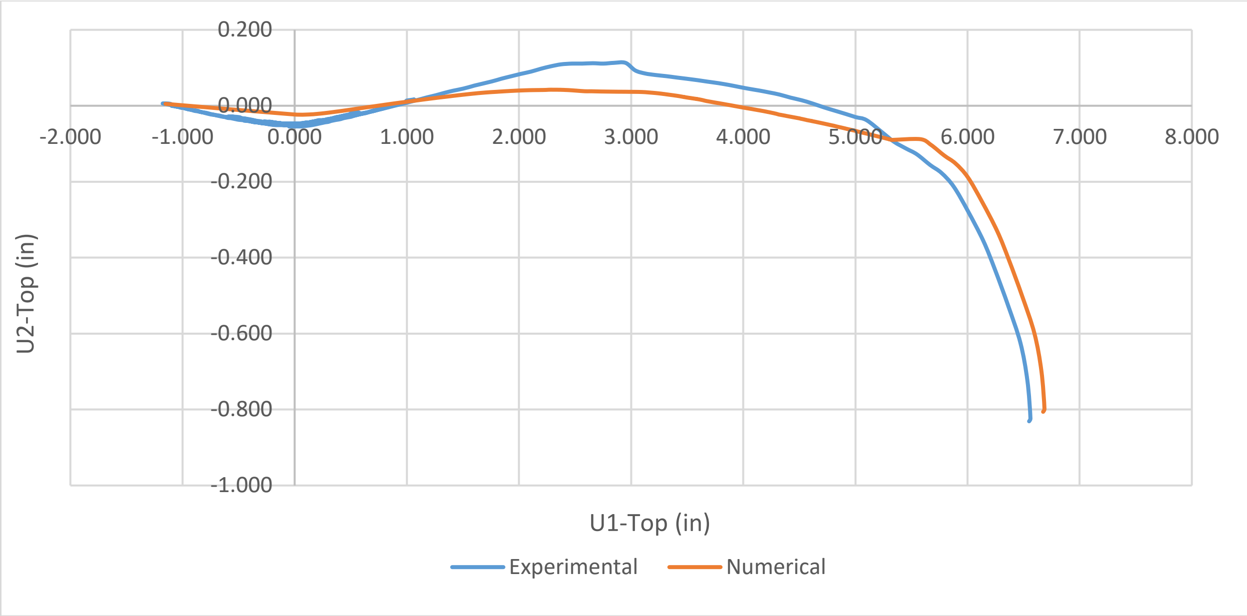

Figure 3.46. Relationship between lateral displacement and vertical displacement for experimental and numerical (Abaqus) test

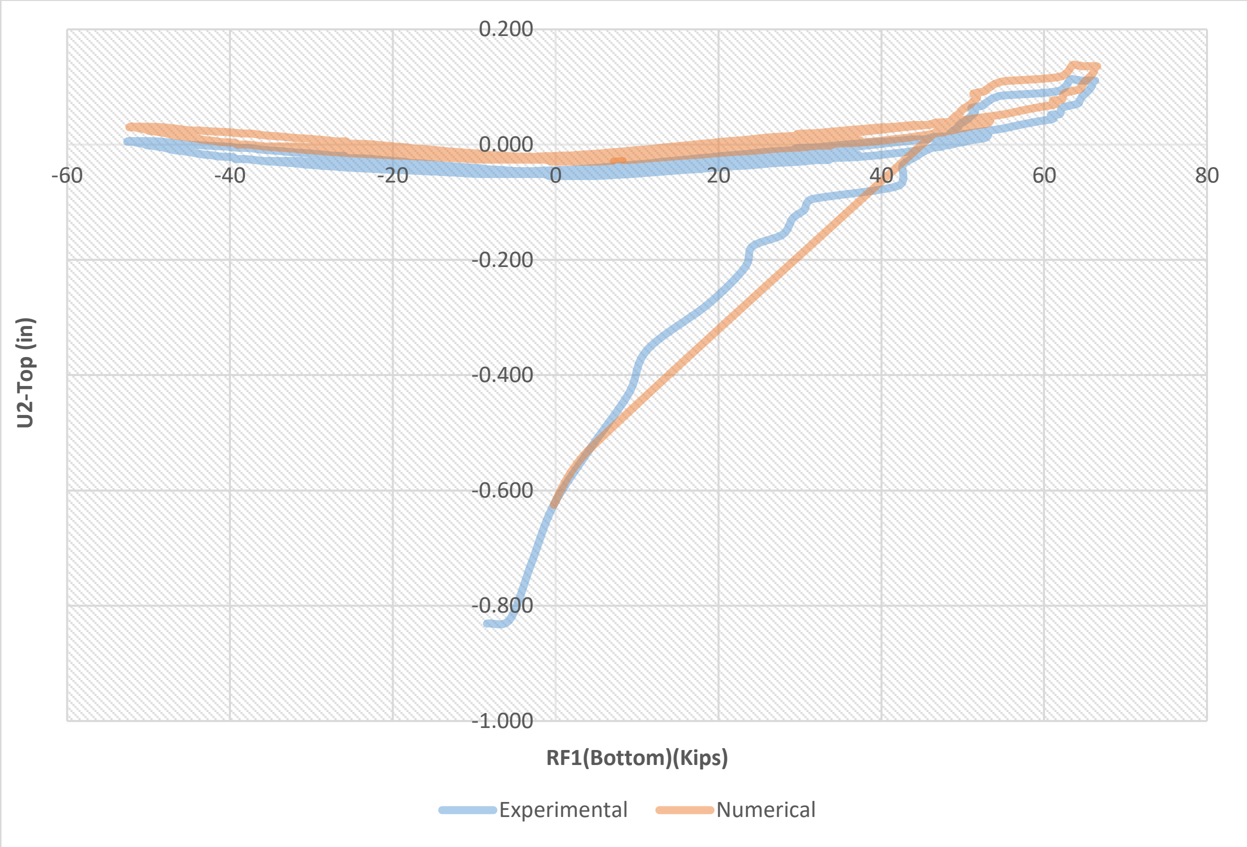

Figure 3.47. Relationship between lateral load and vertical displacement for experimental and numerical (Abaqus) test

For Figures 3.52-3.54, the Chaboche plasticity model, a cyclic plasticity model, was utilized in order for the analysis to match the experimental results properly. Figures 3.52-3.54 elucidate a good concordance between experimental and numerical results calculated with the proposed approaches and the remarkable ability of the proposed methodology to replicate the experimental results, specifically with respect to envelope curve; the models produce strikingly similar envelope results. The outcomes indicate that the Finite Element results using the above-proposed models are well-matched by experiment results and that the model are a good representation of actual column behavior.

3.22 Conclusion

For the stress-strain behavior, one should utilize the Ramberg-Osgood model for the analysis when using Abaqus. This means that Ramberg-Osgood model gives the best results. An interpolation approach has been developed and studied in this work to identify the parameters of the Ramberg-Osgood equation. The proposed method can serve for more accurate FE simulations than considering a linear kinematic hardening rule. The basic parameters of chosen plasticity model are identified using the Ramberg-Osgood equation. The approach is limited by the homogenous plastic deformation assumption. In order to form this analysis, it would be essential to apply suitable correction formulas to obtain equivalent stress–equivalent strain curve properly after the necking point (see works of Bridgman and Gromada et al. [30,31]). By specifying von Mises stress utilization, it is meant that an Abaqus user needs to calculate the equivalent stress, and equivalent strain. He/she should use the von Mises stress concept to do that. Chaboche plasticity model can define the steel kinematic hardening rule by providing parameters of the plasticity model. For Prager's hardening rule, the material parameter of Prager's hardening rule should depend on the strain range based on the problem. Prager's hardening rule gives C_0 (material parameter of Prager's hardening rule); however, it is not enough for utilization in Abaqus; because Gamma (ɣ) is also needed, and the Prager's hardening rule is not able to provide it. For the combined isotropic kinematic hardening model, the materials that harden kinematically and isotropically are particularly appropriate for applications to cyclic plasticity in which kinematic hardening is within an individual cycle, the dominant hardening process, resulting in the Bauschinger effect. However, the material also hardens isotropically over many cycles, so the peak tension and compression stresses in each cycle increase from one cycle to the next until saturation is achieved.

The conclusion of this research study demonstrates that the Ramberg-Osgood models, von Mises stress utilization, Chaboche Plasticity model, and in general, steel plasticity model all together could be used in Finite Element software (Abaqus) if and only if they are appropriately utilized based on their descriptions. If so, it will give acceptable results that correspond to experimental test results.

This research study proposes various approaches to modeling of the reinforcing steel bars (rebars) cyclic response when analyzing RC columns by the finite element method and using advanced built-in material models in Abaqus. The material model properly simulated the key features of steel and all the steel plastic components for various steel hardening, including Drucker-Prager plasticity (Prager's hardening rule), Abdel-Karim-Ohno plasticity model, Chaboche kinematic hardening rule, and Ohno-Wang model I (OWI).

3.23 Acknowledgments

The author would like to express his great appreciation to especially Professor Radim Halama from the VSB-Technical University of Ostrava for his unbelievable and ceaseless support and guidance in defining and interpreting the complex plastic behavior of the steel as well as for defining Abdel–Karim–Ohno Plasticity Model and providing all his research studies and findings on the complex plastic behavior of steel, Professor Maxim Lutovinov from Czech Technical University in Prague, and Professor Niloy Khutia from Indian Institute of Engineering Science and Technology for providing guidance in the definition of Abdel–Karim–Ohno Plasticity Model. The author also wishes to thank Professor Ali Mansouri for his guidance.

References

1. Chen, Wai-Fah, and D. J. Han. 2007. *Plasticity for Structural Engineers*. Ft. Lauderdale, FL: J. Ross.

2. Bohara, Rajendra Prasad, Ganchai Tanapornraweekit, and Somnuk Tangtermsirikul. n.d. "Investigation of Concrete Material Models for the Analysis of Seismic Behavior of Reinforced Concrete under Reversed Cyclic Load." Accessed January 25, 2023. https://www.thaiscience.info/Journals/Article/SONG/10993154.pdf.

3. Tresca, Henri. 1864. "Memoir on the Flow of Solid Bodies under Strong Pressure." *Comptesrendus De l'Académie Des Sciences 59*.

4. Chen, Wai-Fah, and H. Zhang. 1991. *Structural Plasticity: Theory, Problems, and Cae Software*. New York: Springer-Verlag.

5. Dafalias, Y. F., and E. P. Popov. 1975. "A Model of Nonlinearly Hardening Materials for Complex Loading." *Acta Mechanica* 21 (3): 173–92. https://doi.org/10.1007/bf01181053.

6. Krieg, R. D. 1975. "A Practical Two Surface Plasticity Theory." *Journal of Applied Mechanics* 42 (3): 641–46. https://doi.org/10.1115/1.3423656.

7. Ataei, Hossein, and Mohammadhossein Mamaghani. 2018. *Finite Element Analysis: Applications and Solved Problems Using Abaqus®*. United States.

8. Hu, Huiling. 1970. "Numerical Study of Seismic Behavior of High Strength Steel Replaceable Shear Links: Semantic Scholar." Undefined. January 1, 1970. https://www.semanticscholar.org/paper/Numerical-study-of-seismic-behavior-of-high-steel-Hu/e3ba4088a3c157c93d0273a134c80ddab62dee24.

9. You, J.-H., and M. Miskiewicz. 2008. "Material Parameters of Copper and CuCrZr Alloy for Cyclic Plasticity at Elevated Temperatures." *Journal of Nuclear Materials* 373 (1-3): 269–74. https://doi.org/10.1016/j.jnucmat.2007.06.005.

10. Dunne, Fionn, and Nik Petrinic. 2011. Introduction to Computational Plasticity. Oxford: Oxford University Press.

11. Frederick, C.O., and P.J. Armstrong. 2007. "A Mathematical Representation of the Multiaxial Bauschinger Effect." *Materials at High Temperatures* 24 (1): 1–26. https://doi.org/10.3184/096034007x207589.

12. Li, Ruipeng, Yunfeng Zhang, and Le-Wei Tong. 2014. "Numerical Study of the Cyclic Load Behavior of Aisi 316L Stainless Steel Shear Links for Seismic Fuse Device." *Frontiers of Structural and Civil Engineering* 8 (4): 414–26. https://doi.org/10.1007/s11709-014-0276-4.

13. Mander, Thomas J., and Adolfo B. Matamoros. 2019. "Constitutive Modeling and Overstrength Factors for Reinforcing Steel." *ACI Structural Journal* 116 (3). https://doi.org/10.14359/51713320.

14. Ramberg, Walter, and William R Osgood. n.d. "Description of Stress-Strain Curves by Three Parameters - NASA Technical Reports Server (NTRS)." NASA. NASA. Accessed October 22, 2022. https://ntrs.nasa.gov/citations/19930081614.

15. Nope, Grace Vanessa De Leon. 2017. "Dot/FAA/Ar-MMPDS-01 Metallic Materials Properties Development and Standardization (MMPDS." Academia.edu. November 6, 2017.

https://www.academia.edu/35071264/DOT_FAA_AR_MMPDS_01_Metallic_Materials_Properties_Development_and_Standardization_MMPDS.

16. Kořínek, Michal, Radim Halama, František Fojtík, Marek Pagáč, Jiří Krček, David Krzikalla, Radim Kocich, and Lenka Kunčická. 2020. "Monotonic Tension-Torsion Experiments and FE Modeling on Notched Specimens Produced by SLM Technology from SS316L." *Materials* 14 (1): 33. https://doi.org/10.3390/ma14010033.

17. Měsíček, Jakub, Tomáš Čegan, Quoc-Phu Ma, Radim Halama, Kateřina Skotnicová, Jiří Hajnyš, Jan Juřica, Pavel Krpec, and Marek Pagáč. 2022. "Effect of Artificial Aging on the Strength, Hardness, and Residual Stress of SLM AlSi10Mg Parts Prepared from the Recycled Powder." *Materials Science and Engineering: A* 855: 143900. https://doi.org/10.1016/j.msea.2022.143900.

18. "Abaqus Analysis User's Manual (6.10) - 130.149.89.49:2080." n.d. Accessed July 30, 2022. http://130.149.89.49:2080/v6.10/books/usb/default.htm?startat=pt05ch20s02abm17.html.

19. Jia, Liang-Jiu, and Hitoshi Kuwamura. 2014. "Prediction of Cyclic Behaviors of Mild Steel at Large Plastic Strain Using Coupon Test Results." *Journal of Structural Engineering* 140 (2). https://doi.org/10.1061/(asce)st.1943-541x.0000848.

20. Abaqus Theory Manual (V6.6). Accessed August 9, 2022. https://classes.engineering.wustl.edu/2009/spring/mase5513/abaqus/docs/v6.6/books/stm/default.htm?startat=ch04s03ath107.html.

21. Abaqus/CAE User's Guide (6.14). Accessed August 9, 2022. http://wufengyun.com:888/books/usi/default.htm?startat=pt03ch12s09s02.html.

22. Halama, R, M Fusek, M Šofer, Z Poruba, P Matušek, and R Fajkoš. n.d. "Ratcheting Behavior of Class C Wheel Steel and Its Prediction by Modified AbdelKarim-Ohno Model." ORCID. 10th International Conference on Contact Mechanics CM2015, Colorado Springs, Colorado, USA. Accessed December 23, 2022. http://nebula.wsimg.com/69167635dccf61dc4812d2982e567df5?AccessKeyId=810D9ED71AACA9F9CBEB&disposition=0&alloworigin=1.

23. Chaboche, Jean-Louis, Gaerard Cordier, and Ky Dang Van. n.d. In *Modelization of the Strain Memory Effect on the Cyclic Hardening of 316 Stainless Steel: Modaelisation De L'effet De Maemoire De La Daeformation Sur Le Durcissement De L'acier Inoxydable 316*.

24. Ohno, N., and J.-D. Wang. 1993. "Kinematic Hardening Rules with Critical State of Dynamic Recovery, Part I: Formulation and Basic Features for Ratchetting Behavior." *International Journal of Plasticity* 9 (3): 375–90. https://doi.org/10.1016/0749-6419(93)90042-o.

25. Abdel-Karim, M., and N. Ohno. 2000. "Kinematic Hardening Model Suitable for Ratchetting with Steady-State." *International Journal of Plasticity* 16 (3-4): 225–40. https://doi.org/10.1016/s0749-6419(99)00052-2.

26. Lutovinov, Maxim, Radim Halama, Jan Papuga, Michal Bartošák, Jiří Kuželka, and Milan Růžička. 2022. "An Approximate Method for Calculating Elastic–Plastic Stress and Strain on Notched Specimens." *Materials* 15 (4): 1432. https://doi.org/10.3390/ma15041432.

27. De Groot, R., M.C.R.B. Peters, Y.M. De Haan, G.J. Dop, and A.J.M. Plasschaert. 1987. "Failure Stress Criteria for Composite Resin." *Journal of Dental Research* 66 (12): 1748–52. https://doi.org/10.1177/00220345870660121001.

28. Payne, Terry. n.d. "Nonlinear Response of Steel Beams." Google Books. U.S. Department of the Interior, Bureau of Reclamation, Dam Safety Office. Accessed August 8, 2022. https://books.google.com/books/about/Nonlinear_Response_of_Steel_Beams.html?id=Z_T4GgAACAAJ.

29. Brannon, Rebecca. 2014. "Distinction between Uniaxial Stress and Uniaxial Strain." University of Utah CSM Group. December 30, 2014. https://csmbrannon.net/2012/08/02/distinction-between-uniaxial-stress-and-uniaxial-strain/#:~:text=Uniaxial%20stress%20is%20a%20form,components%20of%20strain%20are%20zero.

30. *Studies in Large Plastic Flow and Fracture*. 1964. Harvard University Press.

31. Gromada, Magdalena, Gennady Mishuris, and Andreas Öchsner. n.d. "Correction Formulae for the Stress Distribution in Round Tensile Specimens at Neck Presence." SpringerLink. Springer Berlin Heidelberg. Accessed February 12, 2023. https://link.springer.com/book/10.1007/978-3-642-22134-7.

Chapter 4 : Considering both Plastic-Damage of Concrete and Ductile-Damage of Reinforcing Steel in Finite Element Applications; Verification Problem #2

4.1 Introduction

The basis for the research described in this chapter was Specimen A1.220 from the experimental study by Roy and Sozen in 1964 [1]. The numerical analysis verification of Roy and Sozen's experimental tests is done here for the first time by the author through Finite Element Analysis software (namely, Abaqus). Roy and Sozen were two well-established Structural and Earthquake Engineering scientists at the University of Illinois Urbana-Champaign. The test specimen selected here had an average concrete compressive strength of 3,080 psi and was subjected to uniaxial compression.

- Belarbi and Hsu proposed analytical expressions for concrete in tension for defining the concrete tensile stress based on the concrete tensile strain.
- In 2021, Yafei et al. proposed a model to calculate the concrete ultimate tensile strain.
- Tao et al. proposed an equation to determine the concrete damage parameters to implement the damage model.

The methodologies implemented in this research study are as follows:

- Concrete compressive behavior was defined through the modified Hognestad model.
- Concrete tensile behavior was offered through Belarbi and Hsu model.
- The Damage model was provided by Tao et al..

The modeling and methodologies proposed in this research study are valuable because they provide means to numerically verify experimental test results such as those obtained by Roy and Sozen through mechanical testing. The numerical analysis verification of Roy and Sozen's experimental tests is here being done for the first time by the author through Finite Element Analysis software (namely, Abaqus).

In this research study, the author discussed the state-of-the-art methods that can be used to describe and anticipate the actual behavior of the concrete in tension and compression, which was verified through critical experimental tests by Professor Roy and Sozen. For the behavior of the concrete in tension as well as compression, also concrete damage parameters in tension as well as compression, there are extensive models proposed by different scientists. However, in this research study, the author considered the most accurate models for the behavior of the concrete in tension

(Belarbi and Hsu), as well as in compression (modified Hognestad), and concrete damage parameters (Tao et al.). If the models are not strong and good enough, we cannot get acceptable results from the Finite Element Method analysis software.

This research study demonstrates that the Ramberg-Osgood models, von Mises stress utilization, Chaboche Plasticity model, and in general, steel plasticity model all together could be used in Finite Element software (Abaqus) if and only if they are appropriately utilized based on their descriptions. If so, it will give us acceptable results corresponding to experimental test results. The material model adequately simulated the critical features of steel and all the steel plastic components for various steel hardening, including isotropic hardening, kinematic hardening, Drucker-Prager plasticity (Prager's hardening rule), non-linear isotropic hardening, non-linear kinematic hardening, combined isotropic hardening, kinematic hardening, linear kinematic hardening, Abdel-Karim-Ohno plasticity model, Chaboche kinematic hardening rule, and Ohno-Wang model I (OWI) model behaviors were investigated.

4.2 Specimen Description

Specimen A1.220 is a 5 in.×5 in.×25 in. reinforced concrete prism with transverse and longitudinal reinforcing steel. Four #3 longitudinal bars and #2 transverse rectilinear ties spaced 2 in. apart are contained within the concrete prism.

Figures 4.1 and 4.2 show the specimen isometric 3D view and column cross-section details, respectively. Experimental data from the previous study was unavailable, so a Python code was written to digitize the experimental data from the graphs in Roy and Sozen's paper.

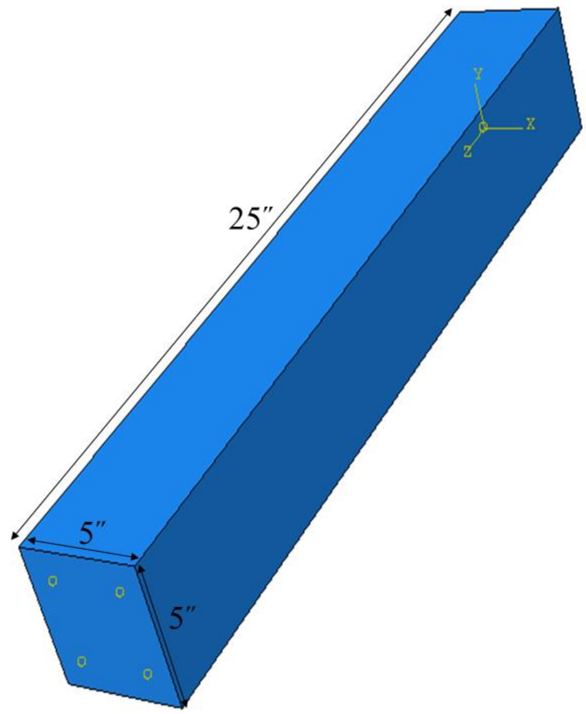

Figure 4.1. Specimen elevation

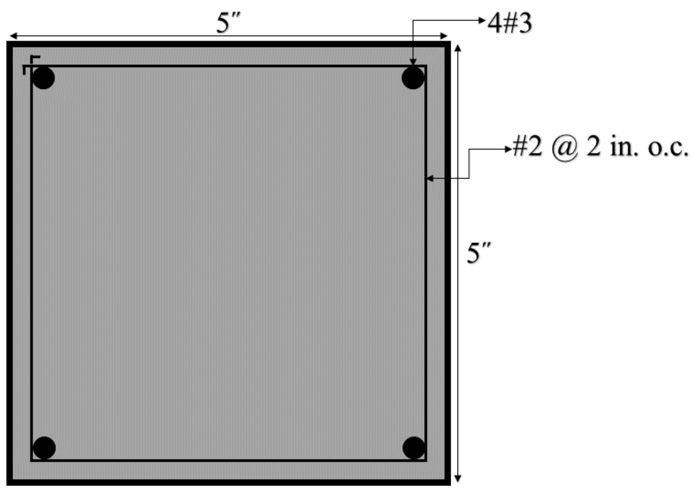

Figure 4.2. Column cross-section details

4.3 Concrete Behavior

4.3.1 Concrete Compressive Behavior

For the purpose of this study, a MATLAB code was written to describe the behavior of concrete with a compressive strength of $f_c^{'} = 3{,}080$ psi (21.23 MPa) in compression based on the modified

Hognestad model described in Section 2.7.1. Table 4.1 shows the stress and strain values for concrete with a compressive strength of $f_c^{'} = 3{,}080$ psi (21.23 MPa).

Table 4.1. Compressive stress-strain values for 3,080 psi (21.23 MPa) concrete

Stress (psi)	Strain	Stress (psi)	Strain
0	0	2,697.1	0.002
340.34	0.0001	2,678.4	0.0021
658.4	0.0002	2,659.7	0.0022
954.17	0.0003	2,641.05	0.0023
1,227.6	0.0004	2,622.3	0.0024
1,478.8	0.0005	2,603.6	0.0025
1,707.8	0.0006	2,584.9	0.0026
1,914.4	0.0007	2,566.2	0.0027
2,098.7	0.0008	2,547.5	0.0028
2,260.8	0.0009	2,528.8	0.0029
2,400.6	0.001	2,510.1	0.003
2,518.1	0.0011	2,491.3	0.0031
2,613.3	0.0012	2,472.6	0.0032
2,686.3	0.0013	2,453.9	0.0033
2,736.9	0.0014	2,435.2	0.0034
2,765.3	0.0015	2,416.5	0.0035
2,772	0.0016	2,397.8	0.0036
2,753.2	0.0017	2,379.1	0.0037
2,734.5	0.0018	2,360.4	0.0038
2,715.8	0.0019		

The corresponding stress-strain curve is illustrated in Figure 4.3.

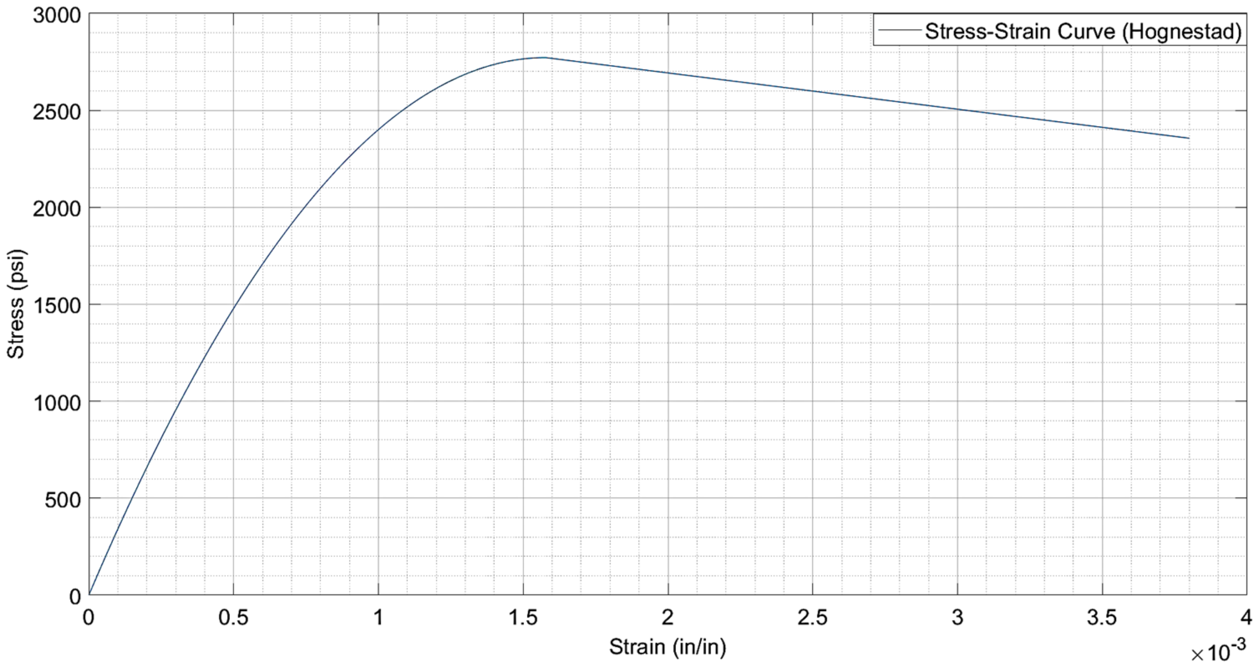

Figure 4.3. Modified Hognestad stress-strain curve for concrete in uniaxial compression

4.3.2 Concrete Tensile Behavior

For this study, the MATLAB code described in Section 2.7.2 was used to represent the behavior of concrete with a compressive strength of $f_c^{'} = 3{,}080$ psi (21.23 MPa) in tension based on the Belarbi and Hsu models. The resulting stress-strain curve is illustrated in Figure 4.4. In Figure 4.4, the curve on the top shows the complete strain-strain curve, while the curve on the bottom represents the initial part of the curve (for strain values ranging from 0 to 0.0012) depicted on a magnified horizontal scale.

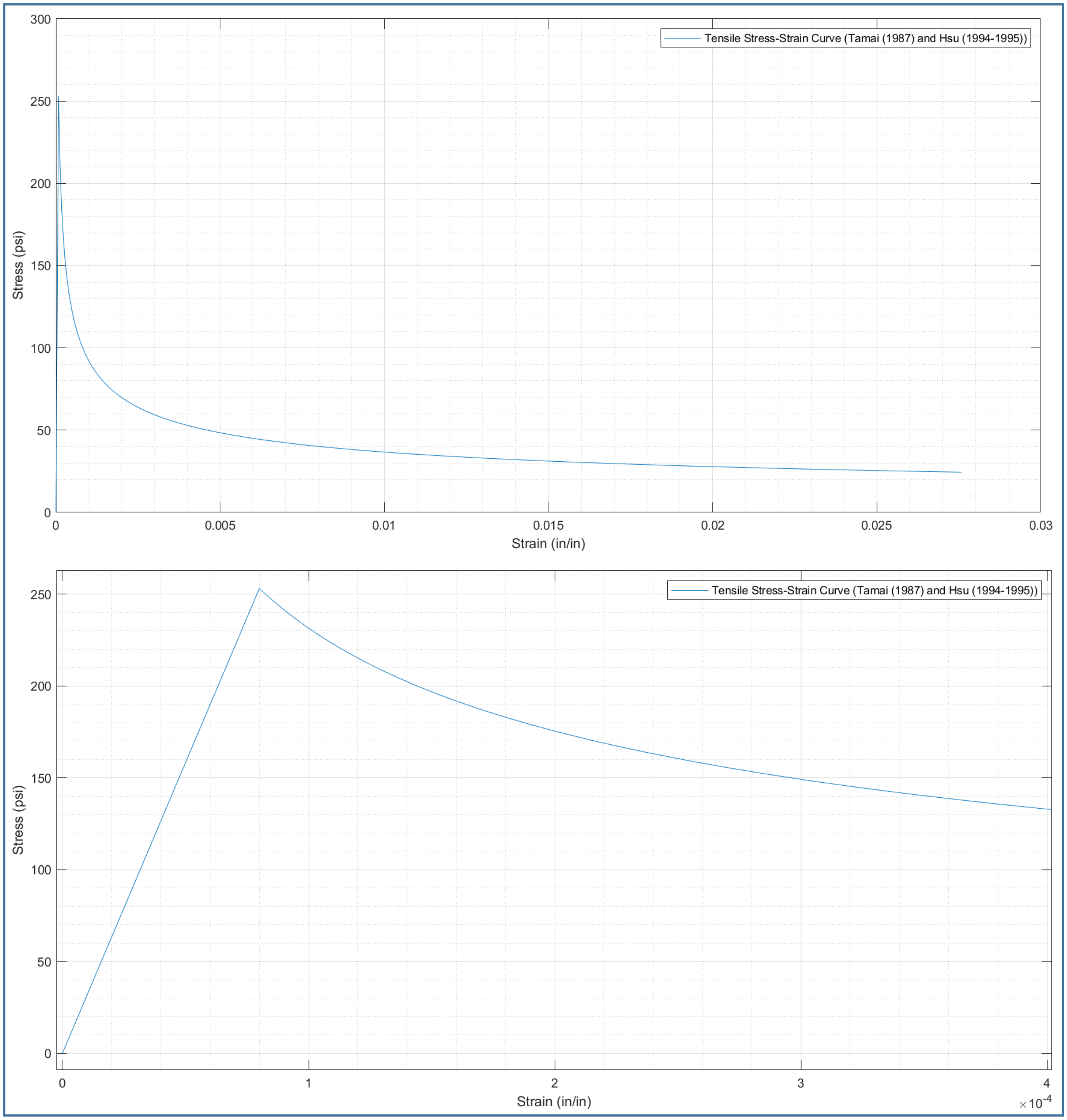

Figure 4.4. Sample tensile stress–strain curve of concrete

4.4 Tension Stiffening Relationship

Table 4.2 shows tensile stress-strain values for concrete in tension with a compressive strength of $f_c^{\prime} = 3{,}080$ psi (21.23 MPa), including yield stresses and cracking strains described in Section 2.9.1.

Table 4.2. Tensile stress-strain values for 3,080 psi concrete

Yield Stress(psi)	Cracking Strain
253.06	0
175.31	0.0001
124.2	0.0002
97.26	0.0003
80.456	0.0004
68.905	0.0005
60.444	0.0006
53.958	0.0007
48.818	0.00079
44.636	0.00089
41.163	0.00099
38.227	0.00109
35.714	0.00119
33.534	0.00129
31.624	0.00139
29.935	0.00149
28.431	0.00159
27.082	0.00169
25.867	0.00179
24.763	0.00189

4.5 Compressive Stress-Strain Relationship

The MATLAB code described in Section 2.9.2 was used to represent the behavior of concrete with a compressive strength of $f_c^{'} = 3{,}080$ psi (21.23 MPa) in compression based on the modified Hognestad model. Table 4.3 shows compressive stress-strain values for concrete in compression with a compressive strength of $f_c^{'} = 3{,}080$ psi (21.23 MPa), including yield stresses and inelastic strains.

Table 4.3. Compressive stress-strain values for 3,080 psi (21.23 MPa) concrete

Yield Stress(psi)	**Inelastic Strain**
762.44	0
1,733.4	0.00034
2,422.8	0.00067
2,833.3	0.00101
3,028.5	0.00135
3,079.9	0.00169
2,995.8	0.00202
2,791.8	0.00236
2,532.05	0.0027
2,260.7	0.00304
2,002.7	0.00337
1,769.3	0.00371
1,563.7	0.00405
1,385.3	0.00438
1,231.4	0.00472
1,099.06	0.00506
985.006	0.0054
886.52	0.00573
801.21	0.00607
727.02	0.00641
662.22	0.00675

4.6 Implementation of the Damage Model

Following the Equations 29 and 30 of Section 2.9.1, and Tao et al. model described in Equations 35-40 of Section 2.10, the developed MATLAB code was used to represent tensile damage of the concrete. Table 4.44 lists the tensile damage behavior of the concrete with a compressive strength of $f_c^{'} = 3{,}080$ psi (21.23 MPa), including damage parameter (d_t) and cracking strain $(\tilde{\varepsilon}_t^{ck})$.

Table 4.4. Tensile damage values for 3,080 psi concrete

Cracking Strain	**Damage Parameter (d_t)**
0	0
0.0001	0.44522
0.0002	0.60695
0.00029	0.69221
0.00039	0.74539
0.00049	0.78194
0.00059	0.80872
0.00069	0.82924
0.00078	0.84551
0.00088	0.85875
0.00098	0.86,974
0.00108	0.87902
0.00118	0.88698
0.00127	0.89388
0.00137	0.89993
0.00147	0.90527
0.00157	0.91003
0.00167	0.91429
0.00176	0.91814
0.00186	0.92163

Figure 4.5 depicts the tensile damage behavior of the concrete with a compressive strength of $f_c' =$ 3,080 psi, including damage parameter (d_t) and cracking strain ($\tilde{\varepsilon}_t^{ck}$) (Equations 29 and 30 of Section 2.9.1, and Equations 35-40 of Section 2.10).

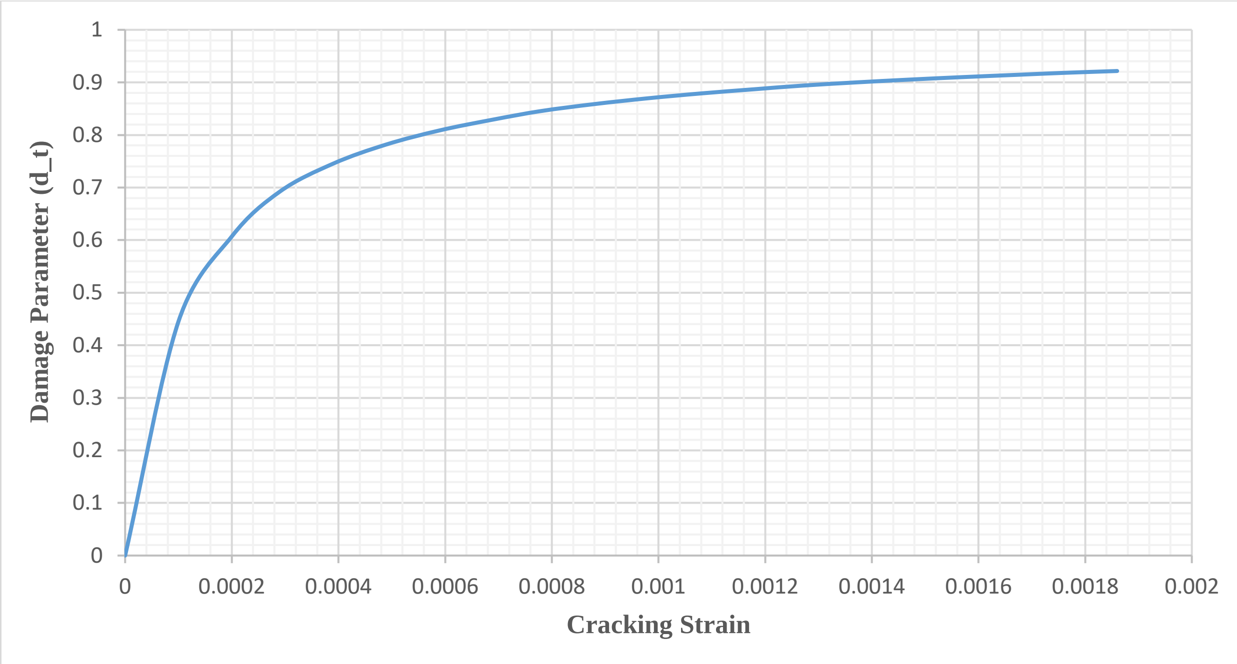

Figure 4.5. Tension damage model for 3,080 psi concrete

Similarly, following the model described earlier in Equations 32 and 33 of Section 2.9.2, the corresponding MATLAB code developed and mentioned earlier in that section was used to represent the compressive damage of the concrete. Table 4.5 lists the compressive damage behavior of the concrete with a compressive strength of $f_c^{'} = 3{,}080$ psi (21.23 MPa), including damage parameter (d_c) and inelastic strain ($\tilde{\varepsilon}_c^{in}$).

Table 4.5. Compressive damage values for 3,080 psi concrete

Inelastic Strain	**Damage Parameter (d_c)**
0	0
0.00034	0
0.00067	0
0.00101	0
0.00135	0
0.00169	0
0.00202	0.02733
0.00236	0.09356
0.0027	0.17791

0.00304	0.266
0.00337	0.34976
0.00371	0.42555
0.00405	0.49228
0.00438	0.5502
0.00472	0.60016
0.00506	0.64316
0.0054	0.68019
0.00573	0.71217
0.00607	0.73986
0.00641	0.76395
0.00675	0.78499

Figure 4.6 shows the compressive damage behavior of the concrete with a compressive strength of $f_c^{'} = 3{,}080$ psi, including damage parameter (d_c) and inelastic strain ($\tilde{\varepsilon}_c^{in}$) (Equations 32 and 33 of Section 2.9.2).

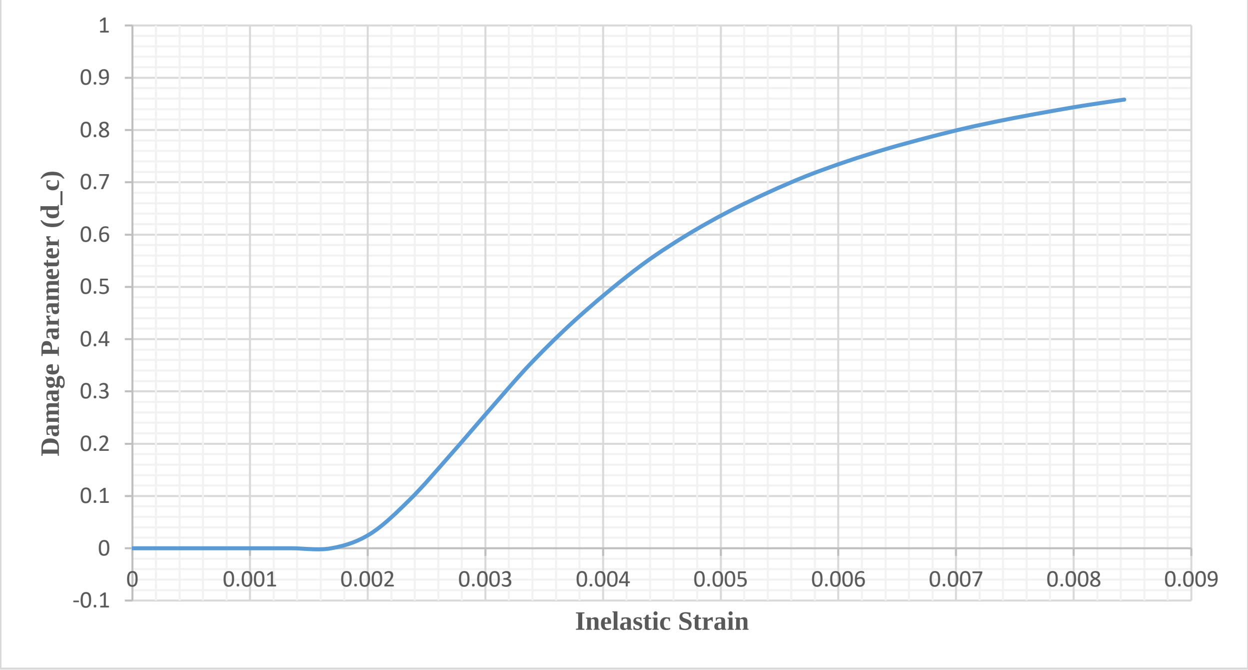

Figure 4.6. Compression damage model for 3,080 psi concrete

4.7 Steel Behavior

4.7.1 Parameters of Steel Stress-Strain Relationship (Mander Model)

4.7.1.1 Longitudinal Steel Bars

The MATLAB code discussed in Section 3.12, was used to determine the behavior of longitudinal steel in tension based on the Mander model. Table 4.6 illustrates the stress-strain values of longitudinal steel with the following case study parameters, Table 4.7 lists the true stress-true strain values, and Table 4.8 gives the values of the true yield stresses and true plastic strains.

ε_y = 0.002

f_y = 50,000 psi

$$\sigma = E.\varepsilon \Rightarrow E = \frac{\sigma}{\varepsilon} \Rightarrow E_s = \frac{\sigma_y}{\varepsilon_y} = \frac{50{,}000}{0.002} = 25 \times 10^6\ psi$$

Interpolation:

$$\begin{cases} f_y = 50 \Rightarrow \varepsilon_{sh} = ? \\ f_y = 48 \Rightarrow \varepsilon_{sh} = 0.015 \\ f_y = 52 \Rightarrow \varepsilon_{sh} = 0.014 \\ \varepsilon_{sh}(50) = 0.015 + (0.014 - 0.015) \cdot \dfrac{50-48}{52-48} = 0.0145 \end{cases}$$

$$\begin{cases} f_y = 50 \Rightarrow E_{sh} = ? \\ f_y = 48 \Rightarrow E_{sh} = 930\ ksi \\ f_y = 52 \Rightarrow E_{sh} = 1{,}200\ ksi \\ E_{sh}(50) = 930 + (1{,}200 - 930) \cdot \dfrac{50-48}{52-48} = 1{,}065\ ksi = 1{,}065 \times 10^3\ psi \end{cases}$$

$$\begin{cases} f_y = 48 \Rightarrow \varepsilon_u = 0.16 \\ f_y = 52 \Rightarrow \varepsilon_u = 0.16 \end{cases} \Rightarrow for\ f_y = 50 \Rightarrow \varepsilon_u = 0.16$$

$$\begin{cases} f_y = 50 \Rightarrow f_u = ? \\ f_y = 48 \Rightarrow f_u = 76\ ksi \\ f_y = 52 \Rightarrow f_u = 78\ ksi \\ f_u(50) = 76 + (78 - 76) \cdot \dfrac{50-48}{52-48} = 77\ ksi = 77 \times 10^3\ psi \end{cases}$$

$$\begin{cases} f_y = 48 \Rightarrow \varepsilon_f = 0.2 \\ f_y = 52 \Rightarrow \varepsilon_f = 0.2 \end{cases} for\ f_y = 50 \Rightarrow \varepsilon_f = 0.2$$

Table 4.6. Tensile stress, strain, plastic strain values for longitudinal steel (Mander)

Stress (psi)	Strain	Plastic Strain
0.024815	0	-9.925E-10

50,040.2	0.01	0.0079983
55,369.8	0.02	0.017785
62,854.9	0.03	0.027485
68,064.8	0.04	0.037277
71,577.1	0.05	0.047136
73,861.9	0.06	0.057045
75,285.8	0.07	0.066988
76,128.0	0.08	0.076954
76,594.8	0.09	0.086936
76,832.6	0.1	0.096926
76,941.07	0.11	0.10692
76,982.6	0.12	0.11692
76,991.8	0.13	0.12692
76,977.5	0.14	0.13692
76,912.5	0.15	0.14692
76,685.05	0.16	0.15693
75,969.7	0.17	0.16696
74,005.5	0.18	0.17703
69,684.7	0.19	0.18721
62,996.7	0.2	0.19748

Table 4.7. Tensile true Stress-true strain values for longitudinal steel (Mander)

True Stress (psi)	True Strain
0.024815	0
50,540.6	0.0099503
56,477.2	0.019802
64,740.5	0.029558
70,787.4	0.03922
75,156.03	0.04879
78,293.6	0.058268
80,555.8	0.067658
82,218.3	0.076961
83,488.3	0.086177
84,515.9	0.095310
85404.5	0.10436
86,220.5	0.11332
87,000.7	0.12221
87,754.4	0.13102
88,449.4	0.13976

88,954.6	0.14842
88,884.6	0.157
87,326.5	0.16551
82,924.9	0.17395
75,596.1	0.18232

Table 4.8. Tensile true stress-true plastic strain values for longitudinal steel (Mander)

True Yield Stress (psi)	True Plastic Strain
43,140.1	0
50,540.6	0.0079287
56,477.2	0.017543
64,740.5	0.026969
70,787.4	0.036389
75,156.03	0.045783
78,293.6	0.055137
80,555.8	0.064436
82,218.3	0.073672
83,488.3	0.082838
84,515.9	0.091929
85,404.5	0.10094
86,220.5	0.10987
87,000.7	0.11873
87,754.4	0.12751
88,449.4	0.13622
88,954.6	0.14486
88,884.6	0.15344
87,326.5	0.16202
82,924.9	0.17063
75,596.1	0.17929

From the results, the true plastic strain is equal to zero at one point, requiring the true stress corresponding to this point for Abaqus as the first point in the table. The MATLAB code (Section 3.12) was used to determine the behavior of steel in tension based on the Mander model, which can find the true stress corresponding to true plastic strain equal to zero.

The stress-strain curve based on the Mander model of longitudinal steel is shown in Figure 4.7.

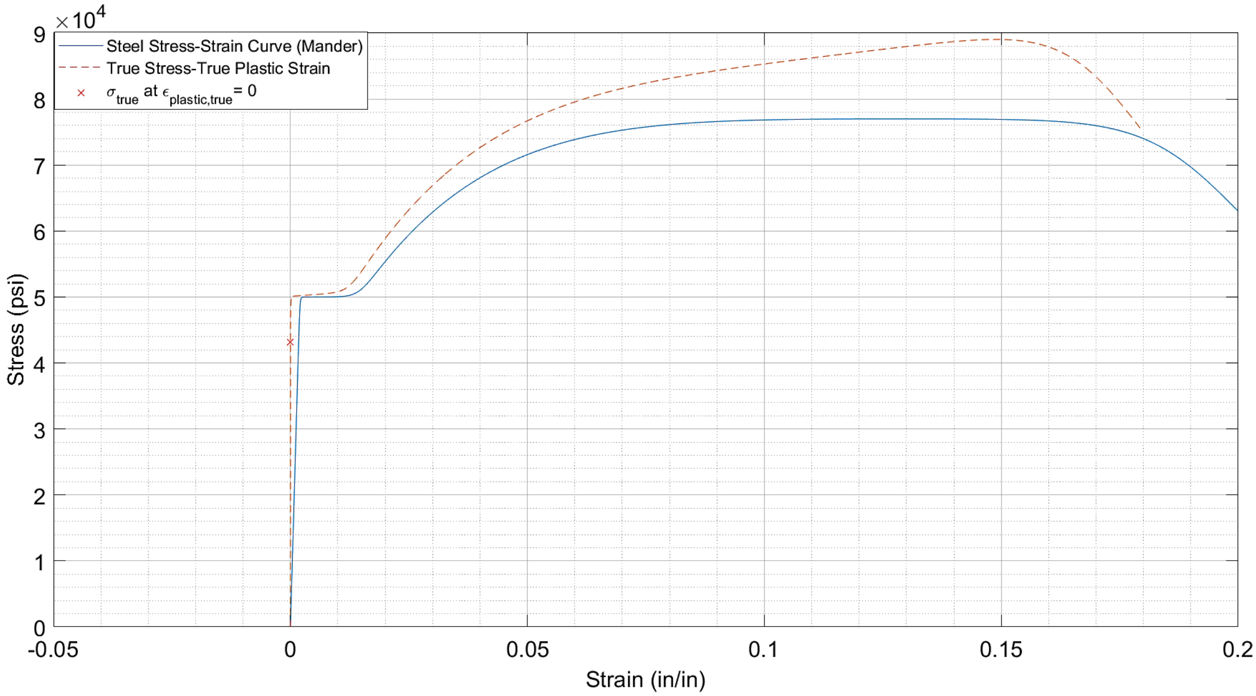

Figure 4.7. Mander stress-strain curve for longitudinal steel in tension

4.7.1.2 Transverse Steel bars

The MATLAB code discussed in Section 3.12 was used to describe the behavior of transverse steel in tension based on the Mander model. Table 4.9 illustrates the stress-strain values of transverse steel with the following case study parameters, while Table 4.10 describes the true stress-true strain, and Table 4.11 gives the values of the true yield stresses and corresponding true plastic strains.

f_y = 72 ksi = 72×10^3 psi

ε_{sh} = 0.009

E_{sh} = 1,200 ksi = 12×10^5 psi

ε_u = 0.1

f_u = 105 ksi = 105×10^3 psi

ε_f = 0.13

E_s = 25×10^6 psi

Table 4.9. Tensile stress, strain, plastic strain values of transverse steel (Mander)

Stress (psi)	Strain	Plastic Strain
3.2086	0	-1.2834E-7

73,803.7	0.01	0.0070478
83,454.2	0.02	0.016661
91,149.5	0.03	0.026354
96,683.6	0.04	0.036132
100,451	0.05	0.045981
102,826	0.06	0.055886
104,160	0.07	0.065833
104,778	0.08	0.075808
104,955	0.09	0.085801
104,816	0.1	0.095807
103,783	0.11	0.10584
98,931.1	0.12	0.11604
86,519.9	0.13	0.12653

Table 4.10. Tensile true stress-true strain values of transverse steel (Mander)

True Stress (psi)	True Strain
3.2086	0
74,541.8	0.0099503
85,123.3	0.019802
93,883.9	0.029558
100,551	0.03922
105,473	0.04879
108,995	0.058268
111,452	0.067658
113,161	0.076961
114,401	0.086177
115,298	0.09531
115,200	0.10436
110,803	0.11332
97,768	0.12221

Table 4.11. Tensile true stress-true plastic strain values of transverse steel (Mander)

True Yield Stress (psi)	True Plastic Strain
63,581.03	0
74,541.8	0.0069686
85,123.3	0.016397
93,883.9	0.025803
100,551.01	0.035198

105,473.5	0.044571
108,995.7	0.053909
111,452.04	0.0632
113,160.8	0.072434
114,401.2	0.081601
115,297.9	0.090698
115,199.9	0.099752
110,802.8	0.10889
97,767.5	0.1183

From the results, the true plastic strain is equal to zero at one point, requiring the true stress corresponding to this point for Abaqus as the first point in the table. The MATLAB code (Section 3.12) was used to determine the behavior of steel in tension based on the Mander model, which can find the true stress corresponding to true plastic strain equal to zero.

The stress-strain curve based on the Mander model of transverse steel is shown in Figure 4.8.

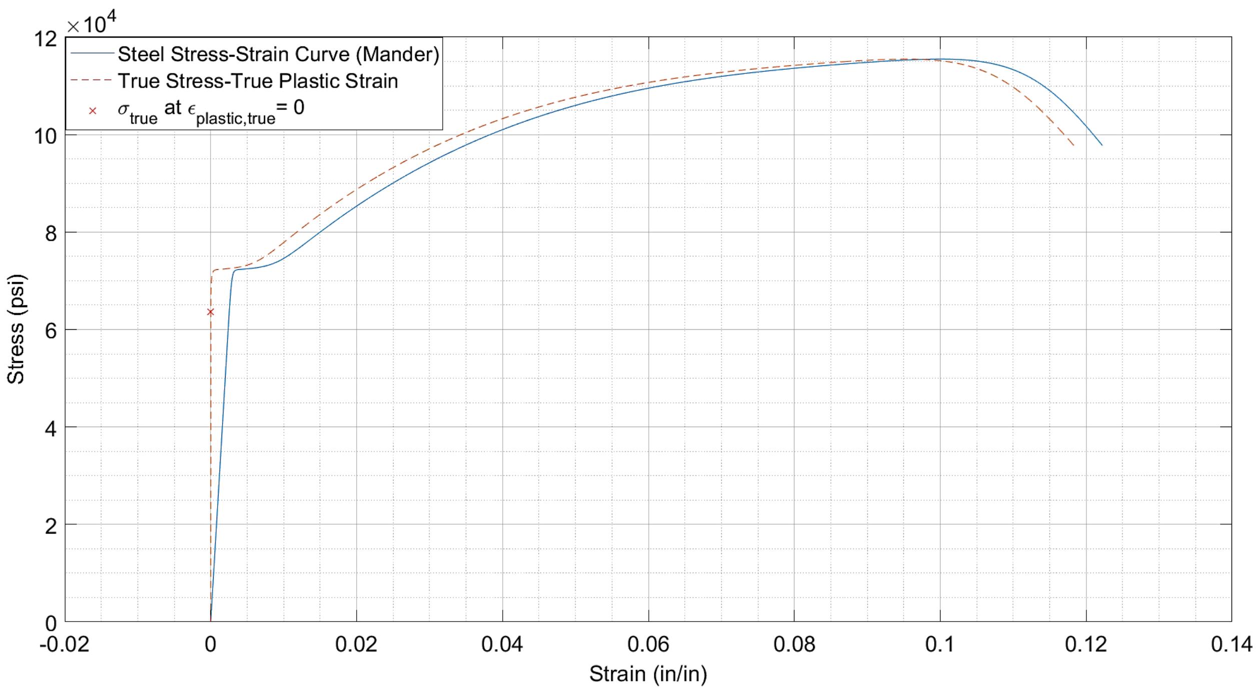

Figure 4.8. Mander stress-strain curve of transverse steel in tension

4.8 Ramberg-Osgood Model

4.8.1 Longitudinal Steel Bars

The MATLAB and Excel codes that were written and presented in Section 3.16.2 were used to determine the behavior of longitudinal steel in tension based on the Ramberg-Osgood model. Table 4.12 illustrates the stress, strain, and plastic strain values of longitudinal steel based on the Ramberg-Osgood model, Table 4.13 lists the true stress-true strain values of longitudinal steel based on the Ramberg-Osgood model, and Table 4.14 gives the values of the true yield stresses and the corresponding true plastic strains.

Table 4.12. Tensile stress, strain, plastic strain values for longitudinal steel (Ramberg-Osgood)

Stress (psi)	Strain	Plastic Strain
0	0	0
5,000	0.0002	4.6933E-14
10,000	0.0004	7.4352E-11
15,000	0.000600005	5.5343E-09
20,000	0.00080011	1.1779E-07
25,000	0.0010012	1.2624E-06
30,000	0.0012087	8.7675E-06
35,000	0.0014451	4.5132E-05
37,720.06	0.0016088	0.0001
40,000	0.0017866	0.0001866
45,000	0.0024526	0.0006526
50,000	0.004	0.002
55,000	0.0077082	0.0055082
60,000	0.016289	0.013889
65,000	0.035123	0.032523
70,000	0.074299	0.071499
75,000	0.15186	0.14886
77,000	0.2	0.19692

Table 4.13. Tensile true stress-true strain values for longitudinal steel (Ramberg-Osgood)

True Stress (psi)	True Strain
0	0
5,001	0.00019998
10,004	0.00039992
15,009	0.00059982

20,016	0.00079979
25,025	0.0010007
30,036.2	0.001208
35,050.5	0.001444
37,780.7	0.0016075
40,071.4	0.001785
45,110.3	0.0024495
50,200	0.003992
55,423.9	0.0076787
60,977.3	0.016158
67,283	0.03452
75,200.9	0.071669
86,390	0.14138
92,400	0.18232

Table 4.14. Tensile true stress-true plastic strain values for longitudinal steel (Ramberg-Osgood)

True Yield Stress (psi)	True Plastic Strain
37,780.7	0
40,071.4	0.00018658
45,110.3	0.00065238
50,200	0.001998
55,423.9	0.0054931
60,977.3	0.013794
67,283	0.032005
75,200.9	0.069059
86,390	0.13877
92,400	0.17975

From the results, the true plastic strain is equal to zero at one point, requiring the true stress corresponding to this point for Abaqus as the first point in the table. A MATLAB code (Section 3.12) was written to show the behavior of steel in tension based on the Ramberg-Osgood model, which finds the true stress corresponding to true plastic strain to be equal to zero.

The engineering and true stress-strain curves of longitudinal steel are illustrated in Figure 4.9.

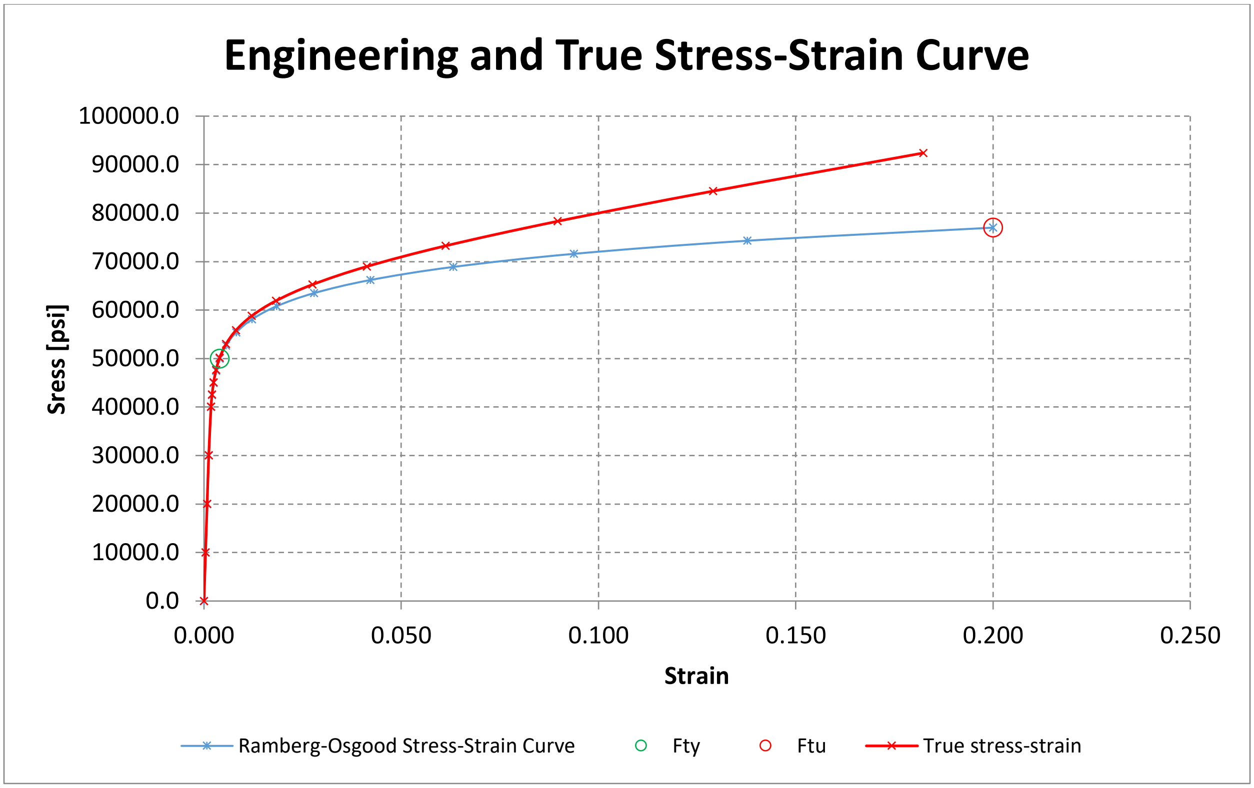

Figure 4.9. Engineering and true stress-strain curves for Ramberg-Osgood model (longitudinal)

The stress-strain curve based on the Ramberg-Osgood model for the longitudinal steel and determined by MATLAB is illustrated in Figure 4.10.

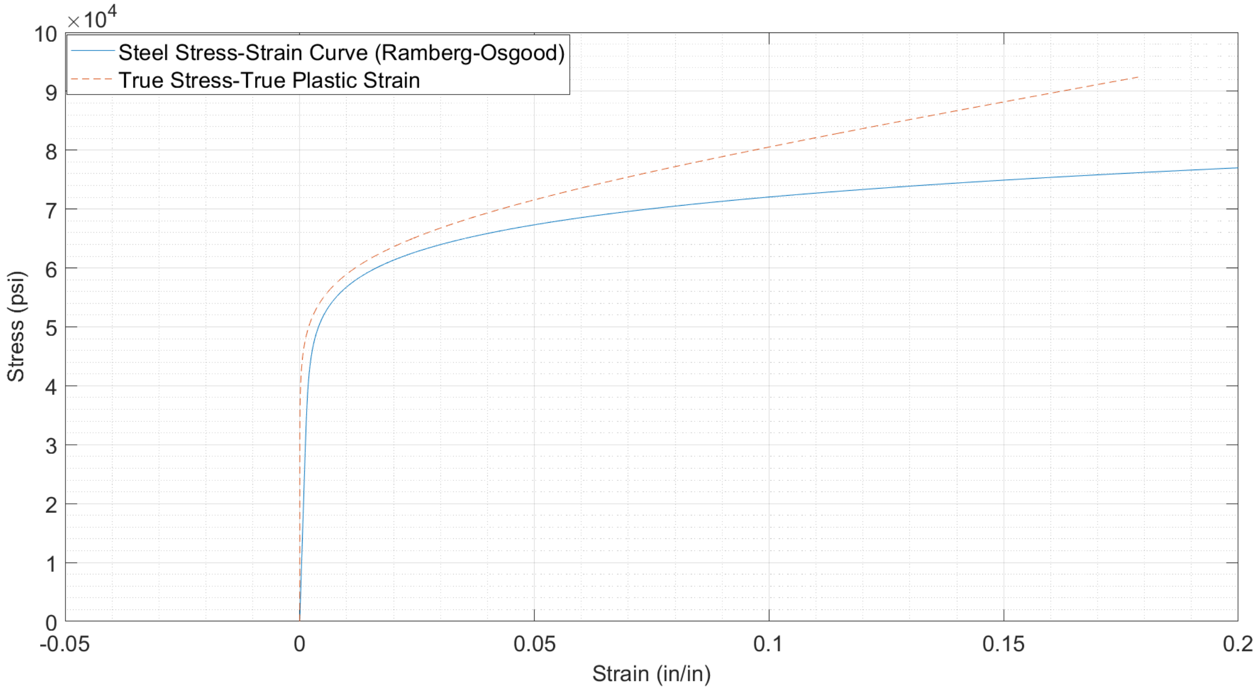

Figure 4.10. Ramberg-Osgood stress-strain curve of the longitudinal steel in tension

4.8.2 Transverse Steel Bars

Table 4.15 lists the stress, strain, and plastic strain values of transverse steel based on the Ramberg-Osgood model, while Table 4.16 lists the true stress-true strain values of transverse steel based on the Ramberg-Osgood model, and Table 4.17 gives the values of the true yield stresses and corresponding true plastic strains.

Table 4.15. Tensile stress, strain, plastic strain values for transverse steel (Ramberg-Osgood)

Stress (psi)	Strain	Plastic Strain
0	0	0
5,000	0.0002	3.8523E-16
10,000	0.0004	7.7646E-13
15,000	0.00060000006	6.6537E-11
20,000	0.000800001	1.565E-09
25,000	0.00100001	1.8125E-08
30,000	0.0012001	1.3411E-07
35,000	0.0014007	7.2834E-07
40,000	0.0016031	3.1543E-06
45,000	0.0018114	1.1492E-05
50,000	0.0020365	3.6533E-05

54,923.7	0.0022993	0.00010243
55,000	0.002304	0.000104
60,000	0.0026703	0.0002703
65,000	0.0032507	0.00065079
70,000	0.004268	0.001468
72,000	0.00488	0.002
75,000	0.0061306	0.0031306
80000	0.0095578	0.0063578
85,000	0.015768	0.012368
90,000	0.026763	0.023163
95,000	0.045733	0.041933
100,000	0.077635	0.073635
105,000	0.13	0.1258

Table 4.16. Tensile true stress-true strain values for transverse steel (Ramberg-Osgood)

True Stress (psi)	True Strain
0	0
5,001	0.00019998
10,004	0.00039992
15,009	0.00059982
20,016	0.00079968
25,025	0.00099951
30,036	0.0011994
35,049	0.0013997
40,064.1	0.0016018
45,081.5	0.0018098
50,101.8	0.0020344
55,049.9	0.0022967
55,126.7	0.0023013
60,160.2	0.0026667
65,211.3	0.0032455
70,298.7	0.0042589
72,351.3	0.0048681
75,459.8	0.0061119
80,764.6	0.0095124
86,340.3	0.015645
92,408.7	0.026411
99,344.6	0.044718
107,763	0.074769

118,650	0.12221

Table 4.17. Tensile true stress-true plastic strain values for transverse steel (Ramberg-Osgood)

True Yield Stress (psi)	True Plastic Strain
55,049.9	0
55,126.7	0.000104
60,160.2	0.00027027
65,211.3	0.00065058
70,298.7	0.0014669
72,351.3	0.001998
75,459.8	0.0031257
80,764.6	0.0063376
86,340.3	0.012292
92,408.7	0.022899
99,344.6	0.041077
107,763	0.07105
118,650	0.11849

From the results, the true plastic strain is equal to zero at one point, requiring the true stress corresponding to this point for Abaqus as the first point in the table. A MATLAB code (Section 3.12) was written to show the behavior of steel in tension based on the Ramberg-Osgood model, which finds the true stress corresponding to true plastic strain to be equal to zero.

The engineering and true stress-strain curves of transverse steel are illustrated in Figure 4.11.

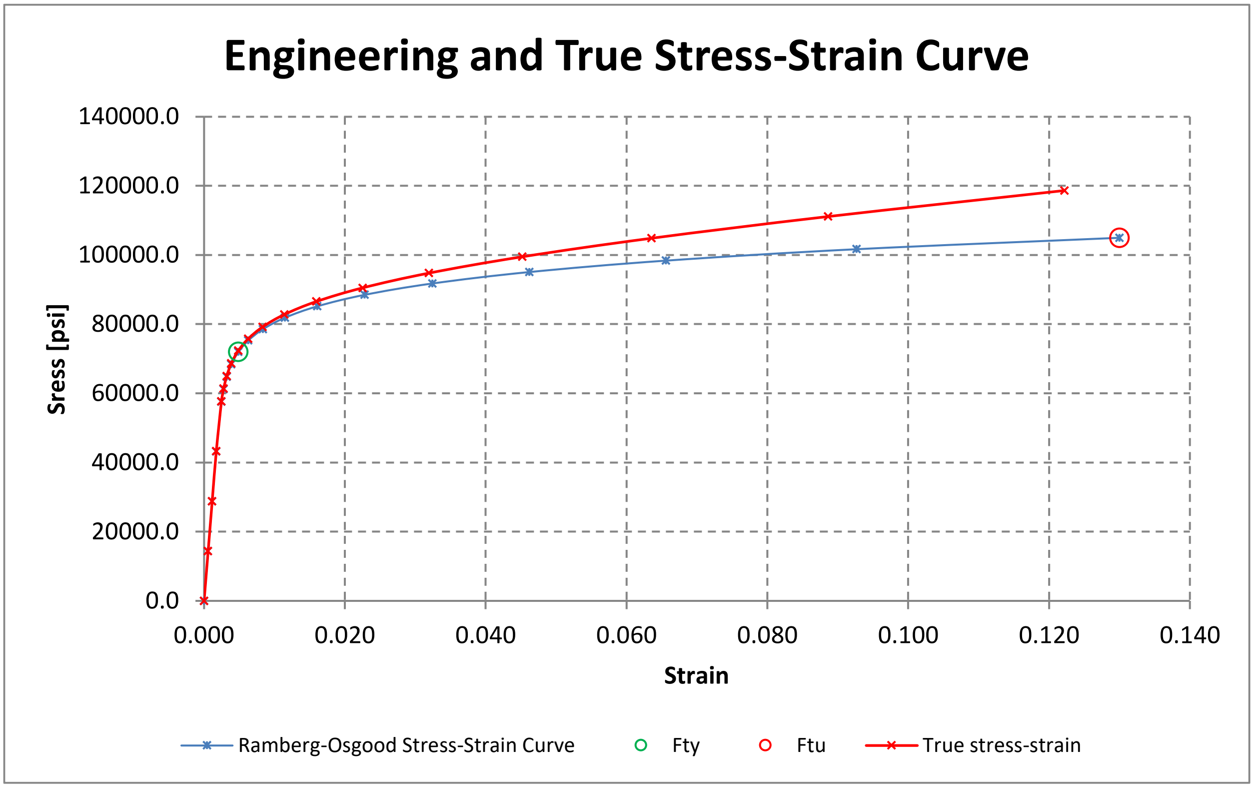

Figure 4.11. Engineering and true stress-strain curves for Ramberg-Osgood model (transverse)

The stress-strain curve based on the Ramberg-Osgood model for the transverse steel and determined by MATLAB is illustrated in Figure 4.12.

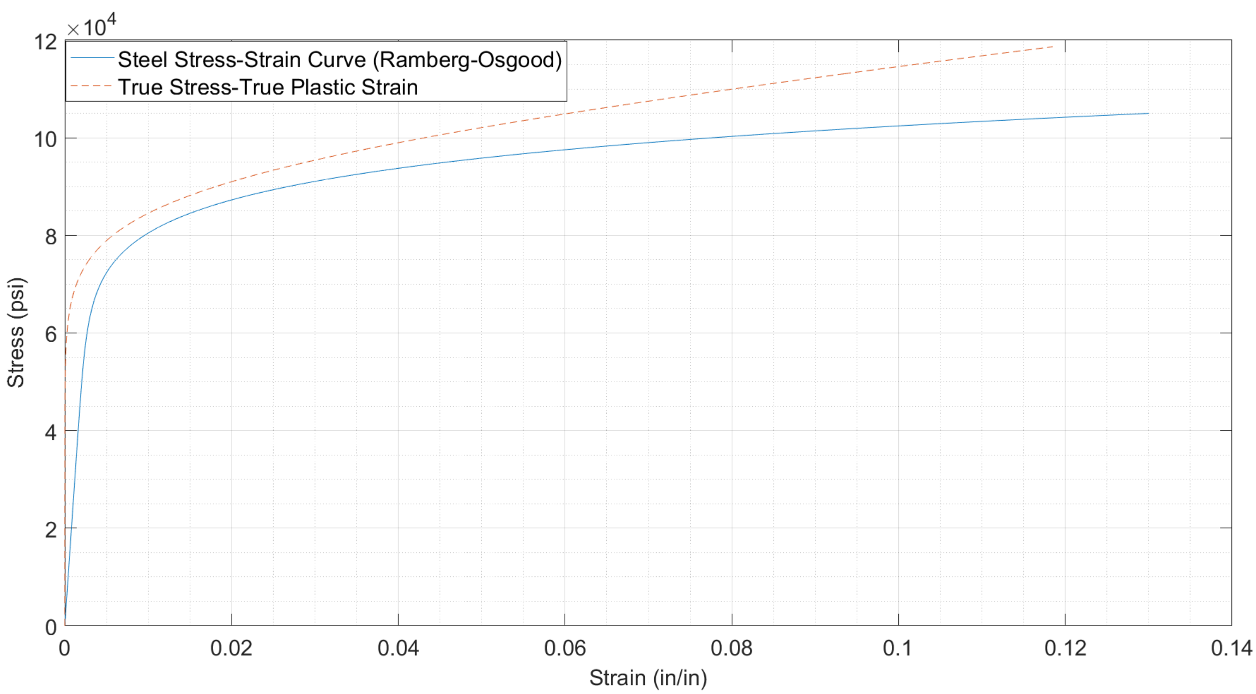

Figure 4.12. Ramberg-Osgood stress-strain curve of the longitudinal steel in tension

4.9 Linear Hardening

4.9.1 Linear kinematic hardening model

Abaqus requires just two data pairs to establish this linear behavior.

$$C = \frac{\sigma - \sigma|_0}{\varepsilon^{pl}} \tag{1}$$

$\sigma|_0$: yield stress at zero plastic strain

σ: yield stress

ε^{pl}: plastic strain at yield stress

C: linear kinematic hardening modulus

Longitudinal steel:

$\sigma = \sigma_y = 50{,}000\ psi$

The elastic limit can be chosen as the stress calculated by the Ramberg-Osgood equation for 0.0001 axial plastic strain. Therefore, we have:

$\varepsilon_{plastic} = 0.0001$

In the Ramberg-Osgood equation:

$$\varepsilon = \frac{\sigma}{E} + 0.002\left(\frac{\sigma}{F_{ty}}\right)^n$$

$$\varepsilon_{total} = \varepsilon_{elastic} + \varepsilon_{plastic} \Rightarrow \frac{\sigma}{E} + 0.0001 = \frac{\sigma}{E} + 0.002\left(\frac{\sigma}{F_{ty}}\right)^n \Rightarrow 0.002\left(\frac{\sigma}{F_{ty}}\right)^n = 0.0001$$

A MATLAB code was written to solve and evaluate the elastic limit stress.

$Elastic\ limit\ stress = 37{,}776.9\ psi = \sigma|_0$

$\varepsilon^{pl} = 0.002$

$$C = \frac{50{,}000 - 37{,}776.9}{0.002} = 6{,}111{,}510\ psi$$

Transverse steel:

$\sigma = \sigma_y = 72{,}000\ psi$

A MATLAB code was written to solve and evaluate the elastic limit stress.

$Elastic\ limit\ stress = 54{,}923.7\ psi = \sigma|_0$

$\varepsilon^{pl} = 0.002$

$$C = \frac{72{,}000 - 54{,}923.7}{0.002} = 8{,}538{,}150\ psi$$

4.10 Prager's Hardening Rule

$$C_0 = \frac{\sigma_u - \sigma_{y0}}{\varepsilon_{u,eq}} \quad (2)$$

C_0: material parameter of Prager's hardening rule

σ_u: true stress at the tensile strength

$\varepsilon_{u,eq}$: plastic strain at σ_u

σ_{y0}: initial yield stress

$$\sigma_{true} = \sigma(1 + \varepsilon) \quad (3)$$

Longitudinal steel:

$\sigma_y = \sigma_{y0} = \sigma_0 = 50{,}000\ psi$

$f_u = 77{,}000\ psi$

$\varepsilon_u = 0.16$

$\sigma_{true} = \sigma_u = 77{,}000(1 + 0.16) = 89{,}320\ psi$

Based on the Ramberg-Osgood model's MATLAB code:

$\varepsilon_{u,eq} = 0.15692$

$$C_0 = \frac{89{,}320 - 50{,}000}{0.15692} = 250{,}573\ psi$$

Transverse steel:

$\sigma_y = \sigma_{y0} = \sigma_0 = 72{,}000\ psi$

f_u = 105,000 psi

ε_u = 0.1

$\sigma_{true} = \sigma_u = 105{,}000(1 + 0.1) = 115{,}500\ psi$

$\varepsilon_{u,eq} = 0.0958$

$$C_0 = \frac{115{,}500 - 72{,}000}{0.0958} = 454{,}071\ psi$$

4.11 Abdel-Karim and Ohno Plasticity Model

This case study uses the kinematic hardening rule presented in Section 3.15, in accordance with the Abdel-Karim and Ohno (AKO) cyclic plasticity model, resulting in a calibrated AKO model.

The chosen points of the cyclic stress-strain curve specify the values of the fundamental material properties directly (C_i, γ_i) by the following relations:

$$C_i = \frac{\sigma_{a(i)} - \sigma_{a(i-1)}}{\varepsilon_{ap(i)} - \varepsilon_{ap(i-1)}} - \frac{\sigma_{a(i+1)} - \sigma_{a(i)}}{\varepsilon_{ap(i+1)} - \varepsilon_{ap(i)}} \ for\ i \neq M \tag{4}$$

$$C_M = \frac{\sigma_{a(M)} - \sigma_{a(M-1)}}{\varepsilon_{ap(M)} - \varepsilon_{ap(M-1)}} \tag{5}$$

$$\gamma_i = \frac{1}{\varepsilon_{ap(i)}} \ for\ all\ i \tag{6}$$

C_i, γ_i: parameters of plasticity model

$\sigma_{a(i)}$: stress amplitude of the given *i*-th point

$\varepsilon_{ap(i)}$: plastic strain amplitude of the given *i*-th point

M: number of backstresses

The number of pairs of C_i and γ_i will provide the number of backstresses.

Longitudinal steel:

For calculating the C_i and γ_i values, the first point of consideration is the elastic limit, which is the stress corresponding to zero plastic strain. Nowadays, the tracking of yield surface is done experimentally with 100 με offset of plastic strain or less. Thus, the elastic limit can be chosen as the stress calculated by the Ramberg-Osgood equation for 0.0001 axial plastic strain. Therefore, we have:

$$\varepsilon_{plastic} = 0.0001$$

In the Ramberg-Osgood equation:

$$\varepsilon = \frac{\sigma}{E} + 0.002\left(\frac{\sigma}{F_{ty}}\right)^n$$

$$\varepsilon_{total} = \varepsilon_{elastic} + \varepsilon_{plastic} \Rightarrow \frac{\sigma}{E} + 0.0001 = \frac{\sigma}{E} + 0.002\left(\frac{\sigma}{F_{ty}}\right)^n \Rightarrow 0.002\left(\frac{\sigma}{F_{ty}}\right)^n = 0.0001$$

A MATLAB code was written to solve and evaluate the elastic limit stress.

Elastic limit stress = 37,720.06 psi

The second point should be the yielding point. The resulting C_i and γ_i values are shown in Tables 4.18 and 4.19.

Table 4.18. C_i values in psi unit for longitudinal steel based on the Ramberg-Osgood model after modification

C_1	4,721,200

C_2	825,613
C_3	322,773
C_4	132,553
C_5	53,197.4
C_6	13,818.4
$C_M = C_7$	146,674

Table 4.19. γ_i values for the longitudinal steel based on the Ramberg-Osgood model after modification

γ_1	500.49
γ_2	182.04
γ_3	72.495
γ_4	31.244
γ_5	14.48
γ_6	7.2058
γ_7	5.5632

Transverse steel:

Similar to the case of longitudinal steel, to calculate the C_i and γ_i values, the first point of consideration is the elastic limit, which is the stress corresponding to zero plastic strain. A MATLAB code was written to evaluate the elastic limit stress. The second point should be the yielding point. The resulting C_i and γ_i values are illustrated in Tables 4.20 and 4.21.

Table 4.20. C_i values in psi unit for transverse steel based on the Ramberg-Osgood model after modification

C_1	5,903,087.3
C_2	1,104,631.2
C_3	715,308.03
C_4	364,176.1
C_5	190,578.5
C_6	100,660.2
C_7	51,424.9
$C_M = C_8$	229,461.7

Table 4.21. γ_i values for transverse steel based on the Ramberg-Osgood model after modification

γ_1	500.49

γ_2	319.91
γ_3	157.78
γ_4	81.348
γ_5	43.669
γ_6	24.343
γ_7	14.074
γ_8	8.4392

4.12 Chaboche kinematic hardening rule

For pure monotonic tension, we have:

$$\sigma = \sigma_Y + \alpha = \sigma_Y + \sum_{i=1}^{M} \frac{C_i}{\gamma_i}(1 - e^{-\gamma_i . \varepsilon_p}) \tag{7}$$

M: number of backstresses

α: backstress

ε_p: plastic strain

σ: Chaboche analytical stress

For the longitudinal steel, based on the Ramberg-Osgood model and Chaboche kinematic hardening rule for pure monotonic tension, the values of α and σ were calculated in MATLAB and are depicted in Table 4.22.

Table 4.22. Chaboche α and σ values

Alpha Chaboche	Chaboche Analytical True Stress (psi)
0	37,776.9
8,626.3	46,403.3
14,976.8	52,753.7
20,684.5	58,461.5
26,709.2	64,486.1
33,627.2	71,404.1
41,183.2	78,960.2
44,107.5	81,884.5

For the transverse steel, based on the Ramberg-Osgood model and Chaboche kinematic hardening rule for pure monotonic tension, the values of α and σ were calculated in MATLAB and are illustrated in Table 4.23.

Table 4.23. Chaboche α and σ values

Alpha Chaboche	Chaboche Analytical True Stress (psi)
0	54,923.7
12,100.4	67,024.1
16,004.6	70,928.3
22,341.4	77,265.1
28,008	82,931.7
33,748.1	88,671.8
39,913.8	94,837.5
46,384.7	101,308
52,652	107,576

A MATLAB code was utilized for the longitudinal steel to calculate the Chaboche true plastic strain and the Chaboche true stress values, as illustrated in Table 4.24.

Table 4.24. Chaboche true plastic strain and Chaboche true stress of longitudinal steel

Chaboche True Plastic Strain	Chaboche True Stress (psi)
0	37,780.7
0.001998	50,200
0.0054931	55,423.9
0.013794	60,977.3
0.032005	67,283
0.069059	75,200.9
0.13877	86,390
0.17975	92,400

A MATLAB code was utilized for the transverse steel to calculate the Chaboche true plastic strain and the Chaboche true stress values, as illustrated in Table 4.25.

Table 4.25. Chaboche true plastic strain and Chaboche true stress of transverse steel

Chaboche True Plastic Strain	Chaboche True Stress (psi)
0	55,049.9
0.001998	72,351.3

0.0031257	75,459.8
0.0063376	80,764.6
0.012292	86,340.3
0.022899	92,408.7
0.041077	99,344.6
0.07105	107,764
0.11849	118,650

Table 4.26 lists the values of the Chaboche analytical true stress (in psi) and Chaboche true plastic strain, and Figure 4.13 depicts the resulting Chaboche model for longitudinal steel.

Table 4.26. Chaboche true plastic strain and Chaboche analytical true stress (in psi) for the longitudinal steel

Chaboche True Plastic Strain	Chaboche Analytical True Stress (psi)
0	37,776.9
0.001998	46,403.3
0.0054931	52,753.7
0.013794	58,461.5
0.032005	64,486.1
0.069059	71,404.1
0.13877	78,960.2
0.17975	81,884.5

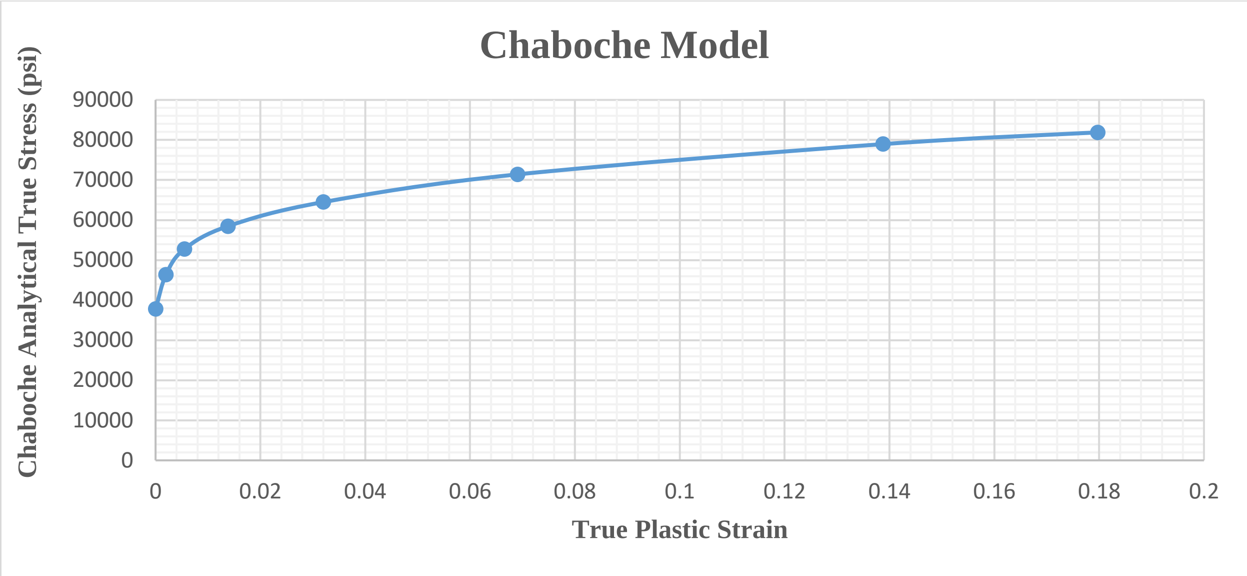

Figure 4.13. Chaboche model for the longitudinal steel

Table 4.27 lists the values of the Chaboche analytical true stress (in psi) and Chaboche true plastic strain, and Figure 4.14 depicts the Chaboche model for transverse steel.

Table 4.27. Chaboche true plastic strain and Chaboche analytical true stress (in psi) of the transverse steel

Chaboche True Plastic Strain	Chaboche Analytical True Stress (psi)
0	54,923.7
0.001998	67,024.1
0.0031257	70,928.3
0.0063376	77,265.1
0.012292	82,931.7
0.022899	88,671.8
0.041077	94,837.5
0.07105	101,308
0.11849	107,576

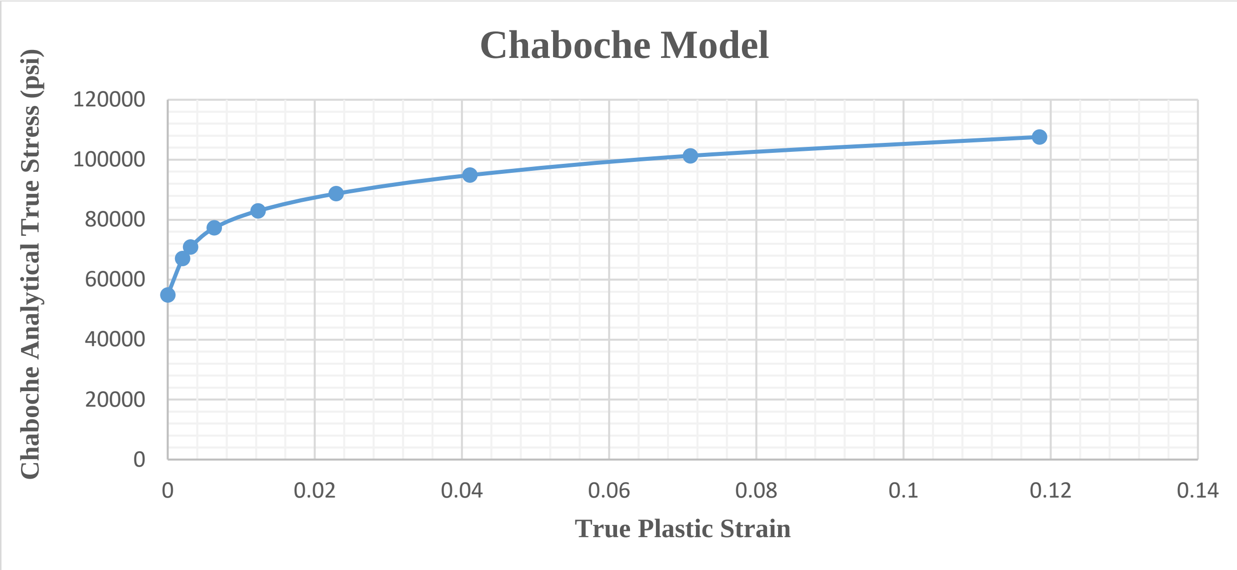

Figure 4.14. Chaboche model for the transverse steel

4.13 Ohno-Wang model I (OWI)

For the OWI diagram, the values of the true stress versus true plastic strain are needed. These are calculated as described in Chapter 3.17. Figure 4.15 illustrates the Ohno and Wang I (OWI) model for the longitudinal steel.

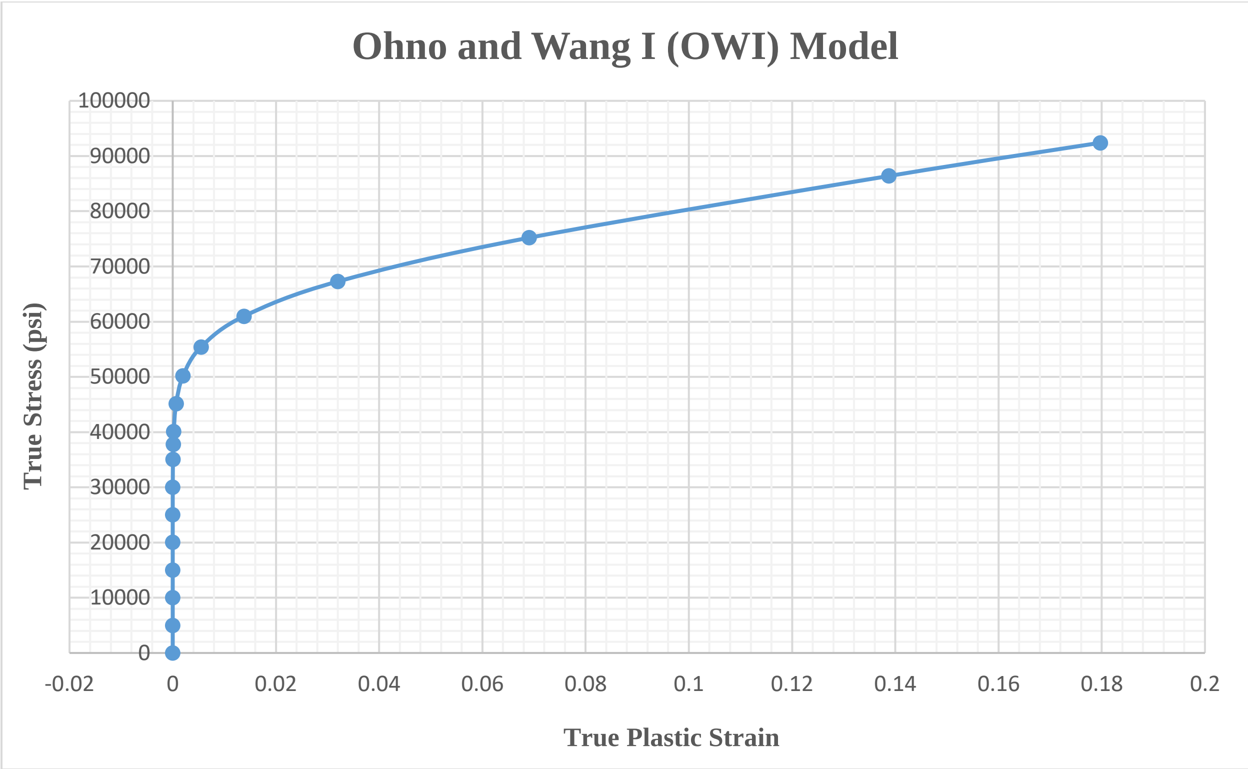

Figure 4.15. Ohno and Wang I (OWI) model for the longitudinal steel

Figure 4.16 depicts the Ohno and Wang I (OWI) model for the transverse steel.

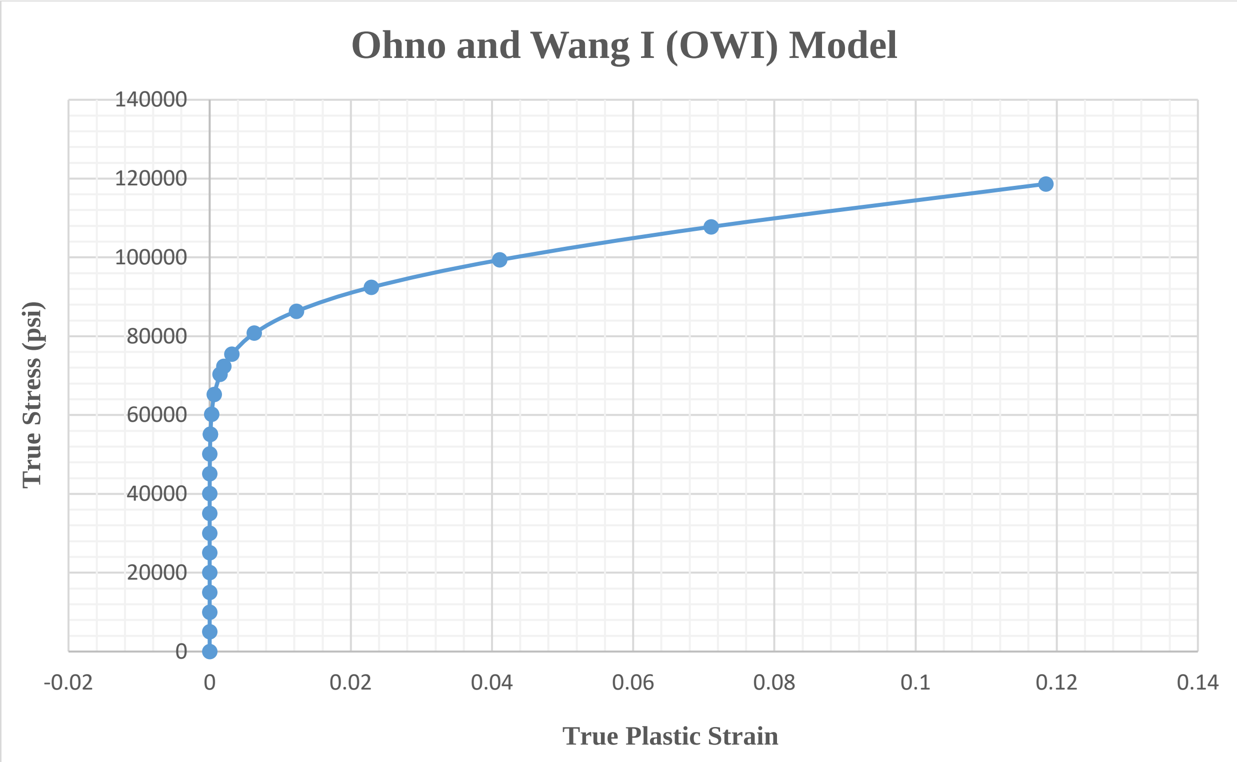

Figure 4.16. Ohno and Wang I (OWI) Model for the transverse steel

4.14 Chaboche model and Ohno-Wang model I (OWI) comparison

Figure 4.17 compares the Chaboche and Ohno-Wang model I (OWI) for the longitudinal steel.

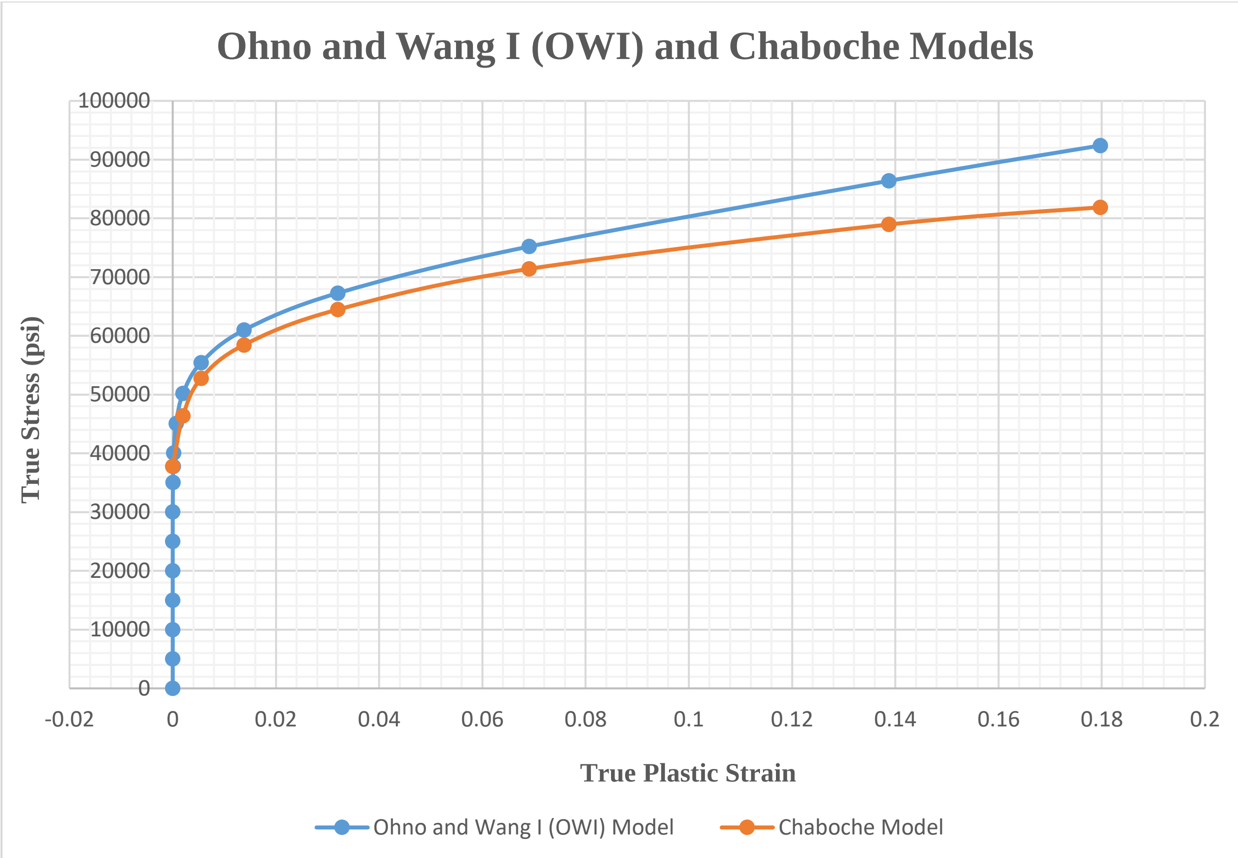

Figure 4.17. Chaboche and Ohno-Wang model I (OWI) of the longitudinal steel comparison

Figure 4.18 compares the Chaboche and Ohno-Wang model I (OWI) for the transverse steel.

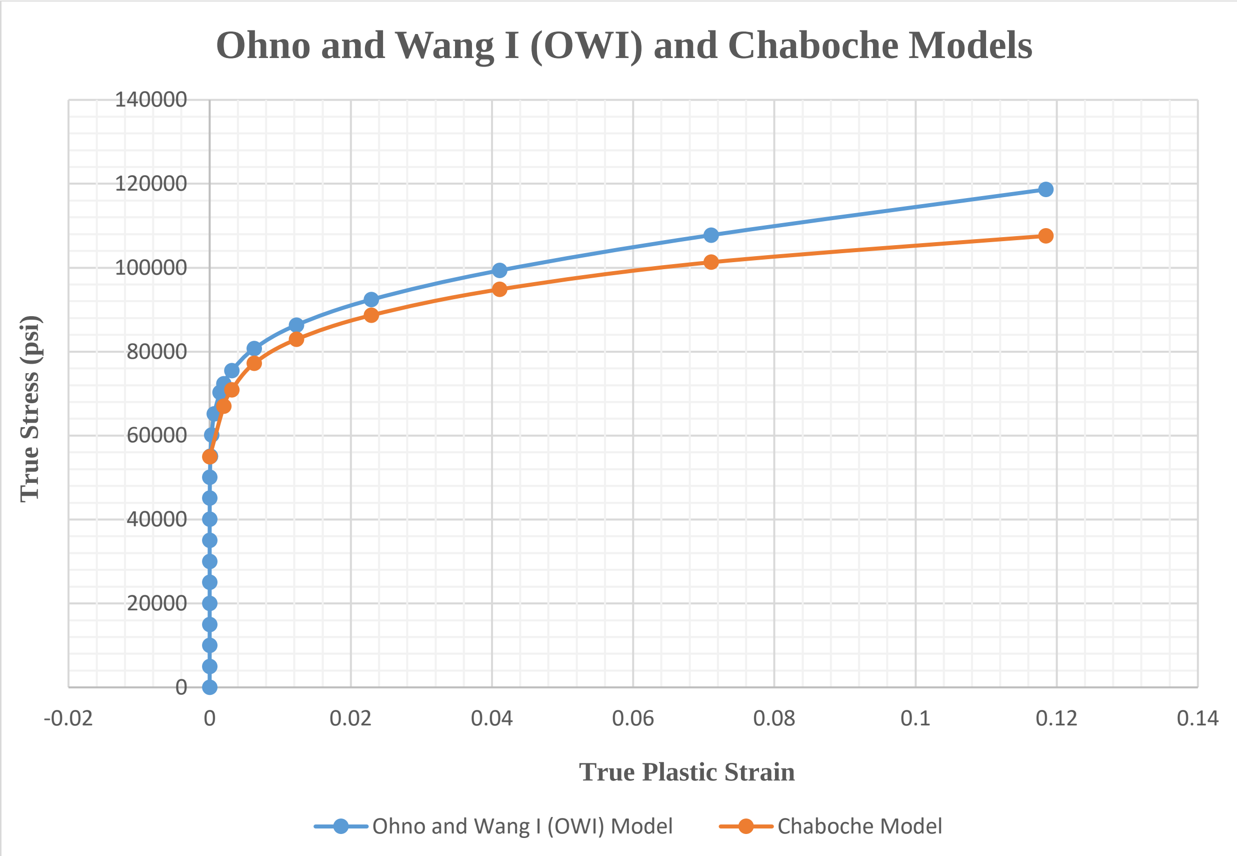

Figure 4.18. Chaboche and Ohno-Wang model I (OWI) of the transverse steel comparison

Figures 4.17 and 4.18 elucidate an excellent concordance between Chaboche and Ohno-Wang model I (OWI) results. The models produce strikingly similar results.

4.15 von Mises stress

Following the procedure described in Section 3.19, the following is determined.

Longitudinal steel:

$\sigma_y = \sigma_Y = \sigma_1 = 50{,}000$ psi

$\sigma_2 = \sigma_3 = 0$

$$J_{2'} = -\frac{1}{3}[\sigma_1{}^2] = -\frac{1}{3}(50{,}000^2) = -833{,}333{,}000\ psi^2$$

$$\mathrm{p} = \frac{3}{\sigma_Y{}^2} = \frac{3}{50{,}000^2} = 12 \times 10^{-10}$$

$$\sigma_{eq1} = \sigma_Y = 50{,}000\ psi$$

$$\sigma_{eq} = |\sigma|$$

$\varepsilon_{eq} = |\varepsilon_{11}^{p}|$

$\phi = \frac{3}{2} \cdot \frac{\varepsilon_{eq}}{\sigma_{eq}}$

Transverse steel:

$\sigma_y = \sigma_Y = \sigma_1 = 72{,}000$ psi

$\sigma_2 = \sigma_3 = 0$

$J_{2'} = -\frac{1}{3}[\sigma_1{}^2] = -\frac{1}{3}(72{,}000^2) = -1{,}728 \times 10^6\ psi^2$

$\mathrm{p} = \frac{3}{\sigma_Y{}^2} = \frac{3}{72{,}000^2} = 5.787 \times 10^{-10}$

$\sigma_{eq1} = \sigma_Y = 72{,}000\ psi$

Table 4.28 shows the values of the required parameters based on the Ramberg-Osgood model resulting from the MATLAB code implemented for longitudinal steel.

Table 4.28. Parameters of longitudinal steel for Ramberg-Osgood's model (evaluated via a MATLAB code)

σ_{eq}	ε_{eq}	ϕ
0	0	
5,000	4.6933E-14	1.408E-17
10,000	7.4352E-11	1.1152E-14
15,000	5.5343E-09	5.5343E-13
20,000	1.1779E-07	8.8342E-12
25,000	1.2624E-06	7.5747E-11
30,000	8.7675E-06	4.3837E-10
35,000	4.5132E-05	1.9342E-09
37,720	0.0001	3.9766E-09
40,000	0.0001866	6.9976E-09
45,000	0.0006526	2.1753E-08
50,000	0.002	6E-08
55,000	0.0055082	1.5022E-07
60,000	0.013889	3.4724E-07
65,000	0.032523	7.5053E-07
70,000	0.071499	1.5321E-06
75,000	0.14886	2.9773E-06
77,000	0.19692	3.8361E-06

Table 4.29 shows the values of the required parameters based on the Ramberg-Osgood model resulting from the corresponding MATLAB code for the transverse steel.

Table 4.29. Parameters of transverse steel for Ramberg-Osgood's model (evaluated via a MATLAB code)

σ_{eq}	ε_{eq}	ϕ
0	0	
5,000	3.8523E-16	1.1556E-19
10,000	7.7646E-13	1.1646E-16
15,000	6.6537E-11	6.6537E-15
20,000	1.565E-09	1.1737E-13
25,000	1.8125E-08	1.0875E-12
30,000	1.3411E-07	6.7055E-12
35,000	7.2834E-07	3.1214E-11
40,000	3.1543E-06	1.1828E-10
45,000	1.1492E-05	3.8308E-10
50,000	3.6533E-05	1.096E-09
54,923.7	0.00010243	2.7975E-09
55,000	0.000104	2.8365E-09
60,000	0.0002703	6.7577E-09
65,000	0.00065079	1.5018E-08
70,000	0.001468	3.1457E-08
72,000	0.002	4.1666E-08
75,000	0.0031306	6.2613E-08
80,000	0.0063578	1.192E-07
85,000	0.012368	2.1826E-07
90,000	0.023163	3.8606E-07
95,000	0.041933	6.621E-07
100,000	0.073635	1.1045E-06
105,000	0.1258	1.7971E-06

4.16 Material Properties

Material properties for steel and concrete included:

- **Steel**
  - *Density*

$$\rho_s = 0.282\ \frac{lb}{in^3}$$

$$g\frac{m}{s^2} = 386.08\frac{in}{s^2} \Longrightarrow Mass\ Density = \frac{0.282\frac{lb}{in^3}}{386.08\frac{in}{s^2}} = 0.0007304\frac{lbf.s^2}{in^4}$$

  - *Elastic properties*

$$E_s = 25 \times 10^6\ psi$$

$$\upsilon_s = 0.29$$

- **Concrete**

$f_c^{'}$ = 3,080 psi

f_r = 320 psi

  - *Density*

$$\rho_c = 142.37\ \frac{lb}{ft^3} \Longrightarrow Mass\ Density = \frac{142.37\ \frac{lb}{ft^3}}{12^3 \times 386.08\frac{in}{s^2}} = 0.0002134\ \frac{lbf.s^2}{in^4}$$

  - *Elastic properties*

$$E_c = 57{,}000\sqrt{f_c^{'}} = 57{,}000\sqrt{3{,}080} = 3{,}163{,}370\ psi$$

$$\upsilon_c = 0.25$$

  - *Plasticity* is defined in Table 4.30.

Table 4.30. Plastic properties of the concrete

Dilation Angle (ψ)	Eccentricity (e)	f_{bo}/f_{co}	*K*	Viscosity Parameter (μ)
35	0.1	1.16	0.667	0.0005

4.17 Control Specimens

From the experimental study [1], the compressive strength of the concrete was determined using 6×12 in. cylinders, and the tensile strength used splitting tests of 6×6 in. cylinders. The strength value represents an average of three tests.

4.18 Test Procedure

Tests were conducted in a screw-type testing machine with a 300,000 lb capacity [1]. The specimen was positioned in the machine to ensure that, after seating, the specimen's top surface was parallel to the loading head of the machine, which could not rotate. A load of approximately 10 lb. was applied before initial readings. The load was increased and decreased (after the maximum) in 10,000 lb. increments. The test was discontinued either when the load was reduced to approximately 10% of the maximum or if a tie fractured.

4.19 Finite Element Modeling of the RC Column

The test was carried on a 90 kips axially loaded 5 in.×5 in.×25 in. prism. The specimen was loaded to failure under axial compression. The investigation's principal purpose was to obtain data on the load-deformation characteristics of concrete as related to the rotation capacity of reinforced concrete connections. The distribution of longitudinal and transverse strain over the middle three-quarters of the specimen, where local deformations were measured, was relatively uniform. The boundary conditions of the numerical model are such that the bottom of the prism is fixed in all three translational degrees of freedom, and the top of the prism is fixed in the two transverse translational degrees of freedom, thus allowing the top of the prism to translate vertically. The concrete, reinforcement, and stirrup “Approximate global size” are 40. For the reinforcement Element Type, the Family is Truss, which changed the reinforcement element type to T3D2 (a 2-nodes linear 3-D truss).

Concrete specifications in Abaqus:

- 3D
- Deformable
- Solid
- Extrusion
- Homogeneous

Mesh:

- Approximate global size: 40
- Element Shape: Hex (hexahedral elements)

Instant Type: Dependent (mesh on part)

Element Type:

- Family: 3D Stress
- C3D8R: An 8-node linear brick, reduced integration, hourglass control
- Solid

The general loading, support conditions, and reinforcement details of the RC numerical model are shown in Figures 4.19.

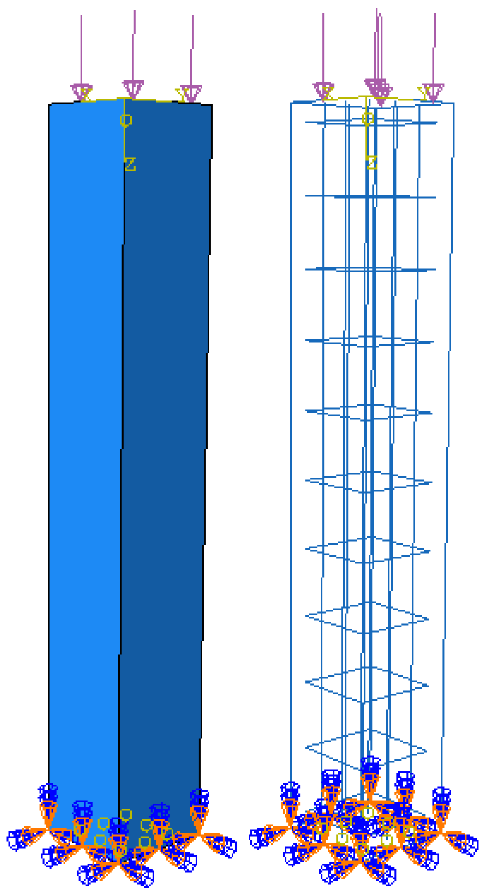

Figure 4.19. Isometric 3-D view

4.20 Results

Figures 4.21, 4.22, and 4.23 are plots of axial force versus average strain computed from the numerical results compared to those obtained from the experimental tests illustrated in Figure 4.20. All three load-deformation curves are based on deformation measured on the same specimen. Axial deformations were measured using two approaches: The first approach was finding the overall change (reduction) in the specimen length which the corresponding measurements were referred to as Gauge 1. The second approach to assess deformation was from the readings of two contiguous longitudinal gauges placed on the test specimen at mid-height. These were denoted as Gauge 2 and Gauge 3.

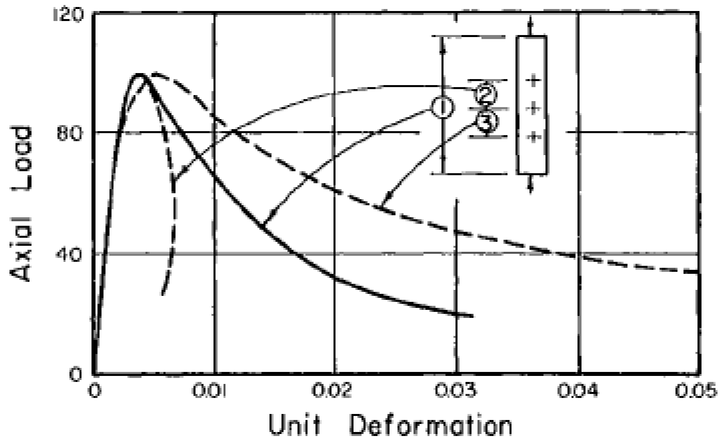

Figure 4.20. Generalized load vs. deformation in terms of overall average strain for experimental test

The gauge length for both gauges was 4 in. It is important to mention that after loading, spalling of the concrete occurred in the area covered by Gauge 3.

Figure 4.21 (Curve 1 in reference [1]) represents the relationship between the force and the overall average strain of the concrete prism. The strain in this curve is computed as the overall deflection divided by the length of the specimen (25 in.). In the experimental study, the overall deflection was measured using two 0.001 in. dial gauges located on opposite sides of the specimen and was denoted in [1] as Gauge 1 measurements. In the numerical analysis, the average strain values are determined by integrating the strains over the entire prism length and dividing the result by the entire length of the prism. Consequently, the plotted curves are shown with the horizontal axis representing the strain as the overall longitudinal deformation divided by the length of the specimen.

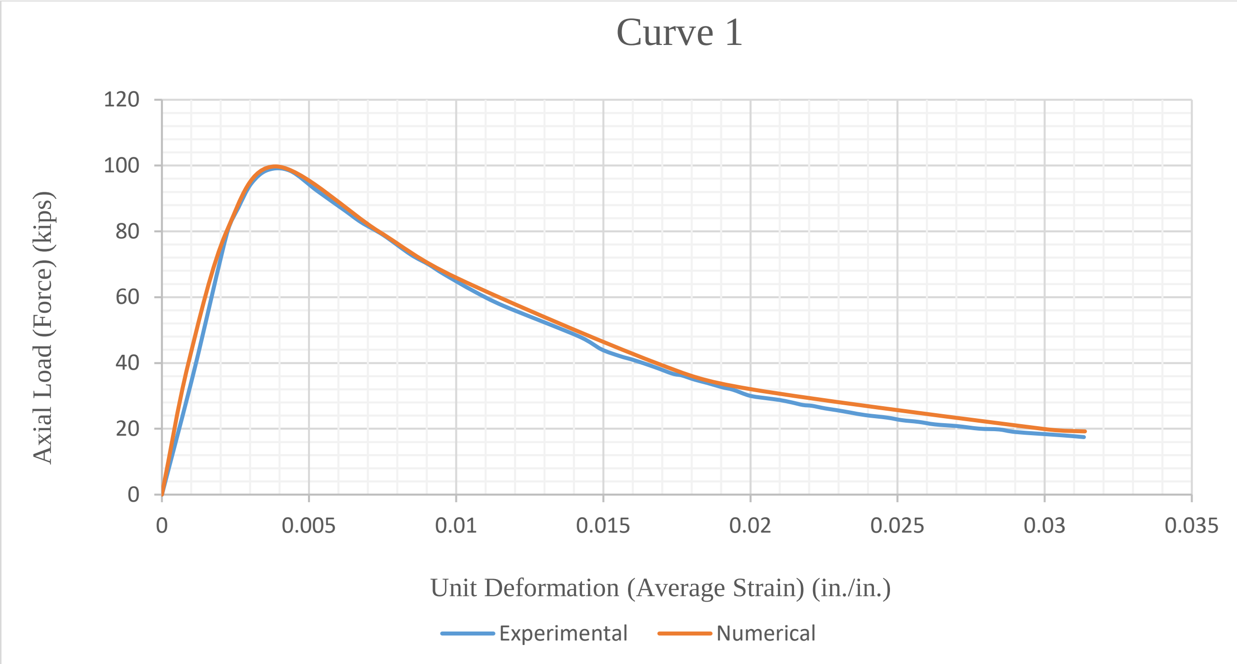

Figure 4.21. Generalized load vs. deformation in terms of overall average strain

It may be worth mentioning here that the generalized load versus unit deformation (strain) is shown here, rather than the typical stress versus strain or load versus deflection, to match the results obtained and published by Roy and Sozen [1].

Figures 4.22 and 4.23 represent the localized strain readings in the vicinity of mid-height of the concrete prism (at 12.5 in. from either the top or bottom ends of the prism). The gauge length used in computing the average strain reading is 4 inches. Figure 4.22 depicts the strains corresponding to the location of Gauge 2 (referred to as Curve 2 in reference [1]), whereas Figure 4.23 depicts the strains corresponding to the location of Gauge 3 (Curve 3 in reference [1]).

In the experimental study, as mentioned earlier, local deflections over the two contiguous 4 in. gauges lengths were measured using a special assembly attached to the specimens (Gauges 2 and 3) placed at mid-height. Curve 2 represents the localized strain reading in the vicinity of a low damage zone of the concrete prism, while Curve 3 represents the localized strain reading in the vicinity of a highly damaged zone of the concrete prism.

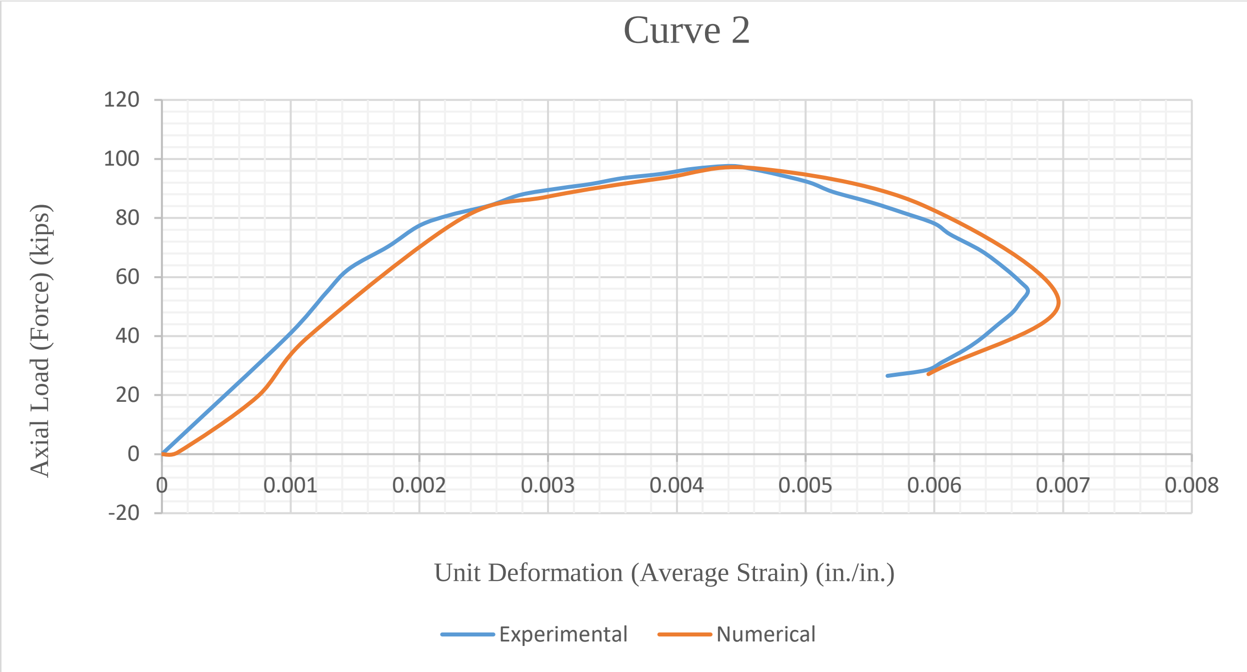

Figure 4.22. Generalized load vs. deformation in terms of localized strain at mid-height, at the location of Gauge 2

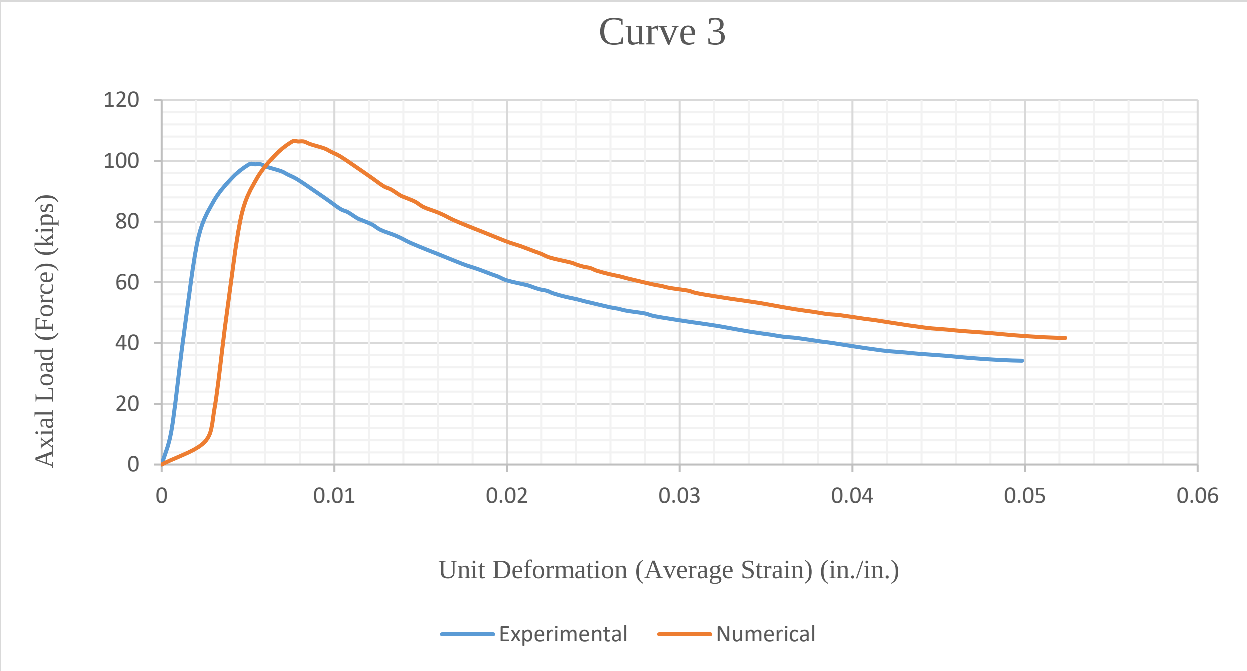

Figure 4.23. Generalized load vs. deformation in terms of localized strain at mid-height, at the location of Gauge 3

As stated above, Curve 3 represents the localized strain readings in the vicinity of the highly damaged zone of the concrete prism at the location of Gauge 3, where concrete spalling has occurred and was observed. Even though both Gauges 2 and 3 where installed next to each other at the prism mid-height, only concrete at the location of Gauge 3 has shown signs of spalling.

The three curves coincide up to approximately 80% of the maximum load; then Curve 3 breaks away from the other two curves due to spalling of the concrete in the area covered by Gauge 3. As deformations increase, deviations between the indications of Gauge 2 in Curve 2 and Gauge 3 in Curve 3 increase to the point that, toward the end of the specimen, Gauge 2 registers a lengthening, while Gauge 3 shows rapid shortening because destruction of the concrete is limited to the lower part of the specimen.

The typical characteristics of Curves 1, 2, and 3 (Figures 4.21, 4.22, and 4.23, respectively), demonstrate that the numerical results obtained from the sophisticated FEM analysis closely matched the experimental results, as the material characteristics in the numerical analysis are accurately represented by the more realistic material models. It is worth mentioning that the numerical analysis matches the actual concrete behavior even where spalling occurs. The spalling is not actually modeled in Abaqus; however, after performing the analysis by applying the loads and the specimen boundary conditions, spalling was clearly detected as indicated in the Abaqus results (this could be detected through different colors at that location). Generally, Curve 1 can be considered as the representation of the crude average of both Curves 2 and 3. As shown in Figure 4.21, the numerical results obtained from the numerical FEM model perfectly match the experimental results performed on the actual structural element.

4.21 Conclusions

In this research study, the author discussed the state-of-the-art methods that can be used to describe and anticipate the actual behavior of the concrete in tension and compression as well as the steel in tension. Numerical results were verified and compared to experimental tests performed by Roy and Sozen at the University of Illinois Urbana-Champaign. The experimental test results were used here to verify the mathematical model and research methodologies introduced in Chapters 2 and 3 of this dissertation. In their experimental investigation, these researchers had not considered modeling their columns in Finite Element Analysis packages, such as Abaqus.

Specimen A1.220 from the experimental data of Roy and Sozen was used to compare test results with those of the numerical modeling. Modeling parameters were discussed earlier in this dissertation. The analysis results are reasonable for a reinforced concrete prism subjected to uniaxial compression. The typical characteristics of the three curves used for comparison indicate that results from the numerical model closely matched the experimental results.

The case study presented in this chapter confirm that the modeling and methodologies proposed in this dissertation are valuable because they provide means to numerically assess the actual performance of constructed RC structures while accurately modeling the true behavior of the structural material. Accurate numerical modeling can be used to verify experimental test results such as those obtained by Roy and Sozen through mechanical testing, or by in-situ nondestructive evaluation of in-service structures. Numerical modeling with accurate representation of the material characteristics is also useful when experimental tests or in-situ structural monitoring are not possible or prohibitively expensive.

References

1) Roy, H. E. H., and Mete A. Sozen. 1965. "Home." Special Publication. January 1, 1965. https://www.concrete.org/publications/internationalconcreteabstractsportal/m/details/id/16718.

Chapter 5 : Summary, Conclusion and Recommendations

5.1 Summary

In his doctoral research, the author first reviewed the literature and presented the fundamental models and equations that govern the behavior of concrete in tension and compression, as well as the damage parameters of concrete (also in tension and compression). Next, the author addressed the different aspects of steel's behavior (in tension) and the various phenomena related to steel plasticity characteristics. Special attention was given to the steel cyclic behavior. The available models and formulations of the stress-strain curves, and parameters and concepts of cyclic steel behavior were studied and summarized. Then selecting the most appropriate methodologies from among the various ones presented, the author verified two fundamental tests performed and published by four well-established researchers in Structural-Earthquake Engineering, namely Professors Sezen and Moehle from the University of California-Berkeley [1], and Professors Roy and Sozen from the University of Illinois Urbana-Champaign [2].

For the behavior of concrete in compression, the author utilized the modified Hognestad model [3]. This was selected because it could correctly represent concretes with strengths up to about 6,000 psi (41.36 MPa) since the entire stress-strain curve is given by one continuous function.

In regard to the behavior of concrete in tension, the author applied the Belarbi and Hsu model [4].

For the damage parameters of concrete in tension and compression, the author employed the Tao et al. model, the state-of-the-art damage model proposed in 2014 in the Journal of Composites for Construction of the American Society of Civil Engineers [5].

Regarding the behavior of steel in tension, the Ramberg-Osgood model was used because the comparison to the tensile and compressive statistics for aluminum alloy, stainless steel, carbon steel, and carbon-steel sheets in Technical Note No. 840 from the National Advisory Committee for Aeronautics (NACA) says that the Ramberg-Osgood formula is sufficient for the majority of these materials [6].

5.2 Conclusions

The current study effectively implements a material model for concrete that simulates the nonlinear behavior of RC elements in finite element applications. The material model requires the maximum compressive concrete strength value and uses two numerical techniques, tension, and compression, to describe the stress-strain curves.

This research study also proposes various approaches to modeling the reinforcing steel bars (rebars) cyclic response when analyzing RC columns using the finite element method (FEM), and utilizing advanced built-in material models in sophisticated commercial FEM software such as Abaqus. The material models adequately simulated the key features of steel and the steel plastic components necessary for the various approaches to describe steel hardening. These models include Drucker-Prager plasticity (Prager's hardening rule), Abdel-Karim-Ohno plasticity model, Chaboche kinematic hardening rule, and Ohno-Wang model I (OWI) model, which were all initially studied in detail and investigated in depth.

After that, a verification study was performed to validate the proposed procedures. Two different applications were used for the verification, which consisted of comparing FEM numerical modeling with mechanically-tested specimens. All two verification applications demonstrated that by adopting the proposed accurate methods to represent material properties, it was possible to match the fundamental tests results. This verification study elucidated an excellent concordance between experimental and numerical results obtained with the proposed approaches, and the remarkable ability of the proposed methodology to replicate the experimental results obtained from testing actual full-size structural components.

The research presented in this dissertation demonstrates that accurate numerical modeling can be used to verify experimental test results such as those obtained through mechanical testing, or through in-situ nondestructive evaluation of in-service structures. Moreover, it can be generalized that FEM numerical modeling of reinforced concrete elements using accurate representations of the material characteristics such as those presented in this study can be very useful when experimental tests or in-situ structural monitoring are not possible or prohibitively expensive.

5.3 Recommendations for future work

This research may be extended to include other research areas. For instance, according to Nayal and Rasheed in 2006 [7], developing the stress-strain relationship for the tensile region requires implementing a numerical technique suitable for RC and fiber-reinforced concrete. Although this current research emphasizes only RC elements, the similarity of the tension stiffening model in RC elements may allow the model to be adopted for fiber-reinforced concrete with minor parametric changes. Hsu and Hsu (1994) proved that the compressive stress-strain relationship could accurately represent the strain-softening regime and adequately stimulate damage triggered by concrete crushing [8]. Thus, the presented material could be used for both RC and fiber-reinforced concrete elements to assess or simulate damage caused by concrete crushing and/or tensile cracking.

For future work in steel-reinforced concrete structural members, it may be beneficial to use finite element software other than Abaqus, such as ANSYS, ATENA and DIANA FEA, to determine if other software can give better numerical results, or if the analysis process can be performed any faster. Also, other test verification cases may be performed on additional structural members subjected to various types of loadings and different load combinations.

References

1. Sezen, Halil, and Jack P. Moehle. 2006. "Seismic Tests of Concrete Columns with Light Transverse Reinforcement." ACI Structural Journal 103 (6): 842–49. https://doi.org/10.14359/18236.

2. Roy, H. E. H., and Mete A. Sozen. 1965. "Home." Special Publication. January 1, 1965. https://www.concrete.org/publications/internationalconcreteabstractsportal/m/details/id/16718.

3. Building Code Requirements for Structural Concrete and Commentary (ACI 318-08): An ACI Standard. 2008. Detroit: American Concrete Institute.

4. Belarbi, Abdeldjelil, and Thomas T. C. Hsu. 1994. "Constitutive Laws of Concrete in Tension and Reinforcing Bars Stiffened by Concrete." Structural Journal. July 1, 1994. https://www.concrete.org/publications/internationalconcreteabstractsportal/m/details/id/4154.

5. Tao, Y., and J. F. Chen. 2014. "Concrete Damage Plasticity Model for Modeling FRP-to-Concrete Bond Behavior." Journal of Composites for Construction. American Society of Civil Engineers. April 21, 2014. https://ascelibrary.org/doi/10.1061/%28ASCE%29CC.1943-5614.0000482.

6. Ramberg, Walter, and William R Osgood. n.d. "Description of Stress-Strain Curves by Three Parameters - NASA Technical Reports Server (NTRS)." NASA. NASA. Accessed October 22, 2022. https://ntrs.nasa.gov/citations/19930081614.

7. Nayal, Rim, and Hayder A. Rasheed. 2006. "Tension Stiffening Model for Concrete Beams Reinforced with Steel and FRP Bars." Journal of Materials in Civil Engineering. American Society of Civil Engineers. December 1, 2006. https://ascelibrary.org/doi/abs/10.1061/%28ASCE%290899-1561%282006%2918%3A6%28831%29.

8. Hsu, L. S., and C.-T. T. Hsu. 1994. “Complete Stress — Strain Behaviour of High-Strength Concrete under Compression.” Magazine of Concrete Research 46 (169): 301–12. https://doi.org/10.1680/macr.1994.46.169.301.